30631693

SEISMIC PROPERTIES OF FAROE ISLAND BASALTS

RADCLIFFE SCIENCE LIBRARY OXFORD
DEPOSITED
16 MAY 2007
THESIS

Felicia M. J. Shaw

St. Edmund Hall

A thesis submitted in partial fulfillment of the requirements for the degree of D.Phil. The Department of Earth Sciences, University of Oxford, Trinity Term 2006.

ADDRESS : 112A CORONATION ROAD, S(269514),
REPUBLIC OF SINGAPORE
TEL. NO. : +65 96703331 (Singapore) / 07989434618 (U.K. mobile)
E-MAIL : fmjshaw8@singnet.com.sg / f.m.j.shaw@btinternet.com

SEISMIC PROPERTIES OF FAROE ISLAND BASALTS

Felicia M. J. Shaw

St. Edmund Hall

submitted in partial fulfillment of the requirements for the degree of D.Phil. in the Department of Earth Sciences, University of Oxford, Trinity Term 2006.

ABSTRACT

The Faroe Islands are part of the North Atlantic Igneous Province and comprise three subaerially erupted basalt formations: the Upper, Middle and Lower Series. Vertical VSP data, core data and wireline log data, acquired in two boreholes, were the basis for studying the seismic attenuation properties of Faroe Island basalts.

Over a restricted bandwidth of 40 – 150 Hz, mean Q in Glyvursnes is estimated to be ~ 25. There is evidence that Q increases with depth, corresponding with a transition from the Upper to Middle Basalt Series. Over 20 – 500 Hz, mean Q in Vestmanna is also estimated to be ~ 25, appearing constant over the full VSP interval.

1-D scattering is likely to be significant only in the upper section of Glyvursnes, where the Upper Basalt Series occurs. In Vestmanna and the lower Glyvursnes section, 1-D scattering Q is substantially higher than effective Q derived from the VSP data. 1-D

scattering in basalts is found to be a frequency-dependent phenomenon, linked to periodicity in velocity structure.

Analyses of log data reveal that geological factors exert primary controls on multifractal character. Multifractality tends to diminish 1-D scattering effects by disrupting the resonance of periodic velocity structures. 1-D multifractality does not give a clear indication of 2-D / 3-D heterogeneity, and synthetic multifractals must be used with caution in basalt modelling studies.

Field observations suggest that 3-D heterogeneity mainly arises from variable morphology of pahoehoe flows, which have low-velocity vesiculated crusts and high-velocity cores. However, pahoehoe-based models appear to produce less 3-D scattering with increasing structural variation. Overall, 1-D and 3-D scattering cannot fully account for the high attenuation in field data.

Hence, while evidence for the necessary fluid flow is inconclusive, indications are that intrinsic attenuation may be a significant component of energy dissipation in Faroe Island basalts.

EXTENDED ABSTRACT

Large igneous provinces cover millions of square kilometres of the Earth's surface. Key to understanding mantle dynamics and the creation of continents, they also cover large sedimentary basins that are targets of hydrocarbon exploration. Seismic imaging of basalt terranes could provide information on their morphology, thickness and evolutionary history.

Seismic profiles in basalt-covered areas commonly exhibit strong contamination with noise and / or severe attenuation at high frequencies. These are thought to result from back-scattering of energy by large velocity contrasts between basalt layers and weathered horizons. Wavefront disruption may also arise from these irregular interfaces. However, low quality imaging is not uniform across all areas. Poor and good quality profiles have been acquired in adjacent areas in the Tertiary Era North Atlantic Igneous Province (NAIP), and datasets display varying amounts of improvement under seismic processing techniques.

The Faroe Islands are an ideal seismic laboratory in which to study seismic properties of basalts in their geological context. The Faroes form part of the NAIP, which contains both productive fields and a number of hydrocarbon prospects. Three major geological formations are present on the islands: the Upper, Middle and Lower Basalt Series. The outcropping strata dip gently towards the east and can be traced offshore. Erupted in a marginal marine, subaerial environment, the lavas comprise varying proportions of

'compound braided' and 'massive tabular' flows. Sediment is thought to occur under 5 to 7 km of basalt but has not been reached by deep drilling.

Boreholes have been drilled at two locations on the island of Streymoy. Glyvursnes-1 samples 355 m of the Upper Basalt Series and 345 m of the Middle Basalt Series. The Vestmanna-1 borehole samples 560 m from the Middle Basalt Series and 100 m from the Lower Basalt Series, in rocks stratigraphically 500 m below the total depth of Glyvursnes-1. Wireline log data and near-zero-offset vertical seismic profiles (VSP) collected from these boreholes have been used extensively in this thesis.

The Glyvursnes VSP was recorded between 50 and 600 m depth. Due to poor source-to-bedrock coupling, the data-carrying bandwidth was restricted to 30 – 150 Hz. The Vestmanna VSP was recorded between 50 and 500 m depth, and had a data-carrying bandwidth of 20 – 500 Hz. Clearly-defined reflection events in the Glyvursnes borehole have been matched to strong acoustic impedance contasts. In comparison, reflections in Vestmanna are not as clear and are unevenly distributed. These differences may be due to the extent of lateral continuity of rocks in the two areas. V_p/V_s ratios were approximately 2.0 in Glyvursnes and 1.9 in Vestmanna, comparable with high values from other studies in the Lower Basalt Series and in the Southeast Greenland Margin.

Making the initial assumption that seismic quality factor (Q) is independent of frequency, effective Q was derived for the in-situ basaltic rocks. Two methods of analysis were applied to the VSP data: the spectral ratio method, which acts in the

frequency domain and thus has increased error bounds in narrow-band data; and an amplitude decay method, which acts in the time domain and requires the data to be first corrected for geometric spreading. Both forms of analysis were restricted to the primary wavelet alone.

As in studies conducted in other basaltic terranes, effective seismic Q from the two field sites was found to be consistently low. Under the spectral ratio method, Q in both boreholes was 20 – 40. The amplitude decay method returned Q values of 1 – 22 in Glyvursnes, and a mean Q value of 38 in Vestmanna. The results indicated an increase in Q values with depth for the Glyvursnes data, but constant Q in the bulk of Vestmanna data.

Acoustic modelling was carried out to assess the extent to which 1-D multiple scattering could account for the attenuation observed in the field data. Models were constructed from P-velocity and density log data of Glyvursnes and Vestmanna, and a method after Kennett was used to generate synthetic P-wave seismograms. The models were constructed to the same depth intervals as the respective VSPs, and the topmost VSP traces used as synthetic sources. In subsequent applications of the spectral ratio method, analysis was also restricted to the same frequency ranges as the VSPs.

Mean 1-D scattering Q was estimated to be 84 in Vestmanna, substantially higher than effective Q from the real data, and 31 in Glyvursnes, within the range of effective Q values from the real data. To investigate whether there were depth trends in 1-D

scattering behaviour, the 1-D models were partitioned into upper and lower sections and the analyses repeated. The Glyvursnes 1-D models exhibited the same low Q estimates as seen in the VSP data, and also the same increasing trend with depth. The Vestmanna estimates were once again higher than those of the real data.

The VSP-derived synthetic sources had different bandwidths and spectral profiles. Acoustic modelling was repeated with synthetic zero-phase sources to investigate the importance of source bandwidth of 1-D Q estimation, and to enable direct comparisons between Vestmanna and Glyvursnes. Two input sources were used: The first wavelet had a centre frequency of 150 Hz, imitating the narrow bandwidth of the Glyvursnes VSP, without the inherent spectral notches and complicated wavetrain of the field data. The second wavelet was broadband, with energy distributed evenly over 1 – 500 Hz and with a maximum frequency exceeding 800 Hz. 1-D Q estimates varied when different sources were used, showing that Q estimation was frequency-dependent.

Time-frequency analysis via Morlet wavelet scalograms revealed the cause of frequency-sensitive Q estimates. Localised spectral minima are created by the destructive interference of multiple energy, and the source bandwidth relative to these spectral minima leads to gradient changes in the linear regression step of spectral ratio Q analysis. The relative persistence of multiples can be distinguished by examining scalograms over longer time intervals. Ephemeral, short-lag multiples are particularly problematic as they have an impact on Q estimation but may not accurately represent the dominant mode of energy loss. Ephemeral multiples have led to the possible

underestimation of 1-D scattering in Vestmanna; in such cases the assigned Q numbers are to be treated as lower-bound estimates.

The upper Glyvursnes interval coincides with the occurrence of the Upper Basalt Series, and generates the most intense and persistent multiples. These basalts were found to have a quasi-periodic velocity structure and underlying resonant properties. Comparison of their time-frequency responses with those of relevant VSP traces showed spectral similarities. 1-D scattering is likely to be a dominant attenuation mechanism in the upper section of Glyvursnes (Upper Basalt Series), but not in Vestmanna or the lower 300 m of Glyvursnes (all classified as Middle Basalt Series).

Although macro-structures are most apparent in the upper Glyvursnes interval, all the log data show self-similarity, i.e. repetitive structure on a range of spatial scales. To assess the extent of fractality and self-similarity, acoustic impedance log data from Glyvursnes, Vestmanna and a third borehole at Lopra (sampling the Lower Basalt Series) were subjected to power spectral method analysis. Some anomalous values were produced and the results did not correspond with the varied seismic responses from 1-D modelling. This suggested that the power spectral method was inadequate to fully describe the fractal character of basalts.

A more sophisticated form of multifractal analysis is the Wavelet Transform Modulus Maxima method (WTMM), which is able to quantify the intensity and intermittency of fluctuations in a signal. Using a Mexican Hat wavelet, the acoustic impedance and

S-velocity log data from all three boreholes were analysed. Neutron porosity logs in Glyvursnes and Vestmanna were also analysed. The multifractal exponent values clustered strongly according to their geological formation. This suggests that geological factors are the primary control on 1-D variability in basalts.

However, multifractality in itself does not lead to strong 1-D attenuation. Synthetic log data were generated using a fractional integration method of non-conservative multiplicative cascades. They were similar to the actual Faroes wireline logs in both statistical measures and visual appearance, but acoustic modelling resulted in negligible multiple energy. The distribution of structures over a range of scales appears to disrupt the resonance which is responsible for intense, periodic multiples. Consequently, scattering attenuation is reduced in multifractal velocity structures. Synthetic multifractal logs must therefore be used with caution in modelling studies, as they cannot be assumed to produce the same seismic response as real logs. Neither is multifractality in 1-D a good indicator of heterogeneity in two and three dimensions. It is important to return to geologically-based models in constructing 3-D volumes.

Field studies of modern and ancient basalt terranes show that basalt architecture can be extremely complex. Heterogeneity is present in three dimensions and occurs from the metre scale to the kilometre scale. Further complexity arises from the deposition of sedimentary layers and intrusion of igneous bodies. However, at the scale of the VSP experiments, observations from the Faroes field sites indicate that pahoehoe lava flows are a major source of heterogeneity, due to their low-velocity vesiculated crusts,

high-velocity cores and variable flow patterns. Flows are commonly hummocky and topography is inverted as each successive flow builds up.

A numerical algorithm was implemented to construct 3-D pahoehoe structures. It was assumed that the aspect ratio of lava flows is smaller in the plane perpendicular to flow direction, and hence a degree of anisotropy was inherent in all the models. Velocity values were then assigned to the structures, generating four main basalt types which progressively increased in complexity.

Basalt 1 was a 3-D extrapolation of periodic two-velocity models previously studied in 1-D. *Basalt 2* tested the effect of larger lateral-to-vertical aspect ratio on seismic response, and was intermediate in structure between a 1-D planar model and *Basalt 1*. *Basalt 3* had a lobular velocity structure superposed on the framework of smaller flows. This introduced macro-scale velocity structure with a degree of spatial periodicity. *Basalt 4* had a varied velocity structure based on the log values of the Vestmanna VSP interval, and expressed the highest degree of heterogeneity. This model was considered to be a plausible analogue for Middle Series rocks.

Elastic wave propagation in two and three dimensions was modelled using a finite difference algorithm (the Discrete Particle Scheme). The amplitude decay method and the spectral ratio method of Q analysis were applied to the synthetic seismograms. Wavefront coherence and the intensity of scattered energy were also assessed by visual inspection.

3-D response deviated from that of 2-D orthogonal cross-sections with increasing lateral variation, especially in horizontal propagation. However, even at vertical incidence, amplitudes varied over a 550 m interval, and at certain depths were higher than amplitudes in a homogeneous control model. This effect was strongest in the model with velocity macro-structure (*Basalt 3*). It is thus possible for the magnitude of attenuation to change with depth, leading to a widely varying Q estimates in the same borehole.

There was also evidence that the spherical shape of the wave envelope cannot be disregarded even in a vertical VSP experiment over several hundred metres of rock. Due to the velocity contrast between pahoehoe crusts and cores, spectral minima were created and reinforced by periodicity in the 3-D volume. These shift in position according to the interaction of the wave with scattering heterogeneities, and have an impact on the calculation of Q.

There was inconclusive evidence as to whether pahoehoe flows were sufficiently rugose to generate surficial scattering.

Generally, scattering was increased when macro-scale velocity structures were present, when the lava flows had a smaller aspect ratio (usually in the plane perpendicular to flow), and when the velocity distribution was strongly bimodal. On the scale of several hundred metres, the presence of 3-D structural variation in basalts appeared to diminish

the effects of 1-D scattering rather than generate further energy loss. Overall, there was insufficient attenuation to account for field observations.

Having concluded that scattering is of diminished importance in Vestmanna and the lower 300 m of Glyvursnes, the remaining feasible mechanism of energy loss is that of anelastic attenuation from the presence of volatiles.

Recently, workers have derived low intrinsic Q estimates from saturated vesicular and pillow basalts in laboratory conditions, and fluid flow is suggested as the attenuation mechanism common to both seismic and ultrasonic scales. Detailed studies of Greenland basalts (which have a similar history to Faroes basalts) suggest that fluid flow is largely confined to highly altered, vesicular lava crusts. While fracture patterns / density are not well-resolved, core samples and optical televiewer images from Vestmanna and Glyvursnes show that alteration and high vesicularity are strongly associated with the lava crusts.

Quantifying intrinsic attenuation in basalts is problematic, as theoretical models incorporating fluid flow between pores, cracks and fractures are largely based on sedimentary rocks. This limits their applicability to Faroes rocks. However, when model parameters were adjusted to values from Faroes core samples, low intrinsic Q was exhibited. One variant model combines equant porosity model with randomly orientated cracks. Within seismic exploration frequencies, with arbitrary values

assigned to crack density, crack aspect ratio and crack radius, a guideline Q estimate of between 30 and 55 was derived.

In this work, robust Q estimates from field data have been compared with estimates from a range of increasingly complex numerical models. At the sub-kilometre scale, 3-D scattering from pahoehoe flow patterns and macro-structures has been found to be insignificant, and 1-D scattering appears to be dominant only in the Upper Basalt Series which occurs in Glyvursnes. While evidence for the necessary fluid flow is inconclusive, elimination of other mechanisms leaves intrinsic attenuation as a significant component of energy dissipation in Faroe Island basalts.

ACKNOWLEDGEMENTS

REG: *Alright*, but *apart* from the words of wisdom, the patience, the existentialist humour, the inspiration, the pleasant company, the never-say-die attitude, the editorial nip-and-tuck AND the water pump, *what have these people ever done for us*?!

Thanks go to my supervisor Prof. M. H. Worthington for guidance and for having huge reserves of patience. I am also grateful for the opportunity to work with the many members of the SeiFaBa project, and for sponsorship and support from SINDRI over the last few years.

The (long-suffering, occasionally amused) residents of the Faroe Islands must be mentioned, for putting up with loud bangs, broken windows and the constant cry of 'The Borrowers'. A list of all the people who have offered me assistance and goodwill would be a very long list indeed.

Thanks to Dr. Tim Pointer, for allowing the use of his intrinsic attenuation modelling software.

Thank you to Dr. A. Thomas-Betts for the moral support needed to begin this project. To my friends scattered across several time zones (i.e. the geólogos, the politicos, the musos, the kalinos, and the rest of you *not* covered in mud): all your helpful distractions in the course of writing up were much appreciated!

Finally, it is with great love that I dedicate this to my parents, for too many reasons to mention.

TABLE OF CONTENTS

Chapter		*Page*
	Abstract	i
	Extended Abstract	iii
	Acknowledgements	xiii
	Table of Contents	xiv
	List of Figures	xviii
	List of Tables	xxviii
1	**INTRODUCTION AND REVIEW**	**1**
1.1	Understanding flood basalts	1
1.2	Geology of the Faroe Islands	3
1.3	The SeiFaBa Project (Petrophysical and Seismic Properties of Faroes Basalts)	5
1.3.1	Boreholes on the Faroe Islands	6
1.3.2	Wireline log data	9
1.4	Vertical Seismic Profiling - a foreword	10
1.5	Attenuation and the seismic quality factor, Q	13
1.5.1	Theoretical derivation of Q	15
1.5.2	Intrinsic attenuation	19
1.5.3	Losses from multiple scattering	21
1.5.4	Losses from scattering in a heterogeneous volume	23
1.5.5	Frequency dependence of Q	26
1.6	Chapter Guide	27

2 DATA ACQUISITION ON THE FAROE ISLANDS 30

2.1 Acquisition of Vertical Seismic Profiles 31
2.1.1 Glyvursnes 31
2.1.2 Vestmanna 40
2.2 Preliminary VSP processing 49
2.2.1 Enhancement of the shear wave 52
2.2.2 Extraction of the upgoing wave 55
2.3 Well-tie 60
2.3.1 Velocity calibration for wireline logs and VSP 60
2.3.2 Deconvolution 62

3 EFFECTIVE ATTENUATION IN THE FAROES BASALTS 66

3.1 Q estimation from the spectral ratio method 67
3.1.1 Results 74
3.2 Q estimation from amplitude decay 79
3.2.1 Geometric spreading corrections 79
3.3 Time-frequency analysis 84
3.3.1 The Morlet Wavelet Scalogram 85
3.3.2 Scalograms of VSP traces 87
3.4 Discussion 93

4 1-D SEISMIC RESPONSE OF FAROES BOREHOLE LOGS 95

4.1 Wave propagation through plane-layered models 96
4.1.1 1-D scattering Q over depth intervals sampled by VSP 99
4.1.2 Trends in 1-D scattering Q with depth 100
4.2 Source bandwidth and 1-D scattering Q 105

4.3 Time-frequency analysis 109
4.3.1 Short-lag multiples 112
4.3.2 Intensity and persistence of multiples 112
4.3.3 Overall spectral profile 113
4.3.4 Comparison with VSP scalograms 114
4.4 Coarse layering and large velocity contrasts 117
4.5 Discussion 120

5 1-D HETEROGENEITY AND STATISTICAL STUDIES OF THE FAROES WIRELINE LOGS 122

5.1 Monofractal analysis 124
5.1.1 Power spectral method 125
5.1.2 Results 126
5.2 Multifractal analysis 131
5.2.1 The wavelet transform modulus maxima method (WTMM) 132
5.2.2 Choice of the analysing wavelet 138
5.2.3 Results 139
5.3 Relationship between 1-D scattering attenuation and multifractal character 143
5.3.1 Synthesis of multifractal logs 144
5.3.2 Seismic response of synthetic multifractal logs 148
5.4 Discussion 154

6 SEISMIC RESPONSE OF 3-D BASALT MODELS 156

6.1 Basalt architecture and emplacement 157
6.1.1 Modern basalts - Hawaii 158
6.1.2 Ancient flood basalts 162

6.2 Basalt architecture observed in the Faroe Islands 163
6.2.1 Field observations 163
6.2.2 Observations from optical televiewer images and borehole cores 167
6.3 Pahoehoe-based basalt models 170
6.4 Discrete Particle Scheme (DPS) implementation 174
6.5 Results from basalt modelling 190
6.5.1 Coherence of the wavefront 190
6.5.2 Amplitude of the primary wave 193
6.5.3 Spectral content of the primary wave 200
6.6 Discussion 206

7 OVERVIEW AND CONCLUSIONS 209

7.1 Overview 209
7.2 Effective attenuation in Faores basalts 211
7.3 Modelling of possible attenuation mechanisms 213
7.3.1 Multiple scattering from near-planar layers 213
7.3.2 Fractals in near-planar layers 214
7.3.3 Scattering in pahoehoe-type basalts 216
7.4 Intrinsic attenuation in basalts 219
7.5 Conclusions 225

REFERENCES 227

LIST OF FIGURES

1.1. Outcrop of Faroes Basalt Formations and the location of study boreholes (Japsen *et al.*, 2004).

1.2. Relation of the SeiFaBa boreholes to basalt stratigraphy (Japsen *et al.*, 2004).

1.3. Schematic VSP geometry compared to a reflection survey array. The relationship between geometry and trace recordings is shown.

1.4. Schematic diagram of the provenance of data on which Attenuation Theory is based.

2.1. The Glyvursnes headland.
Magenta square = Borehole
Yellow circles = Source locations at approx. 14 m, 242 m, and 415 m offset.
Dashed orange line indicates position of a fracture zone.
Adapted from map c. Danish National Survey & Cadastre.

2.2. The dyke at Glyvursgjógv. Remnant dyke rocks are indicated by the dashed red line.

2.3. Zero-offset air gun pit. The Sodera air gun was suspended above the pit by a wooden scaffold whilst being filled with compressed air.

2.4. 3-component geophone resting at the mouth of the borehole, on the pulley head.

2.5. Setup of observation area within the container. Hydraulic pump and reel of hydraulic cable tinted green; geophone cable, reel and winch control box tinted blue; field computer tinted magenta;
ES-3000 seismometer tinted orange. The Aarhus recording van (not pictured) was to the right of this illustrated setup and contained the trigger box.

2.6.
a. Raw data from the 50 m trace of the Glyvursnes VSP. Amplitudes of the three traces have been normalised
b. Raw data from the 600 m trace of the Glyvursnes VSP. Amplitudes of the three traces have been normalised for clearer display.
Gun trigger artefacts are seen at 0 and 0.02 seconds in both levels.

2.7. Vestmanna Sound.
Magenta square = Borehole
Yellow circles = Source locations at approx. 14 m, 230 m, and 610 m offset.
Green arrow indicates an electrical substation.
Adapted / updated from map c. Danish National Survey & Cadastre.

2.8. Overview looking WSW towards Vestmanna Sound. The picture highlights the yellow legs of the pulley on the borehole head. Nick Mohammed is pictured operating the hydraulic pumps for clamping the tool. The green circle highlights the position of the 610 m source (air guns towed behind a boat) in the distance.

2.9. View south from the timber yard. The yellow and red building is an electrical substation. A natural rock pool , seen in the lower right of the picture, was used as a source pit for the airguns.

2.10.
a. Raw data from the 50 m trace of the Vestmanna VSP. Amplitudes of the three traces have been normalised.
b. Raw data from the 500 m trace of the Vestmanna VSP. Amplitudes of the three traces have been normalised for clearer display.

2.11.
a. Raw data at the 335 m depth level. Amplitudes of the three traces have been normalised for clearer display.
b. Raw data at 340 m, showing stronger noise on the horizontal components. This was due to air leakage from the air gun.

2.12.
Band-passed Glyvursnes VSP data, displayed with trace-by-trace scaling.

2.13.
Band-passed Vestmanna VSP data, displayed with trace-by-trace scaling.

2.14.
Shear wave in Glyvursnes VSP, extracted by rotating the primary-wave to minimum energy. Displayed with trace-by-trace scaling.

2.15.
Shear wave in Vestmanna VSP, extracted by rotating the primary-wave to minimum energy. Displayed with trace-by-trace scaling.

2.16.
Extraction of upgoing waves from the Glyvursnes VSP.
a. First arrival times are picked, and the traces are time-aligned.
b. The data are median filtered with a 5 point window to create an approximate downgoing wave.
c. This is subtracted from the data, leaving the upgoing waves clearly visible.
d. Data are re-aligned to their true arrival times.
All data are displayed with trace-by-trace scaling. Only 0.2 seconds of data shown.

2.17.
Extraction of upgoing waves from the Vestmanna VSP.
a. First arrival times are picked, and the traces are time-aligned.
b. The data are median filtered with a 5 point window to create an approximate downgoing wave.
c. This is subtracted from the data, leaving the upgoing waves clearly visible.
d. Data are re-aligned to their true arrival times.
All data are displayed with trace-by-trace scaling. Only 0.2 seconds of data shown.

2.18. VSP first arrivals and integrated travel times from P velocity sonic logs from Glyvursnes (above) and Vestmanna (below).

2.19. Approximate downgoing waves used for deconvolution of Glyvursnes (above) and Vestmanna (below) data.

2.20. Upgoing waves (highlighted in green) matched to the acoustic impedance log of Glyvursnes.

2.21. Upgoing waves (highlighted in green) matched to the acoustic impedance log of Vestmanna.

3.1. Vestmanna VSP data prior to and after 5-point median filtering to suppress upgoing waves.

3.2. Glyvursnes VSP data prior to and after 5-point median filtering to suppress upgoing waves.

3.3.
a. Downgoing wavelets at 60 m and 490 m in the Vestmanna borehole. The time gates are double-tapered.
b. Amplitude spectra for the traces in 3.3a, with marked minima.
c. Spectral ratio plot. Least-squares linear regression is performed over a specified frequency range of 20 – 400 Hz. Q estimates are given for a 95% confidence interval of mean response.

3.4.
a. Downgoing wavelets at 70 m and 580 m in the Glyvursnes borehole. The time gates are double-tapered.
b. Amplitude spectra for the traces in 3.4a.
c. Spectral ratio plot. Least-squares linear regression is performed over a specified frequency range of 30 – 150 Hz. Q estimates are given for a 95% confidence interval of mean response.

3.5.
a. Monitor hydrophone record for the Vestmanna experiment.
b. Amplitude spectra of monitor hydrophone record in 3.5a, plotted to 800 Hz.

3.6.
Effective Q derived from Vestmanna VSP data by the spectral ratio method, for a depth separation of 250 metres between traces. No clear depth trend with Q was seen. b. Effective Q values from the upper half of the Vestmanna VSP data. c. Effective Q values from the lower half of the Vestmanna VSP data.

3.7.
a. Monitor hydrophone record for the Glyvursnes VSP experiment.
b. Amplitude spectra of monitor hydrophone record in 3.7a, plotted to 400 Hz.

3.8.
a. Effective Q derived from Glyvursnes VSP data by the spectral ratio method, for a depth separation of 250 metres between traces. b. Effective Q values from the 50 – 350 m traces of the Glyvursnes VSP data. c. Effective Q values from 360 – 600 m tracesof the Glyvursnes VSP data.

3.9. Q estimates from amplitude decay in the Glyvursnes VSP data, after spherical spreading correction. There appears to be a significant change in gradient at 160 m. Average frequency used was 30 Hz. Q range from 95% confidence intervals and variation in velocity / frequency was 1 – 4 in the upper section and 15 – 40 in the lower section respectively.

3.10. Q estimates from amplitude decay in the Vestmanna VSP data, after spherical spreading correction. The change in gradient is gradual. Average frequency used was 200 Hz upper section, and 71 Hz in the lower section. Q range from 95% confidence intervals and variation in velocity / frequency was 10 – 90 in the upper section and 50 – 200 in the lower section respectively.

3.11. Example seismic trace and its Morlet wavelet scalogram. Red regions represent the greatest energy concentration, blue regions the least. The speckled appearance derives from destructive interference of wavelet components.

3.12. Traces from the Glyvursnes VSP at 50, 180, 320 and 600 m depth, and their corresponding scalograms, displayed to a maximum scale of 100. The greatest energy is centred on scale 30 (~ 33 Hz). The full colour scaling covers a linear, normalised amplitude range of 0 - 100%.

3.13. Detail of the 320 and 600 m trace scalograms shown in Figure 3.7. The very high frequency components seen in the right hand 600 m trace and scalogram, invariant over time, are noise. Note that scale only extends to 20, a minimum pseudo-frequency of 50 Hz. The full colour scaling covers a linear, normalised amplitude range of 0 - 100%.

3.14. Traces from the Vestmanna VSP at 50, 160, 275, 380, 440 and 500 m depth, and their corresponding scalograms. Note that scale only extends to 20, a minimum pseudo-frequency of 50 Hz. The full colour scaling covers a linear, normalised amplitude range of 0 - 100%.

3.15. Traces from the Vestmanna VSP at 50 and 500 m depth, and their corresponding scalograms displayed to a scale of 100. There is relatively little energy between 10 and 30 Hz. The full colour scaling covers a linear, normalised amplitude range of 0 - 100%.

4.1. Velocity and density logs of the Faroes boreholes.

4.2.
a. Input and output primary wavelets of synthetic seismograms, for a 1-D model of the 60 – 275 m interval of the Vestmanna velocity and density logs.
b. Amplitude spectra for the traces in 4.2a.
c. Spectral ratio of the input and output traces. Q estimates are given for a 95% confidence interval of mean response.

4.3.
a. Input and output primary wavelets of synthetic seismograms, for a 1-D model of the 275 – 490 m interval of the Vestmanna velocity and density logs.
b. Amplitude spectra for the traces in 4.3a.
c. Spectral ratio of the input and output traces. Q estimates are given for a 95% confidence interval of mean response.

4.4.
a. Input and output primary wavelets of synthetic seismograms, for a 1-D model of the 70 – 320 m interval of the Vestmanna velocity and density logs.
b. Amplitude spectra for the traces in 4.4a.
c. Spectral ratio of the input and output traces. Q estimates are given for a 95% confidence interval of mean response.

4.5.
a. Input and output primary wavelets of synthetic seismograms, for a 1-D model of the 320 – 580 m interval of the Glyvursnes velocity and density logs.
b. Amplitude spectra for the traces in 4.5a.
c. Spectral ratio of the input and output traces. Q estimates are given for a 95% confidence interval of mean response.

4.6. Results of acoustic modelling of the Faroes borehole logs with synthetic source wavelets. Input primary wavelets are plotted in grey. Output primary wavelets are overlaid in black. In all experiments, the output wavelets are impinged on by multiples but show little actual broadening.

4.7. Broadband response for 1-D models of Glyvursnes (70 – 320 m interval) and Vestmanna (60 – 275 m interval). Primary wavelets were isolated using a double-tapered time gate of 20 ms. The least-squares linear regression lines (red) change in gradient depending on the bandwidth selected. This in turn leads to varying estimates of Q.

4.8. Seismograms of the Vestmanna 1-D model between 60 – 275 m and their corresponding scalograms. Left: Broadband 800 Hz synthetic source. Right: Peak 150 Hz synthetic source. The full colour scaling covers a linear, normalised amplitude range of 0 - 100%.

4.9. Seismograms of the Vestmanna 1-D model between 275 – 490 m and their corresponding scalograms. Left: Broadband 800 Hz synthetic source. Right: Peak 150 Hz synthetic source. The full colour scaling covers a linear, normalised amplitude range of 0 - 100%.

4.10. Seismograms of the Glyvursnes 1-D model between 70 – 320 m and their corresponding scalograms. Left: Broadband 800 Hz synthetic source. Right: Peak 150 Hz synthetic source. The full colour scaling covers a linear, normalised amplitude range of 0 - 100%.

4.11. Seismograms of the Glyvursnes 1-D model between 70 – 320 m and their corresponding scalograms. Left: Broadband 800 Hz synthetic source. Right: Peak 150 Hz synthetic source. The full colour scaling covers a linear, normalised amplitude range of 0 - 100%.

4.12. Seismograms and scalograms of the Glyvursnes VSP trace at 320 m (left) compared with those of the 1-D models (right), between 10 and 50 Hz. The full colour scaling covers a linear, normalised amplitude range of 0 - 100%.

4.13. Seismograms and scalograms of the Glyvursnes VSP trace at 580 m (left) compared with those of the 1-D models (right), between 10 and 50 Hz. The full colour scaling covers a linear, normalised amplitude range of 0 - 100%.

4.14.
a. Two-velocity model (black) based on the upper Glyvursnes section, 60 – 320 m (grey).
b. Amplitude spectrum of seismic response from the two-velocity model (black), when a broadband 800 Hz source is propagated through it. Amplitude spectrum of seismic response from a model with the same velocity contrast, but with layers spaced uniformly, 5 m apart (blue). The first dominant minimum is centred on 225 Hz.
c. Broadband spectral response for primary wavelets only. The least-squares linear regression lines (red) change in gradient depending on the bandwidth selected, and produce similar Q estimates to the unfiltered 1-D model (see Figure 4.7).

5.1.
a. Acoustic impedance log of the Vestmanna borehole.
b. Power spectral analysis of the upper interval, 50 – 255 m.
c. Power spectral analysis of the lower interval, 296 – 500 m.

5.2.
a. Acoustic impedance log of the Glyvursnes borehole.
b. Power spectral analysis of the upper interval, 50 – 255 m.
c. Power spectral analysis of the lower interval, 396 – 600 m.

5.3.
a. Acoustic impedance log of the Lopra borehole.
b. Power spectral analysis of the upper interval, 1250 – 1562 m.
c. Power spectral analysis of the lower interval, 2600 – 2912 m.

5.4. Synthetic discontinuities (top row), their expression in Wavelet Transform space, and corresponding alpha values (from Herrmann, 1998). Abrupt discontinuities take on negative values.

5.5.
a. Vestmanna acoustic impedance log (50 – 255 m) with its continuous Wavelet Transform using the Mexican Hat wavelet.
b. The Continuous Wavelet Transform of the same data as above, using a Morlet wavelet.
c. Detail of the Wavelet Transform and its corresponding modulus maxima or 'skeleton'. Energy occurs at a continuum of scales.
d. Log fractal partition functions vs log scales.
e. The fractal scaling exponent $\tau(q)$ as a function of moment, q.

5.6. A theoretical multifractal singularity spectrum, after Mandelbrot, 1989.

5.7. Experimental singularity spectra, derived from the WTMM method, of acoustic impedance logs from three Faroes boreholes. a. Vestmanna. b. Glyvursnes. c. Lopra.

5.8.
a. α exponents of acoustic impedance, S-velocity and neutron porosity logs from the Faroes boreholes. The analyses used a Mexican Hat wavelet.
b. α exponents of the same Faroes borehole logs using a Morlet wavelet in analyses.

5.9. Normalised synthetic multifractals.
a. Higher C1 values indicate greater intermittency.
b. Lower χ values indicate greater fluctuation.

5.10. Real data points (legend as in Figure 5.8) plotted against the spread of exponents from synthetic multifractals (translucent surface).

5.11. Synthetic seismic responses of multifractal model 10 (see Table 5.4), and corresponding WT scalograms. The full colour scaling covers a linear, normalised amplitude range of 0 - 100%. C1 = 0.04, χ = 0.7. The multifractal was normalised to velocity and density ranges of the upper section of Vestmanna.
Left: The source was a broadband wavelet with frequency content to 800 Hz. Q range ~ 978 - infinity.
Right: The source was a wavelet with peak frequency of 150 Hz. Q range ~ 206 - infinity.

5.12. Synthetic seismic responses of multifractal model 10 (see Table 5.4 and Figure 5.11), with corresponding WT scalograms. The full colour scaling covers a linear, normalised amplitude range of 0 - 100%.
Left: The model was normalised to velocity and density ranges of the upper section of Vestmanna. Q range ~ 206 - infinity.
Right: The model was normalised to velocity and density ranges of the upper section of Glyvursnes. While the multifractal statistics are the same, interference from multiples is stronger. Q range ~ 87 - infinity.
The source was a wavelet with peak frequency of 150 Hz.

6.1. Idealised cartoon of the cross-section through an inflated pahoehoe lobe, from Self *et al.* (1998). The lobe is divided into three sections on the basis of vesicle structures, jointing, and crystal texture.
Upper crust: Vesicular, often with discrete horizontal vesicular zones (VZs) that form during active inflation. Bubble size increases with depth. Prismatic or irregular jointing occurs, sometimes equivalent to the entablature in thick lava flows. Petrographic texture ranges from hypohyaline to hypocrystalline (90–10% glass).
Core: Very few vesicles. Porosity is dominated by diktytaxitic voids. Vesicles are mostly in the silicic residuum, which forms vesicle cylinders (VCs) and vesicle sheets (VSs). Holocrystalline (<10% glass).
Lower crust: Nearly as vesicular as the upper crust, few joints, and 50–90% glass.
This architecture has been observed at smaller scales in Hawaii and Iceland, and on a much larger scale in the Columbia River Basalts (Self *et al.*, 1998).

6.2.
Cartoon cross-sections of the formation of tumuli and inflation pits and the inversion of topography during inflation, from Self *et al.* (1998).
a. Initially, small pahoehoe lobes are confined to the lowest areas.
b, c. As the flows continue to advance, they also inflate and spread laterally, filling the depressions. Because the thickest crust is on the oldest part of the sheet, the highest inflation is over what was originally the lowest ground. Breakouts from the thick inflation features can eventually cover the earlier high ground.

6.2d. Depending on the rate of inflation relative to the rate of crust growth, either a continuous sheet (left) or an inflation pit (right) forms over the previous high points. Most inflation pits widen with depth as the lobe cools inward with time. Inflation pits at the margins of sheet lobes may have steep monoclinal folds.

6.3. Massive tabular flow (from Single *et al.*, 2004).

6.4. Possible pahoehoe inflation structure, old quarry above Glyvursnes. Fence posts are 1.5 metres high.

6.5. Compound braided flow (from Single *et al.*, 2004).

6.6. Optical televiewer image from Glyvursnes borehole, 451.0 m (Middle Basalt Series), showing bands of vesicles.

6.7. Top down view of core boxes 091 / 092 from Glyvursnes borehole, 415 – 423 m (Middle Basalt Series). Vesicular zones and sheets are visible from 419 to 420 m, and a high velocity flow core is visible between ~ 420 and 422 m.

6.8. Model 1, narrow flows, two velocities.
a. Cross-section through midpoint of model, plane perpendicular to lava propagation direction. An asterisk represents he source position. Velocity colour scale is in m/s.
b. Horizontal cross-section through the 200 m depth level.
c. Cross-section through midpoint of model, plane parallel to lava propagation direction.
d. P-velocity profile through the borehole.

6.9. Model 2, wider flows, two velocities.
a. Cross-section through midpoint of model, plane perpendicular to lava propagation direction. An asterisk represents he source position. Velocity colour scale is in m/s.
b. Horizontal cross-section through the 200 m depth level.
c. Cross-section through midpoint of model, plane parallel to lava propagation direction.
d. P-velocity profile through the borehole.

6.10. Model 3, narrow flows, four velocities.
a. Cross-section through midpoint of model, plane perpendicular to lava propagation direction. An asterisk represents he source position. Velocity colour scale is in m/s.
b. Horizontal cross-section through the 200 m depth level.
c. Cross-section through midpoint of model, plane parallel to lava propagation direction.
d. P-velocity profile through the borehole. Larger lobes appear to have a thickness of between 20 and 50 m.

6.11. Model 4, narrow flows, varied velocities.
a. Cross-section through midpoint of model, plane perpendicular to lava propagation direction. An asterisk represents he source position. Velocity colour scale is in m/s.
b. Horizontal cross-section through the 200 m depth level.
c. Cross-section through midpoint of model, plane parallel to lava propagation direction.
d. P-velocity profile through the borehole.

6.12. Wavefield from a homogeneous model, with uniform velocity 5250 m/s, run through 2-D DPS. The source is a force acting in the z-direction, hence the S-wave amplitude approaches zero in the line of the borehole.

6.13.
a. Model 1X. Receivers are represented by black squares.
b. The corresponding wavefield.

6.14.
a. Model 1Y. Receivers are represented by black squares.
b. The corresponding wavefield.

6.15.
a. Model 2X. Receivers are represented by black squares.
b. The corresponding wavefield.

6.16.
a. Model 2Y. Receivers are represented by black squares.
b. The corresponding wavefield.

6.17.
a. Model 3X. Receivers are represented by black squares.
b. The corresponding wavefield.

6.18.
a. Model 3Y. Receivers are represented by black squares.
b. The corresponding wavefield.

6.19.
a. Model 4X. Receivers are represented by black squares.
b. The corresponding wavefield.

6.20.
a. Model 4Y. Receivers are represented by black squares.
b. The corresponding wavefield.

6.21. Details of Models 1 and 2, showing relative rugosity of surfaces.

6.22. Gain/loss in amplitude with depth, relative to propagation through a homogeneous model with velocity 5250 m/s.
a. Vertical receiver amplitudes in plane X, perpendicular to basalt flow direction.
b. Vertical receiver amplitudes in plane Y, parallel to basalt flow direction.
c. Horizontal receiver amplitudes in plane X, perpendicular to basalt flow direction.
d. Horizontal receiver amplitudes in plane Y, parallel to basalt flow direction.
1 = narrow-flow, two-velocity basalt
2 = wide-flow, two-velocity basalt
3 = lobular basalt
4 = varied-velocity basalt

6.23. Normalised vertical receiver array amplitudes from basalt types 3 and 4. Plane X is perpendicular to pahoehoe flow direction, plane Y is parallel to flow. Full 3-D model amplitudes are compared with separately modelled 2-D cross-sections

6.24. Normalised horizontal receiver array amplitudes from basalt types 3 and 4. Plane X is perpendicular to pahoehoe flow direction, plane Y is parallel to flow. Full 3-D model amplitudes are compared with separately modelled 2-D cross-sections.

6.25. Predicted relative amplitudes for a 3-D basalt volume of 600 m depth and 1000 m width, based on 2-D vertical receiver arrays in Figure 6.22. No averaged prediction for the horizontal receivers was made.
1 = narrow-flow, two-velocity basalt
2 = wide-flow, two-velocity basalt
3 = lobular basalt
4 = varied-velocity basalt

6.26. Log of amplitude ratios versus depth for hypothetical 3-D models. (Also see Figure 6.25.) Mean Q estimates corresponding to regression lines are ~ 530, 30, 130 and 90 for Basalts 1- 4 respectively. The range in Q is given by a 95% confidence interval for the mean response.
Basalt 1 = narrow-flow, two-velocity basalt
Basalt 2 = wide-flow, two-velocity basalt
Basalt 3 = lobular basalt
Basalt 4 = varied-velocity basalt

6.27. Log spectral ratios of a receiver at 550 m compared to the source in:
a, b. 2-D models.
c, d. 1-D planar models constructed from vertical velocity profiles through centres of the 2 D models.
1 = narrow-flow, two-velocity basalt
2 = wide-flow, two-velocity basalt
3 = lobular basalt
4 = varied-velocity basalt
X and Y are planes perpendicular and parallel to flow propagation, respectively.
Emboldened lines represent the bandwidth over which linear regression analysis was performed. Corresponding Q estimates are presented in the legend, ranging over a 95% confidence interval.

6.28. Normalised log spectral ratio of primary wavelet at 200 m relative to the source, in basalt types 3 and 4. Plane X is perpendicular to pahoehoe flow direction, plane Y is parallel to flow. Log spectral ratios from the full 3-D model are compared with separately modelled 2-D cross-sections.

6.29. Composite view of log spectral ratios taken with respect to the same source signature. Frequency (Hz) is plotted on the x-axis, depth (m) on the y-axis. Dark areas are spectral minima.

7.1. The range of key Q estimates from experiments in this thesis, and the bandwidths over which they were calculated.

7.2. Attenuation curves for theoretical rock models with petrophysical characteristics of Faroes rock samples. Lava crust: crack density = 0.07, crack aspect ratio = 0.001, crack radius = 3 x 10^{-3} m, permeability = 5.72 x 10^{-16} m^2, porosity = 0.206. Q ~ 33 – 40.
Lava core: crack density = 0.05, crack aspect ratio = 0.001, crack radius = 3 x 10^{-3} m, permeability = 1.97 x 10^{-17} m^2, porosity = 0.072. Q ~ 35 – 55.

LIST OF TABLES

1.1. Summary of datasets studied.

2.1. Comparison between Glyvursnes and Vestmanna acquisition parameters.

2.2. Comparison between Glyvursnes and Vestmanna experimental setup.

4.1. Estimated 1-D scattering Q values. The range is given by a 95% confidence interval of the mean response. Mean Q values are emboldened.

5.1. Depth range of borehole log datasets analysed.

5.2. Hurst exponents over four borehole intervals derived from the power spectral method.

5.3. Alpha values for singularity spectra derived from WTMM analysis using the Mexican Hat wavelet.
AI = acoustic impedance
V_s = S-velocity
Φ_n = neutron porosity

5.4. All the datasets above were normalised to the Vestmanna V_p and density logs.

5.5. First order statistics seen in Vestmanna and Glyvursnes P-velocity and density logs. Emboldened values are those used in normalising the multifractals for 1-D acoustic modelling.

6.1. Q values derived from various models and methods in Chapter 6. The range is given by a 95% confidence interval of the mean response. Mean Q values are emboldened.

CHAPTER 1

INTRODUCTION AND REVIEW

1.1 UNDERSTANDING FLOOD BASALTS

Continental flood basalts, volcanic passive margins and oceanic plateaus represent the largest known igneous episodes over the last several hundred million years. Collectively classified as 'large igneous provinces' and covering millions of square kilometres, they are pivotal in understanding the growth of continents, global plate tectonics and mantle dynamics (Wright *et al.*, 1973; Anderson, 1994; Mahoney & Coffin, 1997). They also carry implications for research into oceanography, atmospheric chemistry, climatic change and mass extinctions (Renne *et al.*, 1995). The origins of large igneous provinces are still debated, though the starting-plume hypothesis (White & McKenzie, 1989) is widely accepted.

To understand the evolution of large igneous provinces, the duration, rate, turbulence and intermittency of extrusion must be quantified. These can only be measured

indirectly, through inter-related proxies such as the chemistry, thickness and morphology of the flows. Here, seismic imaging provides useful constraints, in select circumstances revealing details of internal structure (Planke & Cambray, 1998; Ziolkowski *et al.*, 2003; Richardson *et al.*, 1998; White *et al.*, 2003).

The motivation for seismic imaging of basalts is commercial as well as academic. Flood basalt-covered sedimentary basins exist throughout the world's continental margins and are potential targets for hydrocarbon exploration. This has led to strong interest in sub-basalt imaging. The North Atlantic Igneous Province (NAIP), of which the Faroe Islands are part, has long been a focus for research (Fleet & Boldy, 1999). Covering an area of 1.3×10^6 km^2, (Eldholm & Grue, 1994), it encompasses productive fields and a number of hydrocarbon prospects.

Basalts present unique challenges for seismic imaging. Papworth (1985) observed that seismic data from diverse basalt-covered areas in Northern Ireland, the west of Scotland, Libya and Brazil were contaminated by high levels of noise, and attributed this to back-scattering. There was also low energy returned at frequencies above 40 Hz. The large velocity contrast between basalt layers and palaeosols (weathered horizons) was cited as a possible reason for scattering and the low-pass filtering effect. It was speculated that irregularities on top, within, and at the base of basalts could also have generated noise. Warner *et al.* (2002) review the problems: wave transmission is thought to be disrupted by high velocity contrasts between basalts and adjacent sedimentary strata, as well as by the rugosity of the surfaces.

However, poor quality imaging is not uniform across all basalt-covered areas. Refined processing techniques applied to both recently acquired and older survey data (e.g. Ogilvie *et al.*, 2001) have shown details of basalt stratigraphy, but are unsuccessful in nearby profiles (e.g. Boldreel & Andersen, 1993). This inconsistency highlights the need to study the physical properties of basalts in their three-dimensional geological context.

1.2 GEOLOGY OF THE FAROE ISLANDS

At the beginning of the Tertiary Era, the area of the Hebrides was raised above sea level, leading to the erosion of chalk oozes accumulated during the Cretaceous. Peneplained surfaces dating from the Jurassic and earlier were thus exposed.

An extensive fracture system began to develop in the crust as the incipient North Atlantic Ocean was created, causing the Greenland area to move away from what is now north-western Europe. In what is thought to be the most extensive volcanic episode in the region's history, extrusives from these fractures spread over both margins of the widening North Atlantic. In the present day these cover an area comprising Northern Ireland, the Rockall Bank, the Inner Hebrides, the Faroe Islands, Iceland, Jan Mayen Island and East Greenland (Ziegler, 1988). The onset of volcanism in the Faroes area is presumed to relate to the early magmatic underplating caused by the arrival of the Icelandic plume at about 62 Ma (White & Lovell, 1997).

The Faroe Islands are the exposed part of the Faroes Block, a sizeable fragment of continental crust capped by the Faroe Plateau Lava Group. The Group is composed of three basalt formations that can be traced from outcrop to offshore (Hald & Waagstein, 1984). Termed the Lower, Middle and the Upper Basalt Series / Formations, they are estimated to have a total thickness of up to 7 km (Waagstein, 1988).

The Lower Series is characterised by massive flows on the order of 20 m thickness, interbedded with thin tuffaceous sediments, hyaloclastites and volcaniclastic sediments (White *et al.*, 2003). Exposures have been dated to magneto-chrons C26n, C25r and C25n by Waagstein (1988). The formation's upper limit is marked by a coal-bearing sequence known as the A-horizon, which indicates subaerial extrusion. The A-horizon is chrono-stratigraphically correlated with sediments from the north-east Rockall Trough (Waddams & Cordingley, 1999) and represents a hiatus in volcanic activity of up to 0.5 Ma during the mid to late Thanetian.

The Middle Series is estimated to be about 1.4 km thick, and generally has a dark grey, hummocky appearance. The basalts have been interpreted as thinly-bedded, compound pahoehoe flows, comprising porphyric lavas (Ellis *et al.*, 2002). The beds thicken towards the top of the formation, in what is known as the C-horizon, and then progress without hiatus into the Upper Basalt Series (Rasmussen & Noe-Nygaard, 1970).

Basalts from the Upper Series are lighter grey in appearance, with massive flows of greater average thickness than the Lower and Middle Series. These have been

interpreted by certain workers as aa flows, although recent geological fieldwork in the Glyvursnes area concludes that they may be inflated pahoehoe sheets (Passey, 2005). Geochemical evidence supports a change in the source composition or depth of melting between the Middle and Upper Series (Wood, 1979).

Floral / faunal assemblages provide evidence that the Faroe Plateau Lavas were erupted in a marginal marine, subaerial environment (Ellis *et al.*, 2002). This is congruent with chemical signatures of crustal contamination, which indicate extrusion through and onto continental crust. Progressive uplift has since gently tilted the strata down towards the east (Saunders *et al.*, 1997).

1.3 THE SEIFABA PROJECT (PETROPHYSICAL AND SEISMIC PROPERTIES OF FAROES BASALTS)

Excellent exposure of key rock formations, which can be followed onshore to offshore, make the Faroe Islands a natural test laboratory. The SeiFaBa Project (Petrophysical and Seismic Properties of Faroes Basalts) commenced in 2002, to extend knowledge of elastic properties and three-dimensional heterogeneity of basaltic sequences.

The project's objective was to create data-driven models with data integration at all levels, enabling anisotropy, attenuation and offset-dependent amplitude variations to be studied in detail. Vertical seismic profiles and surface seismic data were to be

combined across a shear zone seen at one of the selected field sites. As a first step, rock core, well log, offset / walkaway vertical seismic profiles and surface seismic data were collected at two main sites.

1.3.1 BOREHOLES ON THE FAROE ISLANDS

Three boreholes are situated onshore of the Faroes. The first, the Lopra-1 well, is located on the island of Suđuroy (Figure 1.1). Initially drilled to a depth of 2178 m in 1981, it was later extended to 3565 m depth via the sidetrack Lopra-1A re-entry well. However, the base basalt boundary was still not reached, and the contact between the lower lavas and the underlying sediments could not be identified.

The Vestmanna-1 borehole, on the north-western coast of Streymoy (Figure 1.1), was drilled in 1980 to a depth of 660 m. The purpose was to find the down-dip extension of the A-horizon, which separates the Lower and Middle Series. The borehole passes through 560 m of Middle Series porphyric lavas and through about 100 m of Lower Series Basalts (Figure 1.2), with the A-horizon occurring as a 3 m thick succession of sedimentary rocks. Coal is not present in the borehole, although seams are commonly found in exposures of the A-horizon on Suđuroy. As part of the SeiFaBa project, the borehole was reamed to 590 m in 2003.

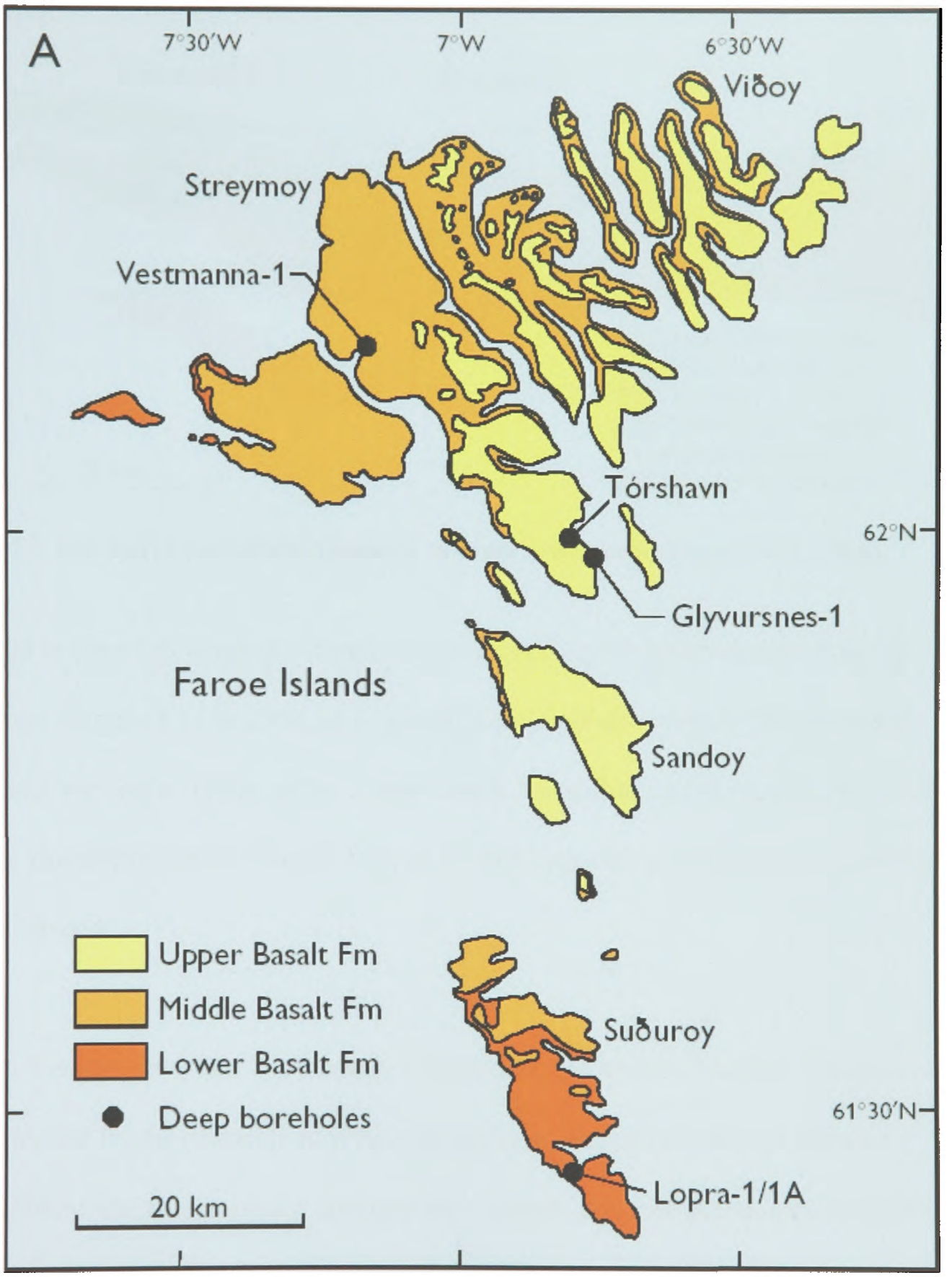

Figure 1.1. Outcrop of Faroes Basalt Formations and the location of study boreholes (Japsen *et al.*, 2004).

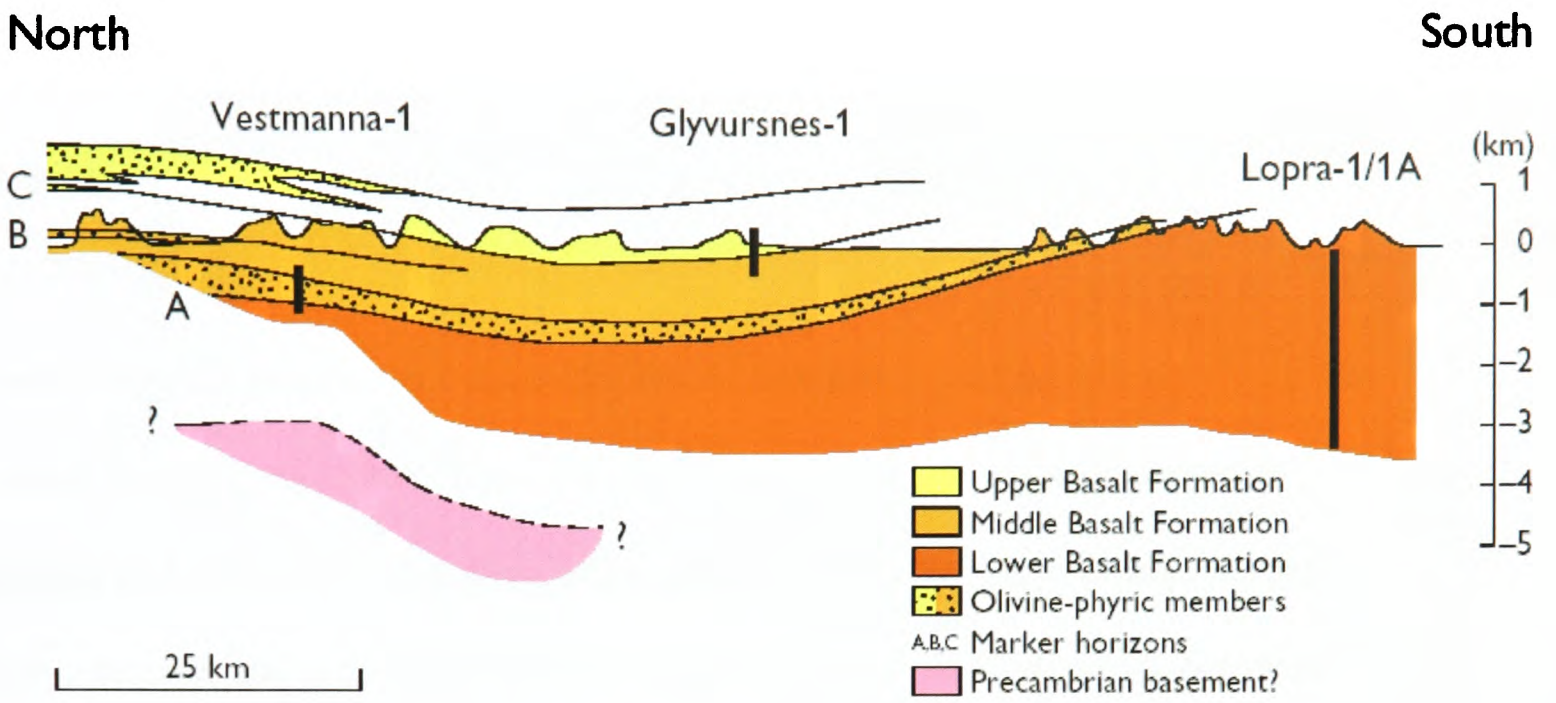

Figure 1.2. Relation of the SeiFaBa boreholes to basalt stratigraphy (Japsen *et al.*, 2004).

The 700 m deep Glyvursnes-1 borehole was drilled on the south-eastern coast of Streymoy (Figure 1.1) in 2003, also as part of the SeiFaBa project. The borehole penetrates the lower 355 m of the Upper Basalt Formation and the upper 345 m of the Middle Basalt Formation (Figure 1.2), and a full rock core and numerous wireline logs were acquired.

In both Vestmanna-1 and Glyvursnes-1 boreholes, the Middle Basalt Formation is characterised by the presence of plagioclase-phyric compound flows, inclusive of thin flow units of variable porosity, and rare beds of tuff. The lowermost part of the Middle Basalt Series in the Vestmanna-1 borehole and the lowermost 70 m of the Upper Basalt Series in the Glyvursnes-1 borehole are similar compositionally and texturally. The overlying section at about 230 to 285 m in Glyvursnes-1 consists of a few relatively thick plagioclase-phyric flow-units, possibly forming two compound flows (the

Tórshavn flows), that are morphologically very similar to the flows of the Lower Basalt Series, except that the latter are near-aphyric (Japsen *et al.*, 2004).

1.3.2 WIRELINE LOG DATA

Extensive logging programmes were run in both boreholes, and the full rock core was recovered from Glyvursnes-1. These have been fully catalogued and interpreted by Waagstein & Andersen (2003). Core photographs, optical televiewer data, neutron porosity, density, and processed velocity logs have been actively used for the work presented in this thesis (Table 1.1). Log data not used in this thesis include caliper, natural gamma ray, resistivity, full wave sonic, spectral gamma and temperature / conductivity measurements.

Table 1.1

Borehole	Glyvursnes	Vestmanna	Lopra
	Depth range /m ***(sampling interval)***	**Depth range /m** ***(sampling interval)***	**Depth range /m** ***(sampling interval)***
Density	50.13 – 600.13 *(0.1)*	50.1 – 500.1 *(0.1)*	1250 – 2912 *(0.1524)*
P-velocity	50.13 – 600.13 *(0.2)*	50.1 – 500.1 *(0.2)*	1250 – 2912 *(0.1524)*
S-velocity	50.13 – 600.13 *(0.2)*	50.1 – 500.1 *(0.2)*	1250 – 2912 *(0.1524)*
Neutron porosity	50.13 – 600.13 *(0.1)*	50.1 – 500.1 *(0.1)*	-
Optical televiewer	6.33 – 600.13 + core photographs	13.1 – 500.1	-

Table 1.1. Summary of datasets studied.

Ambiguity in the original processing scheme of Glyvursnes logs by Robertson Geologging made it necessary for the velocity logs to be reprocessed to a lower resolution (Waagstein & Andersen, 2003). Corrections were also made to the density logs based on core sample measurements (Regin Waagstein, personal communication). All wireline log studies in this thesis are based on the datasets finalised by GEUS.

1.4 VERTICAL SEISMIC PROFILING – A FOREWORD

Vertical seismic profiling (VSP) has been used widely in exploration and academic research since the 1980s. Hardage (2000) offers a comprehensive introduction to the history of VSP, field procedures, processing techniques and applications; a brief introduction is given here.

In a VSP survey, the source is positioned at a fixed offset from the borehole, while the receivers are positioned at varying depths within the borehole. If a single downhole geophone is used, recordings are repeated at different depth levels to give a suite of traces. In Figure 1.3, schematic diagrams show that wavefields in a near-zero-offset VSP pass through the rock volume by a much shorter path than in a standard reflection seismic survey.

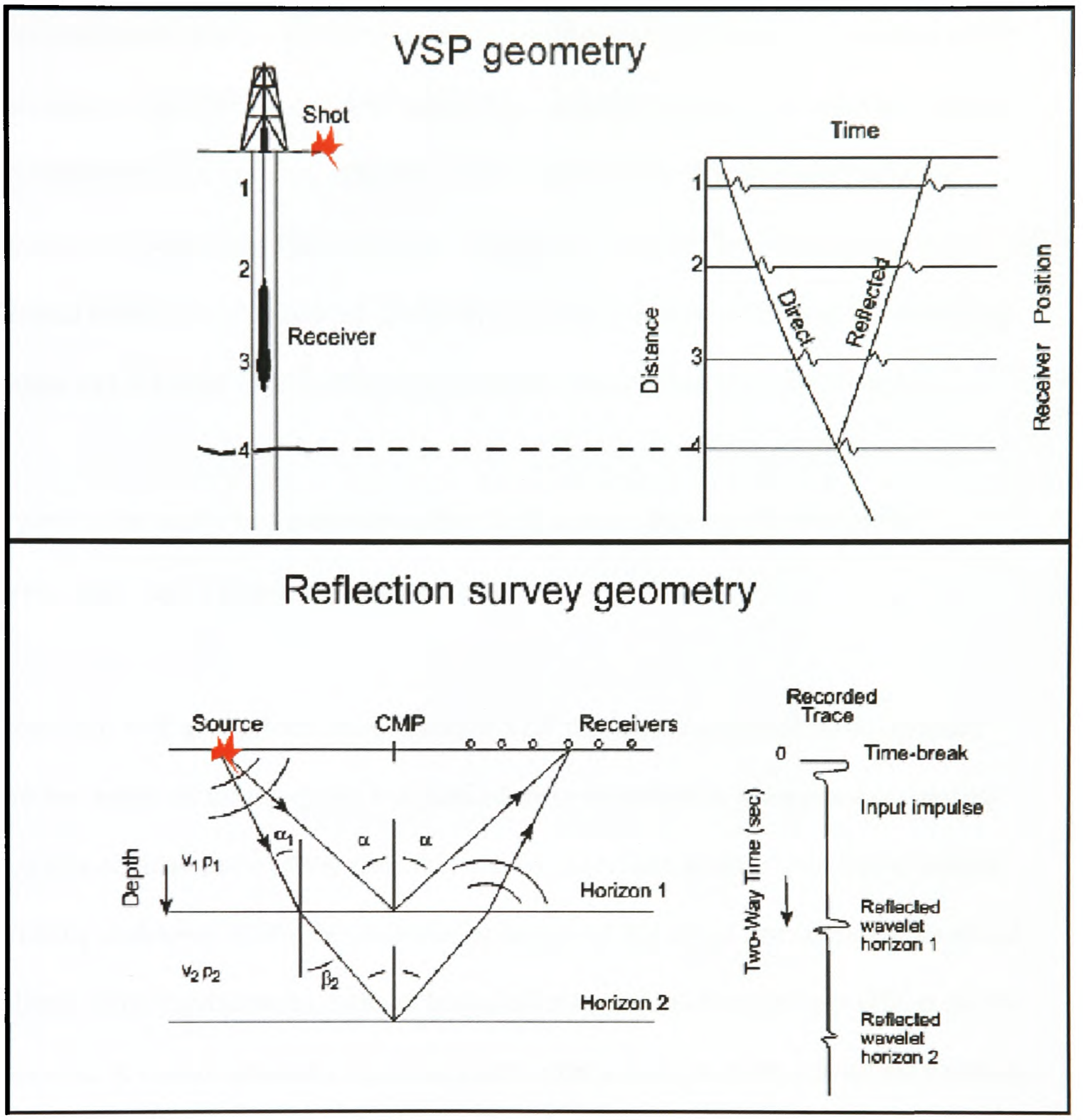

Figure 1.3. Schematic VSP geometry compared to a reflection survey array. The relationship between geometry and trace recordings is shown.

The geometry of the near-zero-offset VSP thus gains several advantages over reflection survey geometry. Compressional wave, shear wave and tube wave arrivals can be clearly differentiated. Also, the wavefield propagates only once through the weathered surficial layer (which compared to bedrock is usually loosely consolidated and highly

attenuative), increasing the frequency content and resolution. Both depth and time are well constrained and can be directly correlated, hence giving accurate velocities of the intervening rock. This type of VSP can act as a checkshot survey for wireline velocity logs collected from the same borehole. Travel times from VSP and integrated log slowness can be analysed for evidence of dispersion, and the amplitude and character of reflected waves can be observed (Balch *et al.*, 1982). Overall, VSP samples a real rock volume and is a vital intermediate step between data at sonic and seismic scales.

As part of this study, two near-zero-offset VSP surveys were performed in the Glyvursnes-1 and Vestmanna-1 boreholes.

Alternative VSP geometries exist: in offset VSP the source is moved some distance from the mouth of the borehole. The path of wave propagation is lengthened, passing through a conical sector of the rock volume. By recording at several co-linear offsets (termed a walkaway VSP), the moveout behaviour of the direct arrival can be analysed in detail. Dipping structures, such as faults, are revealed, and anisotropic effects can be measured. A variant geometry involves moving the source position around the borehole at fixed radius (an azimuthal VSP). This is also used to determine anisotropy and can produce high resolution images of the subsurface.

Walkaway and offset VSP surveys were conducted as part of the SeiFaBa project, but fall outside the scope of this thesis.

1.5 ATTENUATION AND THE SEISMIC QUALITY FACTOR, Q

Attenuation theory has been built up from diverse observational, experimental and theoretical studies. At the macroscopic scale, energy loss from

- acquisition factors (such as geometric spreading, instrument response, noise),
- extrinsic effects (such as scattering from the geometry of heterogeneities), and
- intrinsic effects (such as the presence of cracks, fluids and volatiles)

cannot be completely separated. It is thus important to recognise at an early stage that attenuation studies are carried out at different scales and under different conditions, and describe several interacting phenomena rather than a single attribute. This is shown schematically in Figure 1.4. Key terms will be elaborated on in subsequent sections.

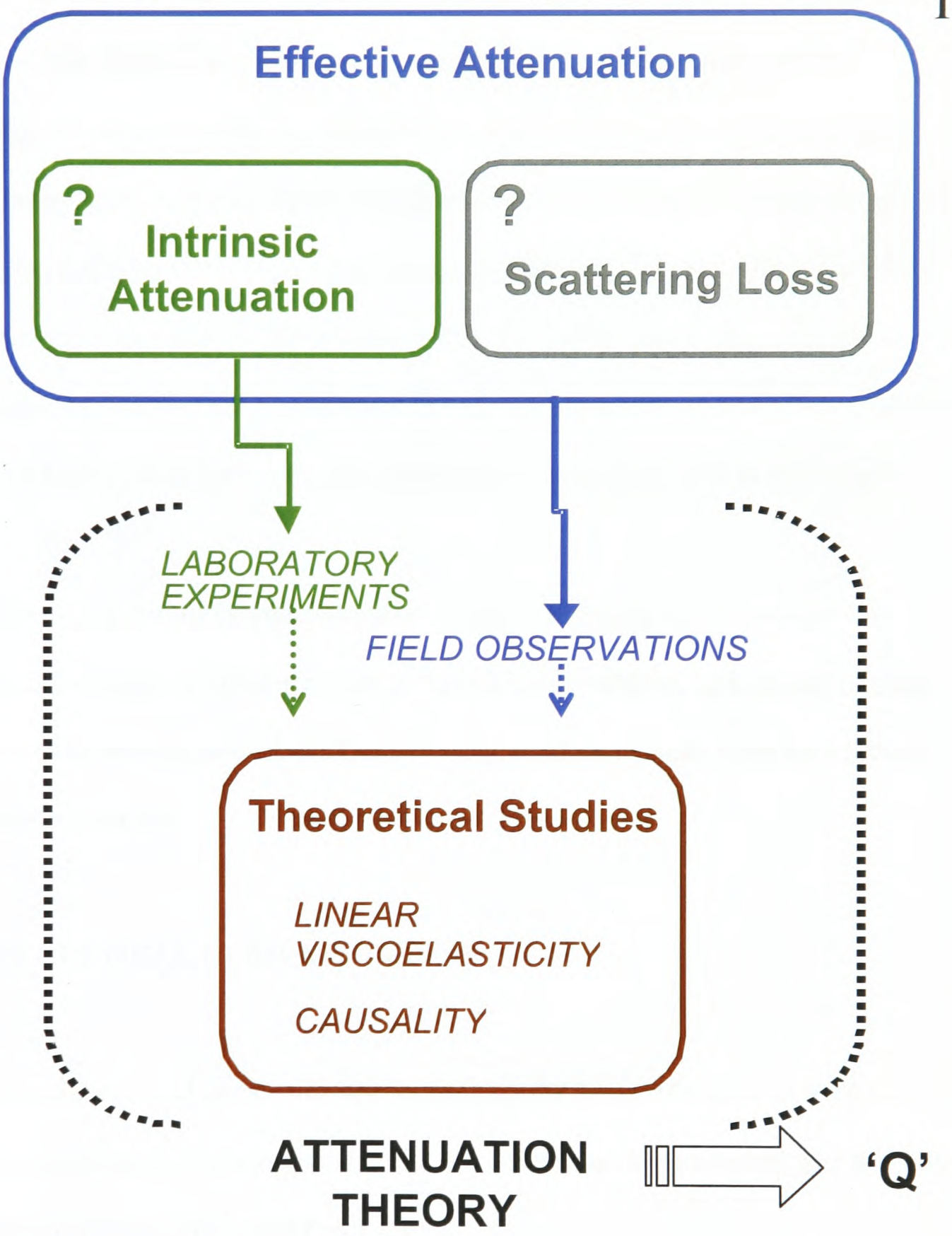

Figure 1.4.
Schematic diagram of the provenance of data on which Attenuation Theory is based.

The term 'attenuation' is commonly confined to anelastic conversion of energy to heat, while other mechanisms of energy loss are denoted by 'apparent attenuation'. In succeeding chapters of this thesis, anelastic dissipation is not immediately assumed. Instead, 'attenuation' is used non-specifically for the loss of energy in a medium due to its bulk physical properties. Where this is directly observed from field data, the loss is dubbed 'effective attenuation'. Where this is seen in synthetic modelling of specific mechanisms, or in experiments performed in a closed environment, the relevant affix is applied. (An example is '1-D scattering attenuation', see section 1.5.3 in this chapter.)

Seismic quality factor, Q, is used extensively in this thesis to quantify attenuation. However, the concept of Q remains tied to theoretical definitions, and carries varying connotations depending on context. The following sections provide some background on prevalent Q models.

1.5.1 THEORETICAL DERIVATION OF Q

Mathematical models of attenuation are based upon the theory of viscoelasticity and causality conditions in wave propagation. (For a comprehensive treatment, see Bourbié *et al.*, 1987; Carcione, 2001; and Pujol, 2003).

The medium is first considered to be linear viscoelastic, as in a standard Zener model (Zener, 1948). This implies that stress-strain relationships are time-dependent, and that if a particular harmonic wave is attenuated, it will remain equally attenuated when

superposed with other harmonic waves. Although the choice of linear viscoelasticity is informed by laboratory and field data (Stacey, 1992, found that linearity is a viable approximation for typical seismic strains of about 10^{-6}), linear models are used primarily for their simplicity. This allows a wider range of dissipative processes to be examined.

The 1-D wave equation is given by:

$$M\frac{\partial^2 u}{\partial x^2} = \rho\frac{\partial^2 u}{\partial t^2} \qquad \textbf{(1.1)}$$

where M is an elastic modulus and ρ is density. v, the velocity of the propagating wave, is assumed to be constant and is given by:

$$v = \sqrt{\frac{M}{\rho}} \qquad \textbf{(1.2)}$$

(Schwab & Knopoff, 1971). The solution to Equation 1.1 is in the form of:

$$u = u_0 \exp[i(\omega t - kx)] \qquad \textbf{(1.3)}$$

where displacement, u, is related to time, t, spatial position, x, angular frequency, ω, and the complex wavenumber, k. Substituting Equation 1.3 into 1.1, the following dispersion relation is obtained:

$$Mk^2 = \rho\omega^2$$
$$\Rightarrow v^2 = \frac{\omega^2}{k^2} \qquad \textbf{(1.4a, b)}$$

As k is complex and the right-hand side of Equation 1.4a is real, M is shown to be a complex modulus, and the velocity v must also have a complex component. To

introduce a loss factor, k can be related to κ, the real wavenumber, and α, the spatial attenuation factor, by:

$$k = \kappa - i\alpha \qquad \textbf{(1.5)}$$

Similarly, the real and imaginary components of v are:

$$\begin{aligned} v &= v_R + iv_I \\ &= |v| e^{i\vartheta} \end{aligned} \qquad \textbf{(1.6a, b)}$$

where $\tan\theta = v_I / v_R$.

Seismic quality factor, Q, is the inverse of dissipation and can be defined as the ratio of M_R to M_I, where M_R is the real part of M and characterises the instantaneous response of the medium at a given angular frequency, while the imaginary part, M_I, characterises the dissipation (White, 1965).

$$Q = \frac{M_R}{M_I} \qquad \textbf{(1.7)}$$

Substituting Equations 1.2 and 1.6b into 1.7 gives:

$$\begin{aligned} Q &= \frac{M_R}{M_I} \\ &= \frac{v_R^2 - v_I^2}{2v_R v_I} \\ &= \frac{v_R}{2v_I} - \frac{v_I}{2v_R} \end{aligned} \qquad \textbf{(1.8a, b, c)}$$

Using Equations 1.4b, 1.5 and 1.6b, v_R and v_I can be expressed in terms of κ and α.

$$\begin{aligned} \kappa &= \omega \frac{v_R}{|v|^2} \\ \alpha &= \omega \frac{v_I}{|v|^2} \end{aligned} \qquad \textbf{(1.9a, b)}$$

Substituting 1.9 into 1.8c, this approximates to:

$$Q \approx \frac{\kappa}{2\alpha} \qquad \textbf{(1.10)}$$

if $\kappa >> \alpha$. This criterion of $\kappa >> \alpha$ restricts Equation 1.10 to low-loss solids, i.e. Q >>1.

For a given angular frequency, the phase velocity, c, is equal to v_R, the propagation velocity. Substituting $\omega = 2\pi f$ and Equation 1.9a into Equation 1.10:

$$\begin{aligned} Q &= \frac{\omega}{2\alpha c} \\ &= \frac{\pi f}{\alpha c} \end{aligned} \qquad \textbf{(1.11a, b)}$$

Q can also be defined by energy dissipation in the temporal domain (Futterman, 1962):

$$Q = \frac{2\pi\ \mathrm{E}_0}{\Delta \mathrm{E}} \qquad \textbf{(1.12)}$$

where E_0 is the maximum strain energy (or amplitude of energy density) and ΔE is the energy dissipated per cycle. Integrating Equation 1.12 gives:

$$E = E_0 \exp\left(\frac{-2\pi\Delta t}{QT}\right) \qquad \textbf{(1.13)}$$

where T is period, Δt is the travel time of the wave, and E_0 is maximum strain energy.

$$\begin{aligned} A &= A_0 \exp\left(\frac{-\pi f \Delta t}{Q}\right) \\ &= A_0 \exp\left(\frac{-\pi f x}{Qc}\right) \\ &= A_0 \exp(-\alpha x) \end{aligned} \qquad \textbf{(1.14a, b, c)}$$

Distance travelled, x, divided by the phase velocity, c, can then be used to replace Δt. Frequency, f, can be substituted for $(1/T)$, and amplitude, A, which is proportional to

the square root of energy, substituted for E. All the variables in Equations 1.14a, b can now be conveniently measured from field / experimental data. The resulting exponential in 1.14c is related back to the spatial attenuation factor, α , as it appears in Equation 1.11b.

For a hypothetical constant value of Q, the number of cycles is greater for high frequencies than low frequencies when the wave travels a fixed distance. This leads to the exponential decay of amplitude in Equation 1.14, and provides a convenient phenomenological framework for the description of seismic attenuation. However, Equations 1.2 - 1.14 do not in themselves impose frequency-dependence on attenuation. Section 1.5.5 briefly introduces the arguments for dependence / independence on frequency.

1.5.2 INTRINSIC ATTENUATION

Intrinsic attenuation is not covered in detail by this thesis; however, it is an important part of attenuation theory and has inspired a large body of research. Detailed introductions to this topic can be found in Bourbié *et al.* (1987) and Carcione (2001).

The mechanisms of intrinsic attenuation operate on the micro- (i.e. grain size) to mesoscopic scale, involving interactions between the porous rock volume and its fluids under the sensing wave. Biot (1956) first compared the behaviour of saturated rocks

with their dry rock properties. Dissipation was hypothesised to be the product of out-of-phase motion between the host solid and its fluids.

At higher frequencies, in part exceeding seismic exploration frequencies, squirt flow (also known as local flow) is thought to be of greater or equal significance to Biot dissipation. It occurs when fluctuating seismic stresses in the rock induce pore pressure gradients over a range of scales. At high frequencies, the gradients are 'unrelaxed' and the elastic moduli are stiffer than at low frequencies (Mavko & Nur, 1979). The validity of the squirt flow model is supported by certain field analyses (Dvorkin & Nur, 1996).

Under laboratory conditions, there is evidence that confining pressure, fluid saturation, temperature and the propagating wave frequency affect the attenuative behaviour of rocks. King (2005) provides a comprehensive summary of findings.

In the specific area of basalts, published laboratory tests are relatively few compared to sedimentary rock studies. Tompkins & Christensen (2001) provide a comprehensive list of reported Q values. In addition they have tested a suite of ocean basalts, sampled from locations which vary in their proximity to ocean ridges and rises. The samples range between < 3 and 110 Ma in age. Q for P-waves was found to be lie between 10 and 110 for water-saturated samples. Two dry samples had Q values of ~ 15 and ~ 56. The ratio of S-wave Q to P-wave Q was also found to support a squirt flow attenuation mechanism.

1.5.3 LOSSES FROM MULTIPLE SCATTERING

The presence of thin layering in rock strata creates a series of intra-bed multiples. These multiple reflections are part of the total scattered wavefield, and can be referred to as one-dimensional (1-D) scattering, as they are formed in approximately planar layers. When reflected twice within each layer, the multiples are re-transmitted downwards with very short lag times after the direct arrival. The amplitude of the purely transmitted wave is reduced, while the amplitudes of the composite waves following it are reinforced. If propagation occurs over sufficient distance, the bulk of the energy is carried in the composite waves rather than the direct arrival *per se*.

The effects of 1-D scattering were investigated by O'Doherty & Anstey (1971), who found that there was a broadening of waves similar to that caused by intrinsic attenuation. This broadening was also observed by Schoenberger & Levin (1978), in synthetic seismograms from actual log data. The following relation was derived by O'Doherty & Anstey (1971):

$$T(\omega,\tau) = \exp[-\tau R(\omega)] \qquad \textbf{(1.15)}$$

where $T(\omega)$ is the amplitude spectrum of the transmitted wave, $R(\omega)$ is the power spectrum of the sequence of reflection coefficients, and τ is the source-receiver travel time. Equation 1.15 was proven by Burridge *et al.* (1988) using a statistical approach. However, Morlet *et al.* (1982) found that the scattering response of the medium was dependent on the ratio of the seismic wavelength to the spatial period of the medium. This is, in effect, frequency-dependent energy loss, and has been observed in the

Columbia Plateau basalts by Pujol *et al.* (1989). VSP data from the basalts showed evidence of destructive interference due to a series of high- and low-velocity layers, which led to a reduction in amplitude.

Scattering attenuation, represented by $1/Q_{scatt}$, and intrinsic losses, represented by $1/Q_{in}$, are hypothesised to be additive, giving effective attenuation, $1/Q_{eff}$.

$$\frac{1}{Q_{eff}} = \frac{1}{Q_{scatt}} + \frac{1}{Q_{in}} \qquad \textbf{(1.16)}$$

This relationship holds true for low attenuation media (Lerche & Menke, 1986). It is found to be approximately satisfied in field studies of porous sands and shales in the Gulf Coast (Hauge, 1981). More significantly, Pujol & Smithson (1991) found that the relation was applicable to data from volcanic rocks, despite some evidence of frequency-dependence.

Forward modelling is the standard approach for calculating the component of energy lost from 1-D scattering. There is a wide array of methods for the generation of synthetic seismograms in planar, laterally invariant models, summarised by Smith (2000). One method involves an invariant embedding formulation for the transfer function of a layered medium (Kennett, 1979). The individual layers are assumed to be isotropic, linear elastic, and the synthetic response of the medium is generated recursively by adding one layer at a time. The spectrum of the synthetic response is then used to calculate $1/Q_{scatt}$. Examples of this application may be found in Levander (1990) and Pride *et al.* (2002).

1.5.4 LOSSES FROM SCATTERING IN A HETEROGENEOUS VOLUME

Three-dimensional (3-D) scattering can be roughly divided into two categories: volume scattering and interface scattering.

Volume scattering occurs in heterogeneous media. Based on the size of the scatterers relative to the sensing wavelength, it can be further sub-classified into several domains. Rayleigh scattering operates when the sensing wavelength, λ, exceeds the diameter of the scattering heterogeneity, d. Mie scattering (also known as stochastic or resonant scattering) occurs when λ is approximately equal to d. The third domain is diffusion scattering, where λ is smaller than d. It is also known as forward scattering, as energy is redistributed mainly in the forward direction; any backward scattering is focused and accompanied by diffraction and interference effects. Comprehensive reviews of these different scattering types are given by Wu & Aki (1988) and Ishimaru (1997).

In a petrophysical context, volume scattering may occur on the scale of rock grains, significantly affecting the behaviour of cracks and pores (Hudson, 1981). Mavko *et al.* (1998) review the scattering attenuation resulting from grain scale heterogeneities. In this thesis, however, the focus will be on macroscopic structures seen in basaltic rocks, where heterogeneities appear in a range of shapes and morphologies, due to physical emplacement mechanisms or chemical fractionation.

Interface scattering is also strongly dependent on scale. The threshold at which a surface appears smooth to the sensing wave is given by the Rayleigh criterion (Ishimaru, 1997):

$$h < \frac{\lambda}{8 \cos \theta} \qquad \textbf{(1.17)}$$

h is the root-mean-square height of the irregularities and θ is the angle of incidence. Over seismic wavelengths, surfaces such as faults, unconformities, or tectonically deformed beds can appear rugose. In basalt terranes, low-velocity palaeosols may also exhibit rugosity (Papworth, 1985). These palaeosols are widespread, and can be both discontinuous and irregular, depending on the local palaeotopography and eruption history.

It is likely that several types of scattering operate over seismic scales. Within a single lava field there can be large variations in the velocity structure (Single *et al.*, 2004), and over wider areas basalt terranes express great diversity (as reviewed by Mahoney & Coffin, 1997). There is evidence that lava emplacement is fractal in nature, leading to the creation of fractal flow morphologies (Bruno *et al.*, 1992). All these factors combine to generate a high level of complexity, which has partly motivated the use of statistically-driven modelling. In such models, heterogeneity at smaller scales can be provided by basalt-derived statistics while larger scale structures are informed by geological fieldwork (e.g. Martini *et al.*, 2005).

3-D models incorporating fractality have been studied by Martini & Bean (2002). Their numerical models of basalts comprise background fractal noise (to generate

volume scattering), and synthetic interfaces embedded with fractal irregularities (to generate interface scattering). It was found that the wavefront was strongly distorted by propagation through the interfaces, obscuring the intervening structures. When the rough interfaces were spaced further apart, volume scattering effects gained greater relative significance over interface scattering.

Studies specific to the phase scattering properties of a 3-D random interface were carried out by Makinde *et al.* (2005). Phase scattering results from the spatial convolution of the seismic signal with the interface height function. It was concluded that its effect is not negligible in 3-D even at roughness scales of $\lambda/10$, where λ is the wavelength of the incident wave. The dephasing effect was especially strong when the rugosity of the scattering interface was of the order of ¼ of the wavelength of the seismic signal. The study also concluded that scattering in 3-D models was more intense than for 2-D slices of those models, and that care is needed when extrapolating results from two to three dimensions.

1.5.5 FREQUENCY DEPENDENCE OF Q

Known processes of relaxation and creep have a dissipation factor that is broader than the relaxation curve of a single Zener model (Carcione, 2001). To account for this, it is possible to introduce a distribution of relaxation curves, superposed such that the resultant Q is stable over a given frequency range. In this vein, Liu *et al.* (1976) have presented a nearly constant Q model (NCQ) which bears a slight frequency dependence for 1/Q and velocity. Kjartansson (1979) has derived a constant Q model (CQ) that is fully independent of frequency. The CQ model effectively has identical characteristics to the NCQ model for $Q > 10$.

Early work suggested that Q is independent of frequency (McDonal *et al.*, 1958; Knopoff, 1964). Certain field studies have supported this requisite over limited bandwidths (e.g. Harris *et al.*, 1997), while others have indicated that Q increases with frequency, albeit weakly and over long propagation distances (e.g. Der, 1998). Recent studies commonly cite 1-D scattering as the cause of frequency-dependence, with or without additional intrinsic attenuation (e.g. Pujol, 1989; Pujol *et al.*, 1998; Maresh & White, 2005). In these observations, there is no explicit adherence to the viscoelastic NCQ and CQ models. Furthermore, the diversity of rock types, survey dimensions and Q estimation methods used in these studies renders comparisons of frequency-dependence inconclusive.

In this thesis, the bandwidth over which attenuation is measured is constrained by field acquisition parameters and numerical modelling capability. Over those bandwidths Q, as a descriptor of attenuation, is implicitly constant. The actual validity of frequency-independent Q in basalts will be examined in the course of this thesis.

1.6 CHAPTER GUIDE

This thesis is organised into seven chapters, each covering different aspects of data collection, processing and interpretation. *Italicised terms* will be defined rigorously in the context of respective chapters.

The acquisition of two Vertical Seismic Profiles (VSP) on the island of Streymoy is described in **Chapter 2**. The quality of the VSP data is assessed, and preliminary processing of the raw data is carried out.

In **Chapter 3**, the VSP data are subjected to two methods of Q analysis: the *spectral ratio method*, which operates in the frequency domain, and the *amplitude decay method*, which operates in the time domain. The relationship of effective Q to borehole depth is investigated. The *Morlet wavelet scalogram*, a form of time-frequency analysis, is first introduced here, and used to study energy distribution in the coda of VSP traces. These results form the baseline from which subsequent studies of attenuation mechanisms are compared.

One-dimensional (1-D) backscattering from horizontally planar basalt models is examined in **Chapter 4**. Acoustic modelling is used to generate synthetic seismograms, from which 1-D scattering Q estimates are derived. These are compared to estimates of Q from the VSP data. The effect of source bandwidth on the estimation of 1-D scattering Q is also investigated. Scattering behaviour in the coda of synthetic seismograms is identified using Morlet wavelet scalograms, and also compared to observations from the VSP data. The attenuative effects of periodic layering and large velocity contrasts in basalt are assessed. There is a preliminary discussion of heterogeneity in the log data, and its link with geological factors.

The study of heterogeneity is extended to the *fractal* dimension in **Chapter 5**. *Multi-scale* characteristics are identified in the 1-D borehole log data, and described using *monofractal* and *multifractal* statistics. Variations in heterogeneity are directly linked with the geological classification of Faroes basalts. The significance of fractality in log data to 1-D scattering attenuation is examined, using the spectral ratio method of Q analysis and time-frequency analysis of the coda energy.

Lateral heterogeneity in basalts forms the basis of **Chapter 6**. Current knowledge of flood basalt architecture and lava emplacement mechanisms is reviewed. Two- and three-dimensional models are generated, incorporating structures which are plausible on the spatial scale of the VSP surveys. The *Discrete Particle Scheme* (DPS) is used to model their seismic response. Three-dimensional (3-D) scattering Q is estimated using spectral ratio and amplitude decay methods, and the effects of lateral heterogeneity on

the seismic wavefield are examined. All interpretations are related to those made in Chapters 3, 4 and 5.

Chapter 7 collates key observations from preceding chapters. The complexity of the real world scenario and the benefits / limitations of synthetic models are discussed, and final conclusions are drawn.

CHAPTER 2

DATA ACQUISITION ON THE FAROE ISLANDS

This chapter reviews the acquisition of Vertical Seismic Profiles (VSP) from two boreholes on the island of Streymoy in the summers of 2003 and 2004. In combination, more than a kilometre of rock was profiled from the Middle and Upper Basalt Series (Figure 2.1). Offset VSP data were also acquired at both locations and their acquisition will be briefly outlined. However, analyses of these data are not included in this thesis.

The quality of the raw datasets is compared, and preliminary processing of data is described, including extraction of shear and upgoing wave modes.

2.1 ACQUISITION OF VERTICAL SEISMIC PROFILES

2.1.1 GLYVURSNES

Vertical seismic profiling was conducted at Glyvursnes in June / July 2003, on a headland on the eastern coast of Streymoy. The headland is edged by cliffs about 20 m in height dropping down to cobble-boulder shorelines. Covered by more than three metres of Quaternary peat / soil and glacial till, the area has a roughly convex topography with gradients of between 3 and 6 degrees. The Glyvursnes-1 borehole is about 20 m from the sea and intersects 355 m of rock from the Upper Basalt Series and 345 m of Middle Basalt Series rocks.

The near-zero-offset source for the main experiment was situated 14 m from the borehole. Two more sources were located at offsets of 242 m (with an elevation +25 m) and 415 m (with an elevation of +35 m). The offset sources straddled a dyke / fracture zone, shown in Figure 2.1. The dyke (Figure 2.2) is composed of primitive, olivine-rich material, with a jointing and weathering pattern different from the country rock. Inland it has eroded out to form a trench, while at the coast it creates a steep-sided cleft known as Glyvursgjógv. A weathered marker bed on either side of the dyke shows little or no displacement, and it is not known whether the dyke is continuous at the depth of the survey (Dougal Jerram, personal communication).

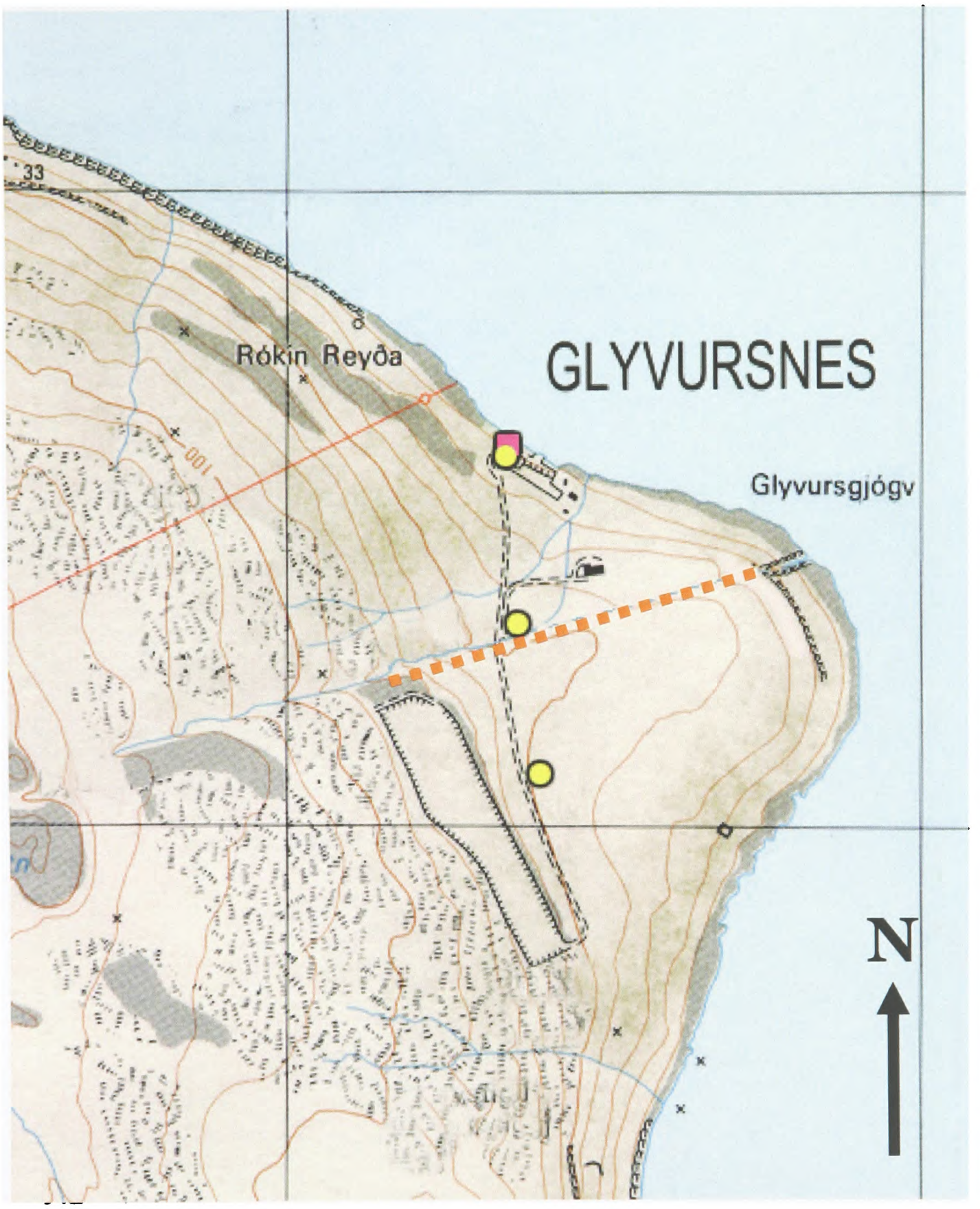

Figure 2.1. The Glyvursnes headland.
Magenta square = Borehole
Yellow circles = Source locations at approx. 14 m, 242 m, and 415 m offset.
Dashed orange line indicates position of a fracture zone.
Adapted from map c. Danish National Survey & Cadastre.



Figure 2.2. The dyke at Glyvursgjógv. Remnant dyke rocks are indicated by the dashed red line.

At each source location, a pit of roughly 2 m in diameter was excavated down to bedrock. The thick Quaternary deposits meant that source-to-bedrock coupling was sub-optimal. The pits were made watertight with a double layer of plastic pond lining and tar roof matting, then filled with water pumped from the ocean and an ephemeral stream. The zero-offset air gun pit is shown in Figure 2.3. The seismic source, a single sleeve Sodera air gun with a capacity of 150 cubic inches, was suspended to a depth of 1.5 m. This was manoeuvred with the aid of a wooden tripod scaffold.

2.3



Figure 2.3. Zero-offset air gun pit. The Sodera air gun was suspended above the pit by a wooden scaffold whilst being filled with compressed air.

The receiver was a custom-made input / output three-component sensor with SM-7M 10 Hz geophones and a hydraulic bow spring clamp system, designed and built by Prof. M. H. Worthington and Mr. Derek Preston in the Department of Earth Sciences, University of Oxford workshops. An in-house fabricated pulley head and sheath was

used to lower it into the borehole (Figure 2.4). The two cables containing the geophone wiring and hydraulic fluid for the clamp were wound on separate reels secured to the observation area. A manually-operated hydraulic pump was used to bring clamping pressure to ~ 2000 psi for each depth recording.

2.4

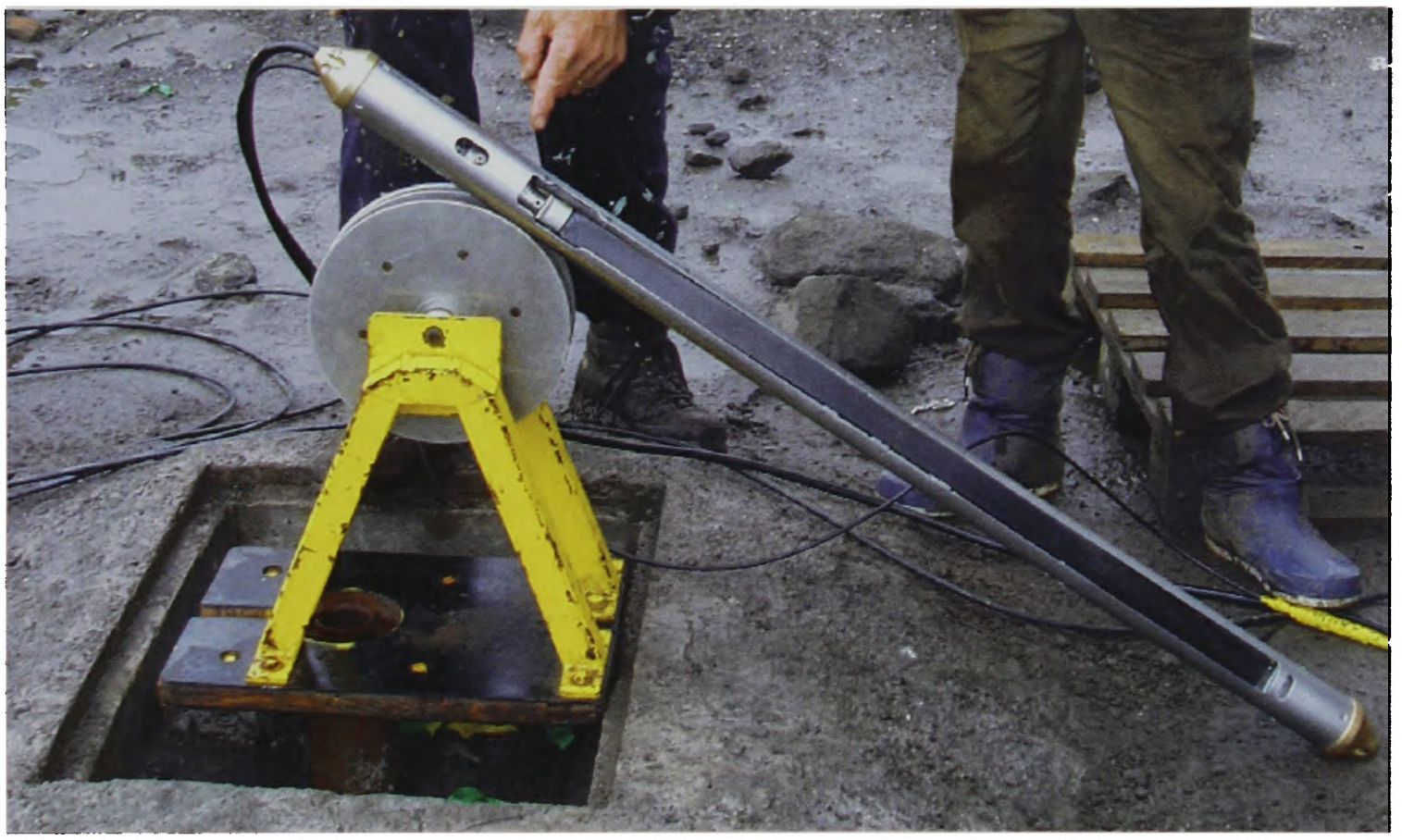

Figure 2.4. 3-component geophone resting at the mouth of the borehole, on the pulley head.

The seismic recording system (a Geometrics ES-3000), the field computer and a GPS timing system provided by SeisUK / Cambridge University were housed in a metal shipping container. Power sources and generators for the equipment were kept outside it. The electronic trigger unit, on loan from the University of Aarhus, was placed in an adjacent recording van. Figure 2.5 shows the layout of the observation area.

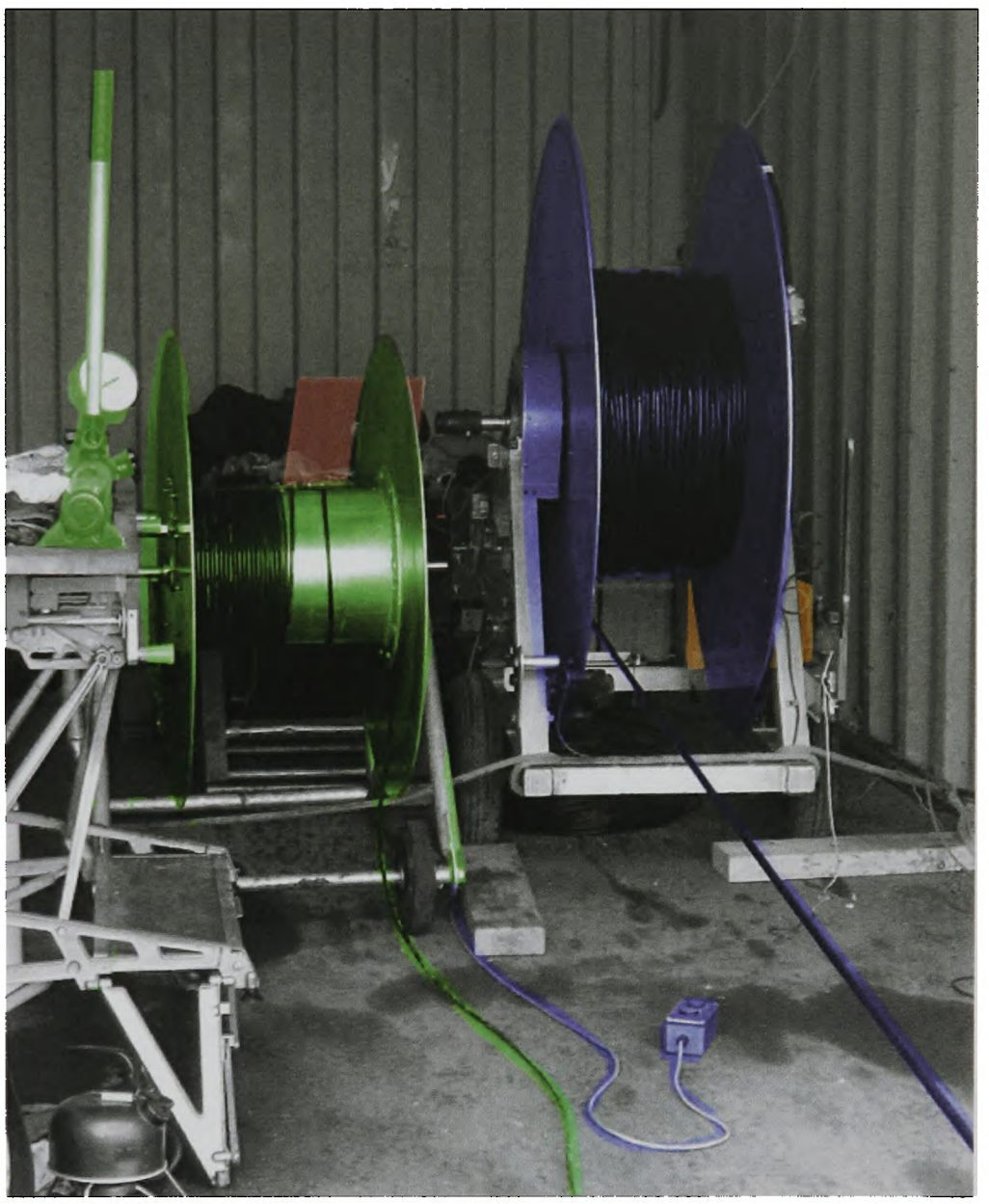

Figure 2.5.
Setup of observation area within the container. Hydraulic pump and reel of hydraulic cable tinted green; geophone cable, reel and winch control box tinted blue; field computer tinted magenta; ES-3000 seismometer tinted orange. The Aarhus recording van (not pictured) was to the right of this illustrated setup and contained the trigger box.

The Glyvursnes near-zero-offset VSP was recorded at 10 m intervals, from a depth of 50 to 600 m. The sampling interval was 0.125 milliseconds, with a record length of 1.95 seconds. No filters were applied to the raw data at the time of acquisition (Table 2.1).

Table 2.1

Location	Glyvursnes (vertical & offset VSP)	Vestmanna (vertical VSP)
Sampling interval (milliseconds)	0.125	0.5
Data length (seconds)	1.95	5.0
Filters	None used	None used
Preamp gain style	36 dB	36 dB
Trigger holdoff (seconds)	0.1	0.1 or 0.2

Table 2.1. Comparison between Glyvursnes and Vestmanna acquisition parameters.

Ensuring pit stability and replenishing water supply were the most challenging aspects of data acquisition, as these were crucial in maintaining a consistent source signature. To monitor the source, a hydrophone was deployed in a slim hole drilled obliquely beneath each pit. The position of this monitor hydrophone varied between 7 and 13 m depth, depending on the water table and irregularities in the slim hole. This, in hindsight, was too close to the source, resulting in inconsistent hydrophone traces. The true source signature was therefore not recorded. (These sub-optimal conditions were recognised and changed in the subsequent Vestmanna experiment.)

There were several sources of noise at Glyvursnes. The borehole area was exposed to strong winds and was only partially shielded by the metal container. As a precaution, the geophone cable was slackened after clamping, and a cloth damper inserted at the mouth of the borehole. Crosstalk from the GPS unit and gun trigger appeared on the recordings, but this was easily identifiable as it occurred at a much earlier time than the direct arrival of the compressional wave (Figure 2.6b). Radio silence was enforced prior to each shot to avoid interference from mobile phone and radio signals. To reduce electrical noise, the recording system was earthed via a connection to the lip of the metal borehole casing.

Micro-fracturing of rocks occurred a few seconds into the clamping procedure, so up to a few minutes were allowed for stabilisation of clamp pressure. Recording only commenced when the noise monitor registered no anomalous signals. 50 Hz noise, found to be persistent after the acquisition was completed, was filtered out at the processing stage. Noise from local livestock and vehicles was negligible. Interference from the power generators was judged to have little effect, but as far as possible, recordings were carried out while the generators were switched off.

Figure 2.6 shows raw data recorded across the three geophone components at 50 and 600 m. Noise spikes at 0 and 0.02 s are caused by interference from the gun trigger. These are especially clear at lower depth levels, where the signal-to-noise ratio is lower.

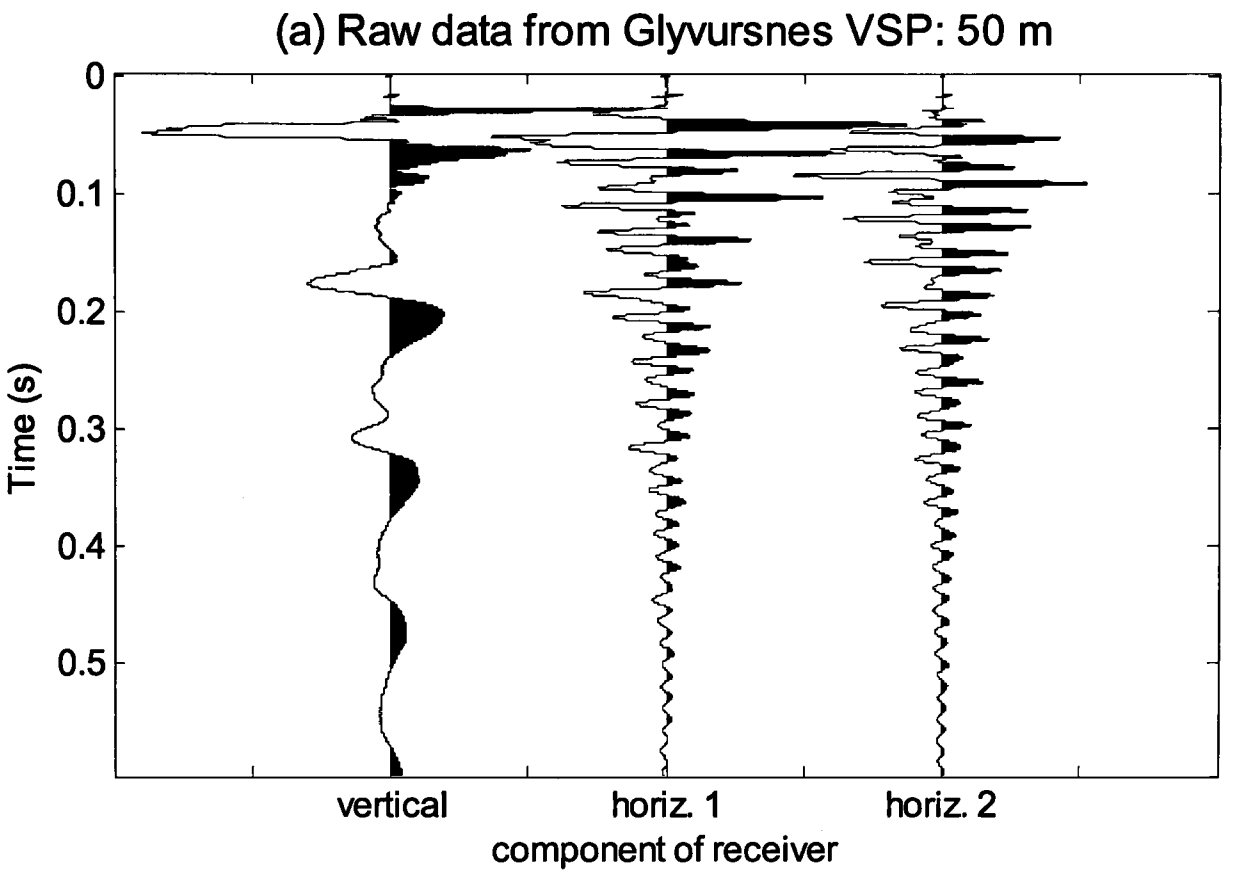

Figure 2.6.
a. Raw data from the 50 m trace of the Glyvursnes VSP. Amplitudes of the three traces have been normalised.
b. Raw data from the 600 m trace of the Glyvursnes VSP. Amplitudes of the three traces have been normalised for clearer display.
Gun trigger artefacts are seen at 0 and 0.02 seconds in both levels.

2.1.2 VESTMANNA

A second VSP experiment was carried out in June / July 2004, in the sheltered *sund* (sound) of Vestmanna, western Streymoy (Figure 2.7). In contrast to the rural Glyvursnes field site, the Vestmanna-1 borehole is adjacent to the warehouses of a busy timberyard, and the experimental setup was confined to a narrow loading strip (Figure 2.8). The immediate field area is at sea level, surrounded by sloping terrain which steepens with height. Vestmanna-1 intersects 550 m of the Middle Basalt Series and 150 m of the Lower Basalt Series. Stratigraphically, the top of the borehole is 500 m below total depth of Glyvursnes-1.

A steep river gully (trending east-west) runs south of the borehole, feeding into a series of natural rock pools. One of these, 18 m from the borehole (Figure 2.9), served as the pit for the near-zero-offset source. Direct exposure of the bedrock ensured good coupling with the source. Water level was unaffected by tidal ebb and flow, as it was constantly replenished by the stream. Notably, the local pressure gradient was high enough for water to pour from the borehole lip throughout the experiment.

Two air guns, each with a capacity of 40 cubic inches, were chained to fishing buoys and suspended to a depth of about 1.5 m in the rock pool. The same three-component geophone used at Glyvursnes was again deployed at Vestmanna, with an improved clamping system. Manually-operated hydraulic pumps were used to increase clamping pressure to ~ 2000 psi for each depth recording, and to decrease pressure to release the tool more quickly.

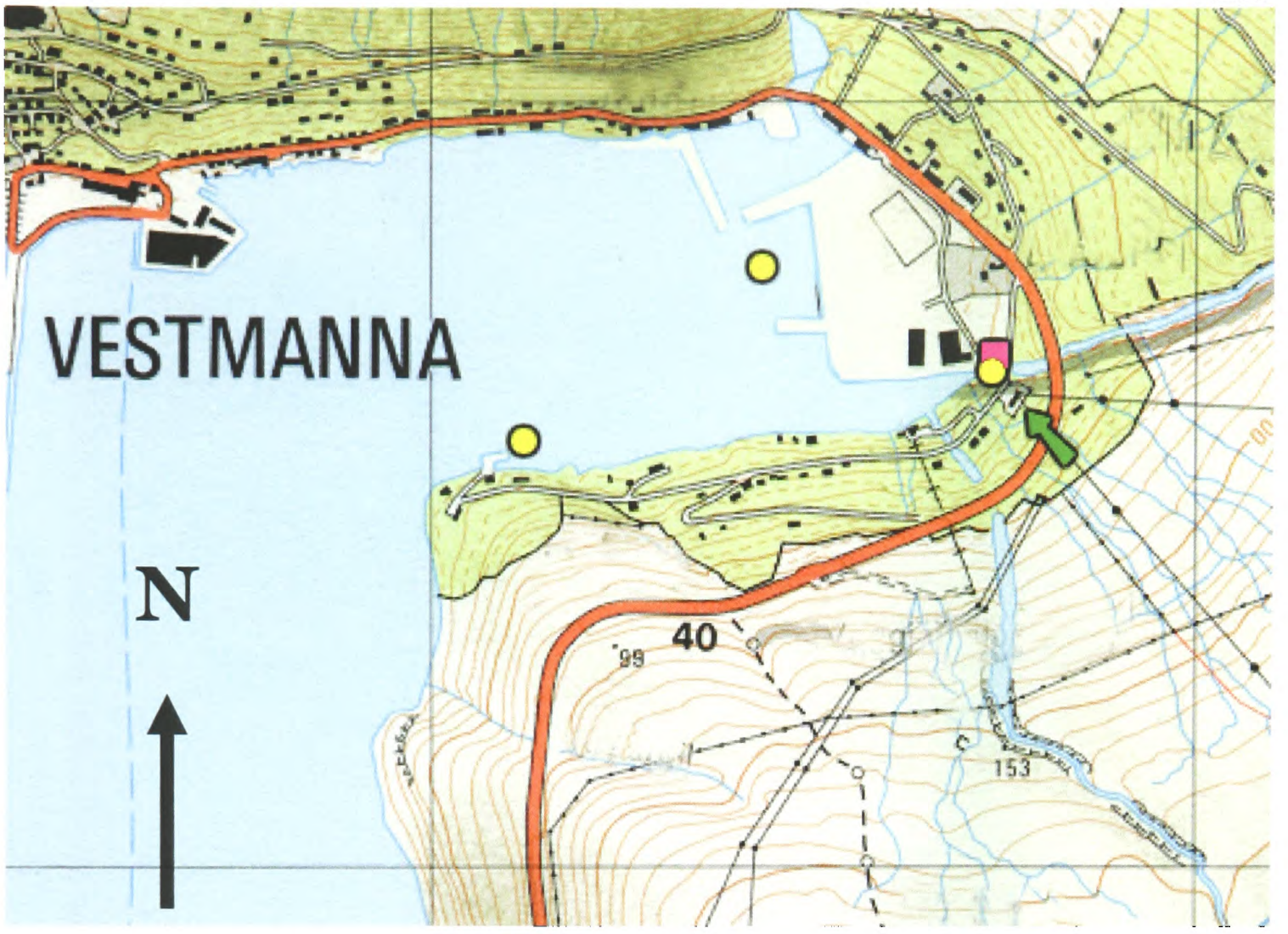

Figure 2.7. Vestmanna Sound.

Magenta square = Borehole
Yellow circles = Source locations at approx. 14 m, 230 m, and 610 m offset.
Green arrow indicates an electrical substation.
Adapted/updated from map c. Danish National Survey & Cadastre.

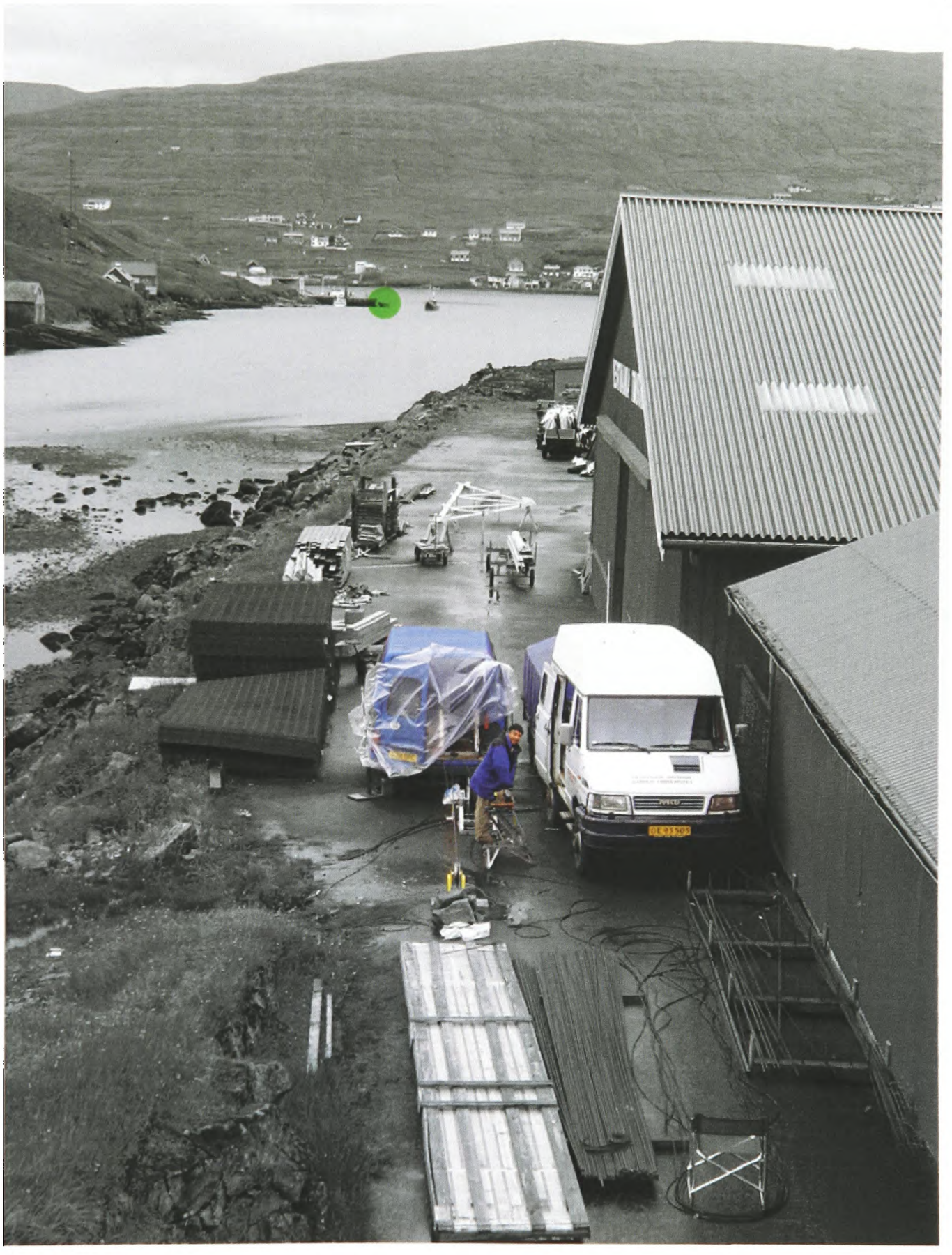

Figure 2.8.
Overview looking WSW towards Vestmanna Sound. The picture highlights the yellow legs of the pulley on the borehole head. Nick Mohammed is pictured operating the hydraulic pumps for clamping the tool. The green circle highlights the position of the 610 m source (air guns towed behind a boat) in the distance.



Figure 2.9.
View south from the timber yard. The yellow and red building is an electrical substation. A natural rock pool, seen in the lower right of the picture, was used as a source pit for the airguns.

The observation areas were the Oxford University field van (which housed the Geometrics ES-3000 seismic recording system and the geophone cable winch) and the University of Aarhus recording van. Power for the field computers and trigger unit was drawn from a separate rig to reduce electrical noise. The hydraulic pumps and cable reel were kept in the open for the duration of the experiment. The setup of the equipment is shown in Figure 2.8.

The Vestmanna near-zero-offset VSP was recorded at 5 m intervals from 50 to 500 m depth. The sampling interval was 0.5 milliseconds, with a record length of 4.995 seconds, and no filters were applied to the raw data at the time of acquisition (Table 2.1). Based on experience from the Glyvursnes field experiment (section 2.1.1), the monitor hydrophone was placed in the borehole above the geophone, at a depth of 20 m. The source signature was successfully recorded and was highly consistent.

As Vestmanna is a populated area, traffic on the main road and movement around the timberyard contributed to ambient noise. Running water from the nearby stream had no noticeable effects on the signal-to-noise ratio. Care was taken in earthing the electrical systems, as connection of the recording equipment to the Aarhus trigger unit increased sensitivity to noise. An optical isolation box was added to further shield the trigger from interference. The GPS unit increased noise to unacceptable levels, without contributing significantly useful information, and was subsequently disconnected. As at Glyvursnes, to avoid anomalous signals, recording only commenced when clamp pressure had equalised and micro-fracturing no longer appeared on the noise monitor.

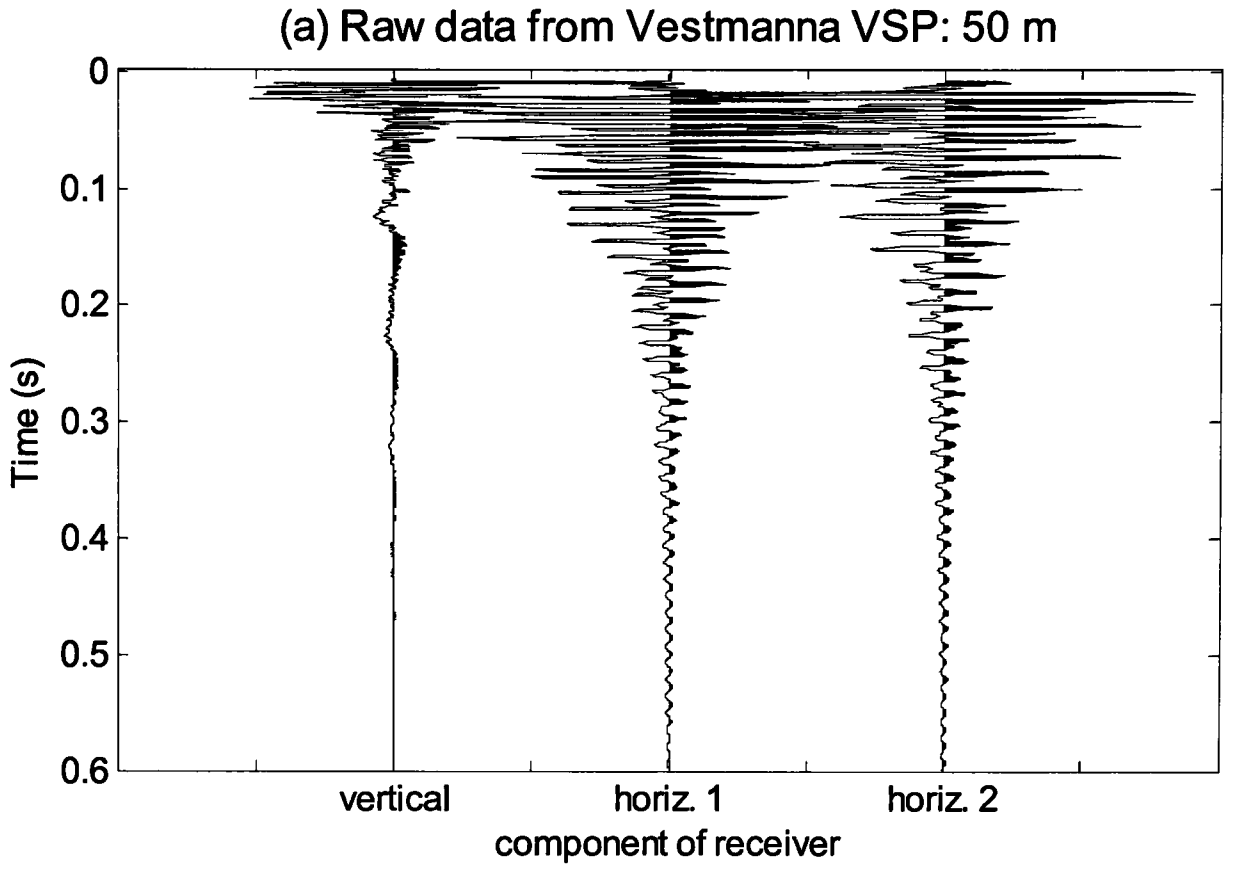

Figure 2.10.
a. Raw data from the 50 m trace of the Vestmanna VSP. Amplitudes of the three traces have been normalised.
b. Raw data from the 500 m trace of the Vestmanna VSP. Amplitudes of the three traces have been normalised for clearer display.

The greatest source of noise came from the electrical substation, occurring at 50 Hz and associated harmonics. The horizontal components were most sensitive to this, as shown by raw data samples in Figure 2.10. The magnitude of noise varied over the survey period, and thus no filters were applied during the acquisition, only at the processing stage.

After collecting near-zero-offset VSP data at depth levels between 340 m and 500 m, it was discovered that the bolts securing one of the two air guns had cracked under strain. The vertical component traces were largely unaffected; however, air leakage had led to a slowly deteriorating horizontal component. Very strong electrical noise on the same acquisition day compounded the problem (Figure 2.11). After replacement of the air gun, the signal-to-noise ratio of shear wave recordings experienced a marked improvement (Figure 2.13). The data quality in Vestmanna is therefore higher at depths above 340 m.

Two further experiments were performed at 230 m and 610 m offsets from the borehole. (Table 2.2 compares the experimental setup with that of Glyvursnes). The positions of these sources are marked in Figure 2.7. Walkaway and azimuthal profiles were also acquired, but do not feature in this thesis.

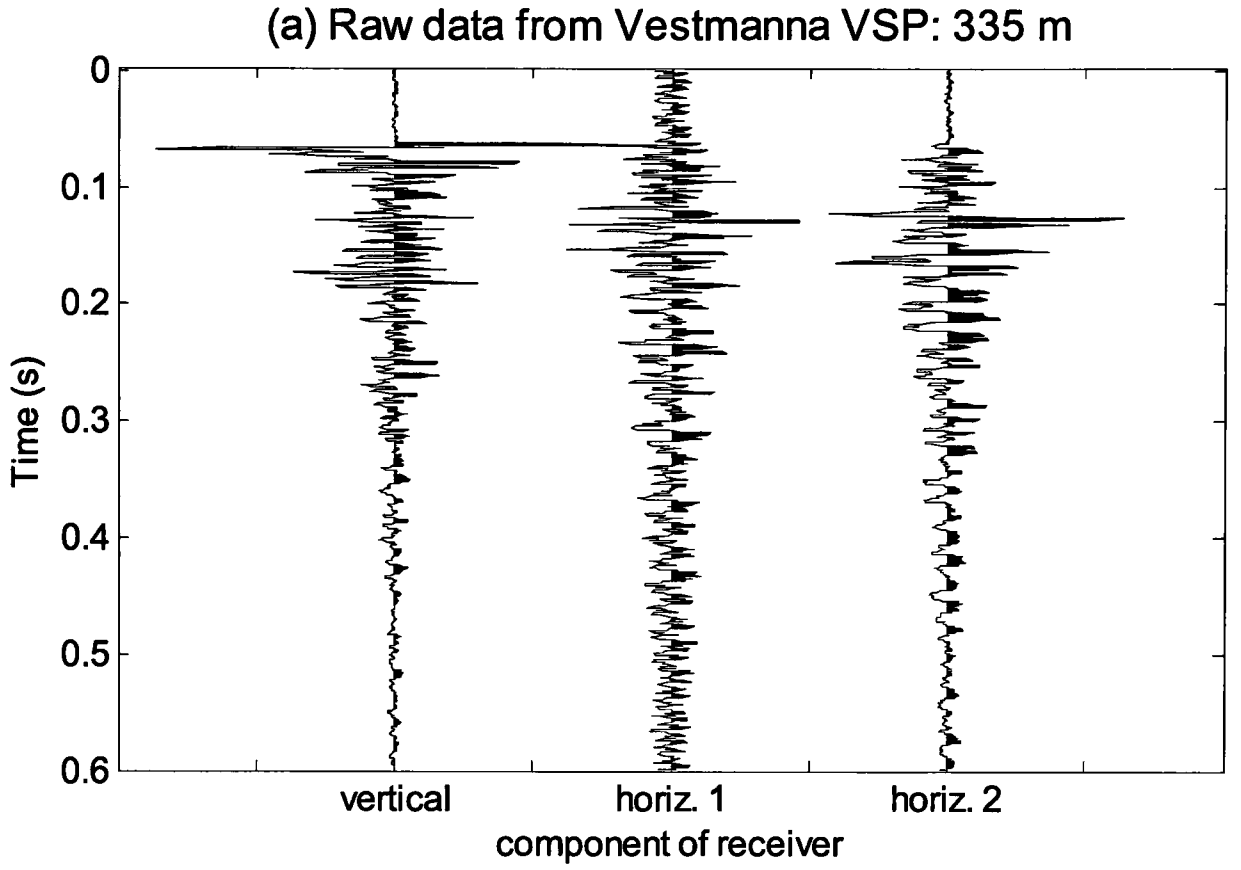

Figure 2.11.
a. Raw data at the 335 m depth level. Amplitudes of the three traces have been normalised for clearer display.
b. Raw data at 340 m, showing stronger noise on the horizontal components. This was due to air leakage from the air gun.

Table 2.2

Location	Glyvursnes	Vestmanna
Zero-offset VSP		
Spacing	10 m	5 m
Depth coverage	50 m – 600 m	50 m – 500 m
Offset VSP	242 m, 415 m	230 m, 610 m
Spacing	10 m	10 m
Depth coverage	50 m – 350 m	100 m – 500 m
Source	Single sleeve gun	Two sleeve guns chained together
Air capacity	150 cubic inches	40 cubic inches in each air gun
Immediate environment of source	Lined pits in soft quaternary soil, excavated down to bedrock where possible	Natural rock pool for zero-offset, open water for offset VSP
Receiver	3 component geophone hydraulic bowstring clamp	Same instrument as Glyvursnes, but with declamping mechanism
Monitor	Hydrophone at ~ 7 – 13 m depth, in oblique slim hole under airgun pit	Hydrophone at ~ 20 m depth, in borehole above geophone

Table 2.2. Comparison between Glyvursnes and Vestmanna experimental setup.

2.2 PRELIMINARY VSP PROCESSING

The data were initially recorded in seg2 format, then converted to DSISoft format for easily handling. DSISoft is a freeware, Matlab® based package for VSP processing (Beaty *et al.*, 1998). Frequencies above 800 Hz were filtered off and the three-component data of Glyvursnes and Vestmanna are displayed in Figures 2.12 and 2.13 respectively.

The compressional wave is consistent in both VSPs and the travel times of the first arrivals could be easily picked. In Glyvursnes the average P-velocity is 4.13 km/s, while in Vestmanna the average P-velocity is 5.29 km/s. The shear wave is visible on the horizontal components. As described in section 2.1.2, the Vestmanna horizontal component data were strongly contaminated by noise between 340 and 500 m.

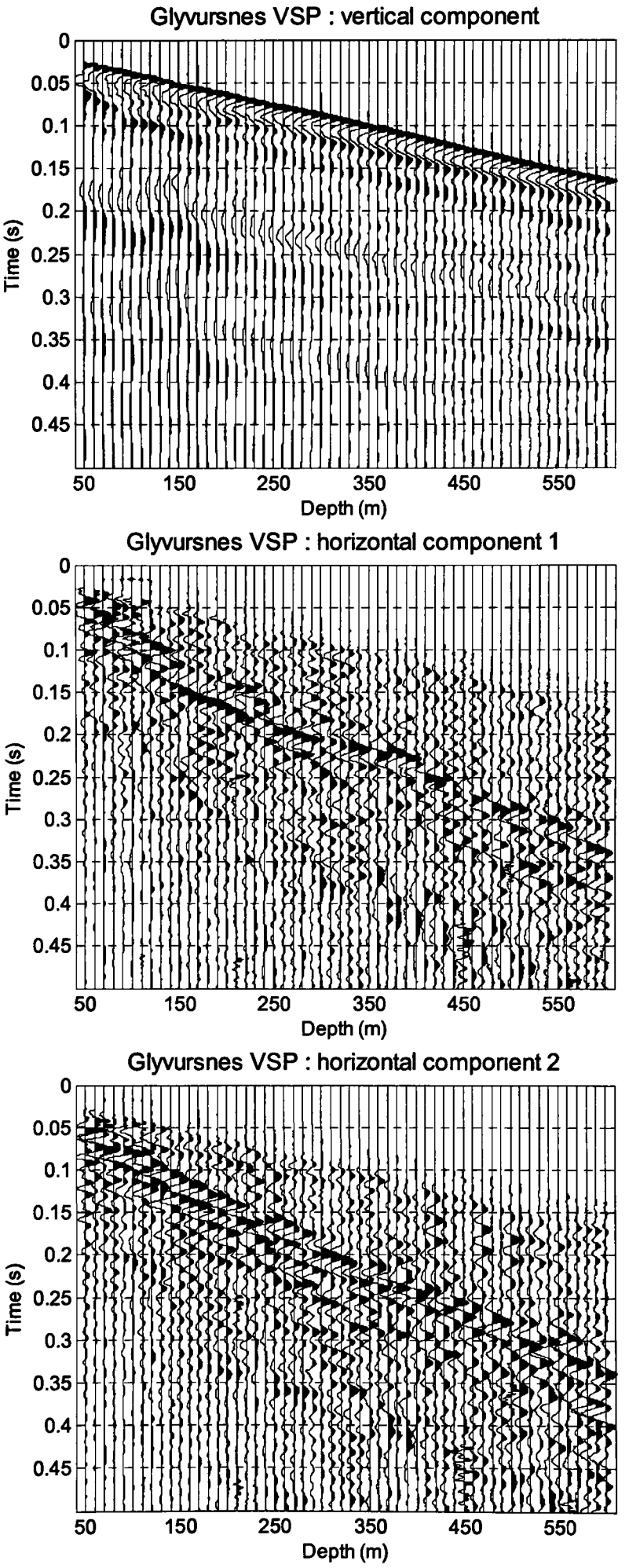

Figure 2.12.
Band-passed Glyvursnes VSP data, displayed with trace-by-trace scaling.

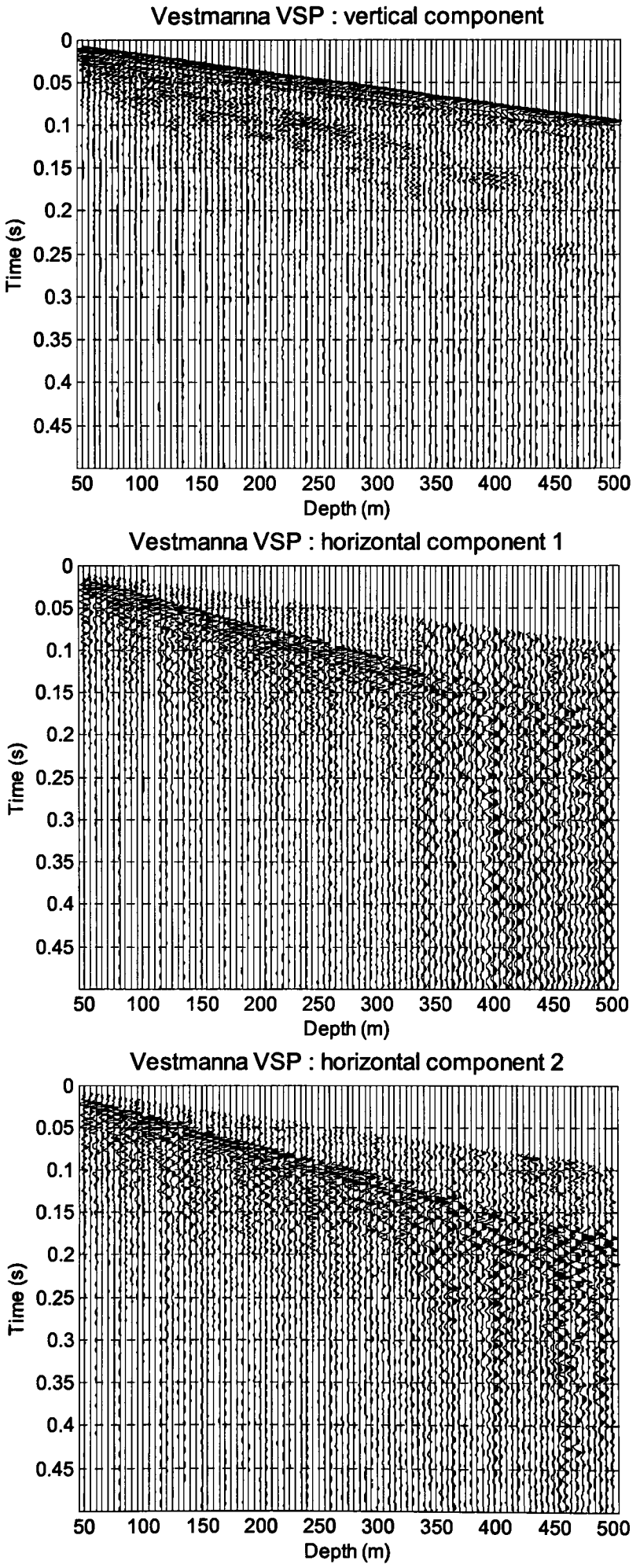

Figure 2.13.
Band-passed Vestmanna VSP data, displayed with trace-by-trace scaling.

2.2.1 ENHANCEMENT OF THE SHEAR WAVE

As the receiver was raised and lowered to different depth levels in the borehole, torque from the reels caused it to twist on its cable. This resulted in differential rotation between trace recordings. In the case of the near-zero-offset surveys in Glyvursnes and Vestmanna, the vertical component was largely unaffected, and the horizontal components could be corrected via rotation about the vertical axis alone.

If shear wave splitting occurs in the rock surveyed, the fast and slow shear waves are projected onto differently orientated coordinate systems in each shot (Macbeth, 2002). However, the Faroes VSP data were rotated only to enhance the clarity of the S-wave, and not to calculate the extent of birefringence.

One method of rotation requires eigenanalysis of the covariance matrix of the motions (Esmersoy, 1984). If $\mathbf{d}^P(t)$ represents the linear P-wave motion as recorded by the sensors, then its covariance matrix $\mathbf{P}$ is

$$\mathbf{P} = \sum_i \mathbf{d}^P(t_i)\,[\mathbf{d}^P(t_i)]^T \qquad \textbf{(2.1)}$$

Decomposition of the matrix is in this form:

$$\mathbf{P} = \mathbf{U}\Lambda\mathbf{U}^T \qquad \textbf{(2.2)}$$

where $\mathbf{U}$ is a matrix of normalised eigenvectors and Λ is the diagonal matrix of eigenvalues. The first element of Λ corresponds to the linear polarisation of the P-wave.

The u_{11} and u_{12} elements of **U** provide an estimate of rotation angle:

$$\hat{\phi}_P = \tan^{-1}\left(\frac{u_{12}}{u_{11}}\right) \qquad \textbf{(2.3)}$$

A 0.01 second window was specified around the P-wave first arrivals. Within this time window, the eigenanalysis method was used to rotate the two horizontal traces of both VSP datasets into pseudo-radial and pseudo-tranverse components (by an algorithm within DSISoft). The result is improved resolution of the shear waves, shown in Figures 2.14 and 2.15, particularly for Vestmanna.

2.14

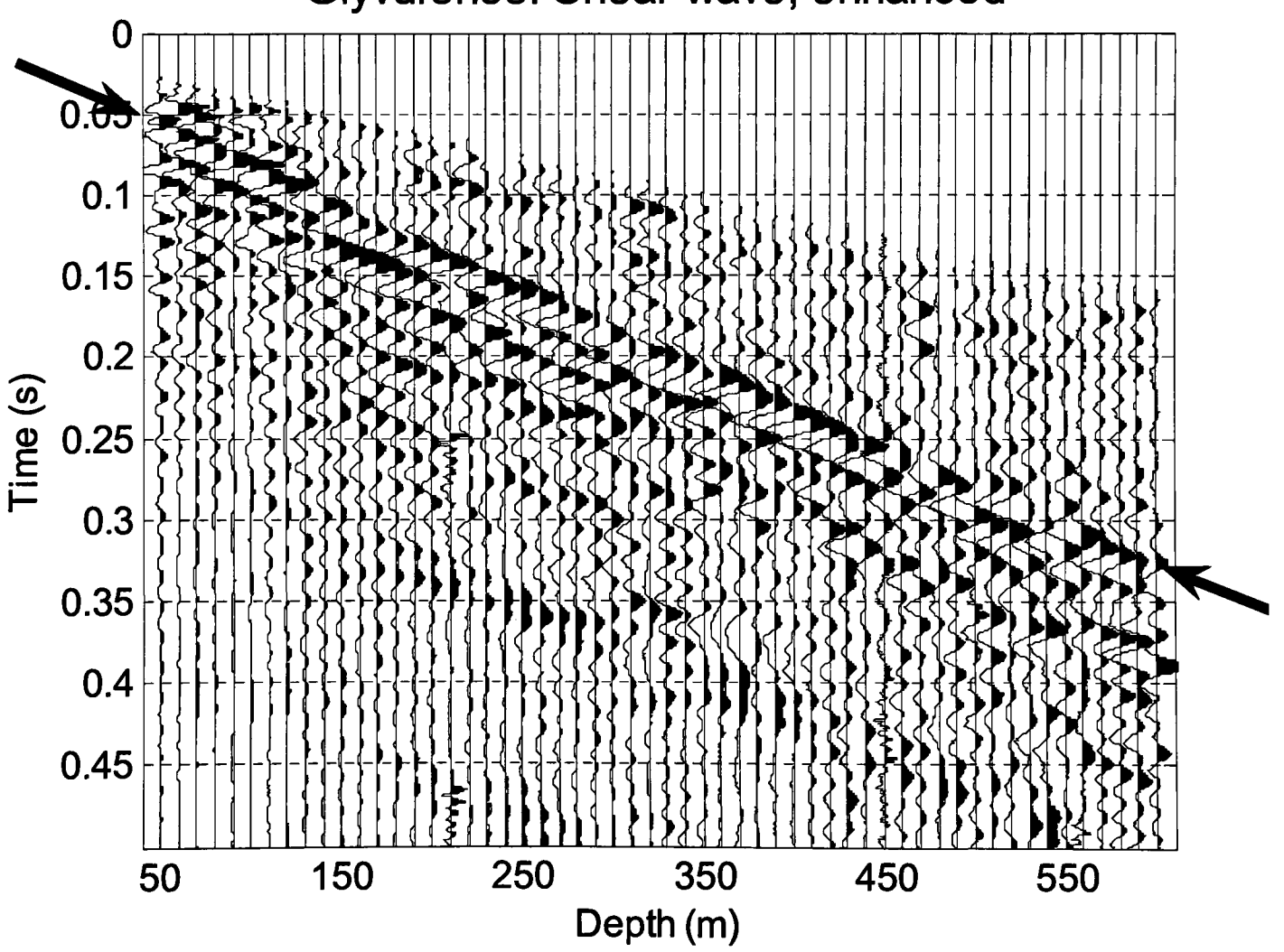

Figure 2.14.
Shear wave in Glyvursnes VSP, extracted by rotating the primary-wave to minimum energy. Displayed with trace-by-trace scaling.

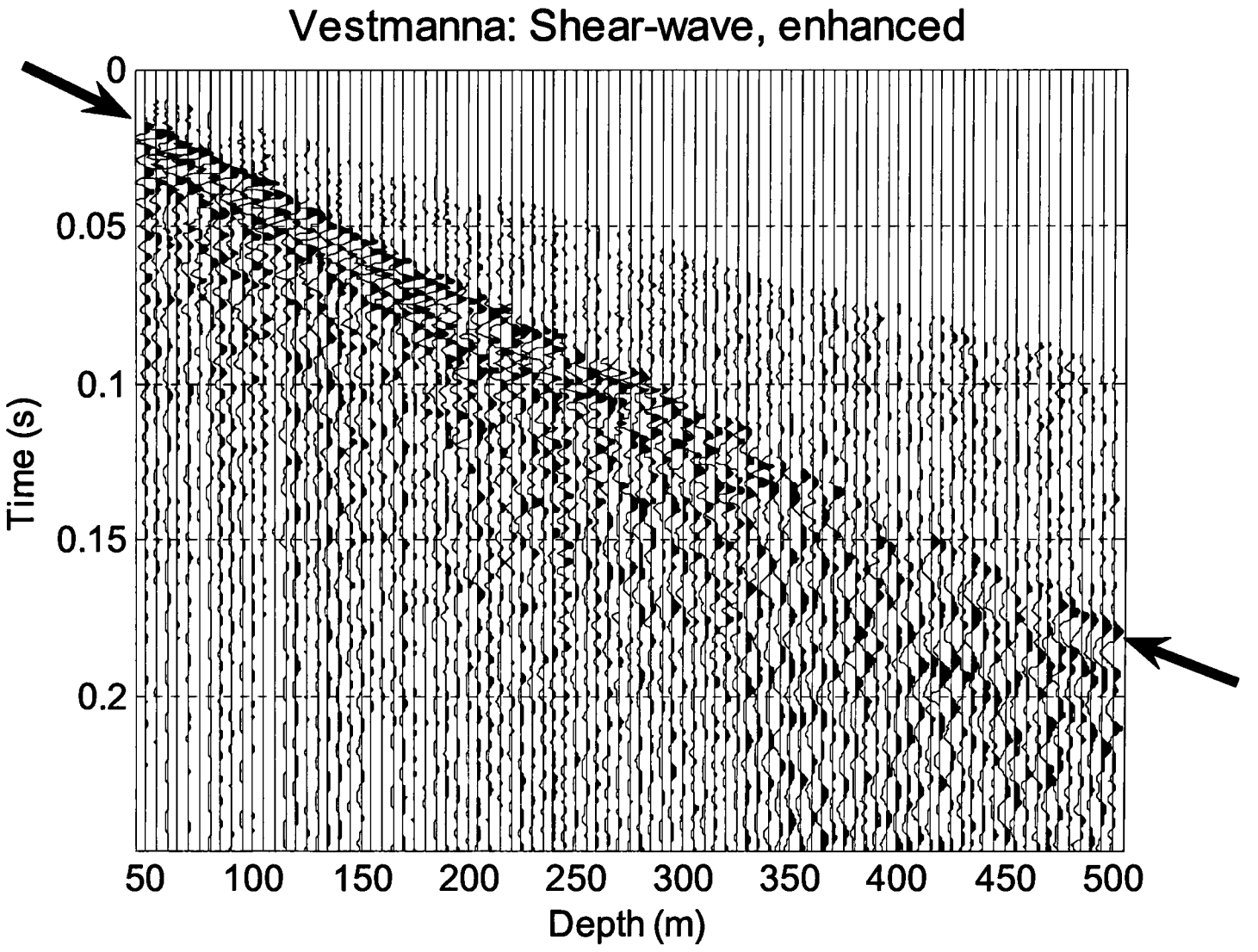

Figure 2.15.
Shear wave in Vestmanna VSP, extracted by rotating the primary-wave to minimum energy. Displayed with trace-by-trace scaling.

Shear wave first arrivals were picked and the shear wave velocity, V_s, calculated. Within error, the same velocity values were measured from both rotated components. In Glyvursnes, average shear-wave velocity over the VSP interval is 2.05 km/s, giving a V_p/V_s ratio of approximately 2.0. Average shear-wave velocity from the Vestmanna VSP interval is 2.83 km/s, giving a V_p/V_s ratio of 1.9. These values are marginally higher than the mean V_p/V_s ratio from the wireline logs, 1.8 (Waagstein & Andersen, 2003), probably due to the effect of averaging over much larger intervals. By way of comparison, mean ratios of 1.8 and 1.9 were found in Lopra (Christie *et al.*, 2002) and the Southeast Greenland margin (Planke & Cambray, 1998) respectively.

2.2.2 EXTRACTION OF THE UPGOING WAVE

Upgoing wave modes are substantially weaker than the downgoing modes, and numerical procedures are required to extract them from VSP data. A first step is to attenuate the downgoing waves, and it is important to choose procedures that do not seriously alter the rest of the data (Hardage, 2000).

The following procedure was used for both VSP datasets:

The first arrivals of the P-waves were picked (Figures 2.16a, 2.17a). The traces were then aligned to these pick-times, and a running 5-point median filter applied (Figures 2.16b, 2.17b).

Median filtering is a non-linear process: an odd-numbered set of data are placed in ascending / descending magnitude, and the middle value is selected. This form of smoothing rejects all noise spikes but passes step functions, and adequately preserves the complicated forms taken by seismic traces. The overall effect on the seismic data is to suppress the upgoing waves and amplify the downgoing mode. Minor inconsistencies in the downgoing wave from trace to trace are also suppressed (Hardage, 2000).

The median-filtered data were then subtracted from the time-aligned data, enhancing the visibility of upgoing modes (Figures 2.16c, 2.17c). Figures 2.16d and 2.17d show the data after re-alignment to their true arrival times.

2.16

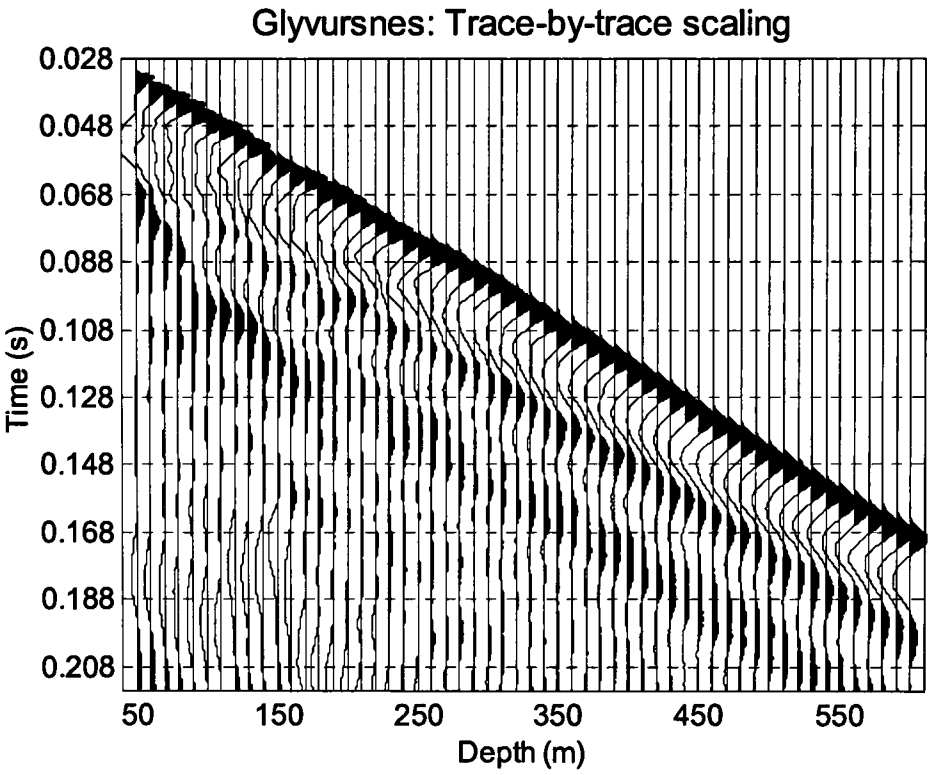

a

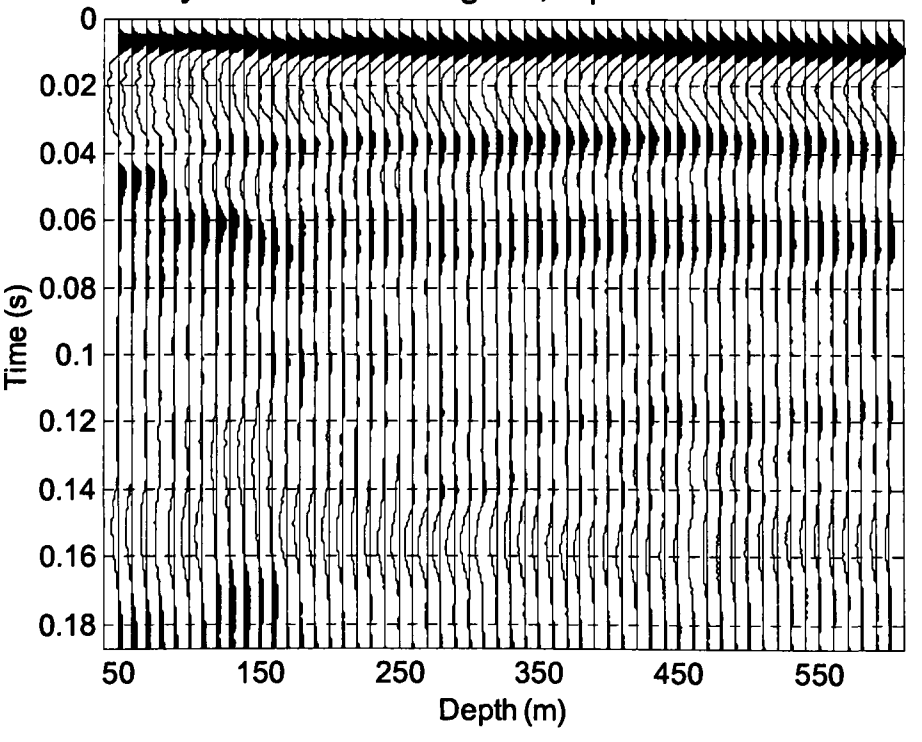

b

Figure 2.16.
Extraction of upgoing waves from the Glyvursnes VSP.

a. First arrival times are picked, and the traces are time-aligned.
b. The data are median filtered with a 5 point window to create an approximate downgoing wave.

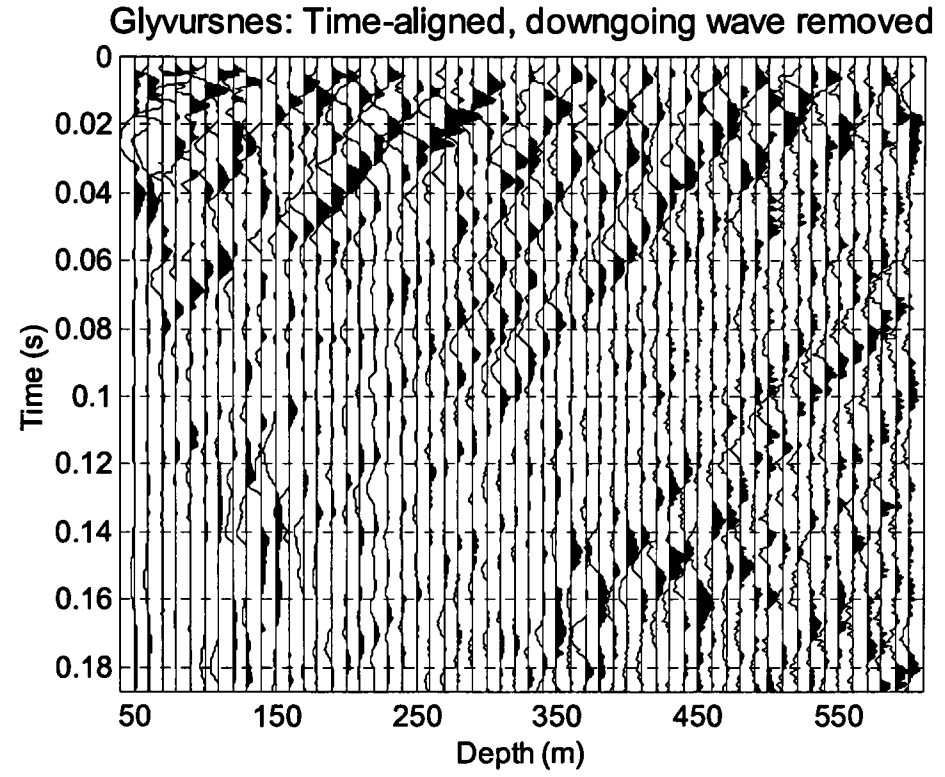

c

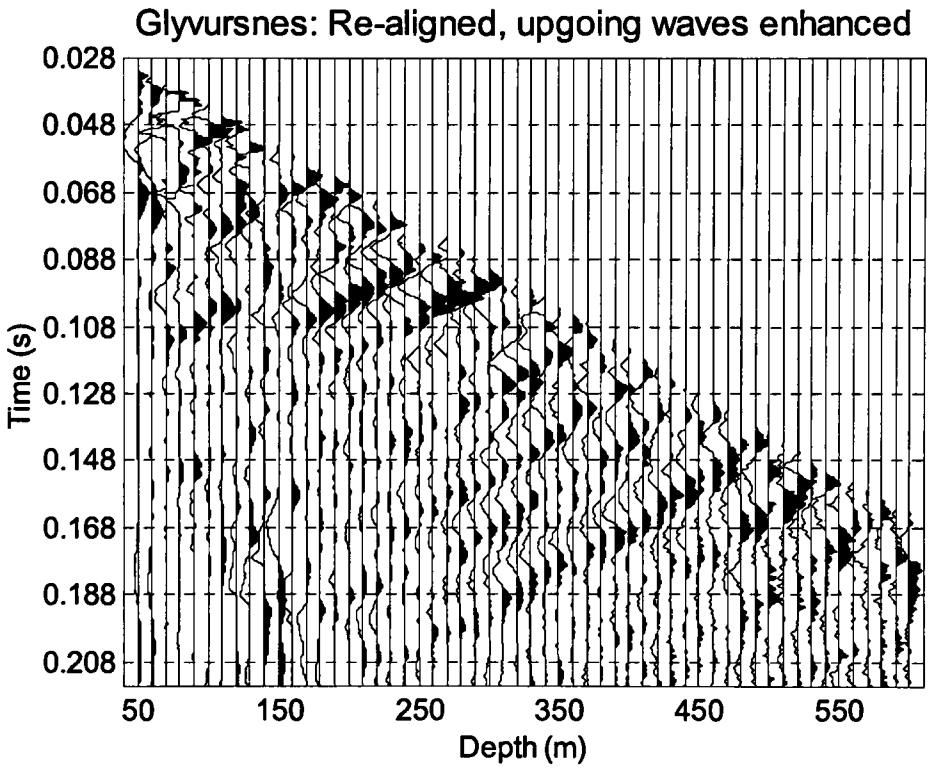

d

Figure 2.16 cont'd.

c. The downgoing wave is subtracted from the data, leaving the upgoing waves clearly visible.
d. Data are re-aligned to their true arrival times.
All data are displayed with trace-by-trace scaling. Only 0.2 seconds of data shown.

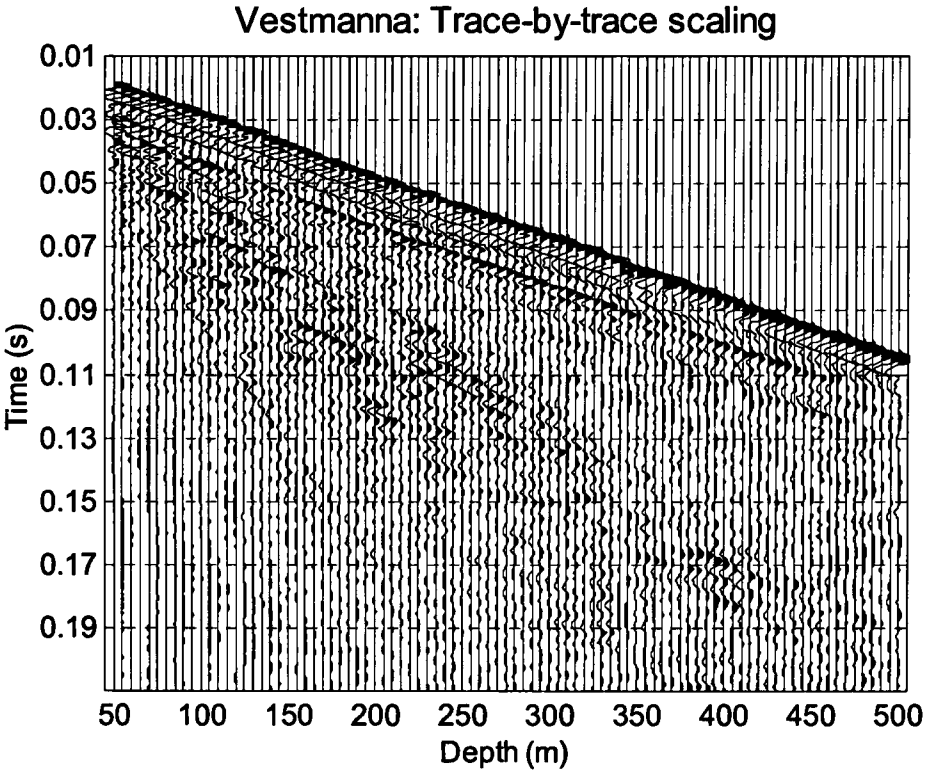

a

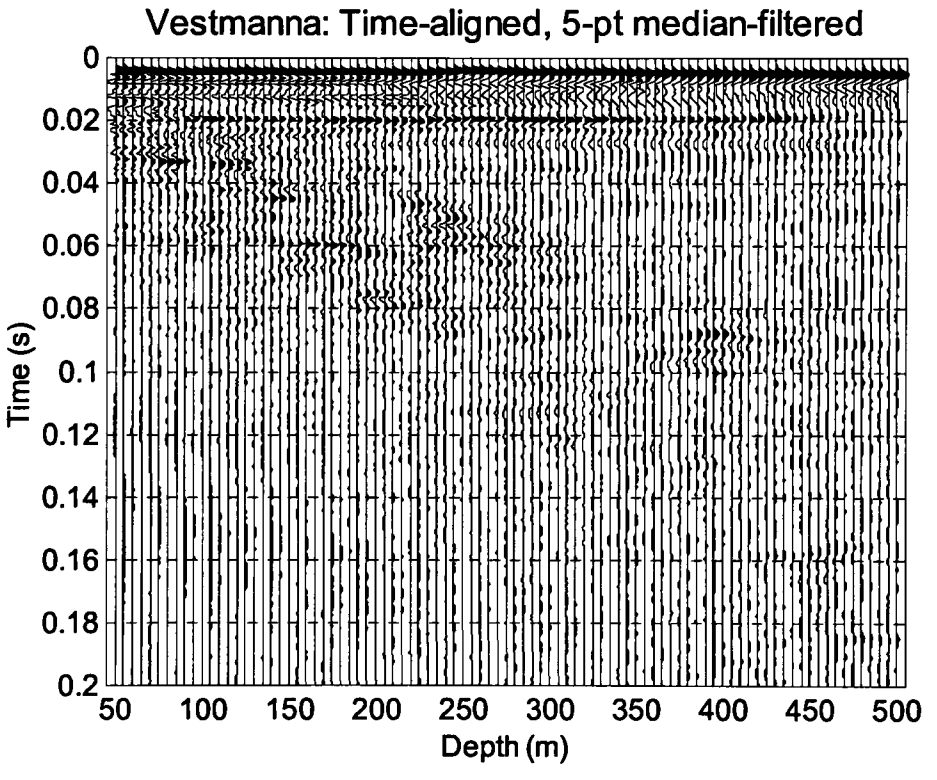

b

Figure 2.17.
Extraction of upgoing waves from the Vestmanna VSP.

a. First arrival times are picked, and the traces are time-aligned.
b. The data are median filtered with a 5 point window to create an approximate downgoing wave.

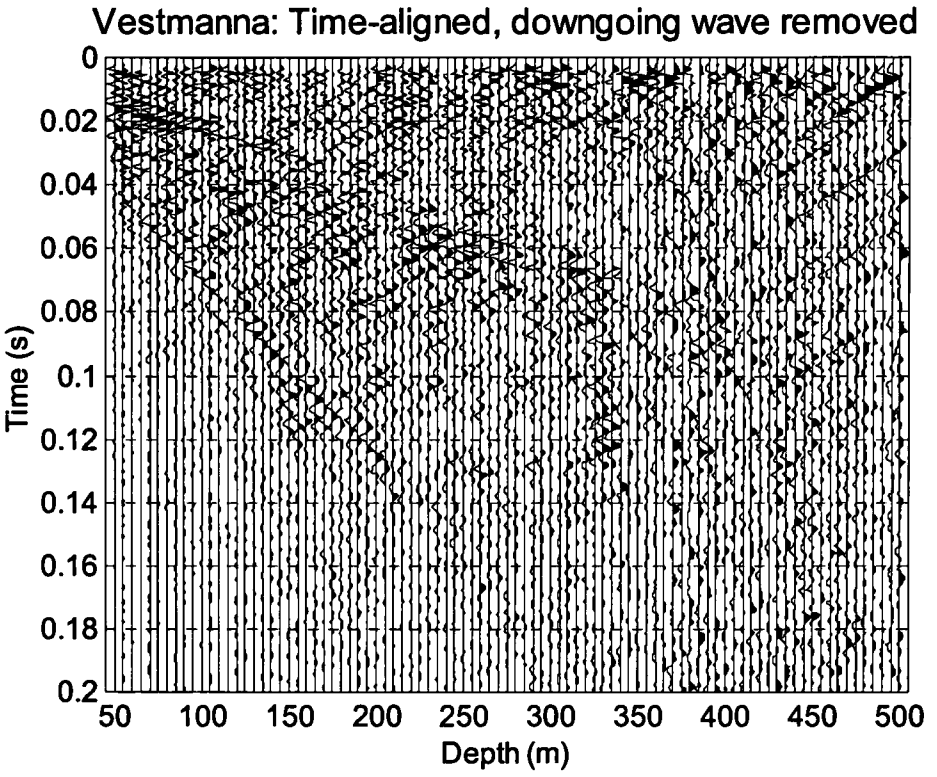

c

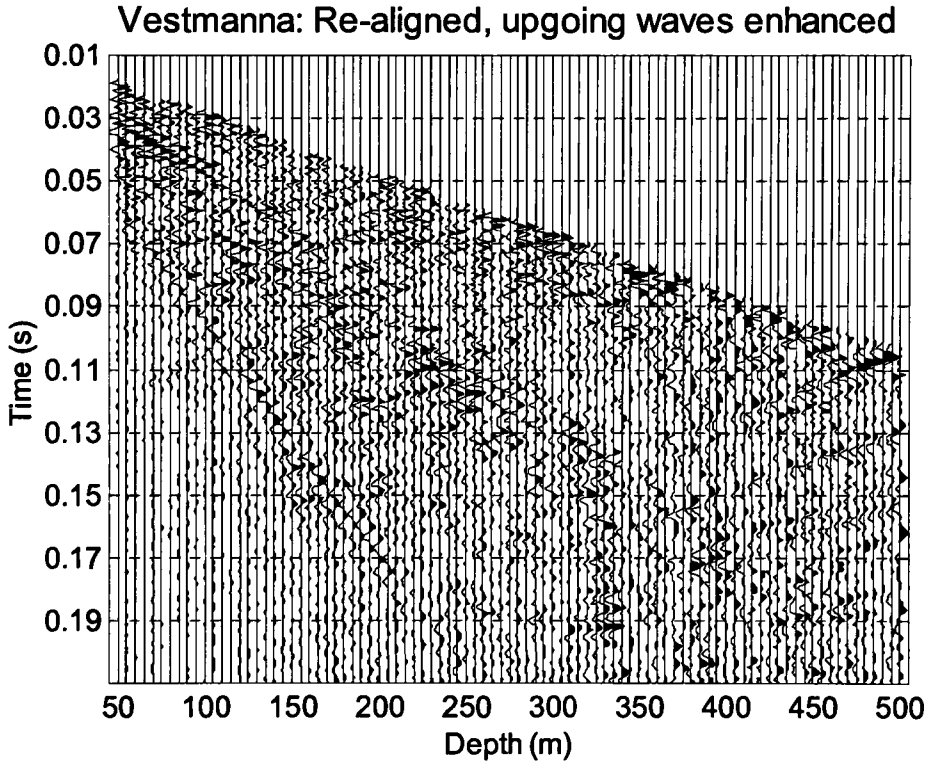

d

Figure 2.17 cont'd.

c. The downgoing wave is subtracted from the data, leaving the upgoing waves clearly visible.
d. Data are re-aligned to their true arrival times.
All data are displayed with trace-by-trace scaling. Only 0.2 seconds of data shown.

2.3 WELL-TIE

2.3.1 VELOCITY CALIBRATION FOR WIRELINE LOGS AND VSP

Integrated travel times from the P-velocity sonic logs are compared with first arrival times of the VSP datasets in Figure 2.18. The cumulative log travel time at 600 m in Glyvursnes is 3 % shorter than the corresponding VSP first arrival time (i.e. the log velocities are faster). At 500 m in Vestmanna, the cumulative log travel time is 2 % longer than in the VSP (i.e. the log velocities are slower). The disparities may derive from experimental error, dispersion or actual rock properties. Despite this, for the purposes of this thesis it is possible to match VSP upgoing waves to log data with reasonable accuracy.

2.18

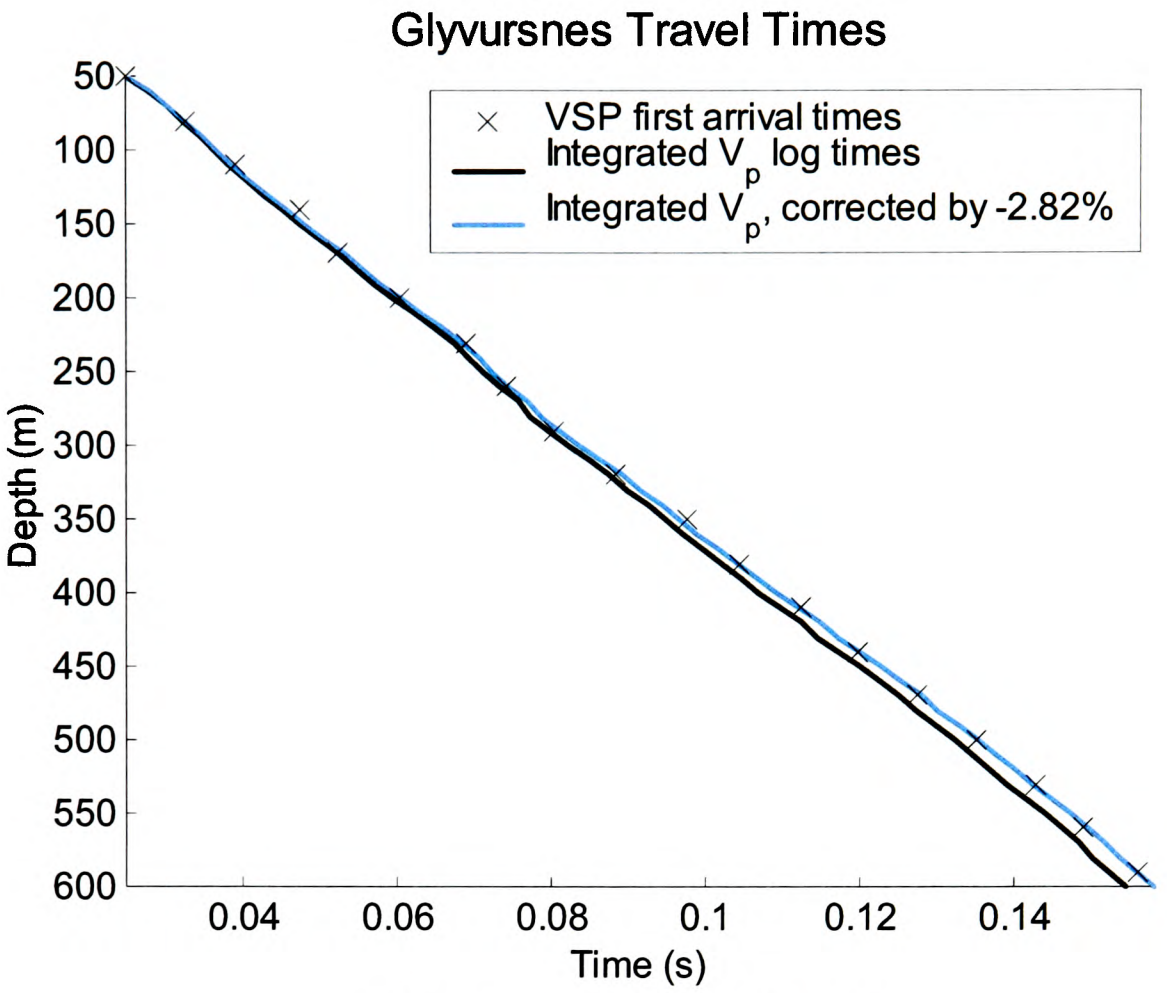

Figure 2.18. VSP first arrivals and integrated travel times from P velocity sonic logs from Glyvursnes (above) and Vestmanna (below).

2.3.2 DECONVOLUTION

For clearer display of upgoing waves, it was desirable to reshape the downgoing wavelets to zero-phase wavelets centred on a dominant frequency. Reshaping was performed as a separate routine to the extraction of the upgoing waves, as the deconvolution process can greatly alter all modes in the data.

2.19

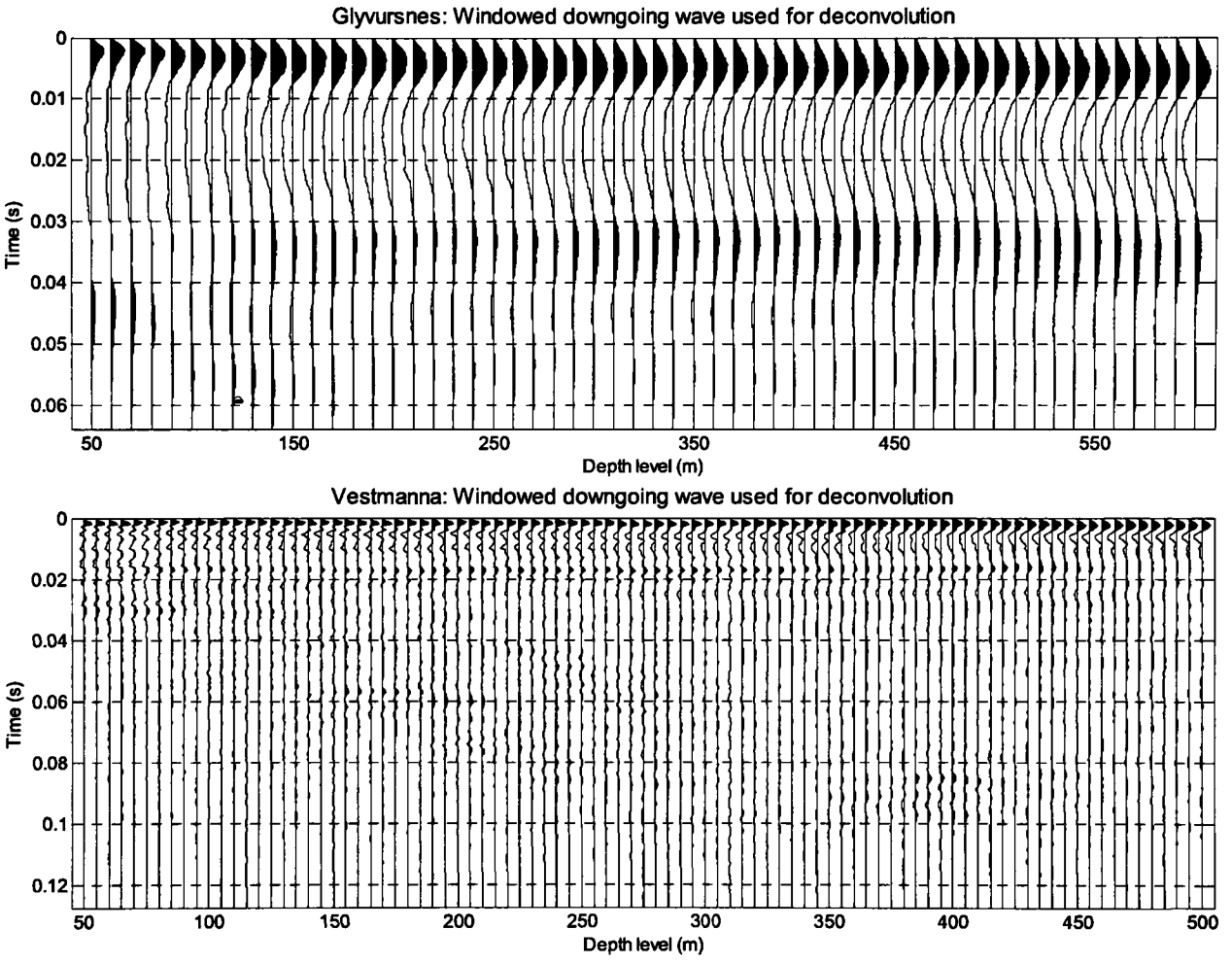

Figure 2.19.
Approximate downgoing waves used for deconvolution of Glyvursnes (above) and Vestmanna (below) data.

To achieve this, the smoothed downgoing wave was isolated from the median-filtered data extracted in section 2.2.2. The optimum size of the window was determined by visual inspection (0.064 s for Glyvursnes, 0.128 s for Vestmanna, Figure 2.19), with all traces tapered using the same half-Hanning function. Wiener filtering was used to

derive a least-squares deconvolution operator for each trace of the isolated downgoing wave. In application of the Wiener filter, it is assumed that the signal and noise are stochastic processes with known auto-correlation and cross-correlation functions (Wiener, 1949).

The deconvolution operators were convolved with upgoing data extracted in section 2.2.2. The reshaped upgoing waves were then matched to the relevant acoustic impedance logs (P-velocity multiplied by density). Figures 2.20 and 2.21 show well-ties from Glyvursnes and Vestmanna, respectively. Upgoing waves have been highlighted for easy comparison with the acoustic impedance logs.

The reflections in Vestmanna are not as clearly defined, nor as evenly distributed, as those in Glyvursnes. The most coherent events are generated at levels deeper than 500 m, in rocks classified as the Lower Basalt Series. The match between the reflections and large acoustic impedance contrasts is also better in the Glyvursnes well-tie. This suggests that strata crossing the Glyvursnes borehole are laterally continuous at least over the radius of a Fresnel zone, while strata crossing the top 500 m of Vestmanna may not be. If so, there are implications for three-dimensional basalt modelling. The relationship between seismic reflectivity and geological formation will be revisited in Chapter 6 of this thesis.

2.20

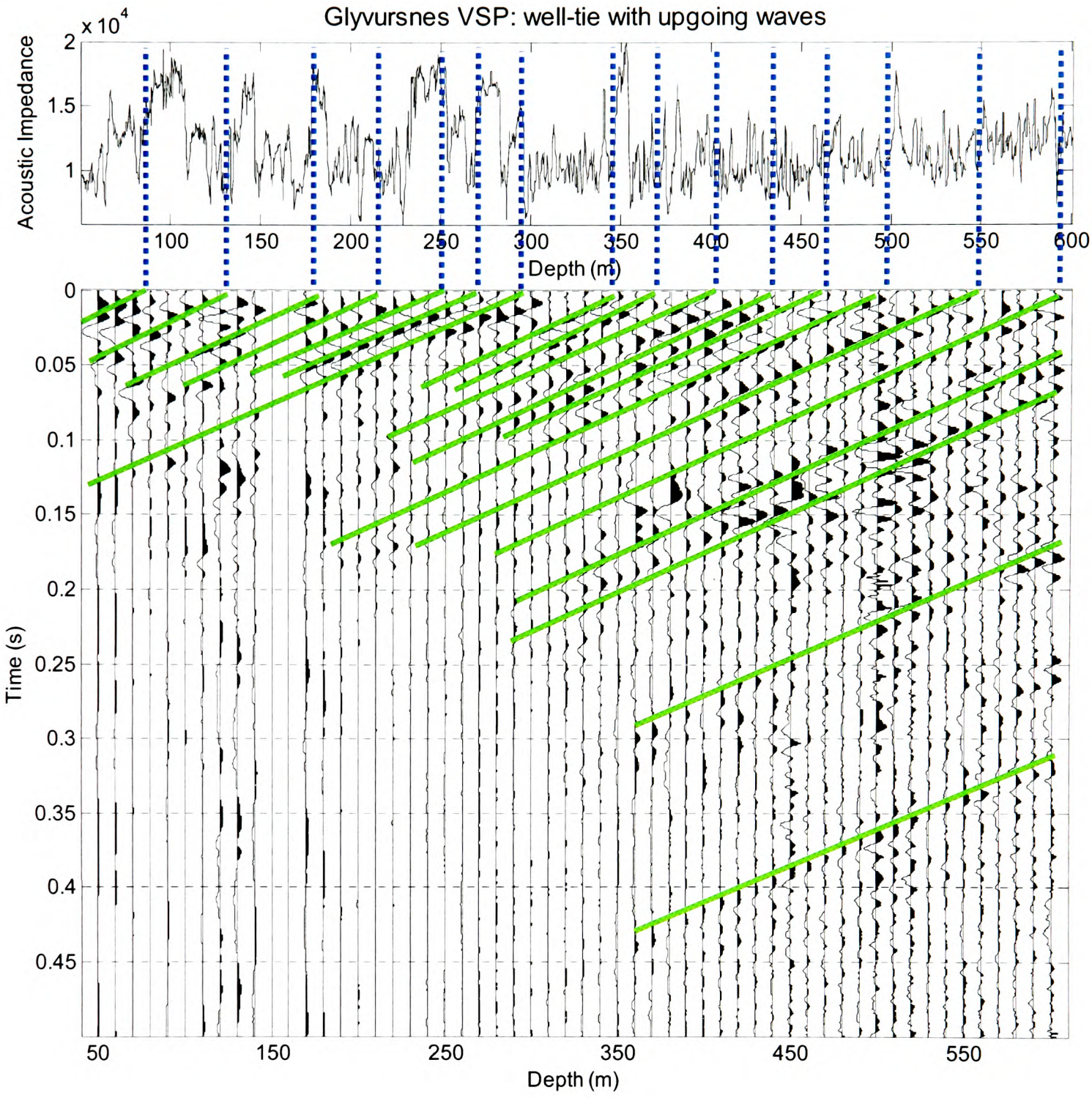

Figure 2.20.
Upgoing waves (highlighted in green) matched to the acoustic impedance log of Glyvursnes.

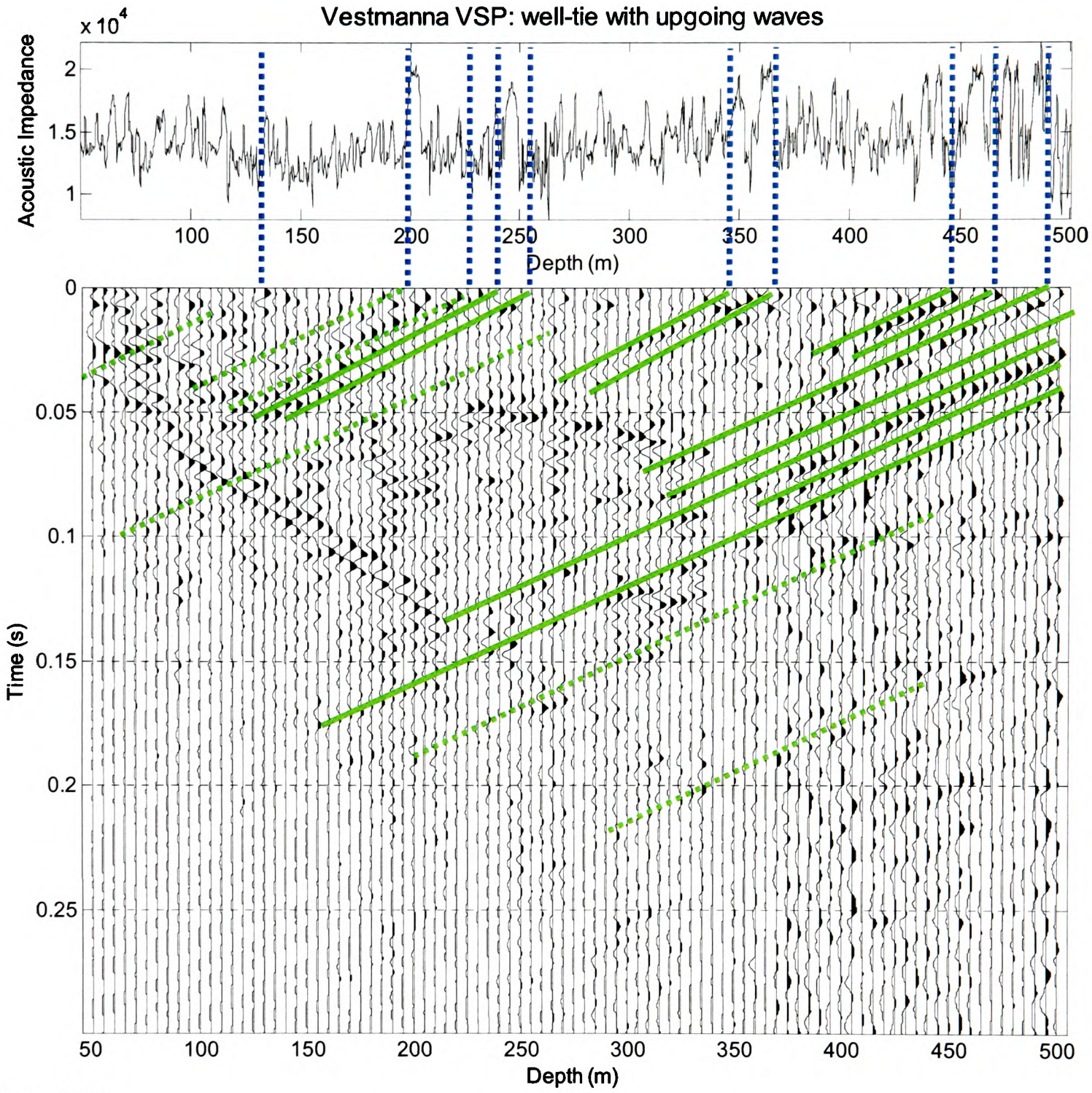

Figure 2.21.
Upgoing waves (highlighted in green) matched to the acoustic impedance log of Vestmanna.

CHAPTER 3

EFFECTIVE ATTENUATION IN THE FAROES BASALTS

VSP data are used widely for attenuation analyses, with numerous studies conducted in basalt terranes such as the Columbia River Basalts (Pujol & Smithson, 1991), the Faroe Islands (Christie *et al.*, 2002) and various other locations in the North Atlantic Igneous Province (Maresh *et al.*, 2003; Droujinine, 2005). In the above studies, effective Q was found to be extremely low, typically varying between 10 and 45.

In this chapter, estimates of seismic Q are derived from VSP data acquired at the Glyvursnes and Vestmanna field sites, using the spectral ratio method (Båth, 1974) and a method based on amplitude decay. The Q trend with depth is investigated.

Time-frequency analysis is introduced, and Morlet wavelet scalograms are used to track the distribution of coda energy in seismic traces.

3.1 Q ESTIMATION FROM THE SPECTRAL RATIO METHOD

The spectral ratio method is applied in the frequency domain and compares the spectrum of a seismic wave entering an attenuative medium with its spectrum as it emerges, with the assumption that the quality factor and velocity are independent of frequency (Båth, 1974). It has been found to be the most robust method for data with good signal-to-noise ratio (Tonn, 1991), and has been used extensively in studies of basalt (Pujol & Smithson, 1991; Christie *et al.*, 2002; Maresh *et al.*, 2003; Droujinine, 2005).

For a constant seismic quality factor over a certain bandwidth, the amplitude of a seismic signal in relation to the source amplitude is given by:

$$A = A_0 \exp(-\pi fx / Qc) \qquad \textbf{(3.1)}$$

(Also see Equation 1.14). A is amplitude at depth x, A_o is source amplitude, f is frequency, Q is seismic quality factor, and c is wave propagation velocity.

Assuming that source amplitude A_o is consistent, the traces from depth levels x_1 and x_2 are related by:

$$\frac{A_2}{A_1} = \frac{A_0 \exp(-\pi fx_2 / Qc)}{A_0 \exp(-\pi fx_1 / Qc)} \qquad \textbf{(3.2)}$$

$$\Rightarrow \quad \ln(\frac{A_2}{A_1}) = \frac{-\pi f \delta t_{2-1}}{Q} \qquad \textbf{(3.3)}$$

A_1 and A_2 are the respective amplitudes and δt_{2-1} is the difference in travel times. In a graph of $ln\ (A_2 / A_1)$ against frequency f, effective seismic quality factor, Q, can be derived from:

$$Q = \frac{-\pi \delta t_{2-1}}{(slope\ of\ \ plot)} \qquad \textbf{(3.4)}$$

It was vital not to make *a priori* assumptions of the sensitivity of Q to the length and bandwidth of the wavelet studied. Therefore a standard estimation procedure was followed rigorously throughout the analyses, as follows:

The VSP data were time-aligned, and a five-point median filter applied (Figures 3.1, 3.2). This step suppressed upgoing waves which may have interfered with the downgoing waves analysed (as shown by Stainsby & Worthington, 1985). Two seismic traces of interest, separated by a depth interval of $(x_2 - x_1)$ m, were time-gated with the same double-tapered, half-Hanning window. The length of the time gate was determined by visual inspection across all traces, and as far as possible, short period multiples were removed leaving only the first arrival. An example is given in Figure 3.3a. The amplitude spectra were examined to find the frequency range over which spectral ratios were relatively stable (Figure 3.3b). Once determined, both the length of the time gate and the stable frequency range were kept constant for all trace pairs analysed. Least-squares linear regression was performed within the stable frequency range (Figure 3.3c), and the corresponding Q value was calculated from Equation 3.4.

Q values were initially derived for the full VSP intervals of Vestmanna and Glyvursnes, by comparing the uppermost and lowermost wavelets of the median-filtered data (Figures 3.3, 3.4). Following this, estimates were taken for fixed intervals between trace pairs. $(x_2 - x_1) = 250$ m was chosen as a sufficiently large depth separation, ensuring statistical independence in the spectra (White, 1992). Analysis was repeated from the top to the base of each borehole, thereby tracking Q with depth.

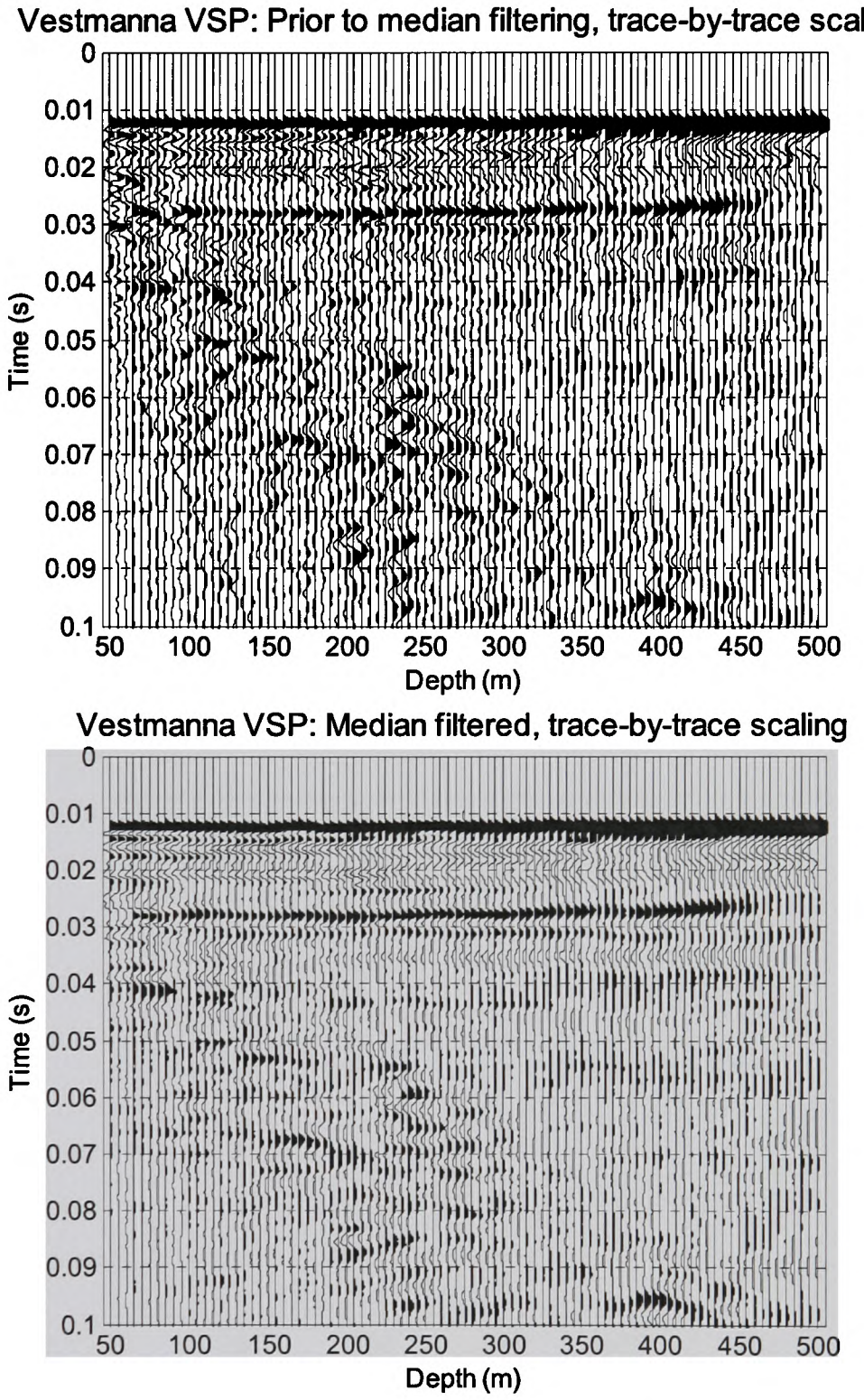

Figure 3.1. Vestmanna VSP data prior to and after 5-point median filtering to suppress upgoing waves.

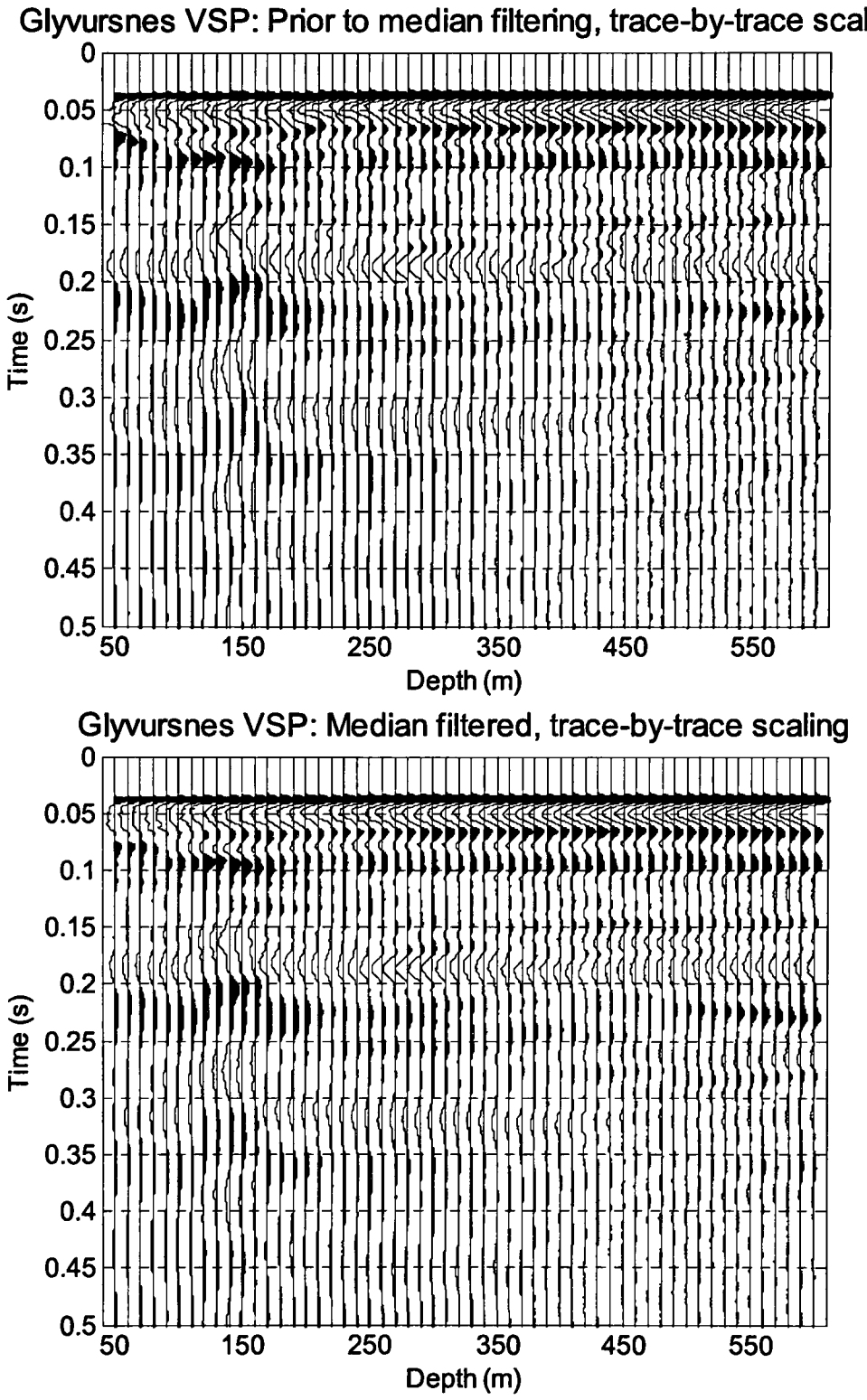

Figure 3.2. Glyvursnes VSP data prior to and after 5-point median filtering to suppress upgoing waves.

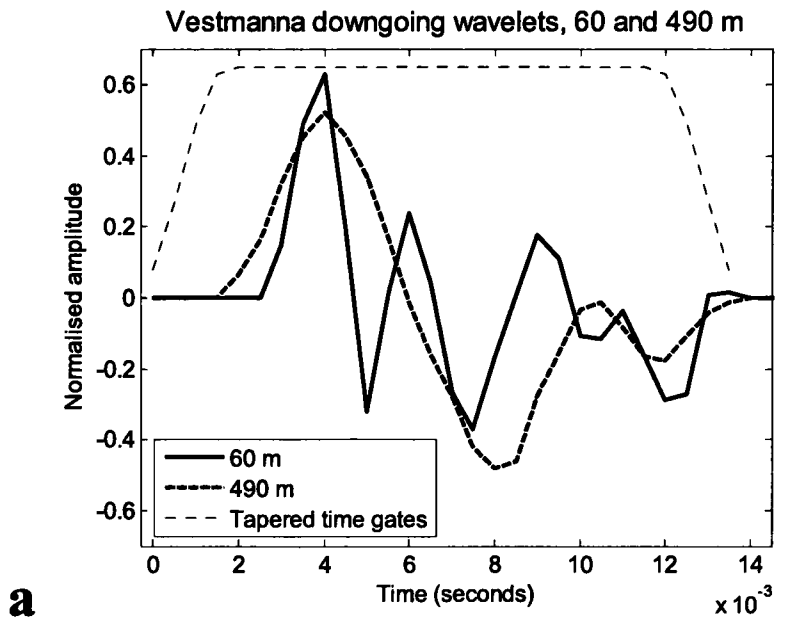

a

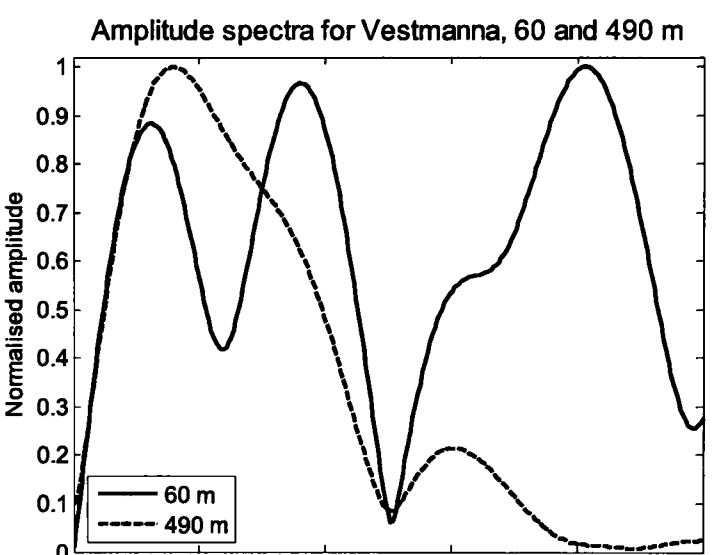

b

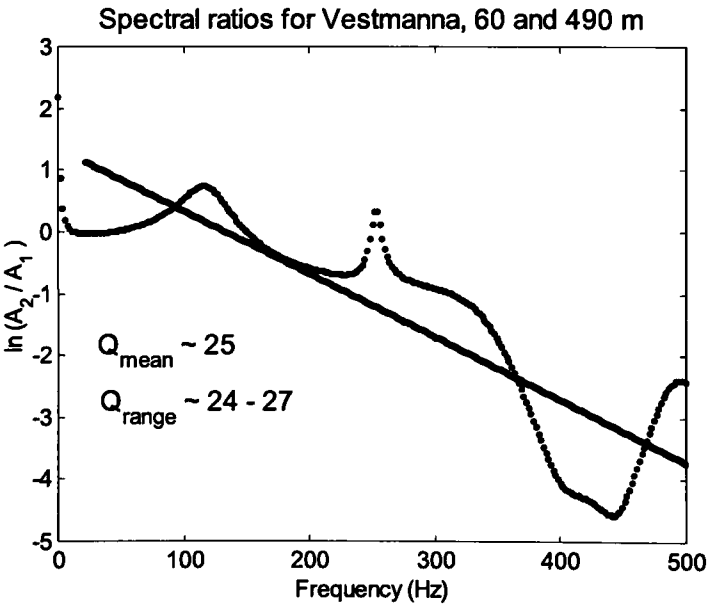

c

Figure 3.3.
a. Downgoing wavelets at 60 m and 490 m in the Vestmanna borehole. The time gates are double-tapered.
b. Amplitude spectra for the traces in 3.3a, with marked minima.
c. Spectral ratio plot. Least-squares linear regression is performed over a specified frequency range of 20 – 400 Hz. Q estimates are given for a 95% confidence interval of mean response.

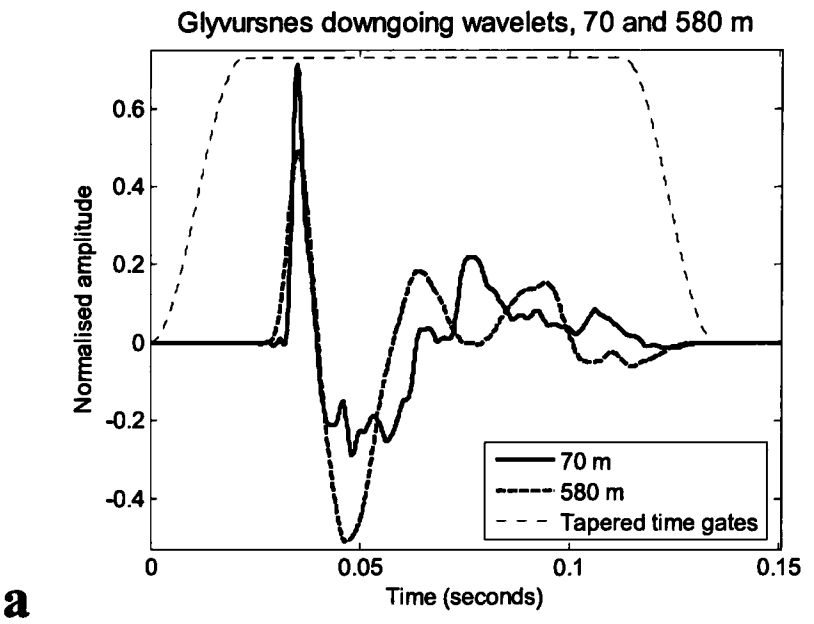

a

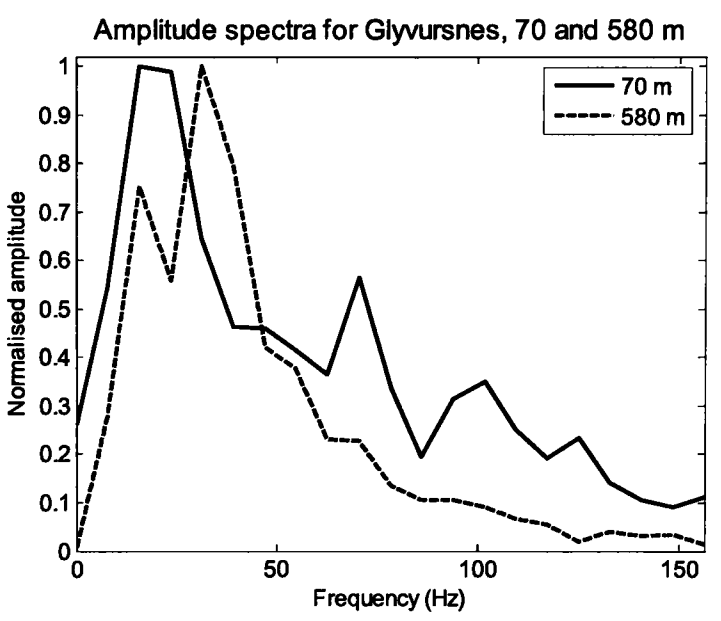

b

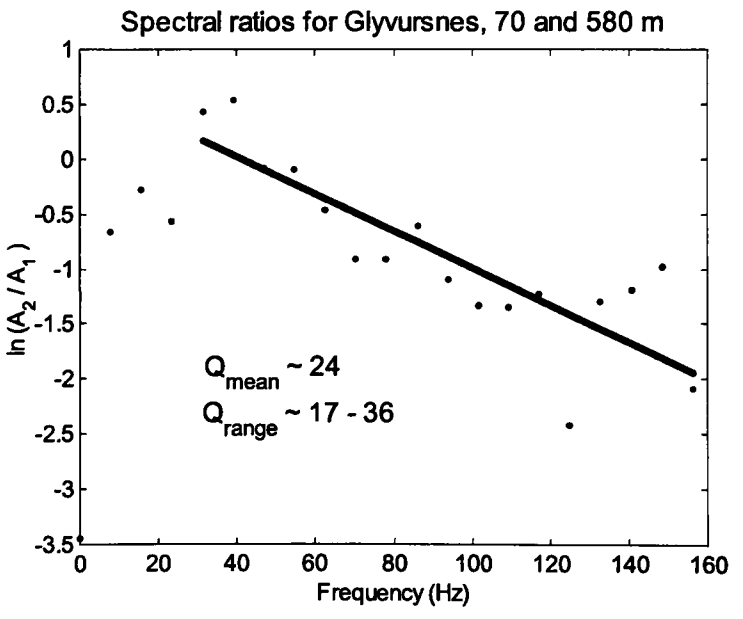

c

Figure 3.4.
a. Downgoing wavelets at 70 m and 580 m in the Glyvursnes borehole. The time gates are double-tapered.
b. Amplitude spectra for the traces in 3.4a.
c. Spectral ratio plot. Least-squares linear regression is performed over a specified frequency range of 30 – 150 Hz. Q estimates are given for a 95% confidence interval of mean response.

3.1.1 RESULTS

Vestmanna

Monitor hydrophone records indicate that the source signals for Vestmanna VSP data were consistent (Figure 3.5). The data had an overall frequency range of 10 – 700 Hz, from which log spectral ratios were found to be stable over 20 – 500 Hz. However, as short period multiples could not be entirely excised by time-gating, a prominent minimum persisted at ~ 250 Hz in the spectra (Figure 3.3b).

3.5

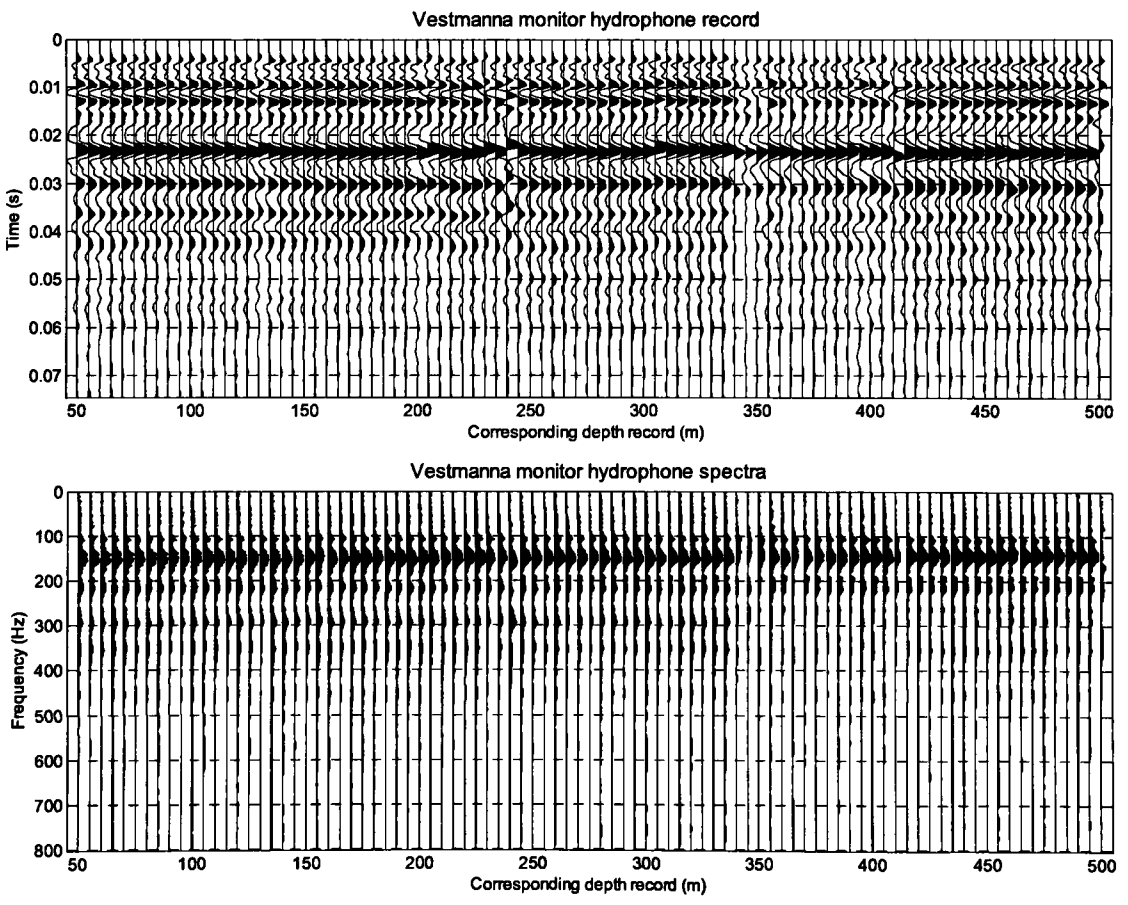

Figure 3.5.
a. Monitor hydrophone record for the Vestmanna experiment.
b. Amplitude spectra of monitor hydrophone record in 3.5a, plotted to 800 Hz.

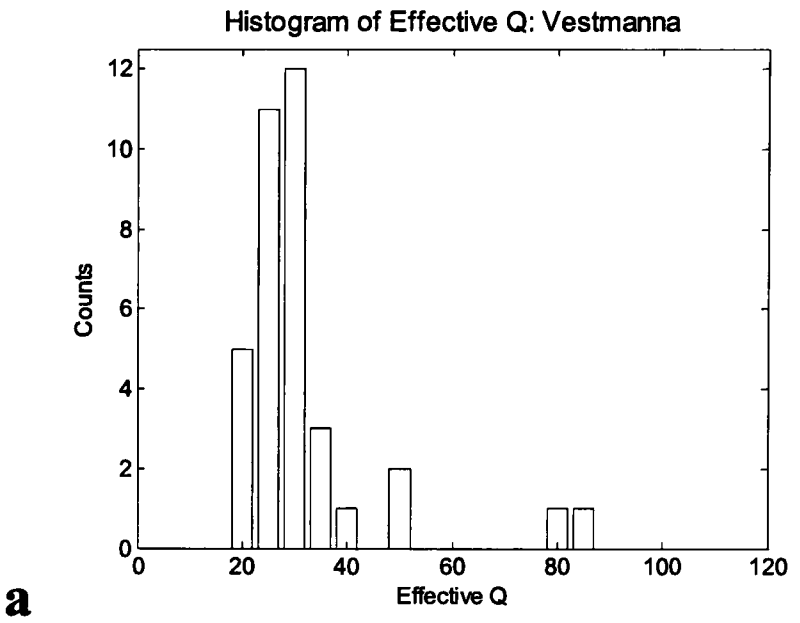

a

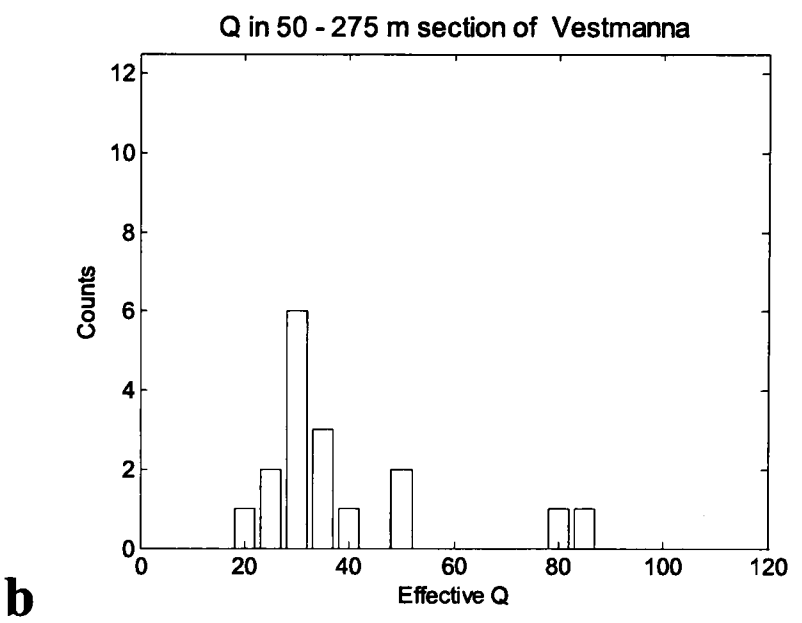

b

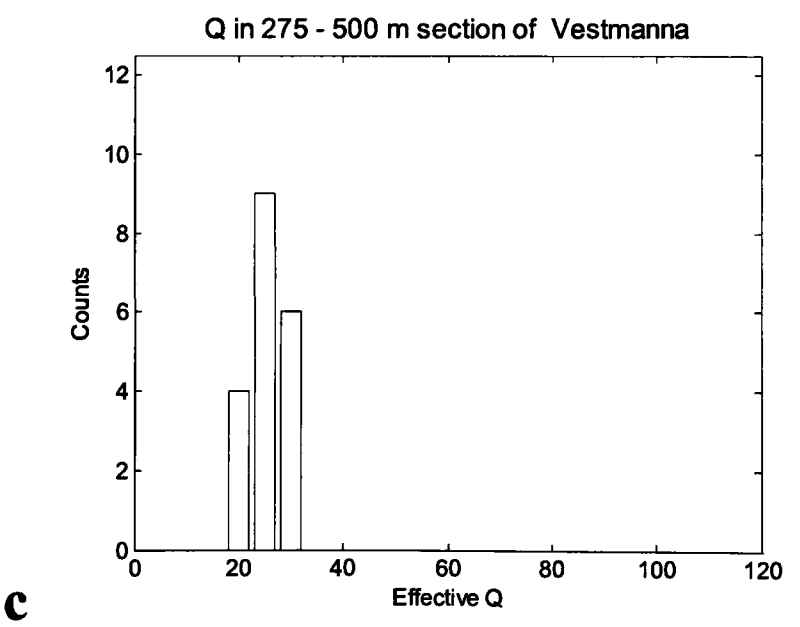

c

Figure 3.6.
a. Effective Q derived from Vestmanna VSP data by the spectral ratio method, for a depth separation of 250 metres between traces. No clear depth trend with Q was seen.
b. Effective Q values from the upper half of the Vestmanna VSP data.
c. Effective Q values from the lower half of the Vestmanna VSP data.

The mean Q derived from the bulk Vestmanna rock volume was 25, with a range of 24 – 27 for a 95% confidence interval (Figure 3.3c). In the analyses over intervals of 250 m, Q values spanned 20 to 90 (Figure 3.6a), with a mean of approximately 30. Comparing Q estimates from shallow and deep sections of the borehole revealed no significant depth trend (Figures 3.6b, c).

Glyvursnes

Poor source-to-bedrock coupling greatly reduced the bandwidth of the Glyvursnes VSP data. Ephemeral noise was also significant in traces recorded from the bottom half of the borehole, where the signal-to-noise ratio was substantially lower (section 2.1.1). Although the effect on Q could not be quantified, narrow bandwidth and high noise levels are known to increase error bounds of spectral-based analyses (White, 1992).

Figure 3.7 shows the monitor hydrophone signature over the 56 shots. The records are extremely varied in both the time and frequency domain, particularly between the 31st and 32nd shots. By contrast, corresponding geophone records at 350 m and 360 m are very regular and remain consistent throughout the profile (Figure 2.12). As detailed in section 2.1.1, the hydrophone did not record the true source signature, and corrections based on hydrophone data were not viable.

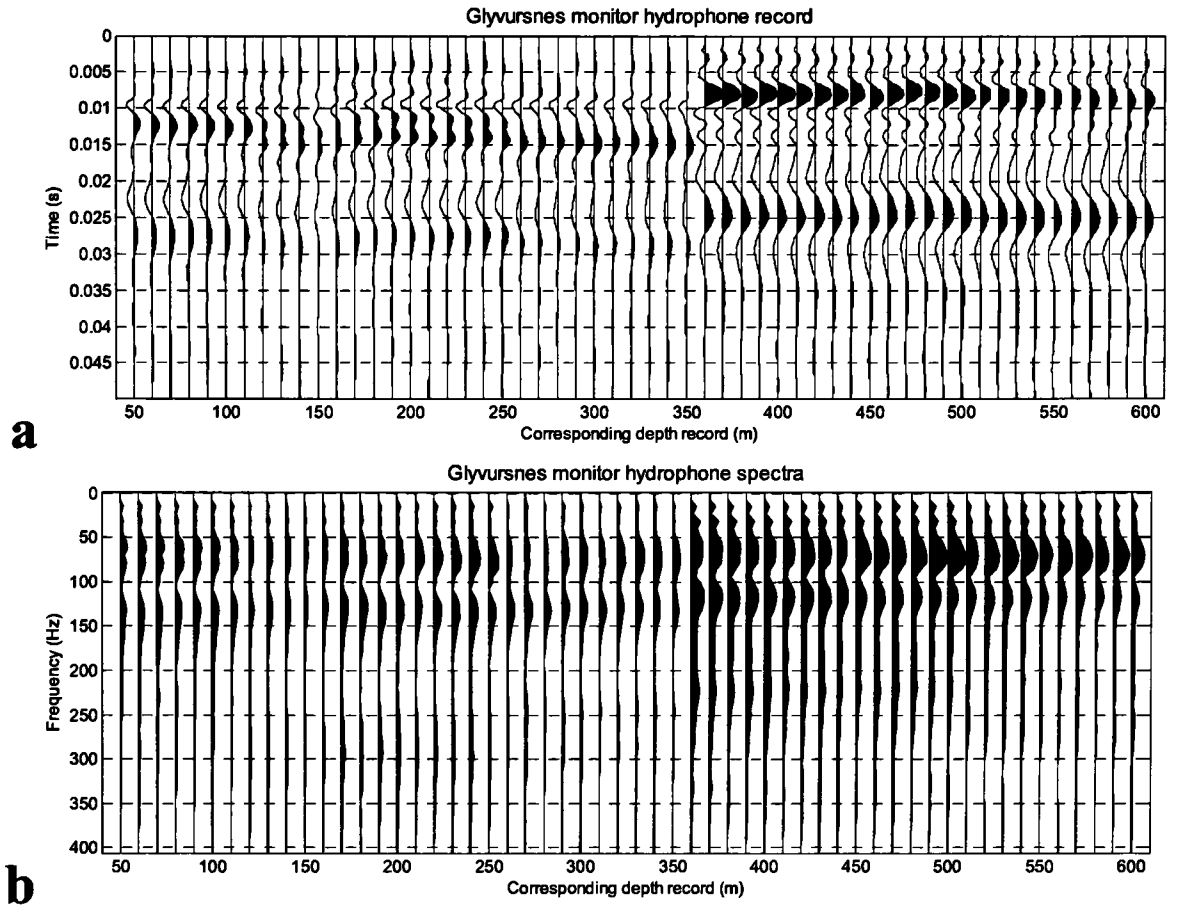

Figure 3.7.
a. Monitor hydrophone record for the Glyvursnes VSP experiment.
b. Amplitude spectra of monitor hydrophone record in 3.7a, plotted to 400 Hz.

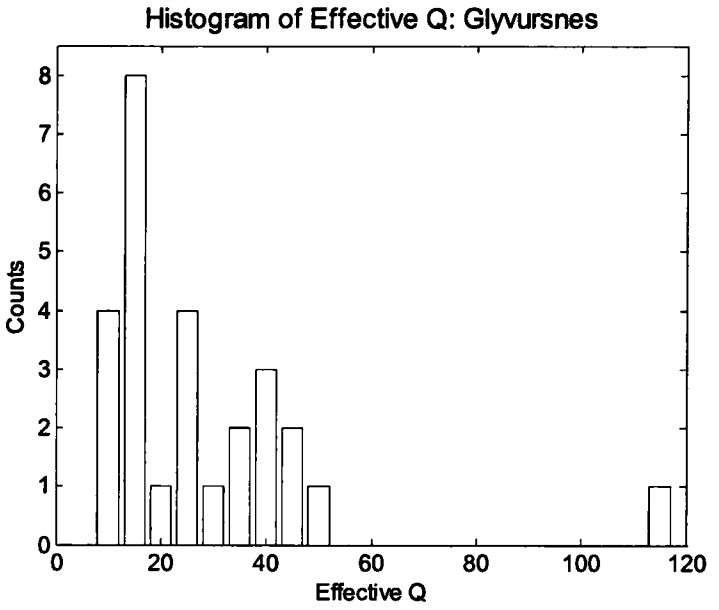

a

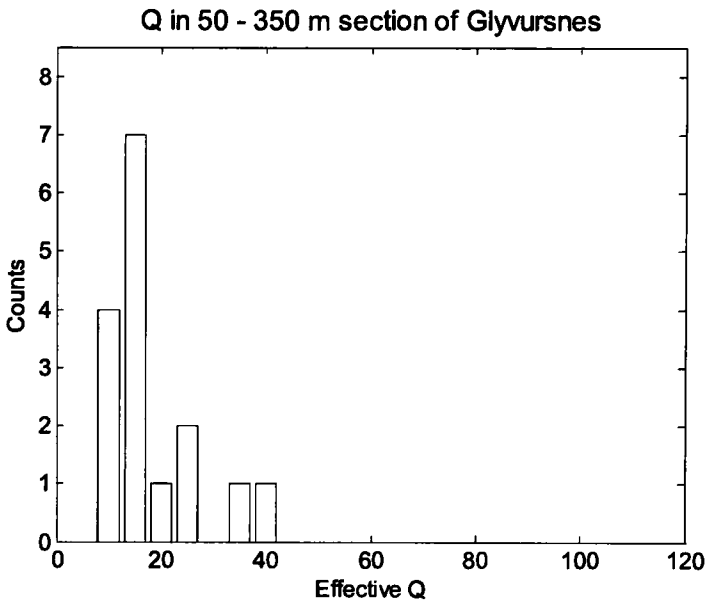

b

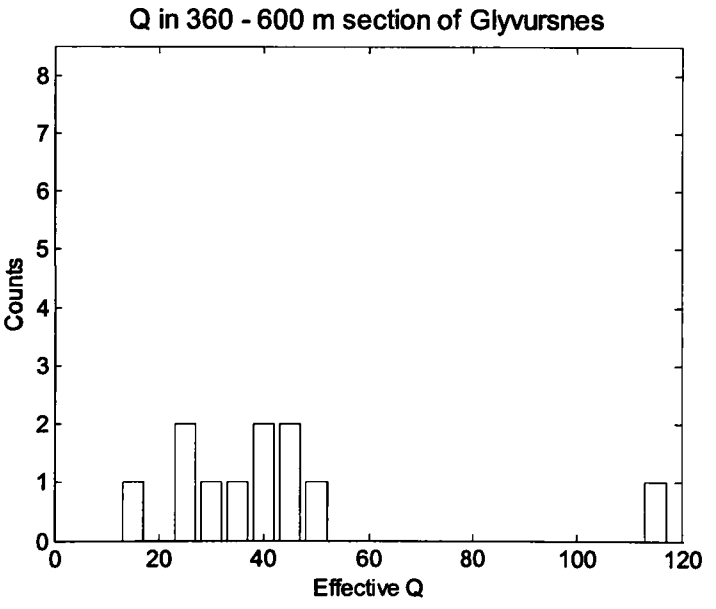

c

Figure 3.8.
a. Effective Q derived from Glyvursnes VSP data by the spectral ratio method, for a depth separation of 250 metres between traces.
b. Effective Q values from the 50 – 350 m traces of the Glyvursnes VSP data.
c. Effective Q values from 360 – 600 m traces of the Glyvursnes VSP data.

Analysis was performed over the region where log spectral ratios were stable: 30 – 150 Hz. The mean Q value derived from the uppermost trace and the lowermost trace was 24, with a range of 17 – 36 for a 95% confidence interval (Figure 3.4c). In the analyses over intervals of 250 m, Q values spanned 5 to 120 (Figure 3.8a), with a mean Q value of approximately 25. Estimates from the shallow and deep sections of the borehole suggested an increase in Q with depth: between 50 and 350 m, mean and modal Q value was ~ 15 (Figure 3.8b), while between 360 and 600 m, the mean increased to ~ 30 (Figure 3.8c).

3.2 Q ESTIMATION FROM AMPLITUDE DECAY

As the spectral ratio method is performed in the frequency domain, confidence in Q estimates was reduced by the narrow bandwidth of the Glyvursnes data. The lack of constraint on source signature also masked evidence of depth trends in Q. A second method of Q estimation, based on the decay of maximum amplitudes, was thus applied.

3.2.1 GEOMETRIC SPREADING CORRECTIONS

Over the spatial dimensions studied, the propagating wave is spherical rather than planar, and it can be shown that the amplitude decreases by a factor related to distance from the source (e.g. Pujol, 2003). This effect, known as geometrical spreading, must be compensated for prior to any amplitude-based attenuation studies.

In a homogeneous medium, the amplitude of a spherical wave decays by $1/r$, where r is distance in metres from the source. For more realistic rock models, velocity-depth trends must be taken into account. O'Brien & Lucas (1971) derived a wavefront divergence factor, D^2, for a stratified, discrete layer medium, with no restriction upon initial incidence angle:

$$D^2 = \sum_{i=1}^{n}\left(\frac{R_i V_i}{V_1}\right)\cdot\sum_{i=1}^{n}\left(\frac{R_i V_i}{V_1}\right)\left(\frac{\cos^2\theta_1}{\cos^2\theta_i}\right) \qquad \textbf{(3.5)}$$

R_i is the slant path distance, V_i is the velocity, and θ_i is the angle of incidence in the ith layer. As θ_i approaches zero, R_i tends to d_i, the vertical thickness of the layer:

$$D_{one-way} = \frac{\sum_{i=1}^{n}(d_i V_i)}{V_1} \qquad \textbf{(3.6)}$$

O'Brien & Lucas' result for one-way loss is half that derived by Newman (1973) for two-way loss in a stratified medium.

Using Equation 3.6, one-way loss was calculated over the full VSP acquisition intervals. V_i values were first taken from logs at a resolution of 0.2 m, then from logs Backus-averaged to $d_i = 3$ m and $d_i = 10$ m. While results from the averaged logs were found to deviate very little, the highest resolution logs were used in the final analyses.

The following relationship was derived from Equation 3.1:

$$\ln\left(\frac{A}{A_0}\right) = \left(\frac{-\pi f}{Qc}\right) r \qquad \textbf{(3.7)}$$

Here, velocity, c, and frequency, f, were assumed to be constant over the interval studied. Reference amplitude A_o was taken to be the maximum amplitude from the uppermost trace (50 m), and r represented the distance from the uppermost receiver. After correction for geometric spreading, maximum amplitude from each depth level, A, was divided by A_o, and the log of this ratio plotted against depth. Q was derived from the gradient of a least-squares regression line via:

$$Q = \frac{-\pi f}{c\,(slope\ of\ \ plot)} \qquad \textbf{(3.8)}$$

The use of peak-to-peak amplitudes and half-wavelength amplitudes produced the same Q estimates to the nearest round number. In both boreholes, due to the increase in P-velocity of the basalts, the discrete layer correction compensated more strongly for spreading than the $1 / r$ correction. However, usage of either correction method did not significantly change the slope of the regression lines. The greatest variation in Q arose from the frequency and velocity parameters, more so than the uncertainty in line-fitting. Mean, minimum and maximum c and f values have been substituted into Equation 3.8 to give a range of Q estimates.

In the Glyvursnes data, the condition of constant frequency is approximately satisfied, and a mean value of 30 Hz was used throughout. Between 50 and 160 m, the velocity range is 3500 – 6000 m/s (averaged to 4500 m/s). Between 160 and 600 m, the velocity range is 3100 – 6300 m/s (averaged to 4300 m/s). A clear change in slope was seen in the amplitude decay ratio at 160 m (Figure 3.9). Above this level, Q values ranged between 1 and 4 (mean value 2), and below this level, Q fell within a range of 15 – 40 (mean value 22). These estimates were extremely low, but as in the spectral ratio analysis, there was a relative increase in Q with depth.

3.9

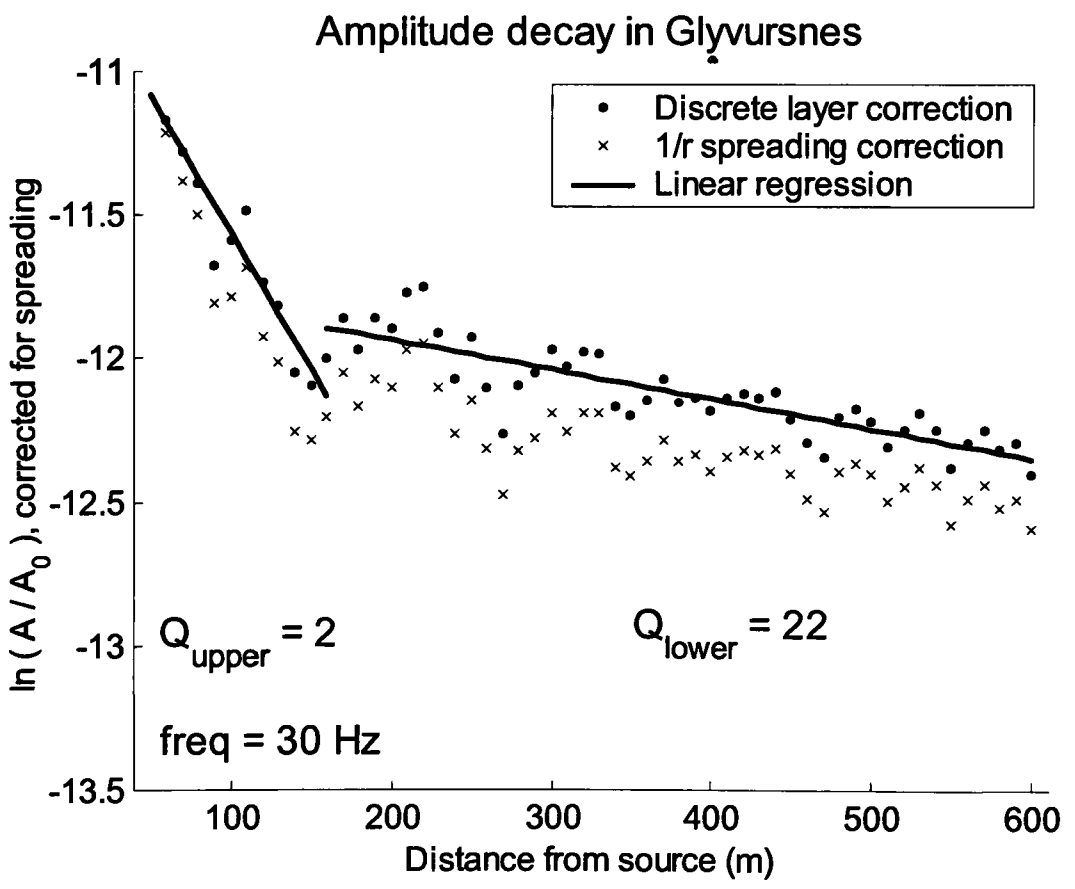

Figure 3.9.
Q estimates from amplitude decay in the Glyvursnes VSP data, after spherical spreading correction. There appears to be a significant change in gradient at 160 m. Average frequency used was 30 Hz. Q range from 95% confidence intervals and variation in velocity / frequency was 1 – 4 in the upper section and 15 – 40 in the lower section respectively.

In the upper section of Vestmanna, the velocity range is 4500 – 6600 m/s (averaged to 5100 m/s). In the lower section, the velocity range is 4400 – 6700 m/s (averaged to 5400 m/s). Peak frequency varies between 60 and 400 Hz, averaging to 200 Hz and 71 Hz in the upper and lower sections respectively. This large range made the amplitude decay method less suitable in Vestmanna than in Glyvursnes data, but it gave an indication that Q is constant over the top 400 m of the borehole. Corresponding Q estimates ranged between 10 and 90 (mean value 38). Seismic quality factor may be higher between 405 and 500 m, as Q estimates in this region lay between 50 and 200 (Figure 3.10).

3.10

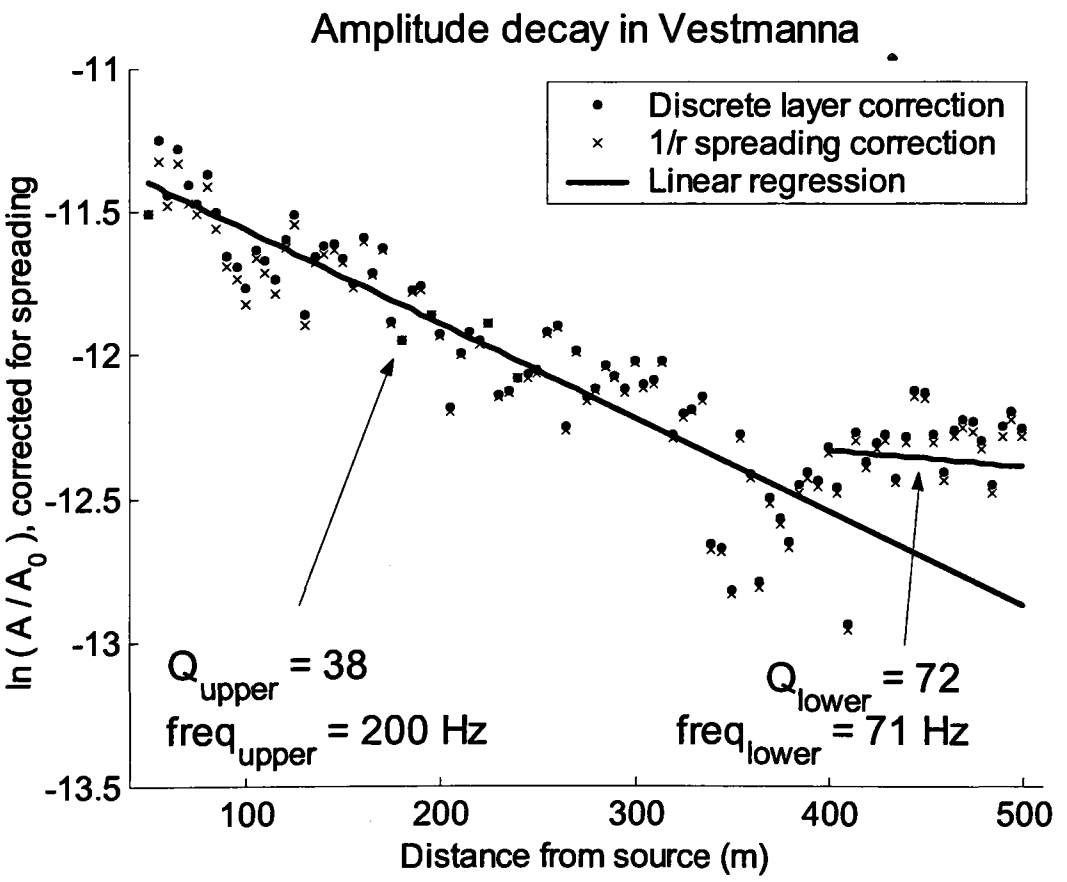

Figure 3.10.
Q estimates from amplitude decay in the Vestmanna VSP data, after spherical spreading correction. The change in gradient is gradual. Average frequency used was 200 Hz upper section, and 71 Hz in the lower section. Q range from 95% confidence intervals and variation in velocity / frequency was 10 – 90 in the upper section and 50 – 200 in the lower section respectively.

3.3 TIME-FREQUENCY ANALYSIS

Data from the two field experiments differ not only in total bandwidth, but also in the distribution of energy across time and frequency. While it is necessary to confine spectral ratio analyses to the primary wavelets alone, later arrivals can be studied using time-frequency analysis, which is applicable over longer time intervals. The importance of coda information is discussed by Frankel & Wennerberg (1987), Richards & Menke (1983), and Kang & McMechan (1994), who found that it can be diagnostic of attenuation mechanisms, but difficult to incorporate into Q analyses.

Non-exhaustive tests were first carried out with readily available software packages in Matlab®, Wavelab and Uvi_Wave. Good time resolution was achieved with spectrograms constructed from the Short-Time Fourier Transform (STFT). However, different window sizes were needed for different frequency structures to be resolved fully. For the purposes of this project, scalograms constructed from the Continuous Wavelet Transform, using Morlet wavelets, proved to be the most efficient and insightful form of analysis.

3.3.1 THE MORLET WAVELET SCALOGRAM

The Wavelet Transform (WT) is a powerful tool for tracking the frequency content of a signal over time. In the WT, a wavelet base is stretched and compressed to create a series of child wavelets over a range of scales, then correlated with the signal (Jensen & la Cour-Harbo, 2000). The resulting scalogram is plotted in two-dimensional space, with time and scale as the x and y axes respectively (Figure 3.11).

3.11

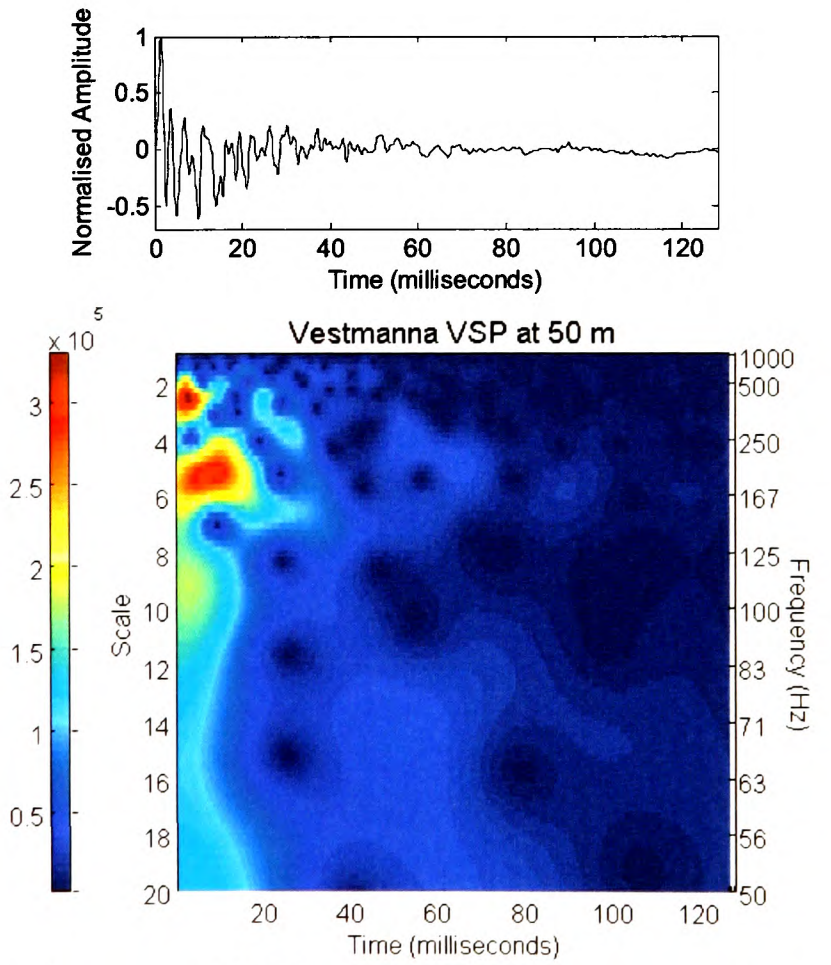

Figure 3.11. Example seismic trace and its Morlet wavelet scalogram. Red regions represent the greatest energy concentration, blue regions the least. The speckled appearance derives from destructive interference of wavelet components. A linear, interpolated colour range has been used.

In general, wavelet filters have better time localisation than STFT filters (Strang, 1993; Jensen & la Cour-Harbo, 2000), and the scaling of the wavelet base automatically changes the window size needed to resolve different frequency structures. Furthermore, specific wavelet bases can be selected (or created) for their frequency and time

localisation properties. One wavelet base known to have excellent frequency localisation properties is the complex, or 'analytic' Morlet wavelet, defined in time and frequency by:

$$\psi(t) = C\exp(-i\omega_0 t)\exp\left(-\frac{t^2}{2}\right) \qquad \textbf{(3.9)}$$

where C is a normalisation constant, ω_0 is the centre frequency of the wavelet base, and t is time. A key property of this analytic wavelet is the absence of negative frequencies.

The wavelet base of Equation 3.9 is then stretched and compressed according to a scale, s, and shifted in time by a quantity, u:

$$\begin{aligned}\psi_S(t) &= \frac{1}{\sqrt{s}}\psi\left(\frac{t-u}{s}\right) \\ &= \frac{1}{\sqrt{s}}\exp\left(\frac{-2\pi it}{s}\right)\exp\left(-\frac{1}{2}(\frac{t-u}{s})^2\right)\end{aligned} \qquad \textbf{(3.10a, b)}$$

where ω_0 is 1 cycle per second (2π), and time is specified between -6 and 6 time units (as significant energy of the Morlet wavelet is contained within this range).

Each wavelet contains more than one frequency, and so scale cannot be directly equated to one frequency value. However, the concept of 'pseudo-frequency', f_p, is useful in visualisation; f_p is related to the scale, s, centre frequency of the wavelet in Hz, f_c, and the wavelet sampling interval, δt, by:

$$\begin{aligned} f_p &= \frac{f_c}{s.\delta t} \\ &\Rightarrow \frac{1}{s.(0.001)}\end{aligned} \qquad \textbf{(3.11a, b)}$$

In this thesis, all scalograms have been generated using the University of Vigo's Uvi_Wave software, using complex Morlet wavelets with a centre frequency of 1 Hz, and a wavelet sampling interval of 0.001 s (as in Equation 3.11b). For display, a linear, interpolated colour range has been used. This gives a normalised amplitude range of 0 – 100 %.

The use of false-colour scalograms has distinct advantages. Firstly, where the wave-train is long, the scalogram reveals information that might otherwise be masked or filtered off by time-gating. Secondly, it enables easy comparison of the frequency content of the primary wavelet relative to the coda. Thirdly, local destructive interference creates dark areas in the scalogram, showing the extent to which multiples impinge on the primary wavelet (Figure 3.11). These three factors are significant in diagnosing the causes of attenuation and will be discussed further in succeeding chapters. Scalograms also aid in recognition and analysis of wave modes other than the P-wave.

3.3.2 SCALOGRAMS OF VSP TRACES

Figure 3.12 shows VSP traces from Glyvursnes at 50, 180, 320 and 600 m depth, with their corresponding scalograms. A gradual narrowing of bandwidth with depth is clearly seen. By 320 m, the bulk of energy has become concentrated around scale 30 (33.3Hz), and both low-end and high-end frequency components (< 20 Hz and > 100 Hz) are relatively weaker. The parcel of energy between 10 and 20 Hz is likely to

come from the shear wave, which lags behind the primary wave by 26 ms (at 50 m), 67 ms (at 180 m) and 101 ms (at 320 m). However, this observation is ambiguous, as sensitivity of the borehole tool geophone drops off at about 10 to 20 Hz.

At depths below 320 m, the low frequency content seems largely invariant, but further attenuation of higher frequency components occurs down to 600 m. Details of the 320 m and 600 m trace scalograms (Figure 3.13) reveal a subtle broadening of the wavelet and a shift of energy in the 70 -150 Hz region.

Vestmanna VSP traces at 50, 160, 275, 380, 440 and 500 m depth are displayed together with their scalograms in Figure 3.14 (note that scale only extends to 20, a pseudo-frequency of 50 Hz). The waveforms have an entirely different temporal and spectral profile from Glyvursnes, due to experimental conditions discussed in Chapter 2.

At 50 m, energy is concentrated in frequency 'islands' separated by spectral minima at 65 – 125 Hz, and at ~ 250 Hz. As the wave propagates downwards, later arrivals remain concentrated in regions of 70 – 90 Hz and 160 – 200 Hz, despite the changing spectral content of the primary wavelet (Figure 3.15). These persistent events are most probably expressions of the shear wave, which lags behind the primary wave by 9 ms (at 50 m), 28 ms (at 160 m), 46 ms (at 275 m), 66 ms (at 380 m), 75 ms (at 440 m), and 83 ms (at 500 m).

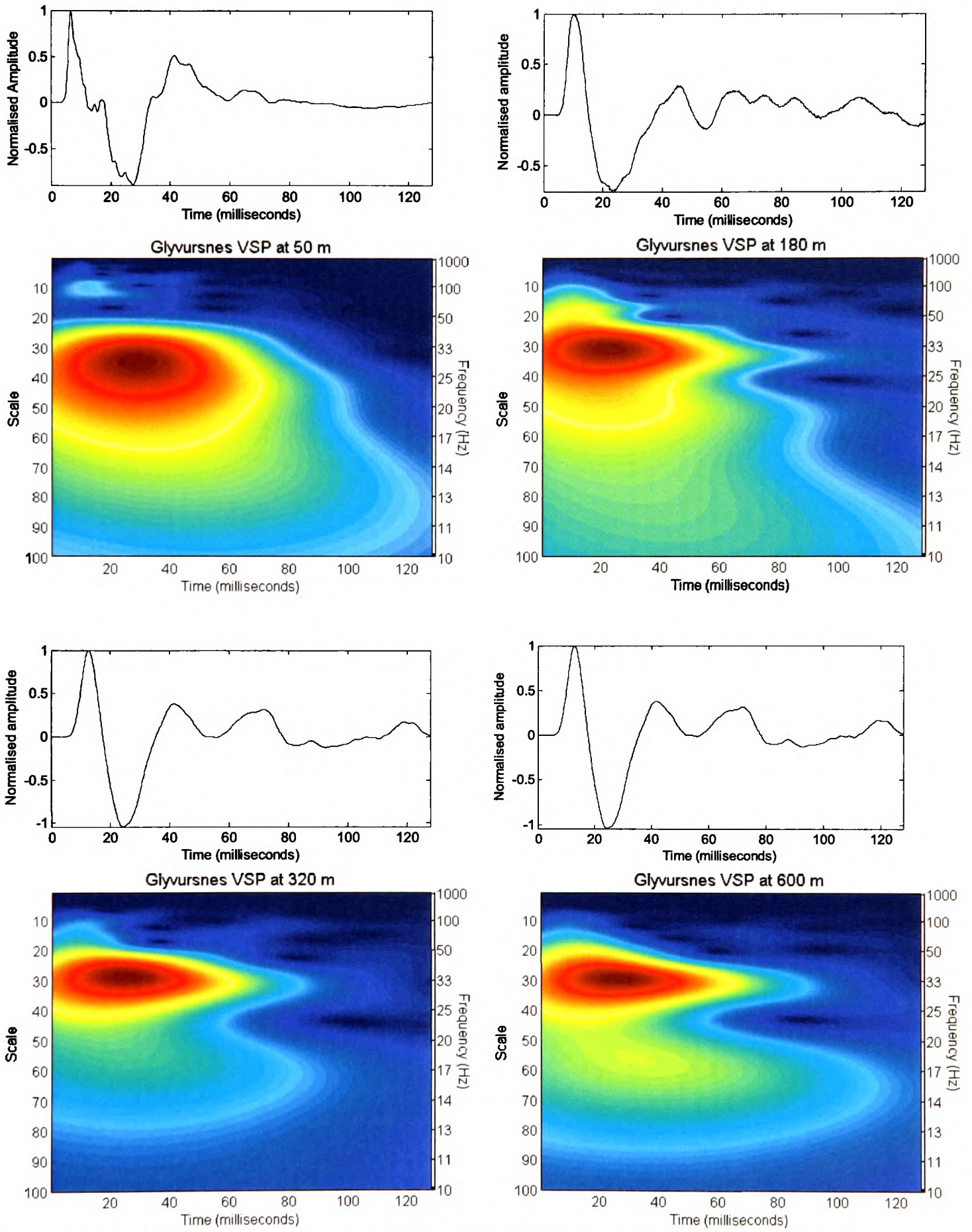

Figure 3.12. Traces from the Glyvursnes VSP at 50, 180, 320 and 600 m depth, and their corresponding scalograms, displayed to a maximum scale of 100. The greatest energy is centred on scale 30 (~ 33 Hz). The full colour scaling covers a linear, normalised amplitude range of 0 - 100%.

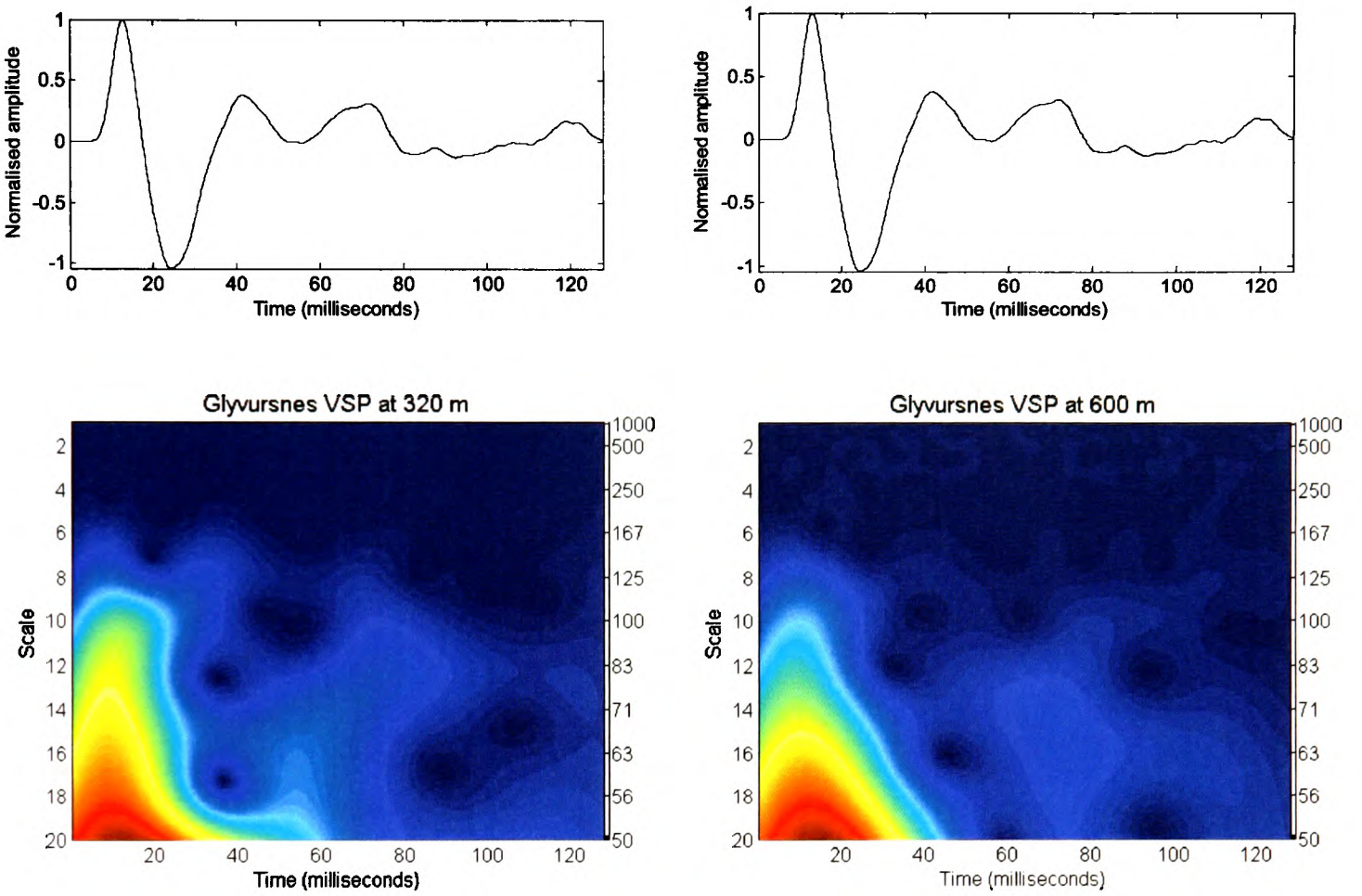

Figure 3.13. Detail of the 320 and 600 m trace scalograms shown in Figure 3.7. The very high frequency components seen in the right hand 600 m trace and scalogram, invariant over time, are noise. Note that scale only extends to 20, a minimum pseudo-frequency of 50 Hz. full colour scaling covers a linear, normalised amplitude range of 0 - 100%.

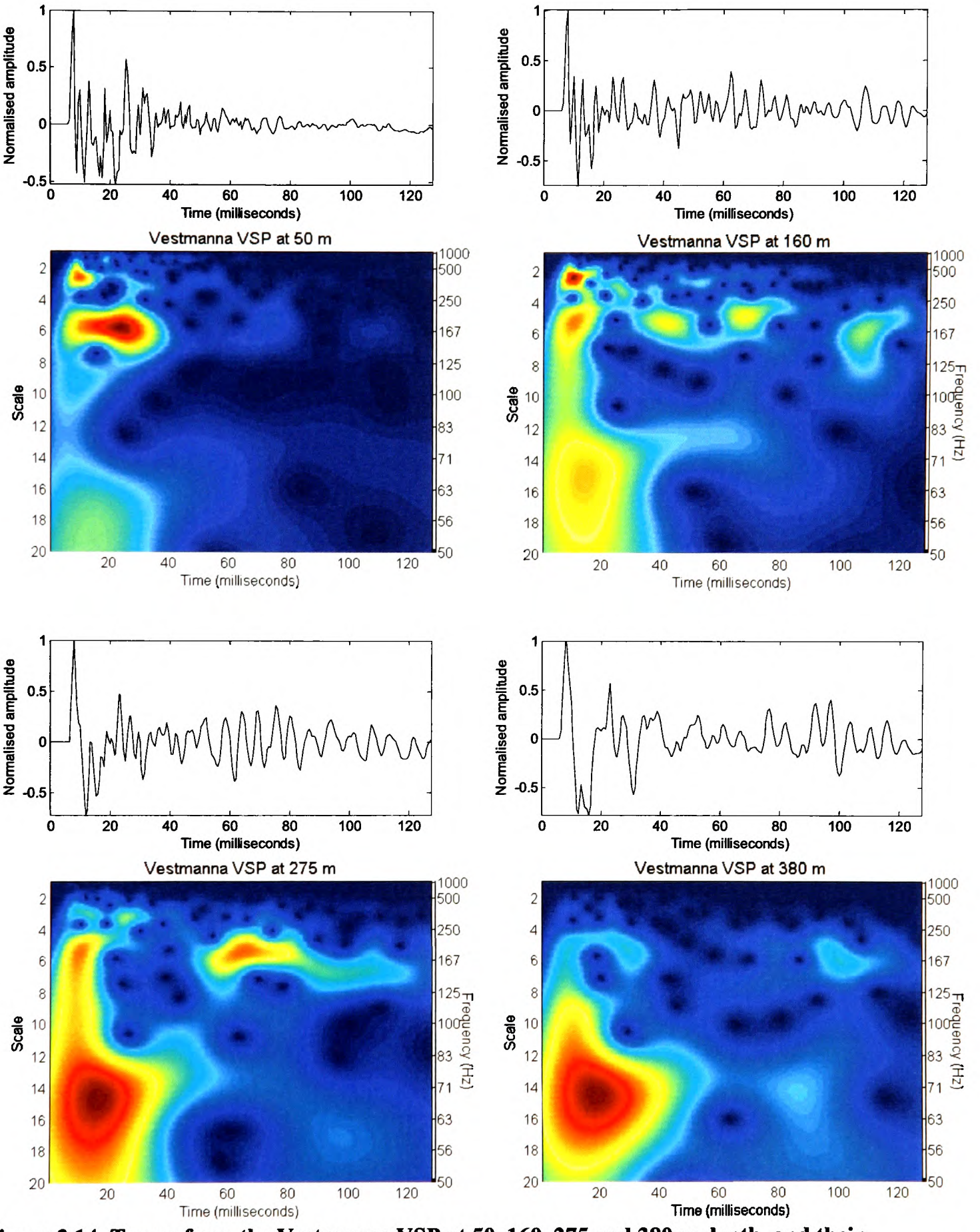

Figure 3.14. Traces from the Vestmanna VSP at 50, 160, 275 and 380 m depth, and their corresponding scalograms. Note that scale only extends to 20, a minimum pseudo-frequency of 50 Hz. The full colour scaling covers a linear, normalised amplitude range of 0 - 100%.

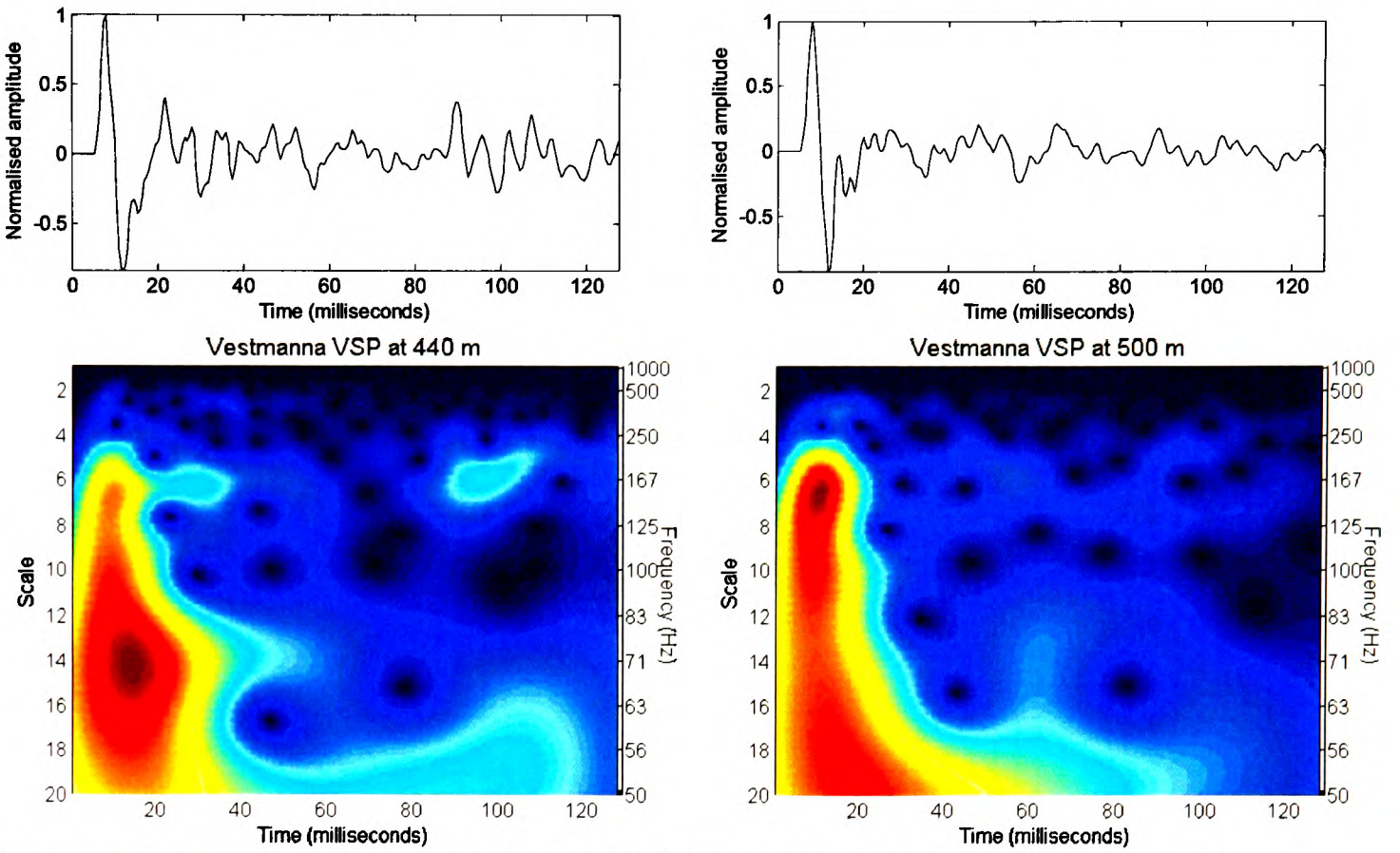

Figure 3.14 cont'd. Traces from the Vestmanna VSP at 440 and 500 m depth, and their corresponding scalograms. Note that scale only extends to 20, a minimum pseudo-frequency of 50 Hz. The full colour scaling covers a linear, normalised amplitude range of 0 - 100%.

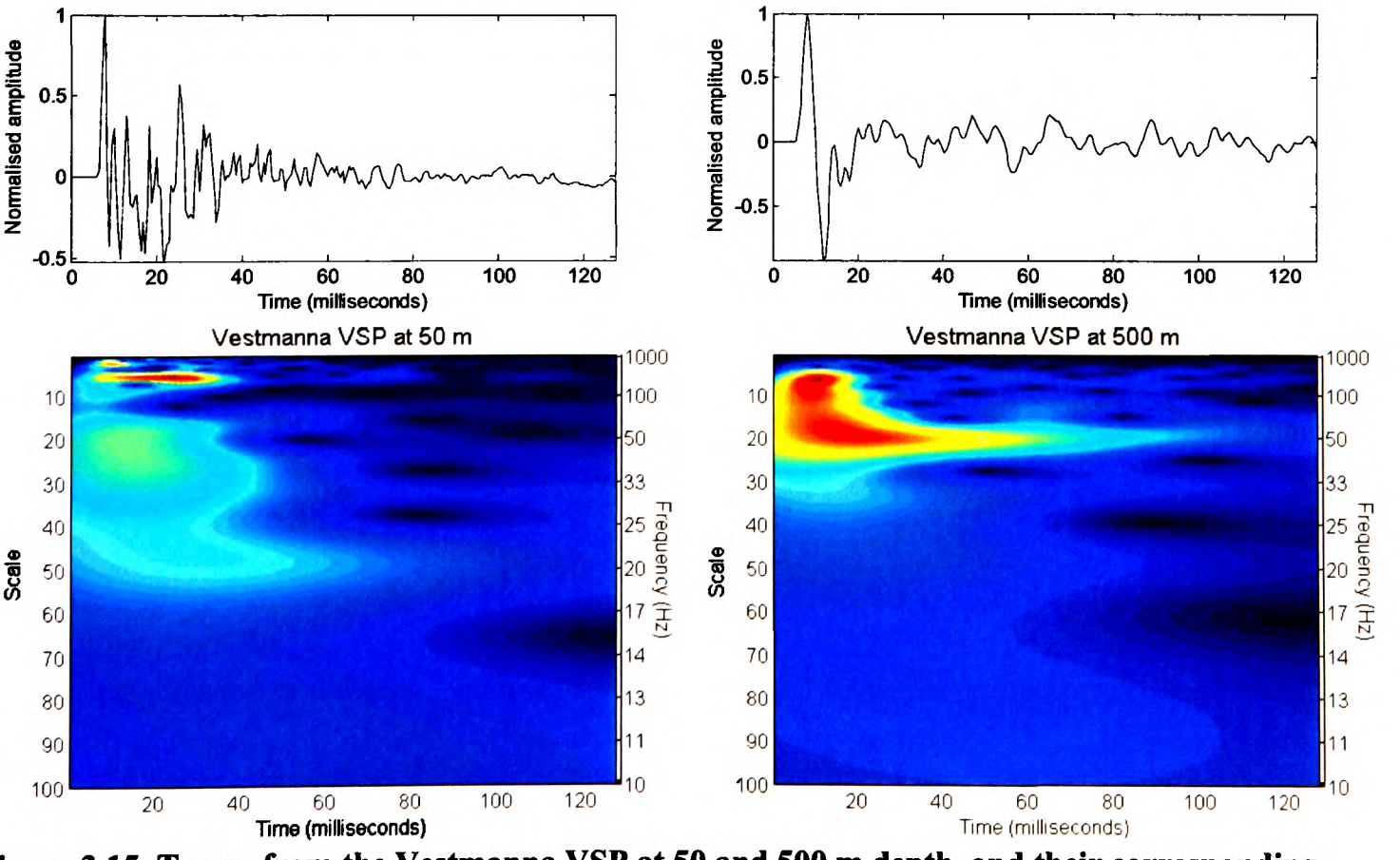

Figure 3.15. Traces from the Vestmanna VSP at 50 and 500 m depth, and their corresponding scalograms displayed to a scale of 100. There is relatively little energy between 10 and 30 Hz. The full colour scaling covers a linear, normalised amplitude range of 0 - 100%.

3.4 DISCUSSION

Effective Q from the two field sites is consistently low. From the spectral ratio method, mean and modal values of effective Q in both boreholes were found to lie between 20 and 40. The amplitude decay method, most applicable to Glyvursnes data between 160 and 600 m depth, returned a similar Q value of ~ 22. In the upper 160 m of Glyvursnes, Q was found to be between 1 and 4. However, the strict definition of seismic quality factor requires Q >> 1 (as outlined in Bourbié *et al.*, 1987), and this anomalously low value must be considered with caution.

A constant Q model (Kjartansson, 1979) has been assumed to operate, but there is some indication from the foregoing analysis that this may not be viable over the bandwidths studied. For example, there is some evidence that the upper 320 m of the Glyvursnes basalts attenuates both low and high frequency energy. Given their limitations, both methods of Q analysis still provide evidence for an increase in Q values with depth for the Glyvursnes data, and for constant Q over the full Vestmanna VSP interval.

WT scalograms of the seismic traces were used to track the evolution of both the primary wavelet and coda waves with depth. In Vestmanna, energy is persistent in the frequency regions of 70 – 90 Hz and 160 – 200 Hz. These are likely to be shear-waves and their associated multiples, with frequency content that does not appear to match that of the primary wavelet. This may have implications for the frequency content of the coda, and for multiple-scattering as a mechanism of attenuation.

In Glyvursnes, the scalograms show that below 320 m, attenuation is concentrated in frequencies above 100 Hz. These observations reinforce the results from the Q analyses, and confirm that the attenuative properties of Glyvursnes basalts change with depth. The nature of this transition may be relatively abrupt. A geological boundary between Upper and Middle Basalt Series is known to occur at 355 m (Waagstein & Andersen, 2003). To determine the importance of this boundary, the characteristics of the log data must be scrutinised – the foci of Chapters 4 and 5.

CHAPTER 4

1-D SEISMIC RESPONSE OF FAROES BOREHOLE LOGS

At outcrop, Faroes basalts have distinctive horizontal layering which appears continuous over tens or hundreds of metres. Such sequences are likely to produce strong intra-bed multiples and energy loss through one-dimensional (1-D) back-scattering, a phenomenon first described by O'Doherty & Anstey (1971).

In this chapter, 1-D scattering is investigated as a possible mechanism for the high attenuation observed in real VSP data. Acoustic modelling after a method by Kennett (1979) is carried out on plane-layered models constructed from borehole velocity and density log data. 1-D scattering Q is estimated using the spectral ratio method, and compared to estimates from VSP analysis. The spectral profile of the source is investigated for its effect on measured Q values, and the spectral ratio method is found to be sensitive to the bandwidth and spectral shape of the source wavelet.

Due to the non-uniqueness of Q estimates, the scattering behaviour of the planar models is analysed in the time-frequency domain using Morlet wavelet scalograms. Characteristics in the coda, which may be diagnostic of attenuation mechanisms, are identified and compared to those of the VSP traces. 1-D scattering is found to be a dominant attenuation mechanism in one section of the Glyvursnes rocks. Periodic velocity contrasts are shown to play a key role in their scattering behaviour.

4.1 WAVE PROPAGATION THROUGH PLANE-LAYERED MODELS

After a method by Kennett (1979), seismograms were generated for hypothetical plane-layered models of the Faroes rocks. The algorithm uses Fourier synthesis and plane wave superposition to calculate transmission and reflection coefficients for multi-layered media. The model is a half-space, and the vanishing of normal and tangential stress is imposed as the boundary condition at the surface (Kennett, 1979). Kennett (1979) has shown that by expanding the expression for surface displacements that includes all surface reflections, it is possible to isolate that portion corresponding to the contribution of waves which have not suffered any free surface reflection. No free surface multiples were modelled in the work presented here. The ray parameter was set to zero so as to consider only plane-wave propagation at normal incidence to the layering. Thus, no shear moduli are required and only synthetic P-waves are generated.

For all implementations of Kennett modelling in this thesis, intrinsic Q is set to 1000. This high value ensures that virtually all energy loss is from elastic 1-D scattering processes.

The 1-D models consisted of P-velocity and density values taken from borehole logs of the two field sites (Figure 4.1). In studies of wave propagation through finely layered equivalent media, Schoenberg (1993) found that the threshold at which Backus averaging (Backus, 1962) affects seismic wave propagation is $1/10^{th}$ the smallest wavelength. Taking the lowest possible velocity and highest possible frequency in the Faroes log data, a maximum spatial interval of 0.25 m is required. The highest resolution of the sonic logs, 0.2 m, was therefore retained in constructing the models.

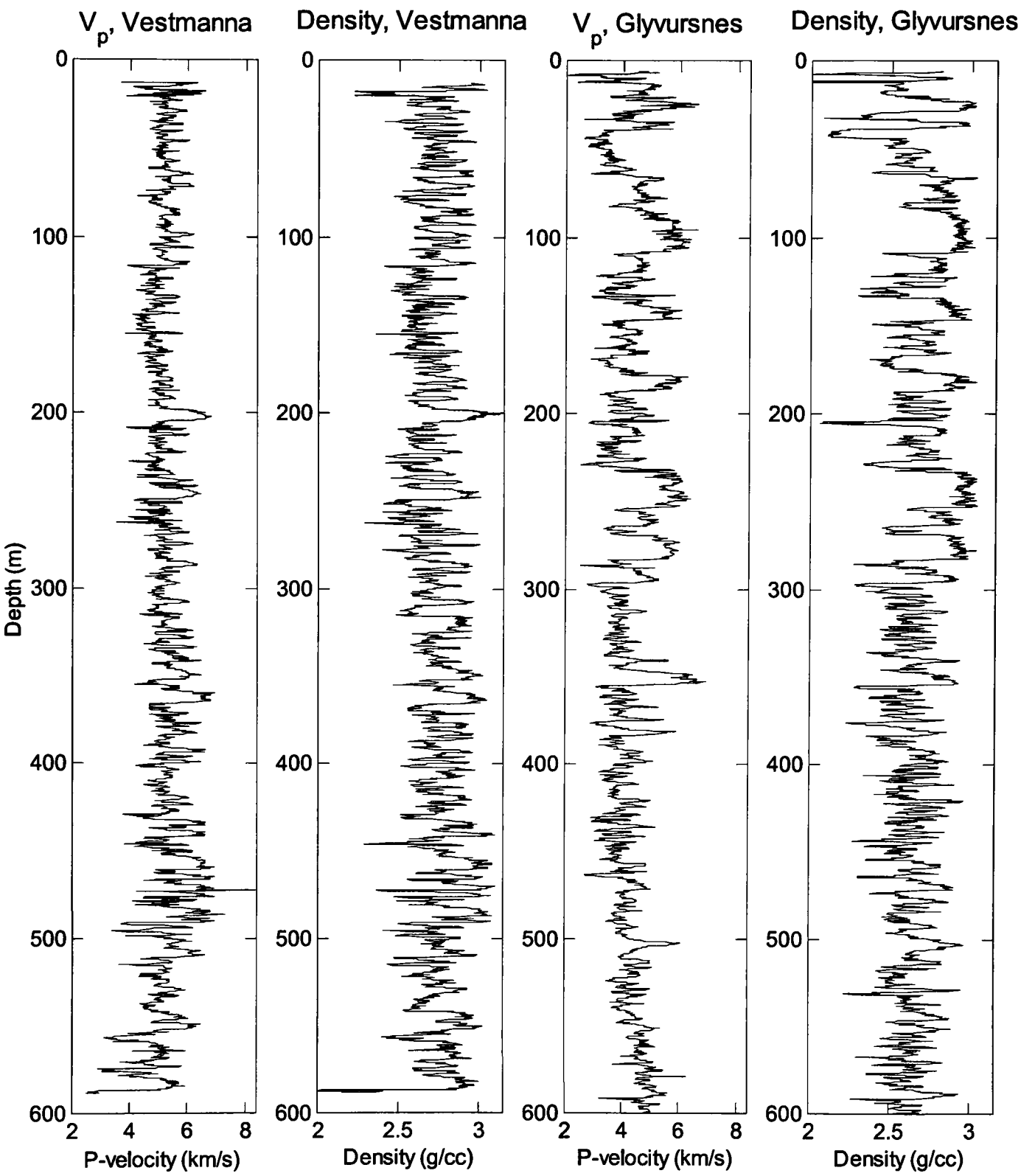

Figure 4.1. Velocity and density logs of the Faroes boreholes.

4.1.1 1-D SCATTERING OVER DEPTH INTERVALS SAMPLED BY VSP

Studies were made of the same depth intervals as those in the VSPs: 60 – 490 m for Vestmanna and 70 – 580 m for Glyvursnes.

Synthetic source wavelets were created from median-filtered data used in the VSP Q analyses (Chapter 3). The primary wavelet in each dataset was isolated from the topmost VSP trace by time-gating with a double-tapered, half-Hanning window, then propagated through the relevant 1-D model. Primary wavelets of the resulting seismograms were isolated using the same double-tapered windows as those applied to the source wavelets.

Estimates of Q were derived using the spectral ratio method (detailed in Chapter 3). As in the VSP analyses, log spectral ratios were deemed to be stable over 20 – 500 Hz in the Vestmanna data and over 30 – 150 Hz in the Glyvursnes data. Least-squares linear regression was performed only within these bandwidths to calculate Q.

Q in the Vestmanna 1-D model ranged from 75 to 93, with a mean value of 84, substantially higher than effective Q measured in the actual rocks. The range of estimates from the Glyvursnes 1-D model was 19 – 87, with a mean value of 31. Allowing for some uncertainty, this lies within the range measured from VSP data (see section 3.1.1).

4.1.2 TRENDS IN 1-D SCATTERING Q WITH DEPTH

In Chapter 3, analyses of the field data showed that Q is close to constant over the entire Vestmanna VSP interval, but appears to increase with depth in Glyvursnes. To investigate whether these trends are related to 1-D scattering attenuation, the models in 4.1.1 were divided at their approximate midpoints (275 m depth in Vestmanna, 320 m in Glyvursnes) and analysed separately.

Synthetic source wavelets were isolated from VSP traces corresponding to the top of each model section, as in 4.1.1. After propagation through the 1-D models, the spectral ratio method was used to calculate Q values over the stable bandwidths previously mentioned.

Figures 4.2 and 4.3 show the input / output waves (a), their amplitude spectra (b) and the regression lines for log spectral ratios (c) of the upper and lower sections of Vestmanna. The range of 1-D scattering Q (for a 95% confidence interval) was 92 – 111 in the upper section and 64 – 82 in the lower section, once again higher than mean estimates from the VSP. In Glyvursnes, the range of 1-D scattering Q was estimated to be 13 – 47 in the upper section and 38 – 272 in the lower section (Figures 4.4 and 4.5). Though marginally higher than the VSP estimates, these are consistent with the trend of seismic quality factor increasing with depth.

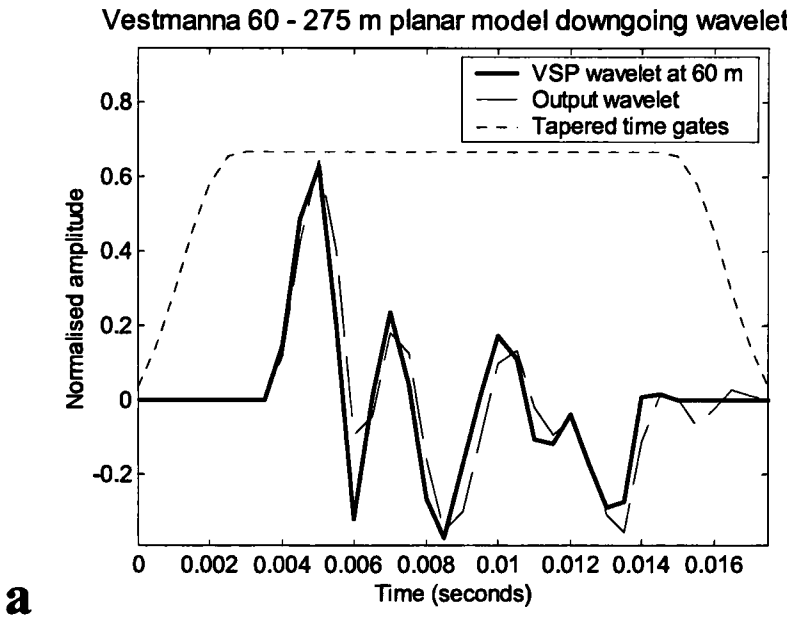

a

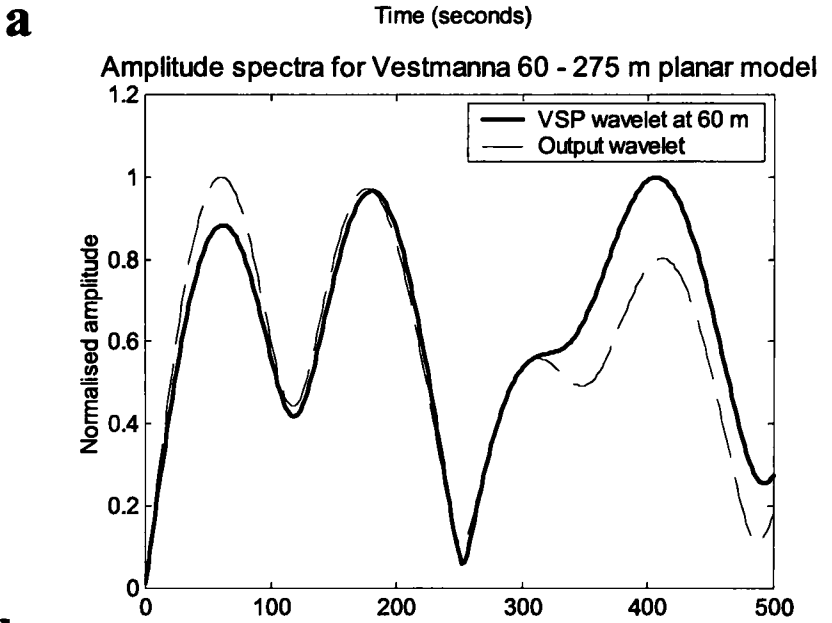

b

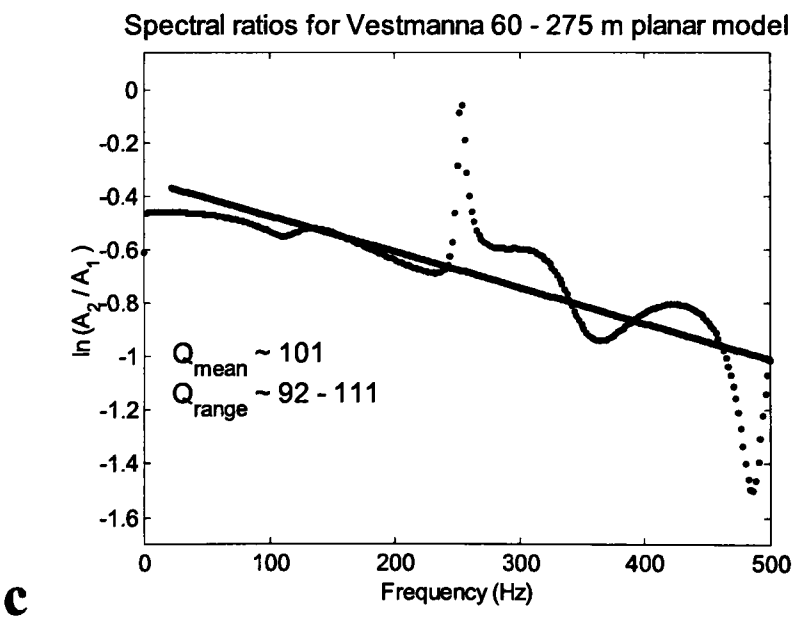

c

Figure 4.2. a. Input and output primary wavelets of synthetic seismograms, for a 1-D model of the 60 – 275 m interval of the Vestmanna velocity and density logs.
b. Amplitude spectra for the traces in 4.2a.
c. Spectral ratio of the input and output traces. Q estimates are given for a 95% confidence interval of mean response.

a

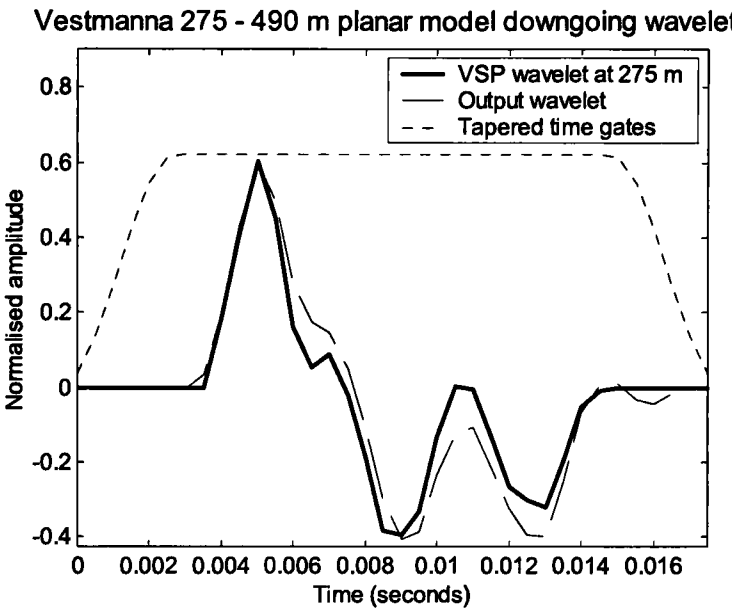

b

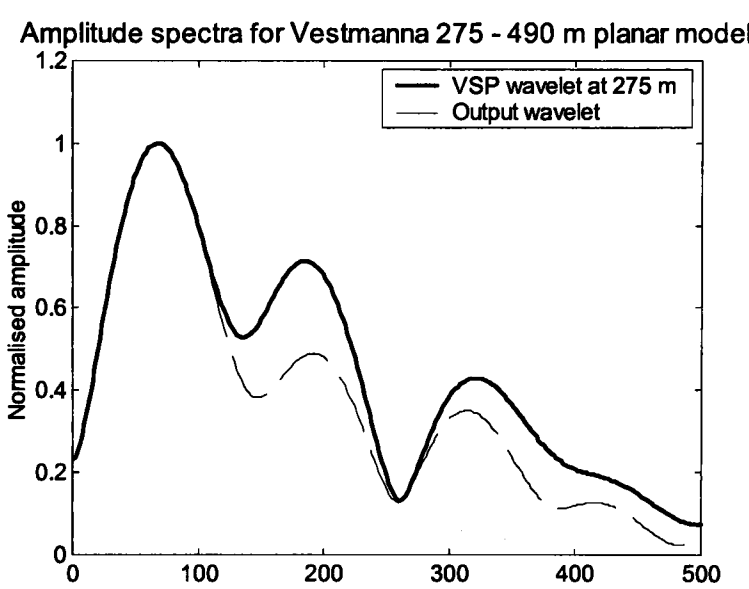

c

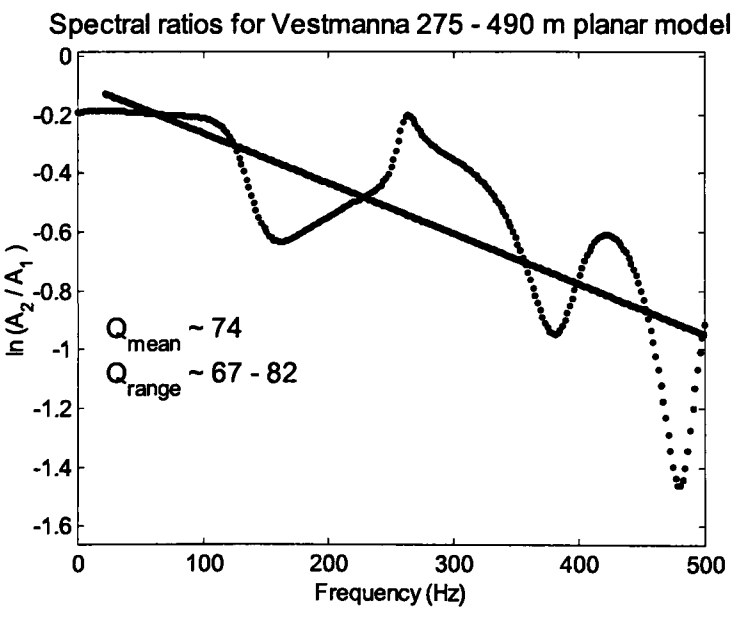

Figure 4.3. a. Input and output primary wavelets of synthetic seismograms, for a 1-D model of the 275 – 490 m interval of the Vestmanna velocity and density logs.
b. Amplitude spectra for the traces in 4.3a.
c. Spectral ratio of the input and output traces. Q estimates are given for a 95% confidence interval of mean response.

a

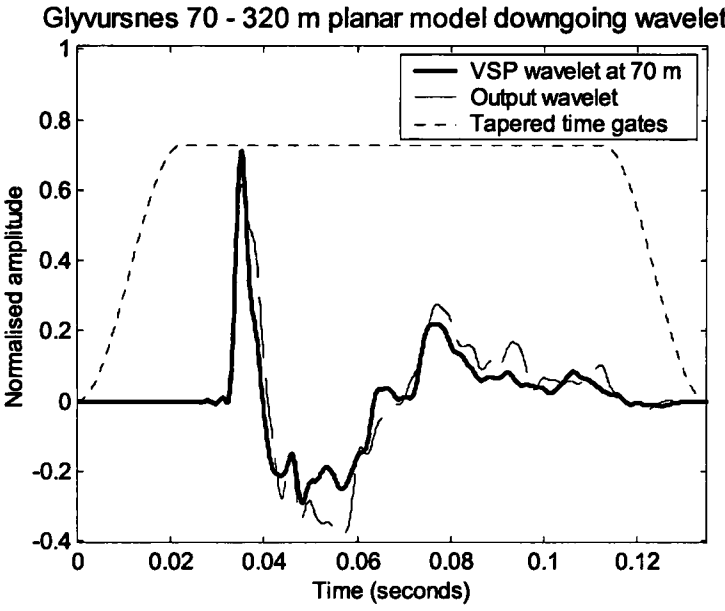

b

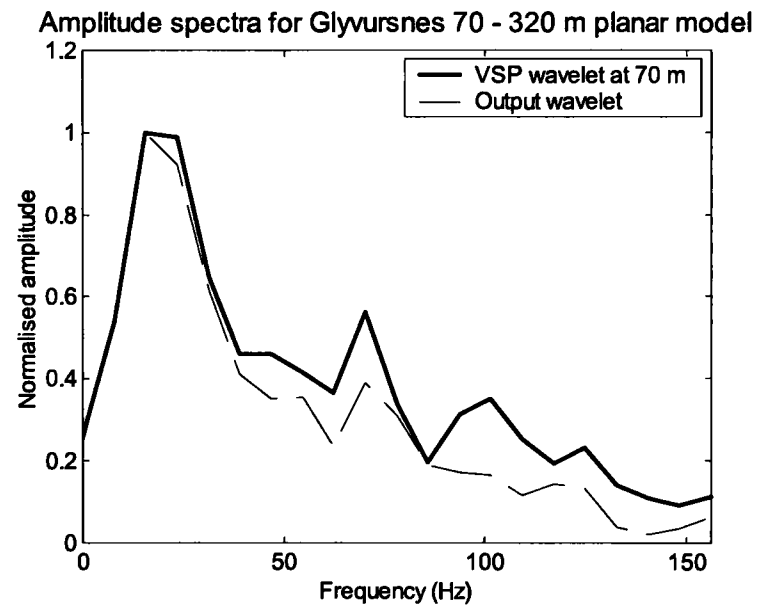

c

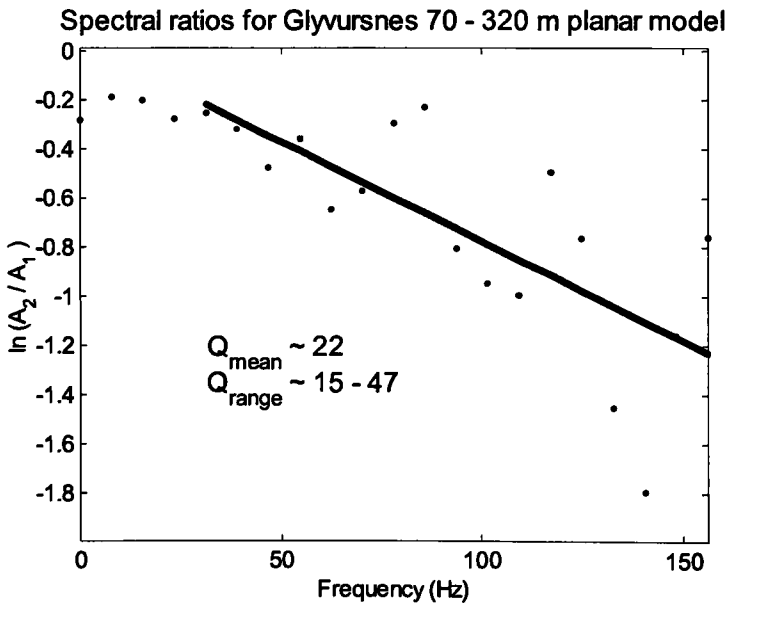

Figure 4.4. a. Input and output primary wavelets of synthetic seismograms, for a 1-D model of the 70 – 320 m interval of the Vestmanna velocity and density logs.
b. Amplitude spectra for the traces in 4.4a.
c. Spectral ratio of the input and output traces. Q estimates are given for a 95% confidence interval of mean response.

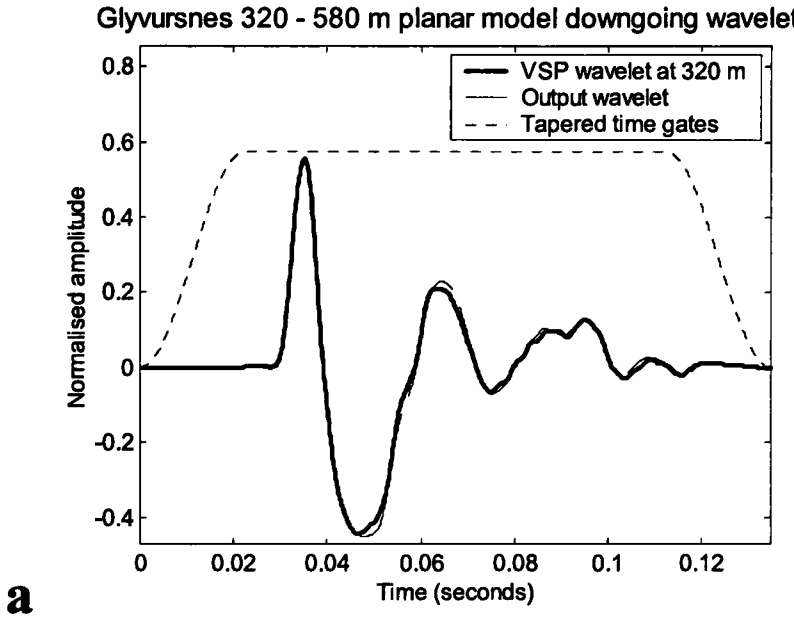

a

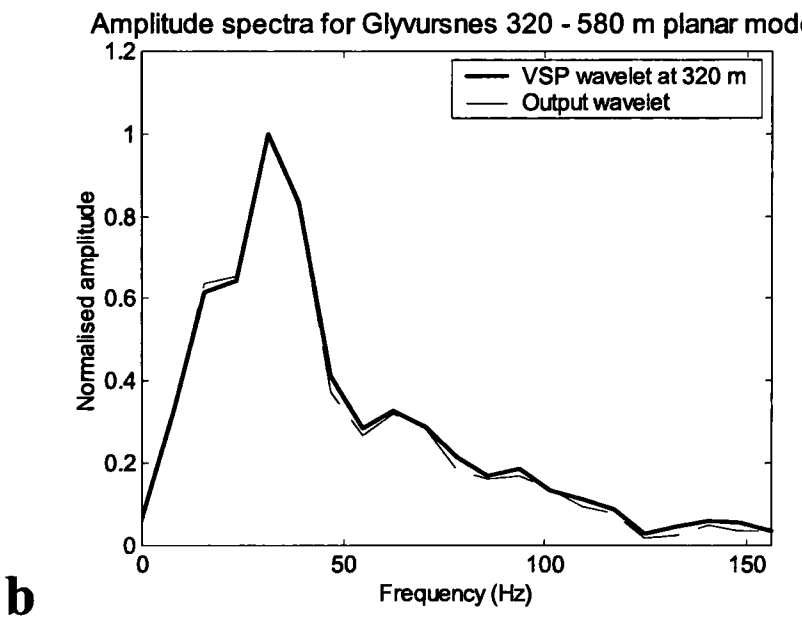

b

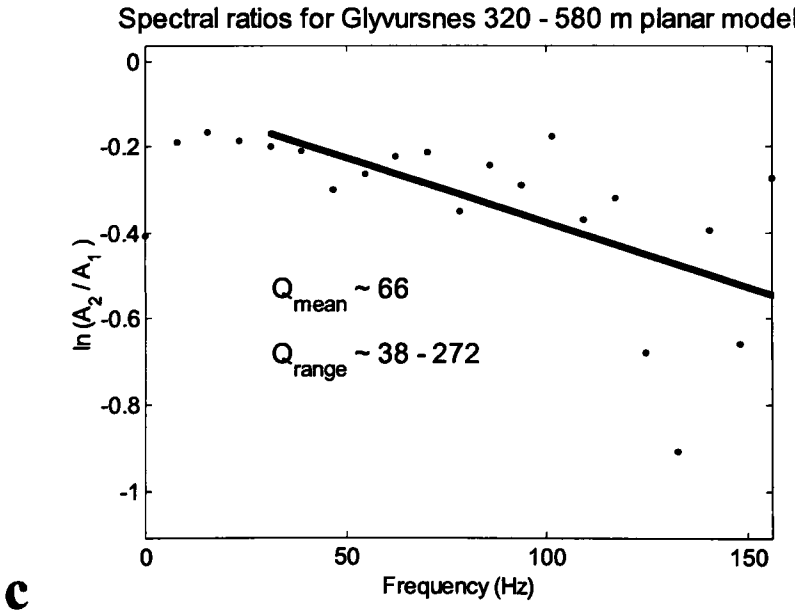

c

Figure 4.5. a. Input and output primary wavelets of synthetic seismograms, for a 1-D model of the 320 – 580 m interval of the Glyvursnes velocity and density logs.
b. Amplitude spectra for the traces in 4.5a.
c. Spectral ratio of the input and output traces. Q estimates are given for a 95% confidence interval of mean response.

All four experiments show fluctuation in their log spectral ratios. However, there is a marked notch centred on 130 Hz in the spectrum of the lower Glyvursnes response (Figure 4.5c). If the upper frequency of analysis is limited to 115 Hz, avoiding this minimum, the range of Q from a 95% confidence interval is 84 – infinity, with a mean of ~ 200. The source bandwidth can thus be significant in Q estimation, an issue which is explored further in the following section.

4.2 SOURCE BANDWIDTH AND 1-D SCATTERING Q

One consequence of using VSP-derived synthetic sources was that the experiments were limited by the spectral content of the field data. The narrow bandwidth of the Glyvursnes traces at 70 and 320 m contrasted starkly with that of the Vestmanna traces at 60 and 275 m. Wavelet shape also varied considerably between the four VSP-derived sources, inducing spectral minima at different positions. As seen in Figures 4.2 – 4.5, these could disrupt the stability of the log spectral ratios.

Acoustic modelling of the four borehole sections was repeated with synthetic zero-phase sources. 1-D scattering behaviour could hence be directly compared between the datasets, and dependence of Q on source bandwidth could be examined. Two input sources were used. The first wavelet had a centre frequency of 150 Hz, imitating the narrow bandwidth of the Glyvursnes VSP, without the inherent spectral notches and complicated wavetrain of the field data. The second wavelet was broadband, with

energy distributed evenly over 1 – 500 Hz and with a maximum frequency exceeding 800 Hz. The scattering characteristics of the logs at high frequencies could thus be studied. Figure 4.6 shows these zero-phase sources and output responses from the four log sections.

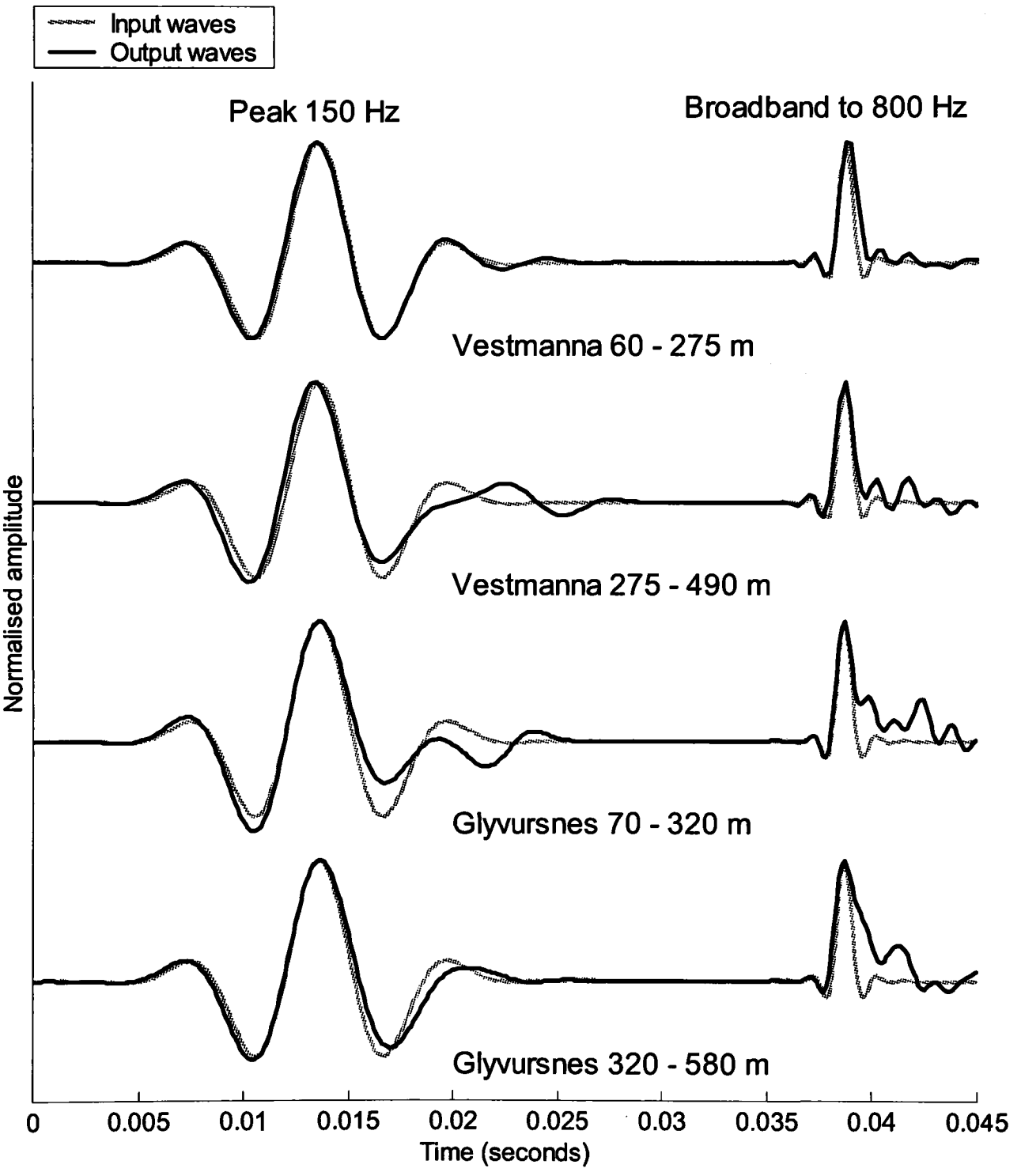

Figure 4.6. Results of acoustic modelling of the Faroes borehole logs with synthetic source wavelets. Input primary wavelets are plotted in grey. Output primary wavelets are overlaid in black. In all experiments, the output wavelets are impinged on by multiples but show little actual broadening.

The Vestmanna VSP-derived sources and the broadband zero-phase source have a comparable frequency range, and their spectral ratio Q estimates are similar. This correspondence of total bandwidth with Q range is repeated in the Glyvursnes experiments, where VSP-derived sources produce Q values similar to those of the 150 Hz zero-phase source. In all cases, the 150 Hz wavelet gave systematically lower Q estimates than the broadband wavelet. The disparity is largest in the upper section of Glyvursnes, where Q is 33 in the 10 – 250 Hz band, but is 171 in the 10 – 800 Hz band. The acoustic modelling results, summarised in Table 4.1, imply that scattering in 1-D Faroes basalt models is frequency-sensitive.

Table 4.1

Range of Q estimates from 1-D acoustic modelling			
Borehole section	**Input wavelet**		
	VSP-derived *(frequency range in Q analysis)*	**Peak frequency 150 Hz, zero-phase**	**Broadband 800 Hz, zero-phase**
Vestmanna 60 – 490 m	75 – **84** – 93 *(20 – 500 Hz)*		
Vestmanna 60 – 275 m	92 – **100** – 111 *(20 – 500 Hz)*	72 – **81** – 96 *(10 – 250 Hz)*	86 – **94** – 102 *(10 – 800 Hz)*
Vestmanna 275 – 490 m	64 – **75** – 82 *(20 – 500 Hz)*	47 – **52** – 60 *(")*	84 – **92** – 103 *(")*
Glyvursnes 70 – 580 m	19 – **31** – 87 *(30 – 150 Hz)*		
Glyvursnes 70 – 320 m	13 – **22** – 47 *(30 – 150 Hz)*	28 – **33** – 46 *(")*	118 – **171** – 302 *(")*
Glyvursnes 320 – 580 m	38 – **66** – 272 *(30 – 150 Hz)*	47 – **53** – 63 *(")*	68 – **81** – 98 *(")*

Table 4.1. Estimated 1-D scattering Q values. The range is given by a 95% confidence interval of the mean response. Mean Q values are emboldened.

A direct indication of frequency-sensitivity is provided by broadband spectral responses from the upper sections of Glyvursnes and Vestmanna. The output primary wavelets were isolated with a double-tapered time window of 20 ms, and their spectra are plotted in Figure 4.7. The gradient of the least-squares regression line (and hence the Q estimate) is seen to change according to the bandwidth of analysis, almost entirely due to the position of the first dominant spectral minimum. This minimum occurs at ~ 230 Hz in the Vestmanna response, with subsequent loss distributed evenly across higher frequencies. For the Glyvursnes response, the spectral 'trough' occurs between 0 and 250 Hz. In both cases, varying the time gate around the primary wavelet changes the shape and intensity of the minimum, and to a lesser extent, its position in the spectrum.

The origins of these dominant minima are examined in the following sections.

4.7

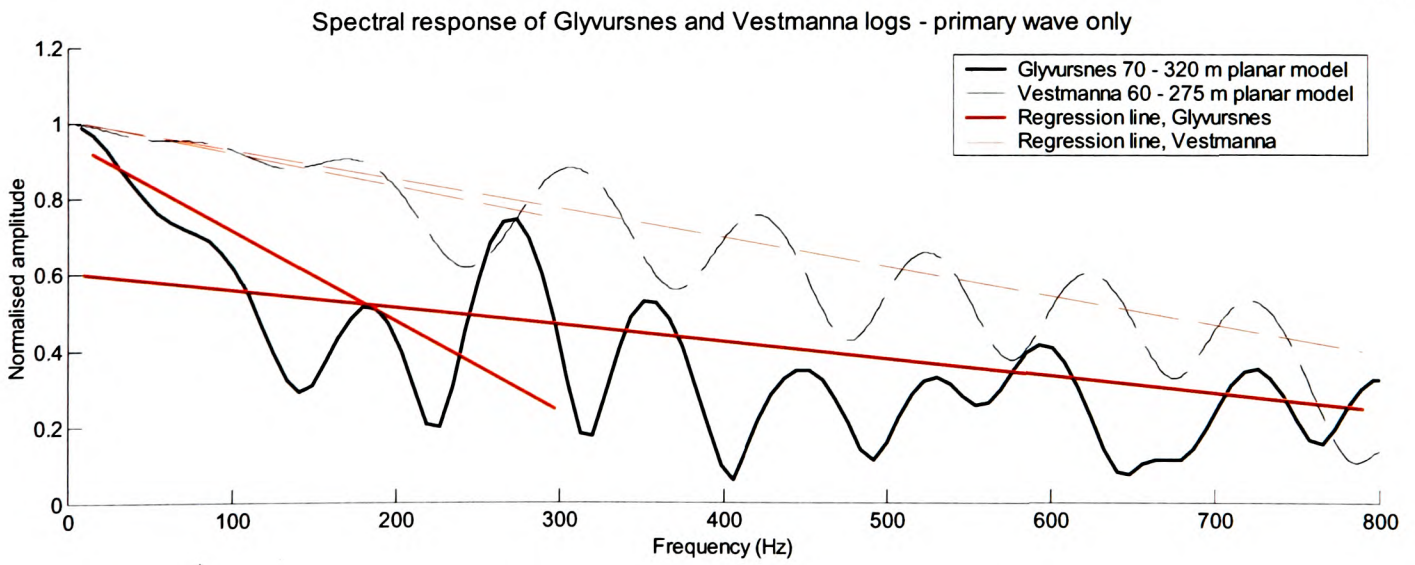

Figure 4.7.
Broadband response for 1-D models of Glyvursnes (70 – 320 m interval) and Vestmanna (60 – 275 m interval). Primary wavelets were isolated using a double-tapered time gate of 20 ms. The least-squares linear regression lines (red) change in gradient depending on the bandwidth selected. This in turn leads to varying estimates of Q.

4.3 TIME-FREQUENCY ANALYSIS

Morlet wavelet scalograms have been introduced as tools for time-frequency analysis (Chapter 3). The WT has excellent time-frequency resolution, and can be applied to a time-window of any length without masking or filtering out later arrivals. The events which produce spectral minima can thus be pinpointed in time.

Seismograms from the zero-phase source experiments were analysed following the procedure described in section 3.3.1. The traces and their scalograms are shown in Figures 4.8 – 4.11, the following observations being key to interpretation:

- the influence of short-lag multiples on the primary wavelet (section 4.3.1)
- intensity and persistence of multiples at certain frequencies, a form of resonance (section 4.3.2)
- the overall spectral profile (section 4.3.3)

4.8

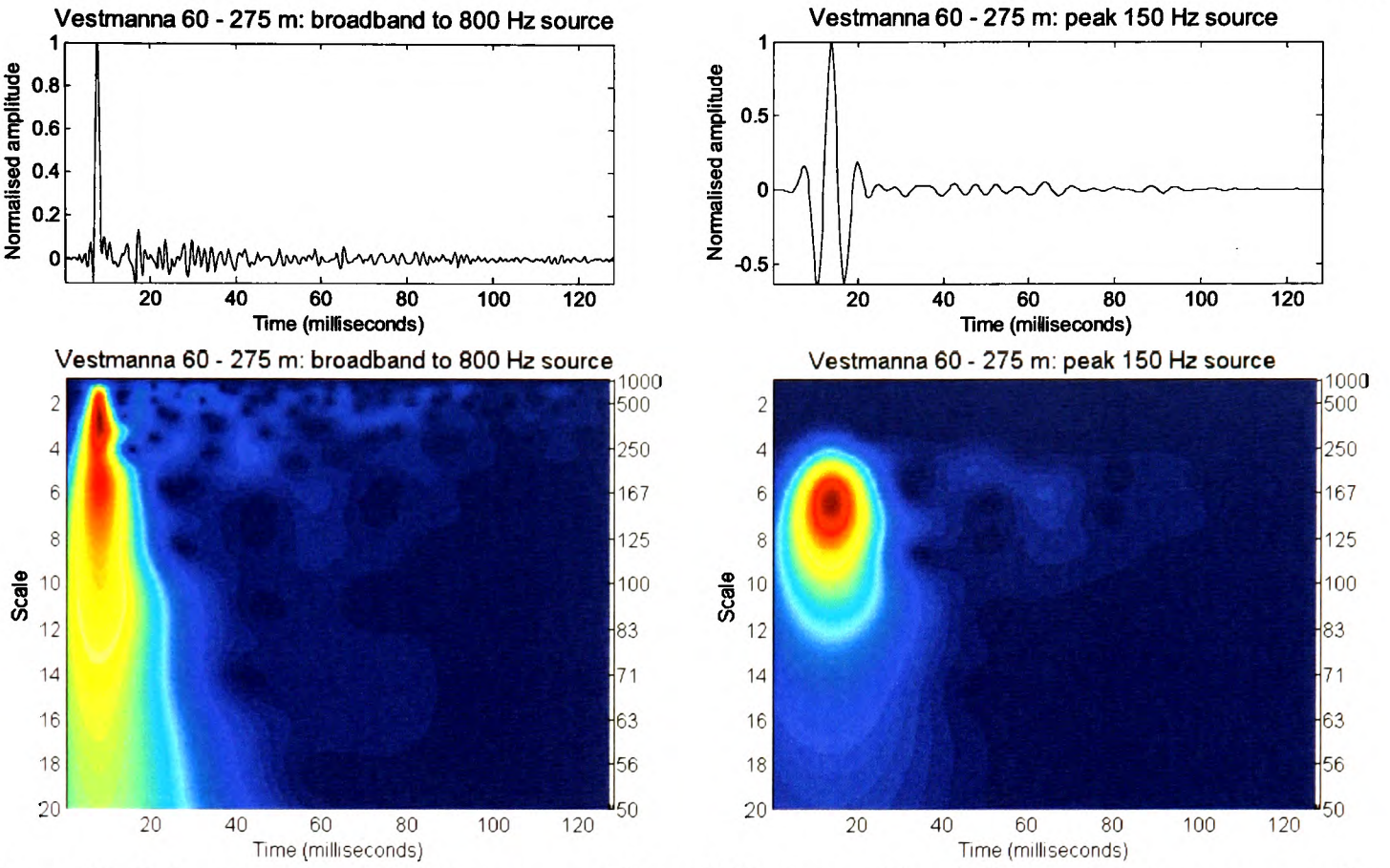

Figure 4.8. Seismograms of the Vestmanna 1-D model between 60 – 275 m and their corresponding scalograms. Left: Broadband 800 Hz synthetic source. Right: Peak 150 Hz synthetic source. The full colour scaling covers a linear, normalised amplitude range of 0 - 100%.

4.9

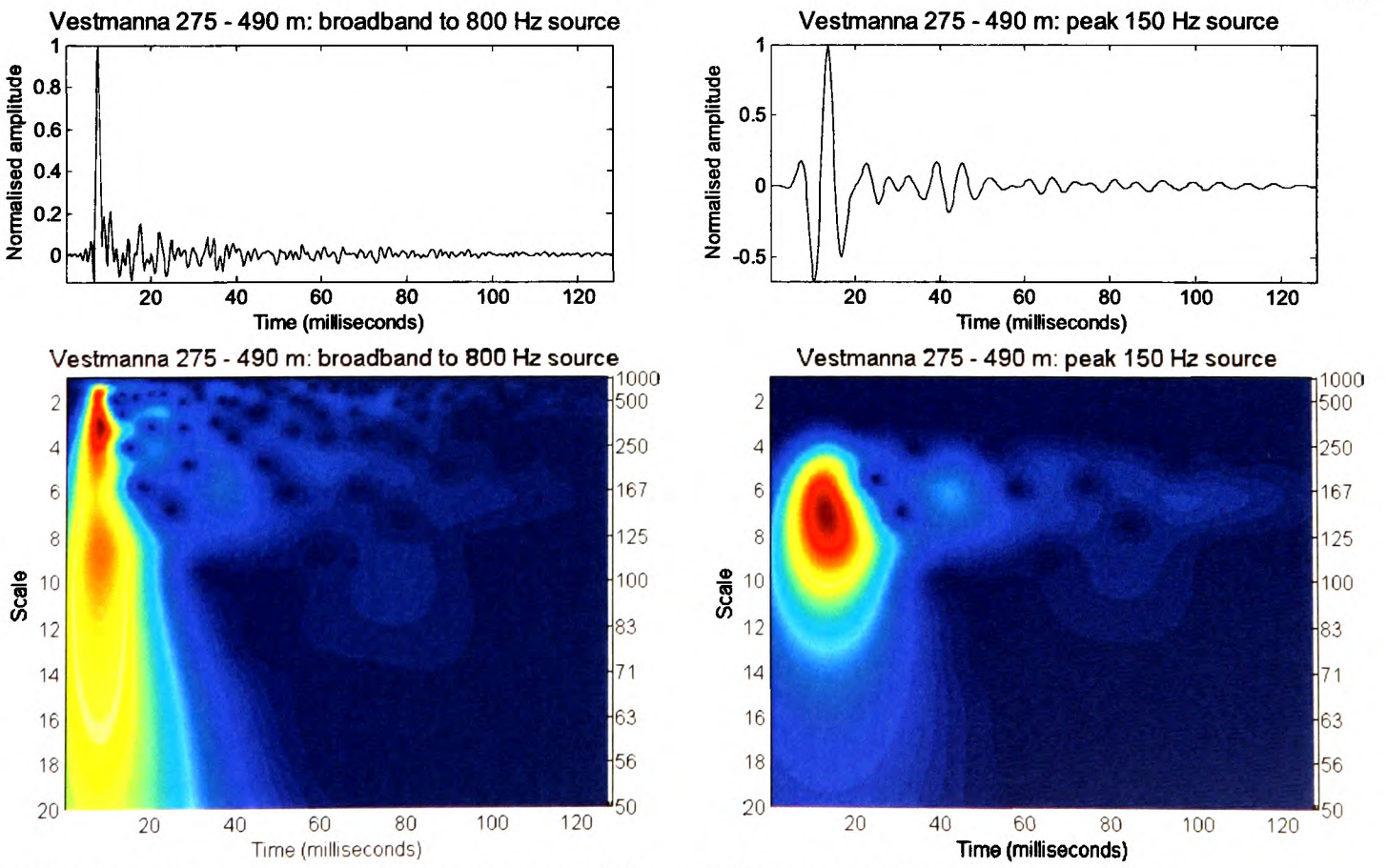

Figure 4.9. Seismograms of the Vestmanna 1-D model between 275 – 490 m and their corresponding scalograms. Left: Broadband 800 Hz synthetic source. Right: Peak 150 Hz synthetic source. The full colour scaling covers a linear, normalised amplitude range of 0 - 100%.

4.10

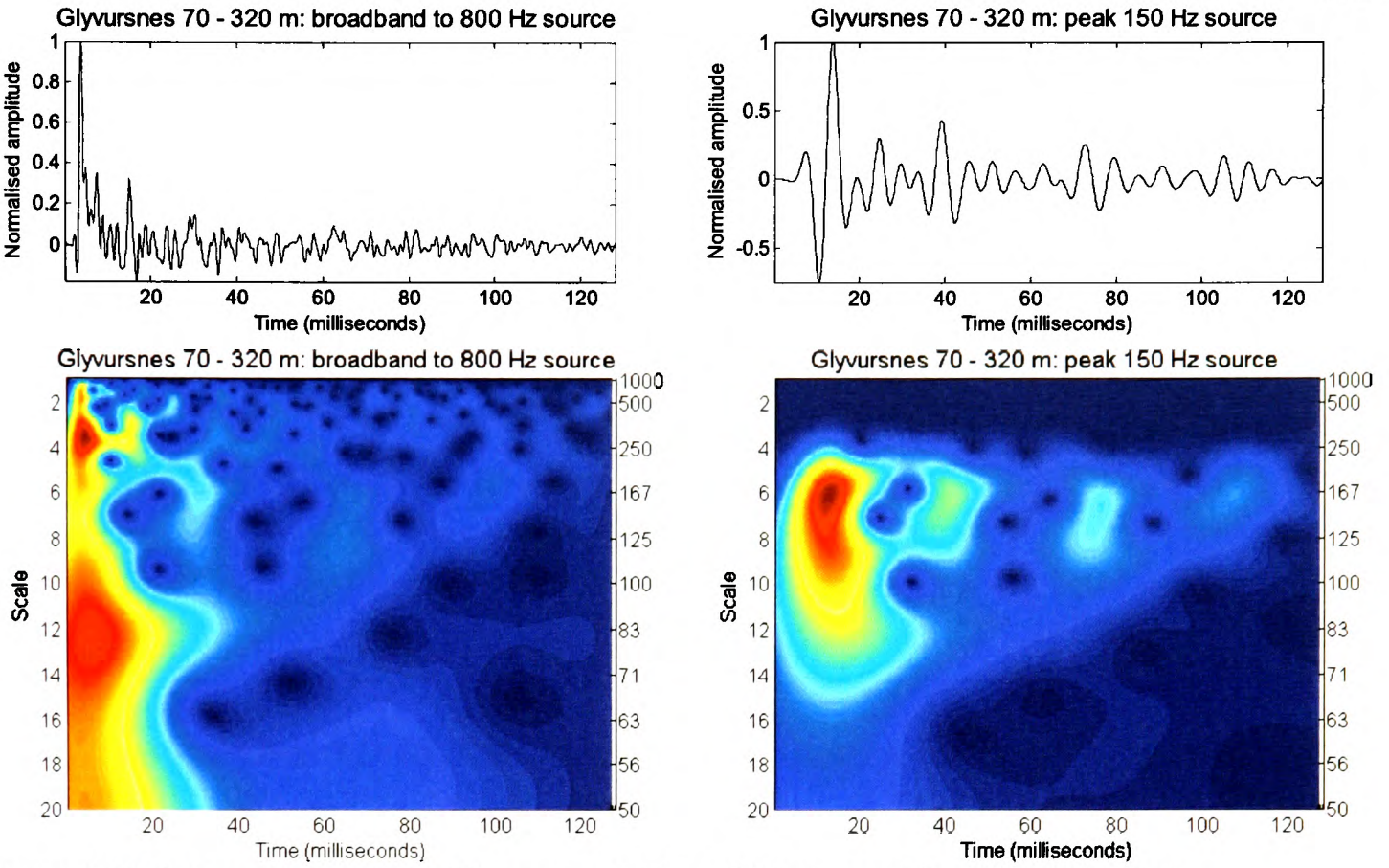

Figure 4.10. Seismograms of the Glyvursnes 1-D model between 70 – 320 m and their corresponding scalograms. Left: Broadband 800 Hz synthetic source. Right: Peak 150 Hz synthetic source. The full colour scaling covers a linear, normalised amplitude range of 0 - 100%.

4.11

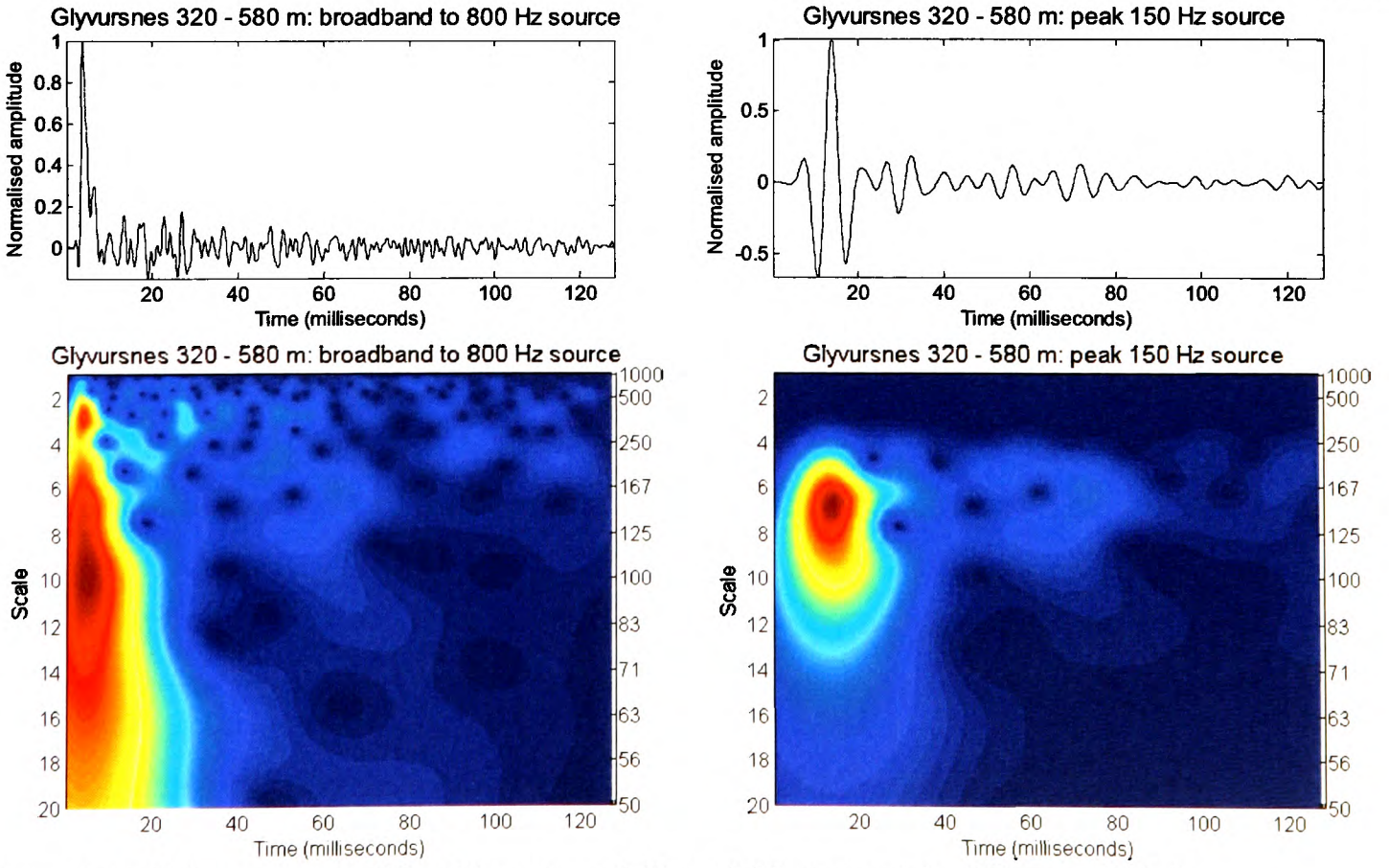

Figure 4.11. Seismograms of the Glyvursnes 1-D model between 70 – 320 m and their corresponding scalograms. Left: Broadband 800 Hz synthetic source. Right: Peak 150 Hz synthetic source. The full colour scaling covers a linear, normalised amplitude range of 0 - 100%.

4.3.1 SHORT-LAG MULTIPLES

The broadband trace from the upper Vestmanna model and its scalogram are shown in Figure 4.8 (left panel). The 230 Hz minimum of Figure 4.7 appears as a destructive interference feature at 15 ms, and is caused by a short-lag multiple impinging on the primary wavelet. A similar phenomenon is observed in the lower section of Vestmanna (Figure 4.9, left panel), where the primary wavelet is strongly impinged upon by isolated multiple events at ~ 150, 250 and 500 Hz.

The first conclusion is that the primary wavelet is strongly influenced by early-arriving multiples. In both Vestmanna sections, the minima appear to be local, ephemeral features, and energy at these frequencies does not dominate the rest of the coda. Since these short-lag multiples cannot be entirely removed by time-gating, Q estimates from spectral ratio analyses are skewed towards lower values by their presence.

The Vestmanna 1-D Q values (Table 4.1, columns 3, 4) are therefore treated as lower-limit estimates.

4.3.2 INTENSITY AND PERSISTENCE OF MULTIPLES

In contrast to the transient multiples in Vestmanna, the upper section of Glyvursnes produces intense interference patterns persisting over a longer time (Figure 4.10, left panel). The primary wavelet is attenuated by spectral minima at ~ 65, 150 and 400 Hz. These match well with minima seen in Figure 4.7 (the differences arising from isolation

of the primary wavelet with a tapered time gate). Remnant energy is present at ~ 85 and 280 Hz, which may be amplified by constructive interference. This suggests that the velocity structure of upper Glyvursnes has resonant properties. Persistent 110 – 180 Hz multiples seen in the narrow bandwidth experiment (Figure 4.10, right panel) may be further evidence for this.

In more complicated wavetrains (as in a real-world scenario) intense, persistent multiples would cause greater disruption to a signal than the ephemeral events described in 4.3.1.

4.3.3 OVERALL SPECTRAL PROFILE

The broadband responses show that basalts generate multiples over a range of frequencies (Figures 4.8 – 4.11, left panels). This latent scattering potential is selectively filtered by the bandwidth of the source wavelet. In the 150 Hz experiments, interference events below 50 Hz and above 250 Hz are suppressed, altering the overall spectral profile (Figures 4.8 – 4.11, right panels). This affects the value of Q to varying extent in the 1-D models.

In the Vestmanna upper section, the 50 – 250 Hz band experiences negligible scattering relative to the full 0 – 800 Hz response, and the redistribution of spectral minima is largely unaffected (Figure 4.8). In the Vestmanna lower section, the high end of the

50 – 250 Hz range is preferentially attenuated (Figure 4.9). Substantially lower Q is therefore estimated for the 150 Hz source than for the broadband source (Table 4.1). The lower depth section of Glyvursnes appears to have a scattering response intermediate to the upper Glyvursnes and Vestmanna sections. Correspondingly, it returns an intermediate Q value (Table 4.1).

In sum, 1-D scattering attenuation in Vestmanna and Glyvursnes rocks is frequency-dependent over seismic wavelengths. Q is a convenient descriptor of the primary response of synthetic seismograms, but is unable to distinguish between ephemeral short-lag multiples and persistent, more intense multiples. Hence, it may not give a clear indication of the basalts' attenuative potential.

4.3.4 COMPARISON WITH VSP SCALOGRAMS

The scattering characteristics of the 1-D models were compared to VSP data through their relevant scalograms (see Chapter 3, section 3.3.2).

The Vestmanna VSP trace at 50 m contains energy at frequencies above 500 Hz. By 275 m this is drastically attenuated in both the primary wavelet and coda, and by 500 m depth, energy is mainly distributed between 30 and 250 Hz (Figure 3.14). The 1-D coda, by contrast, retains its high frequency content, and shows very little shift in the frequency of peak energy. 1-D scattering is therefore unlikely to be responsible for the low Q values of the VSP.

In the upper section of Glyvursnes, comparisons could only be made within the bandwidth of the VSP. Important features were observed within this region: At 50 m in the VSP, energy is strongest between 10 and 50 Hz, but by 320 m this is highly concentrated in a narrow band around ~ 33 Hz. This effect is reinforced by destructive multiple interference at ~ 50 Hz and ~ 25 Hz. The 1-D seismogram shows this same concentration of energy at 33 Hz (Figure 4.12), and the same attenuation in the regions of 50 and 27 Hz. The two scalograms differ significantly below 20 Hz, but this is probably due to the bandwidth constraints of the VSP geophone (the 1-D synthetic source has no such dropoff). Apparent attenuation of frequencies greater than 100 Hz is also replicated by 1-D modelling.

4.12

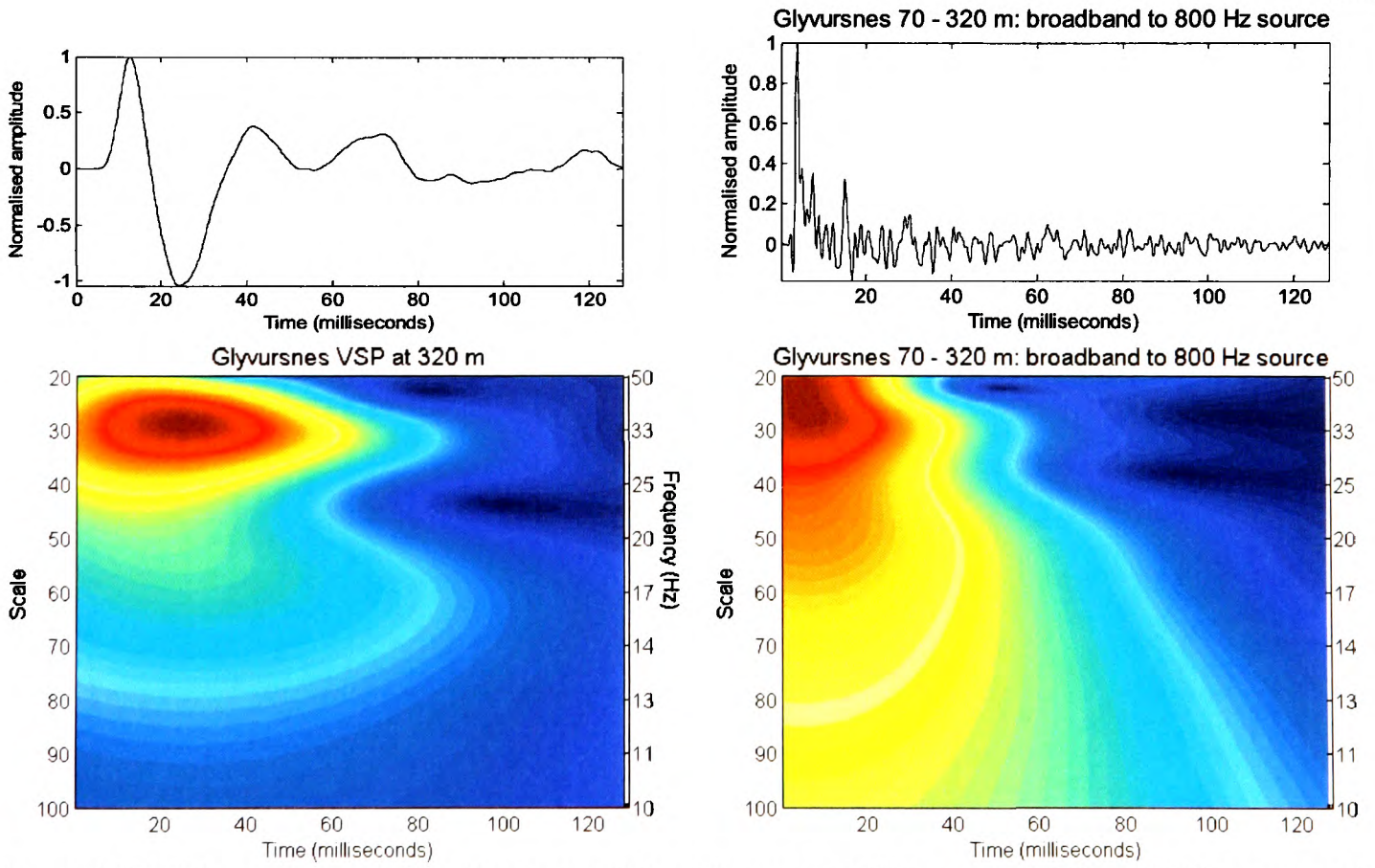

Figure 4.12. Seismograms and scalograms of the Glyvursnes VSP trace at 320 m (left) compared with those of the 1-D models (right), between 10 and 50 Hz. The full colour scaling covers a linear, normalised amplitude range of 0 - 100%.

No conclusions were drawn as to the lower section of Glyvursnes, due to the extremely narrow bandwidth of the VSP below 320 m. As reference, the scalograms of both VSP and 1-D synthetic traces are shown in Figure 4.13.

4.13

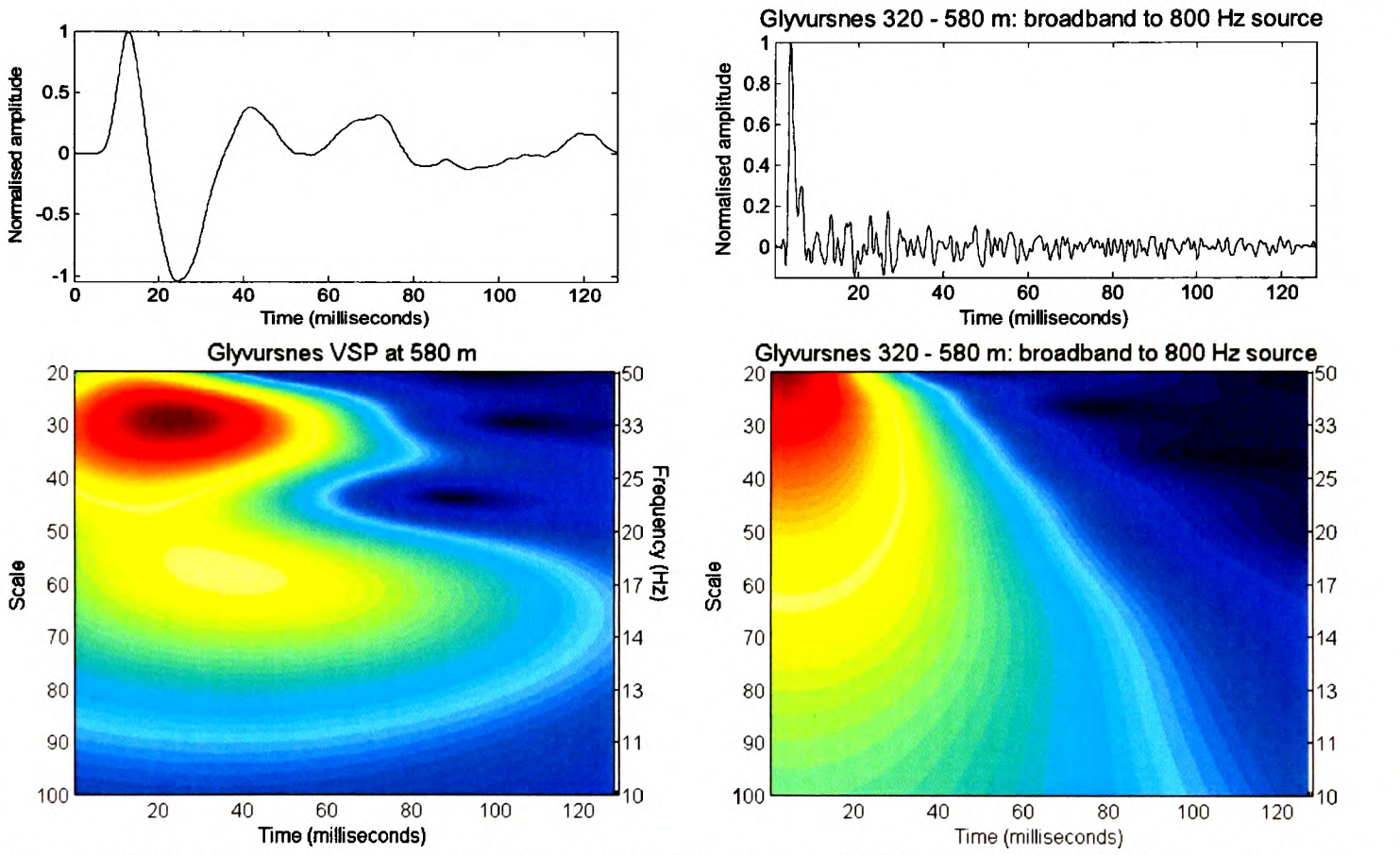

Figure 4.13. Seismograms and scalograms of the Glyvursnes VSP trace at 580 m (left) compared with those of the 1-D models (right), between 10 and 50 Hz. The full colour scaling covers a linear, normalised amplitude range of 0 - 100%.

4.4 COARSE LAYERING AND LARGE VELOCITY CONTRASTS

Large velocity contrasts in basalts have been cited as a major cause of overall amplitude loss and incoherence of the wavefield (Pujol *et al.*, 1989; Kiørboe & Petersen, 1995; Maresh & White, 2005).

Morlet *et al.* (1982) found that the scattering response of the medium was dependent on the ratio of the seismic wavelength to the spatial period of the medium. If multiples are due to a predominant spatial frequency in the rock, a distinctive interference pattern appears in the spectrum. The greater the regularity of the velocity structure, the stronger the intensity of any constructive / destructive interference; subtle details in the spectrum are tuned by variations in velocity contrast and layer thickness.

In the case of a two-velocity planar model with uniformly spaced layers, the interference patterns converge onto a set of well-defined notches (Figure 4.14b). This is the end member of a wide range of 1-D scattering scenarios. Multiplying the given velocities by k multiplies the new frequencies at which minima appear by k. If the layer thickness is increased by a factor of k, the new positions of the spectral minima decrease to $1/k$ the original. The intensity and width of the minima are related to the number of interfaces through which the wave propagates.

a

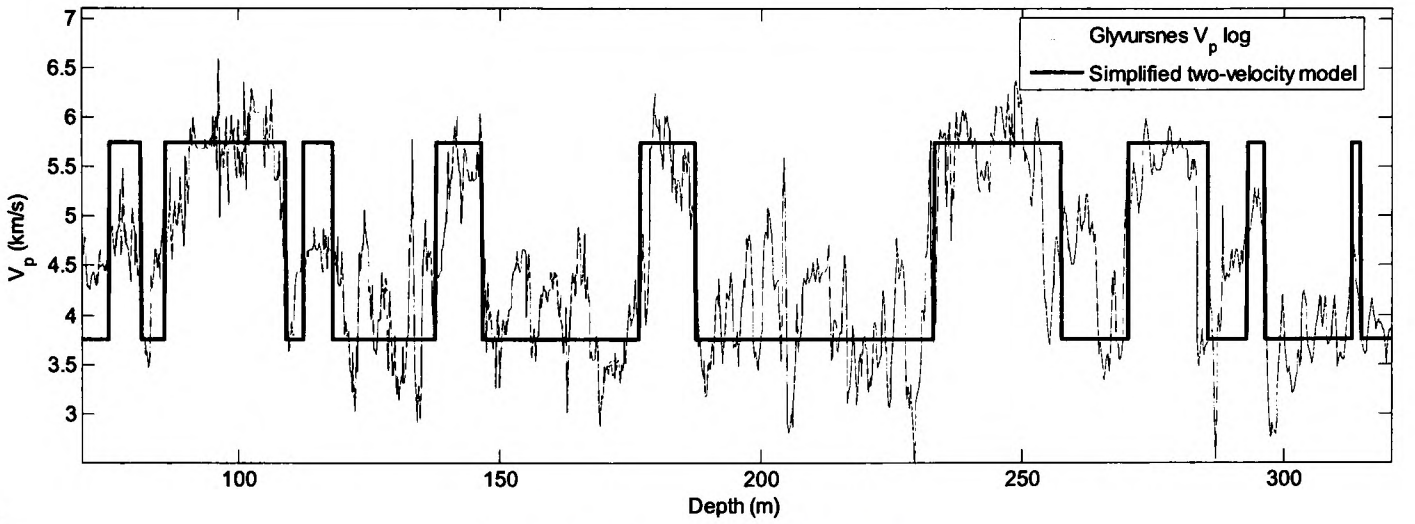

b

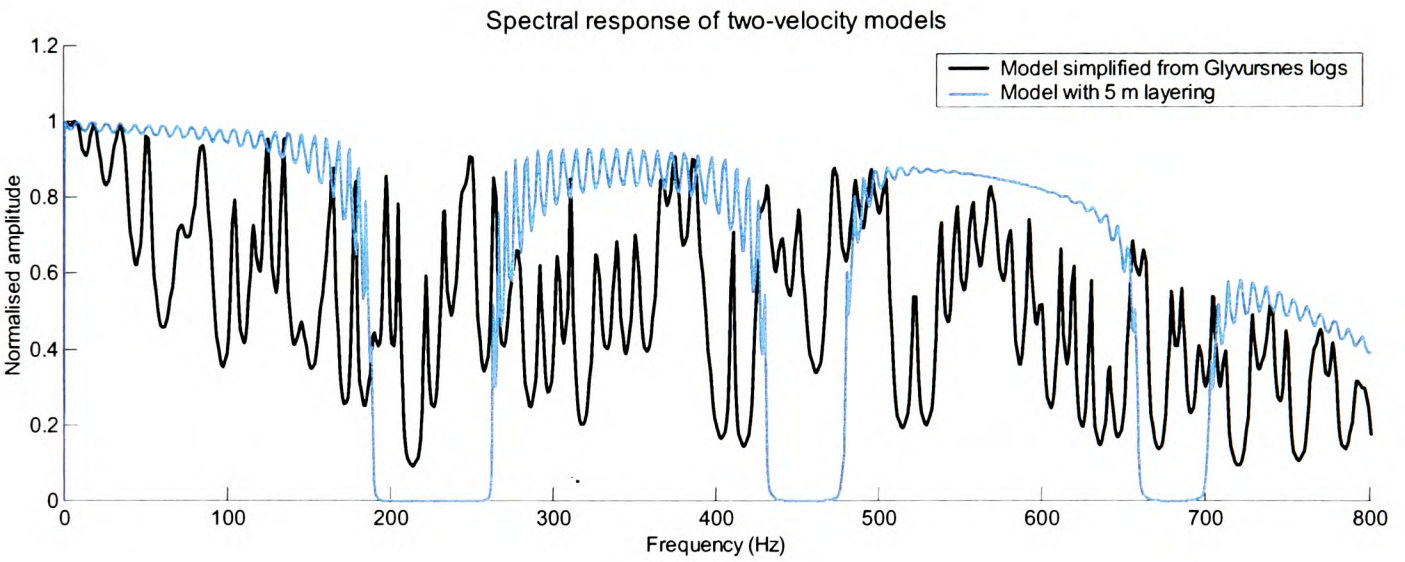

c

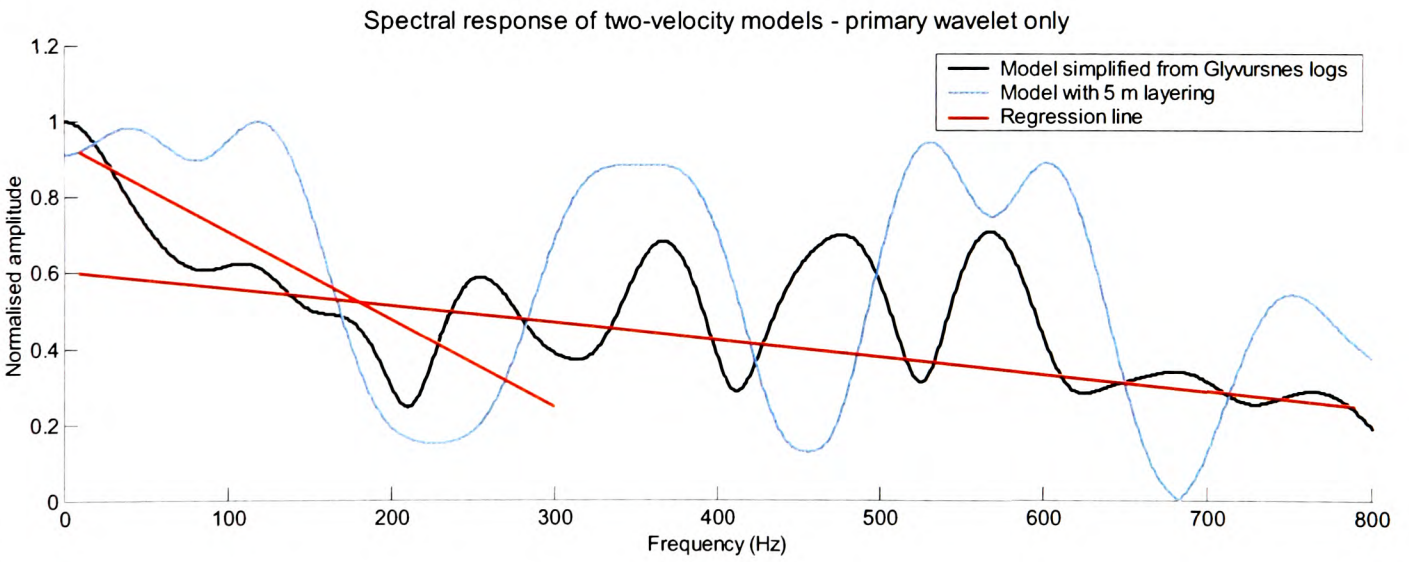

Figure 4.14.
a. Two-velocity model (black) based on the upper Glyvursnes section, 60 – 320 m (grey).
b. Amplitude spectrum of seismic response from the two-velocity model (black), when a broadband 800 Hz source is propagated through it. Amplitude spectrum of seismic response from a model with the same velocity contrast, but with layers spaced uniformly, 5 m apart (blue). The first dominant minimum is centred on 225 Hz.
c. Broadband spectral response for primary wavelets only. The least-squares linear regression lines (red) change in gradient depending on the bandwidth selected, and produce similar Q estimates to the unfiltered 1-D model (see Figure 4.7).

The 70 – 320 m interval of Glyvursnes has a velocity macro-structure with apparently longer spatial wavelengths than the other log sections (Figure 4.1). The intensity and persistence of multiples generated also indicate that it may have a latent periodicity (section 4.3.2). Using a wavelet filter, small-scale fluctuations were removed, leaving only a two-velocity model (3750 and 5750 m/s) with coarse layers between 2 and 32 m in thickness (Figure 4.14a, plotted in black). A broadband wavelet was propagated through this simplified structure and the spectral response compared to that of the 5 m layered model (Figure 4.14b).

When all the multiples were considered, the variation in layer thickness was shown to disrupt the previously regular interference pattern. However, when only the spectrum of the primary wavelet was considered, the simplified model reproduced the main feature of the original Glyvursnes 1-D model: a dominant minimum between ~ 50 and 250 Hz (Figures 4.7, 4.14c). Least-squares regression produced similar trend lines: for a 95% confidence interval, Q was estimated to be 43 – 50 for the bandwidth of 10 – 250 Hz, and 329 – 464 for the bandwidth of 10 – 800 Hz. While these values are higher than those of the original 1-D Glyvursnes model, the experiments show that coarse layering is sufficient to create frequency-dependent effects.

4.5 DISCUSSION

It has been shown that multiple scattering in basalts creates spectral interference patterns, and the resulting minima can have a strong localised effect on the spectrum. This leads to Q estimates which are sensitive to source frequency.

1-D models generated from the wireline logs vary in their 1-D scattering behaviour and in their Q values. Over a seismic bandwidth of 10 – 250 Hz, the upper section of Glyvursnes produced the lowest Q estimate of all the models and the strongest multiples. Its time-frequency response also replicated key interference features seen in the corresponding VSP trace. This indicates that 1-D scattering is a dominant attenuation mechanism. The lower Glyvursnes section and the Vestmanna sections did not return sufficiently low Q estimates to match the VSP results. More importantly, they did not produce the same scattering features as those observed in corresponding VSP traces. 1-D scattering is therefore unlikely to be significant in these rocks.

The strong scattering potential of the upper section of Glyvursnes may be due to its coarse-layered velocity macro-structure, which distinguishes it from the other basalt sections. This is coincident with its geological classification as part of the Upper Series Basalts. The lower section of Glyvursnes forms part of the Middle Series Basalts, with the boundary identified at 355 m depth by Waagstein & Andersen (2003). No major geological boundaries are represented in the Vestmanna VSP interval, which samples

only the Middle Basalt Series. The emplacement history of each basalt section is therefore important to its 1-D scattering potential.

A dominant minimum occurs in the broadband spectrum of the upper Glyvursnes 1-D model between 0 and 250 Hz. The very low 1-D Q value in the upper section of Glyvursnes can be directly attributed to this minimum. It can also be shown that an extremely coarse two-velocity model is able to reproduce this minimum. However, this is a highly artificial model, and crude layering cannot be treated in isolation. The upper Glyvursnes section appears to be heterogeneous over a range of scales. Such multi-scale heterogeneity is the subject of detailed investigation in Chapter 5.

CHAPTER 5

1-D HETEROGENEITY AND STATISTICAL STUDIES OF THE FAROES WIRELINE LOGS

Acoustic modelling in Chapter 4 has shown that the style of 1-D attenuation varies between rocks in Vestmanna and Glyvursnes, and that geological factors exert a direct control on scattering potential. While the upper Glyvursnes section is notable for its velocity macro-structures, all the log data show strong fluctuations, seemingly repeated over a range of spatial scales. In this respect, the log data satisfy the first criterion of fractal geometry: self-similarity, i.e. when sub-units on multiple levels statistically resemble the structure of the object as a whole (Mandelbrot, 1989).

Self-similarity appears to be a widespread phenomenon in the Earth's upper crust. Despite differences in petrology, tectonic structure and overall formation history, wireline logs from the Cajon Pass (California), the KTB (Germany), Stenberg (Sweden), Sudbury (Canada) and the Abitibi (Canada) boreholes exhibit fractal characteristics (Marsan & Bean, 2002).

In this chapter, the statistics of 1-D wireline logs at Glyvursnes and Vestmanna are measured and fractal behaviour is assessed. The relationship between perceived fractal characteristics and 1-D synthetic seismic response is also examined using the spectral ratio method of Q analysis and WT scalograms.

The data analysed are subsets of the VSP intervals. In Glyvursnes, the data are sampled so as to avoid crossing the known Upper / Middle Series transition at 355 m. The upper and lower sections of Vestmanna are likewise sampled from the extremities of the VSP interval. For comparison, two datasets from the Lopra-1 borehole are included in the analyses. In the absence of detailed petrographic descriptions, the Lopra sections are chosen based on their contrasting visual characteristics. All datasets are kept at their highest resolution (0.2 m in Glyvursnes and Vestmanna, 0.1524 m in Lopra). These same intervals are used for all subsequent studies in this chapter, and are listed in Table 5.1.

Table 5.1

Borehole	Glyvursnes	Vestmanna	Lopra
	Depth range /m *(sampling interval)*	Depth range /m *(sampling interval)*	Depth range /m *(sampling interval)*
Borehole Intervals	**50 – 255 *(0.2)*** *Upper Basalt Series* **396 – 600 *(0.2)*** *Middle Basalt Series* **50 – 600 *(0.2)*** *VSP Interval*	**50 – 255 *(0.2)*** *Middle Basalt Series* **296 – 500 *(0.2)*** *Middle Basalt Series* **50 – 500 *(0.2)*** *VSP Interval*	**1250 – 1562 *(0.1524)*** **2600 – 2912 *(0.1524)*** *Lower Basalt Series* *with varied lithological changes. Detailed interpretation unavailable.*

Table 5.1. Depth range of borehole log datasets analysed.

5.1 MONOFRACTAL ANALYSIS

One commonly used descriptor of self-similarity is the Hurst exponent, first formulated to assess the fluctuation of water level in reservoirs (Hurst *et al.*, 1965). The Hurst exponent provides a measure of whether the data is a pure random walk or has underlying trends, and has been extended to discrete time series, as follows (Turcotte, 1997).

The running sum of a series, y_n, relative to its mean, $\bar{y}$, is represented by:

$$y_n = \sum_{i=1}^{n} (y_i - \bar{y}) \qquad \textbf{(5.1)}$$

The range, R_N is defined by:

$$R_N = (y_n)_{\max} - (y_n)_{\min} \qquad \textbf{(5.2)}$$

The Hurst exponent, H, is given by:

$$\frac{R_N}{S_N} = \left(\frac{T}{2}\right)^H \qquad \textbf{(5.3)}$$

Where S_N is the standard deviation and T is a chosen period. Over a certain range of time or space, the degree of autocorrelation decays with lag according to the power law in Equation 5.3. A Hurst exponent of exactly 0.5 indicates a random or Brownian walk. In a random walk there is no correlation between current and future elements. A Hurst exponent between 0.5 and 1 indicates persistence, or positive autocorrelation, where preceding values influence succeeding values to follow the same trend. A Hurst exponent between 0 and 0.5 indicates anti-persistence, or negative autocorrelation, where succeeding values tend to be the reverse of preceding values.

5.1.1 POWER SPECTRAL METHOD

One indicator of fractality is power-law dependence, where decay is inversely proportional to the wavenumber of the spatial frequencies. This is expressed as a linear trend in the graph of $\log_{10}$(power) versus $\log_{10}$(wavenumber). The slope of the trend-line, β, is related to the Hurst exponent, H, by:

$$\beta = 2H + 1 \qquad \textbf{(5.4)}$$

(Turcotte, 1997).

A common procedure is to separate depth-velocity and structural trends from background fluctuation. However, there are no systematic trends in the Faroes datasets which could be easily removed without imposing arbitrary scale lengths (Dolan *et al.*, 1998; Holliger, 1996). Similarly, padding the data with zeros or with data fragments introduces energy at extraneous scales, skewing the Hurst exponents calculated, and therefore artificial extension of the datasets was also avoided.

5.1.2 RESULTS

Power spectral plots of the acoustic impedance logs are shown in Figures 5.1 to 5.3. Breaks in slope may be due to the averaging effect of the sonic tool, which acts like a boxcar window of the data in the frequency domain and alters the gradient of the trend-line (Dolan *et al.*, 1998). The extent of averaging is controlled by the maximum source-to-receiver distance of the sonde: at Vestmanna and Glyvursnes this was 1.1 m (corresponding to a $\log_{10}$ (wavenumber) of approximately -0.5), and at Lopra this was 3 m (corresponding to a $\log_{10}$ (wavenumber) of approximately -0.1). Dashed grey lines in Figures 5.1 – 5.3b, c indicate where breaks in slope are predicted to occur, but there is some mismatch with the actual gradient changes. This leaves open the possibility that fractal character changes over different spatial scales.

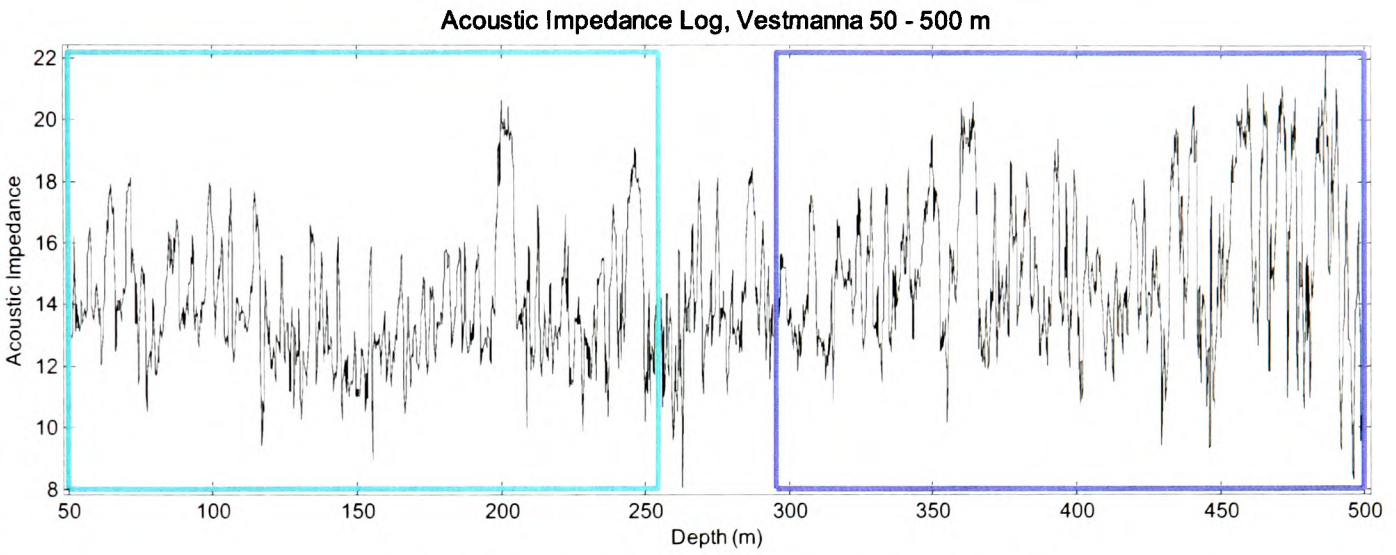

a

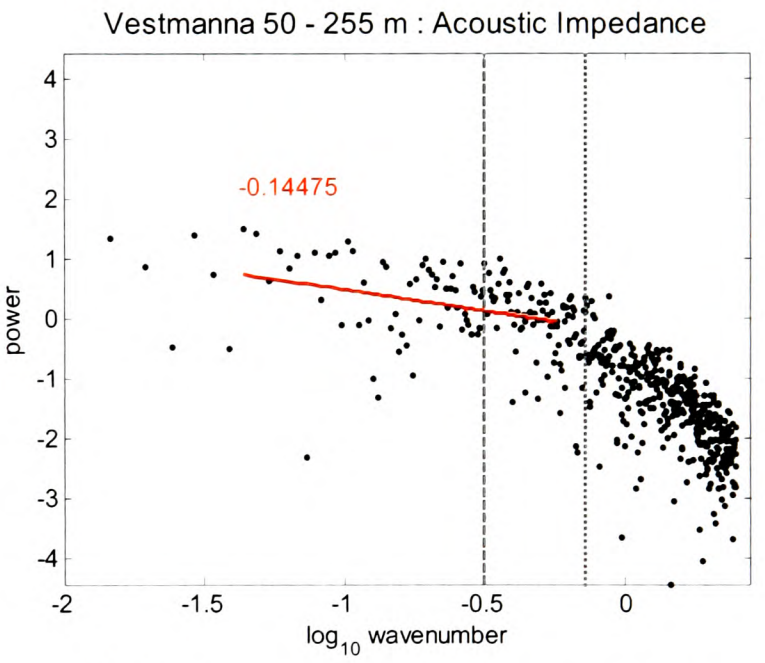

b

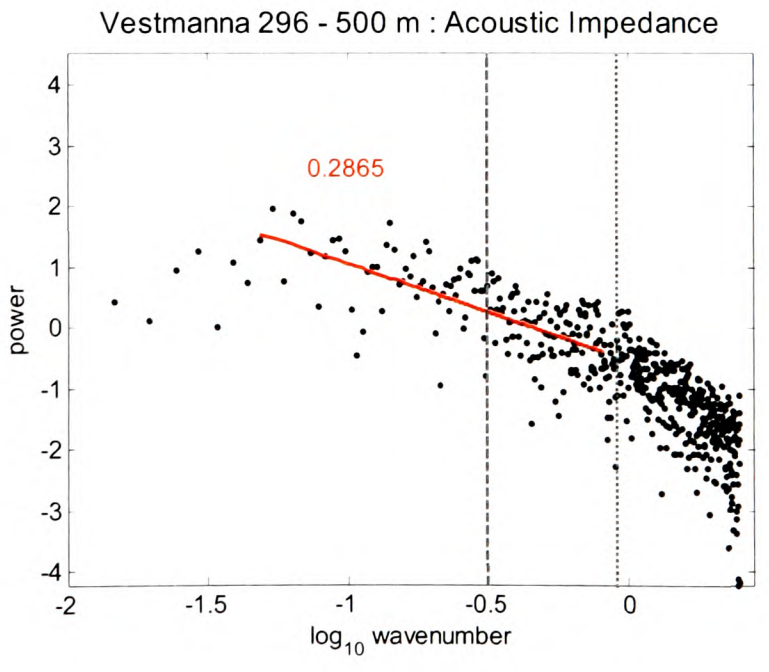

c

Figure 5.1. a. Acoustic impedance log of the Vestmanna borehole.
b. Power spectral analysis of the upper interval, 50 – 255 m.
c. Power spectral analysis of the lower interval, 296 – 500 m.

a

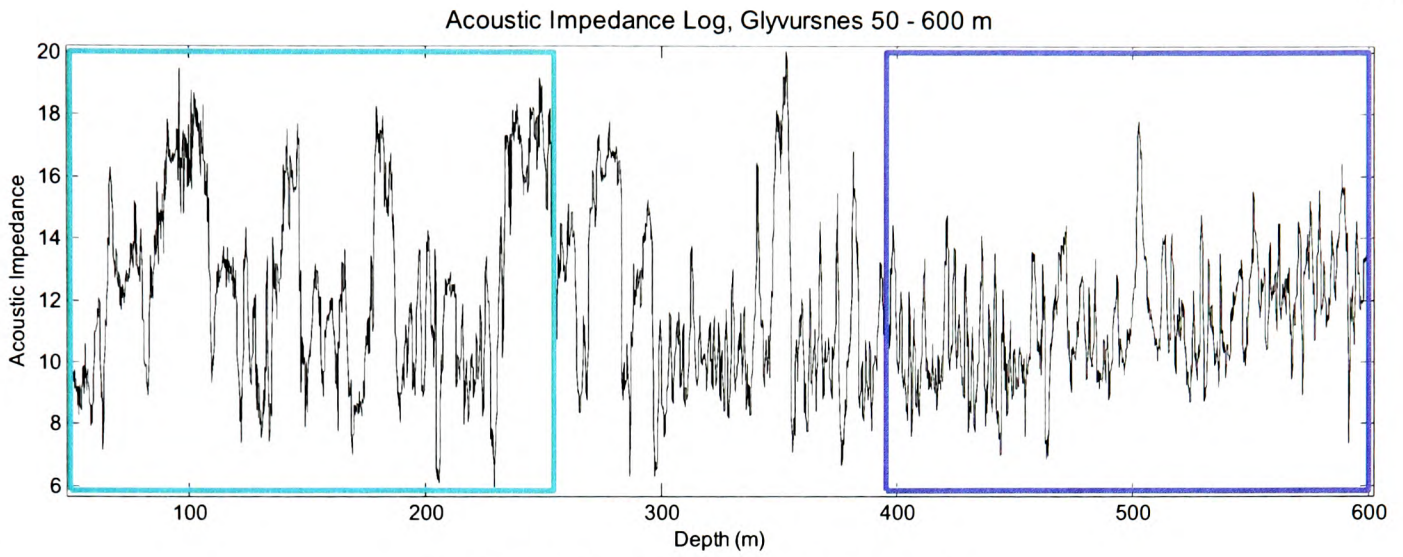

b

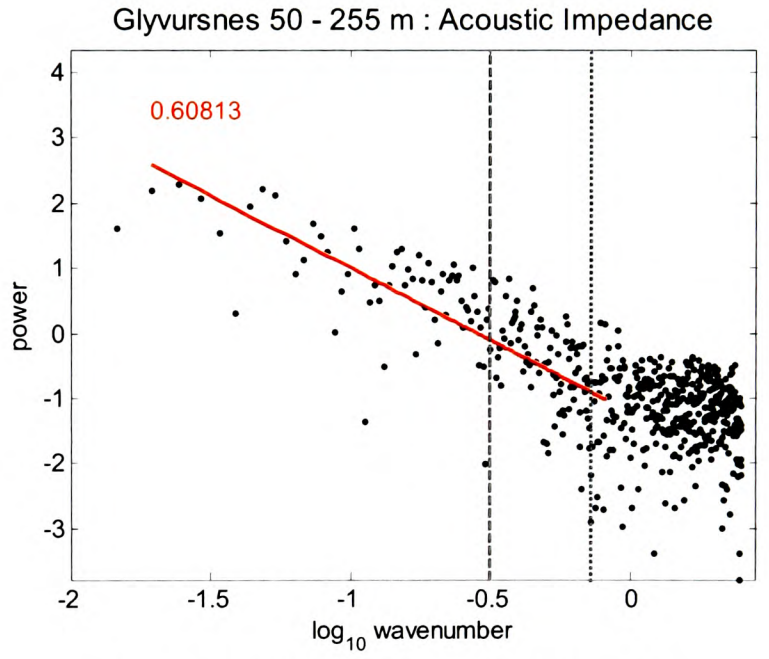

c

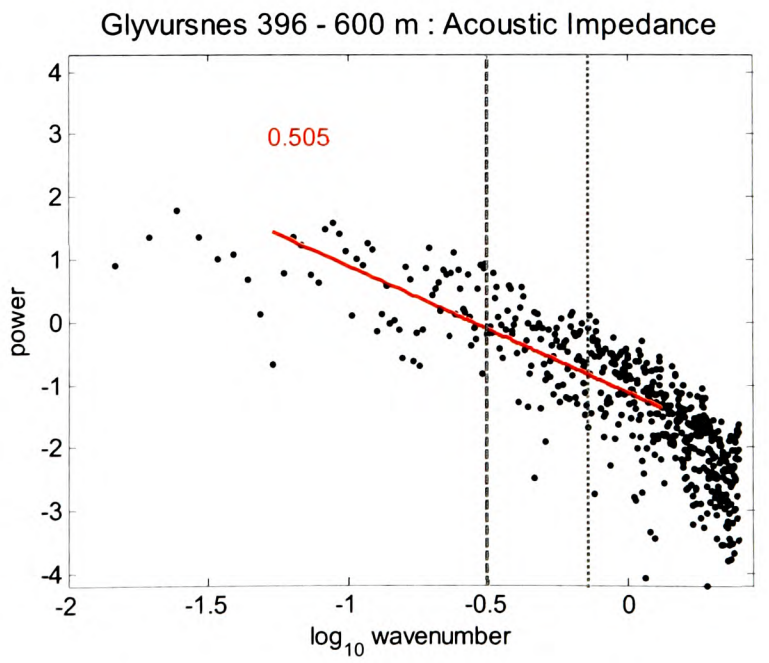

Figure 5.2. a. Acoustic impedance log of the Glyvursnes borehole.
b. Power spectral analysis of the upper interval, 50 – 255 m.
c. Power spectral analysis of the lower interval, 396 – 600 m.

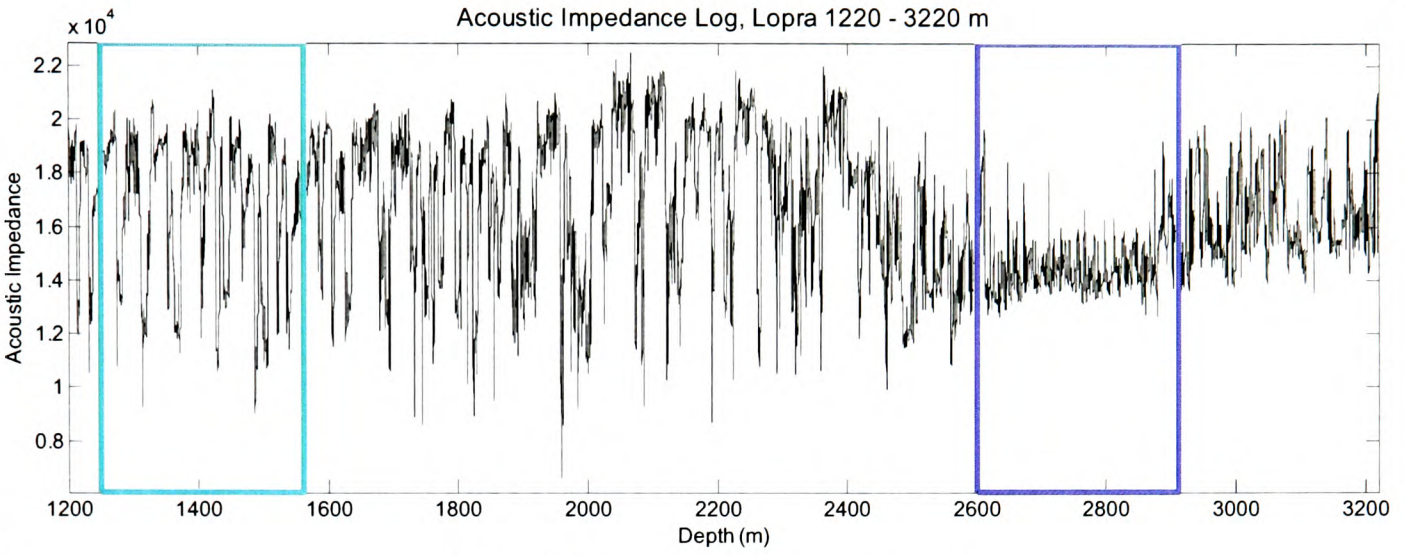

a

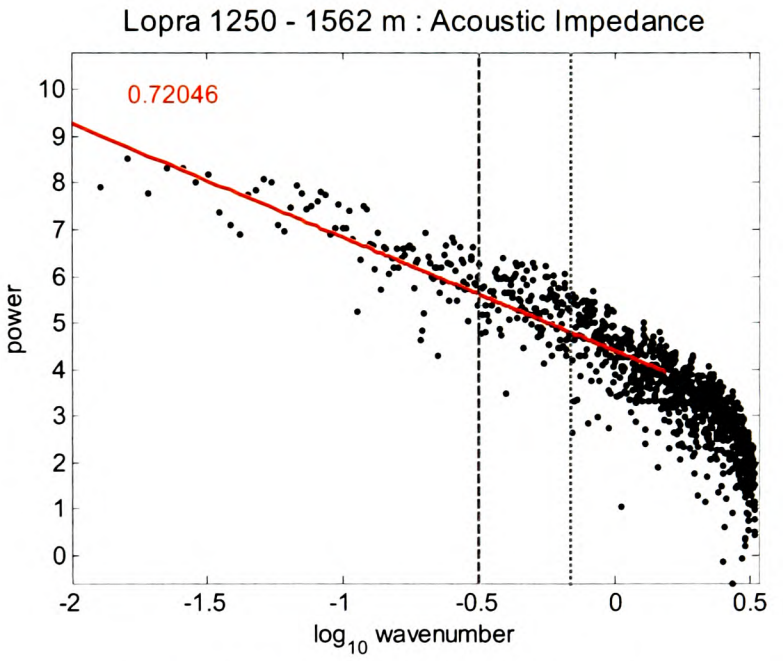

b

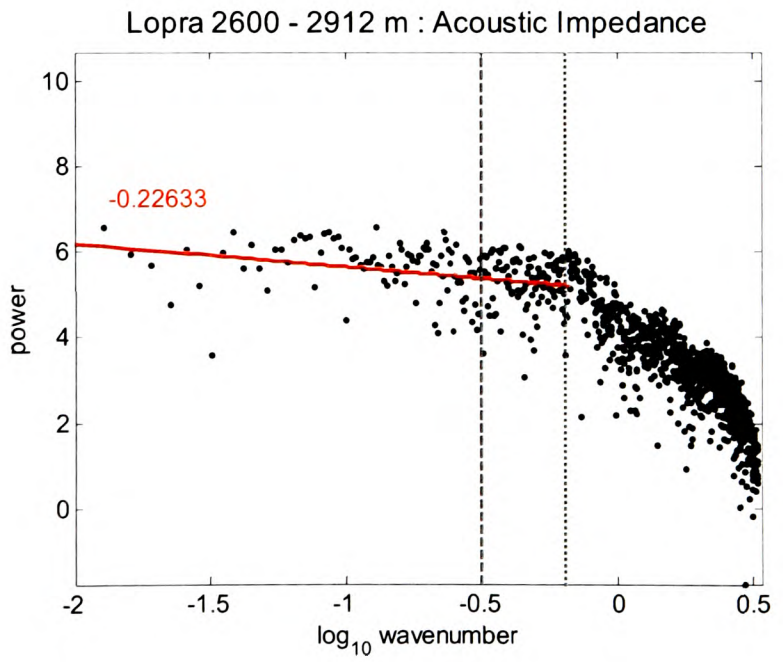

c

Figure 5.3. a. Acoustic impedance log of the Lopra borehole.
b. Power spectral analysis of the upper interval, 1250 – 1562 m.
c. Power spectral analysis of the lower interval, 2600 – 2912 m.

Table 5.2 lists Hurst exponents of acoustic impedance from the three boreholes and the spatial scales over which they were derived. The lower Vestmanna section is shown to be anti-persistent. The lower Glyvursnes section has the characteristics of a random walk, and both the upper Glyvursnes section and the upper Lopra section exhibit persistence.

Table 5.2

Borehole and depth interval	Hurst Exponent		Scales over which linear trend persists (m)
Vestmanna 50 – 255 m	Negative	-	2 – 20
Vestmanna 296 – 500 m	**0.3**	anti-persistent	1 – 20
Glyvursnes 50 – 255 m	**0.6**	persistent	1 – 50
Glyvursnes 396 – 600 m	**0.5**	random walk	1 – 20
Lopra 1250 – 1562 m	**0.7**	persistent	1 – 150
Lopra 2600 – 2912 m	Negative	-	1 – 150

Table 5.2. Hurst exponents over four borehole intervals derived from the power spectral method.

Despite sampling different basalt formations, the Hurst exponents do not greatly differentiate between the upper and lower Glyvursnes sections. This contradicts the results from 1-D acoustic modelling (Chapter 4). Anomalous Hurst exponents from Vestmanna and Lopra, however, indicate that the power spectral method cannot fully describe the characteristics of the basalts.

The Hurst exponent is the scaling exponent for a second order statistical measure, and can only characterise fractal behaviour of order 2. Intermittency of the fluctuating signal cannot be retrieved by this method. To measure the degree of fluctuation, a location-dependent scaling exponent is required, itself distributed in a scale-invariant way (Marsan & Bean, 2002).

5.2 MULTIFRACTAL ANALYSIS

Advances in the study of fractal turbulence (Mandelbrot, 1990, Bacry *et al.*, 1993) have extended the concept of fractal dimensions to multifractal measures. Higher order statistical measures of the signal are taken into account and analysed for scale-invariant behaviour.

Turcotte (1997) defines a multifractal set by dividing an original line of unit length into n equal segments, where r is the length of each segment. The fraction f_i of the remaining line in segment i is the ratio of the length of line in segment i to the total length of the line. The definition of the generalised moments, $M_q(r)$, of a set of fractions, $f_i(r)$ is thus:

$$M_q(r) = \sum_{i=1}^{n} f_i^q \qquad \textbf{(5.5)}$$

where q is the order of the statistical moment.

The generalised multifractal dimension, D_q, is defined by:

$$M_q(r) = Cr^{(q-1)D_q} \qquad \textbf{(5.6)}$$

It is implicit in Equation 5.6 that different power law decay behaviour may be exhibited at different statistical moments, and that this leads to intermittency and roughness of a signal. For $q = 2$, the associated D_2 is the 'correlation dimension', effectively the same statistical level measured by the Hurst exponent (Marsan & Bean, 2002). For $q = 0$, the associated D_0 is the 'fractal dimension' or 'fractal exponent', another commonly-used descriptor of complexity. These levels of detail are vital in understanding the complexity of basalt log data.

5.2.1 THE WAVELET TRANSFORM MODULUS MAXIMA METHOD (WTMM)

In section 5.1, the log data were analysed in the 2nd statistical moment, $q = 2$. In multifractal analysis, a range of moments must be considered. The singularity spectrum, f(α), describes this range and gives an intuitive understanding of the statistical measures of a multifractal (Halsey *et al.,* 1986; Mandelbrot, 1989).

Wavelets are a natural diagnostic tool for multifractals. A method pioneered by Bacry, Muzry & Arnéodo (1993) uses Wavelet Transform Modulus Maxima (WTMM) to derive fractal dimensions and has been tested by Herrmann (1998) on borehole log and seismic data. This technique has been used in the following analyses and is outlined below.

A borehole log can be treated as a function which fluctuates with depth. The irregularity of the function can then described by how it behaves under mathematical differentiation. At any point where the function cannot be differentiated, it is termed a singularity and its type characterised by the Lipschitz exponent α (also referred to as the Hölder exponent). More negative α values indicate greater abruptness (tending towards a Dirac delta function) while positive α values indicate smoother discontinuities, as seen in Figure 5.4 (Herrmann, 1998).

5.4

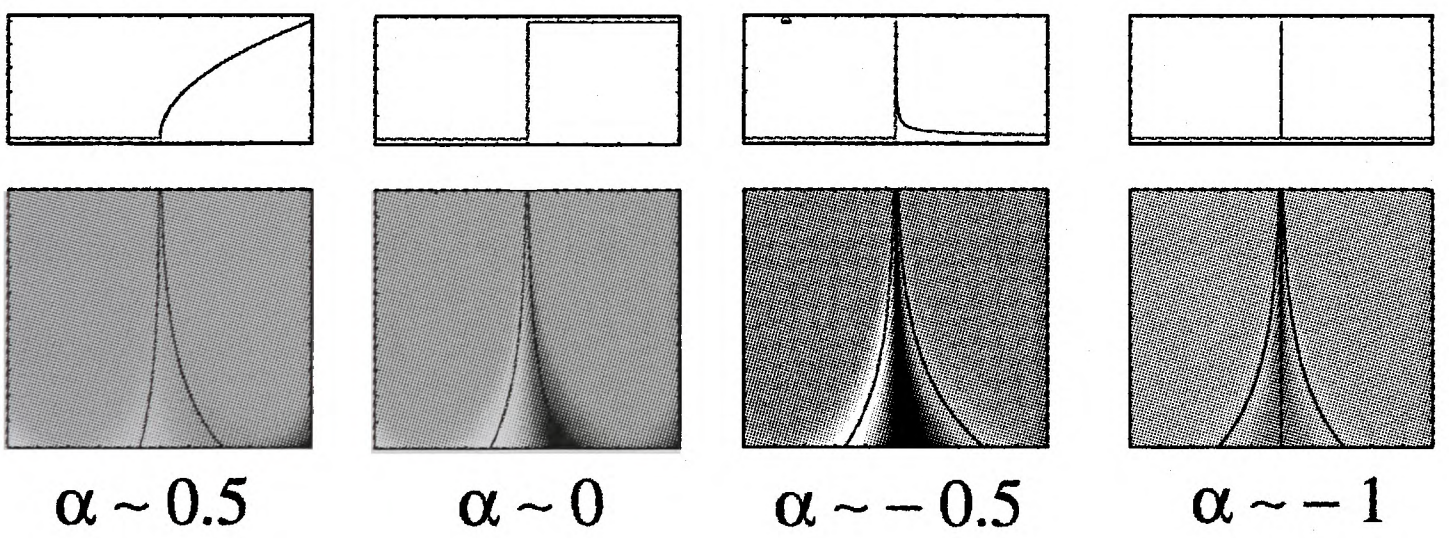

Figure 5.4.
Synthetic discontinuities (top row), their expression in Wavelet Transform space, and corresponding alpha values (from Herrmann, 1998). Abrupt discontinuities take on negative values.

The Wavelet Transform enables simultaneous analysis of a signal's temporal / spatial and frequency properties. Based on the dilation and translation of elementary wavelets, it possesses greater versatility over Fourier analysis and related transforms, especially

when zooming into and out of signal structures. Unlike in Fourier analysis, the filters used are well localised in time / space. It is therefore possible to use the Wavelet Transform to measure Lipschitz exponents over both intervals and points (Mallat, 2001).

Figures 5.5a and b show real, Continuous Wavelet Transforms (CWT) of the Vestmanna acoustic impedance log between 50 and 255 m, under two different analysing wavelets. Local maxima correspond to singularities, with small scale (i.e. high spatial frequency) features mapped at the top of the transform and larger scale (low spatial frequency) features mapped at the base. In appearance the transformed data are self-similar, demonstrating that the log data are self-similar in the spatial domain. The modulus maxima of the transforms are chained in order to avoid the inclusion of spurious structures (Bacry *et al.*, 1993). In the example of Figure 5.5c, small and large scale features are seen to be contiguous with one another, a key characteristic of multi-scale data.

5.5

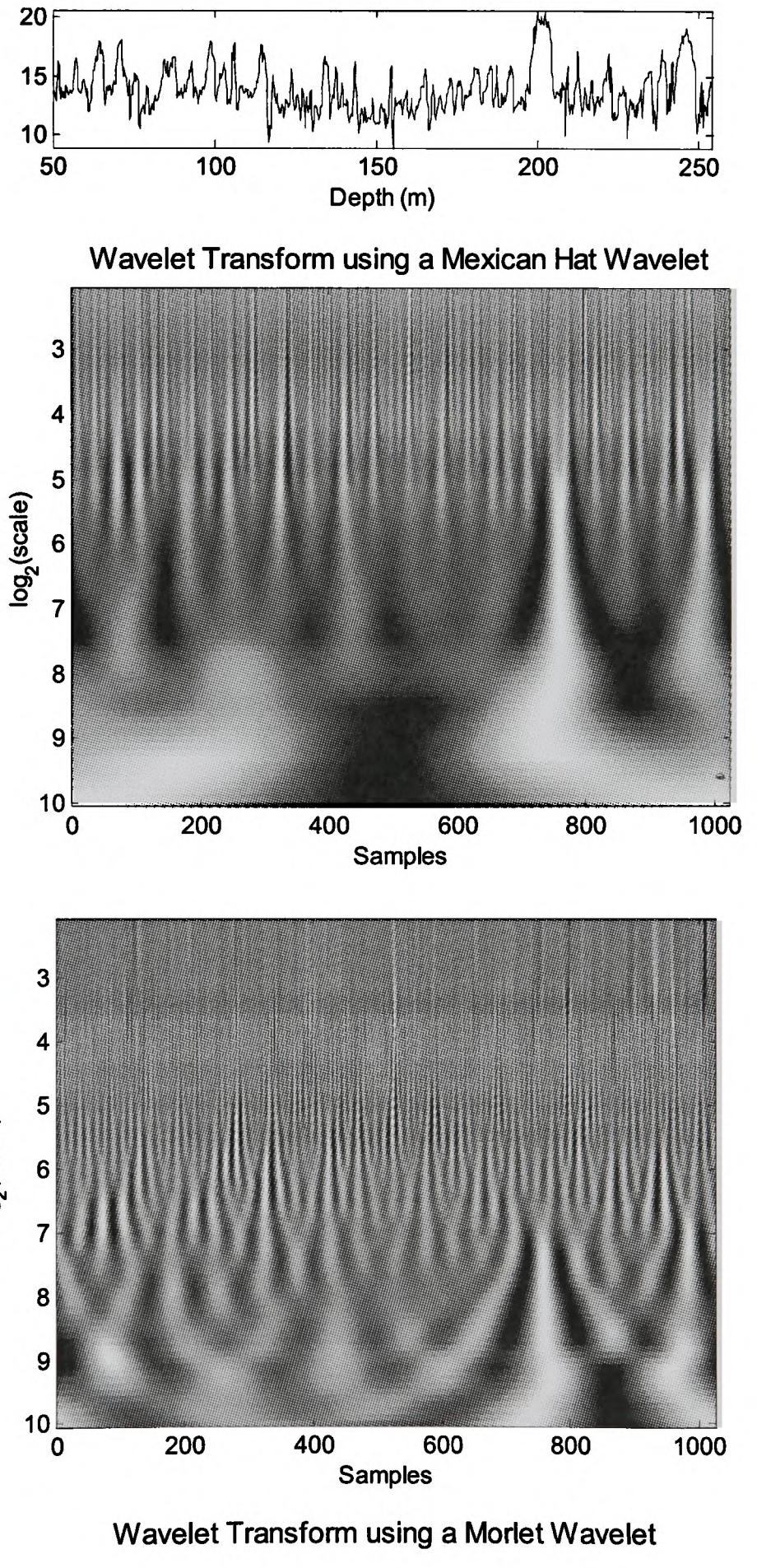

Figure 5.5.
a. Vestmanna acoustic impedance log (50 – 255 m) with its continuous Wavelet Transform using the Mexican Hat wavelet.
b. The Continuous Wavelet Transform of the same data as above, using a Morlet wavelet.

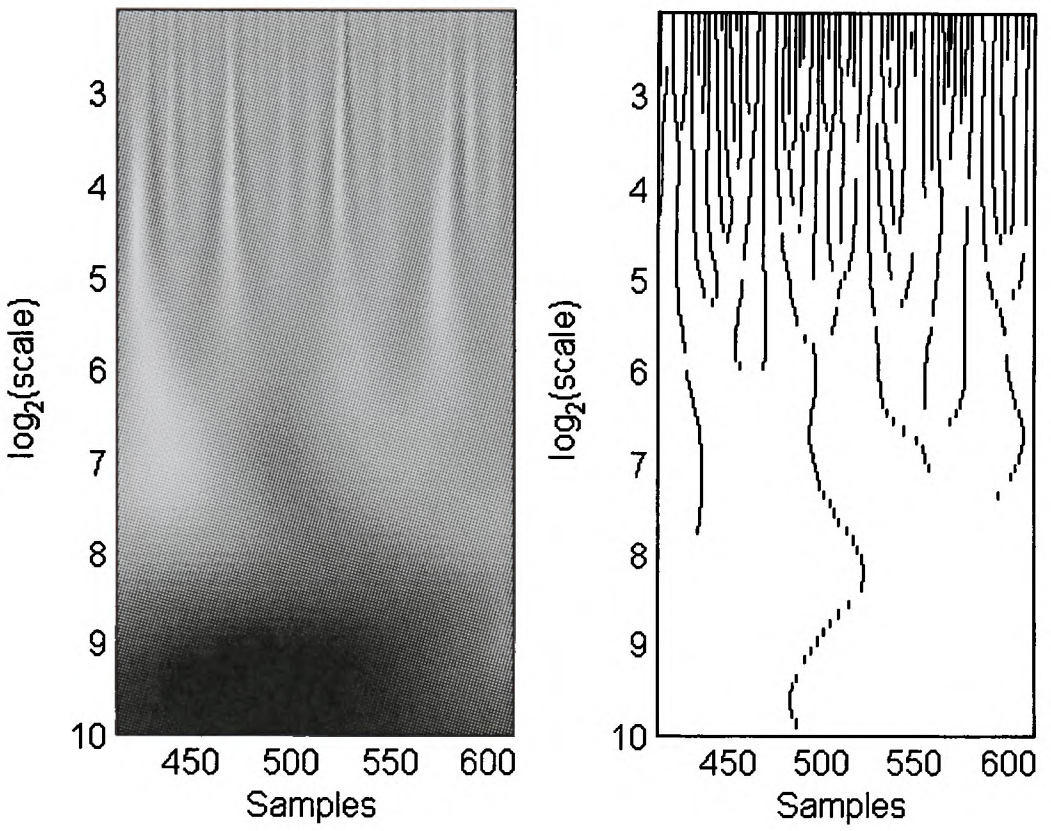

c

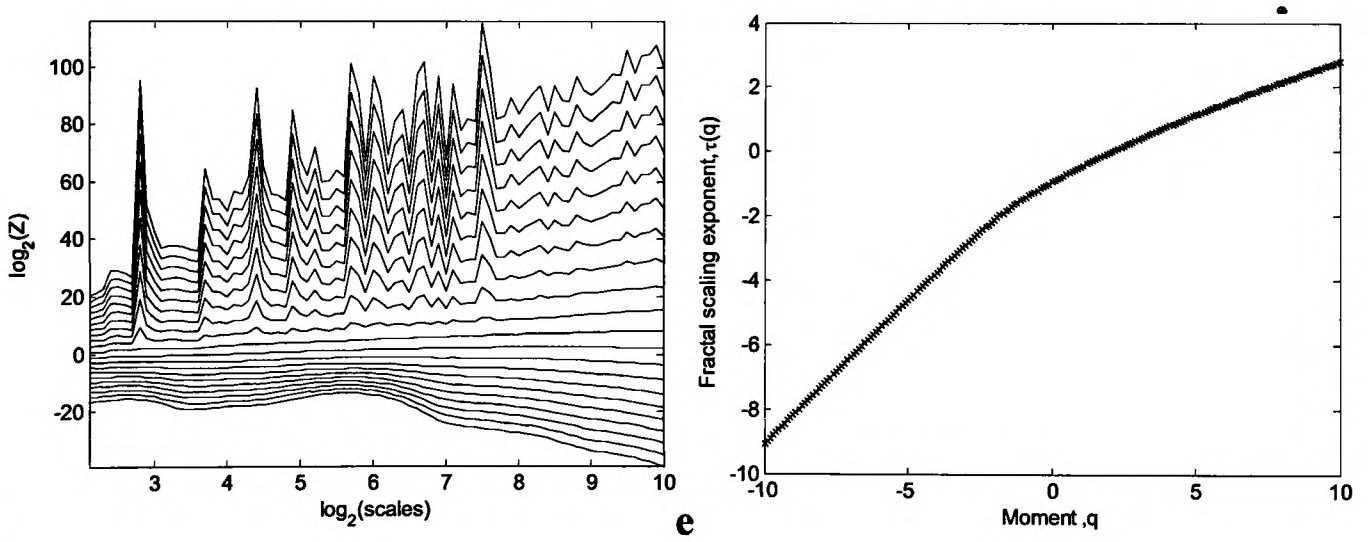

d e

Figure 5.5 cont'd.

c. Detail of the Wavelet Transform and its corresponding modulus maxima or 'skeleton'. Energy occurs at a continuum of scales.
d. Log fractal partition functions vs log scales.
e. The fractal scaling exponent τ(q) as a function of moment, q.

The chained modulus maxima are spatially averaged to produce a fractal partition function for each moment, q (Figure 5.5d). As in monofractal analysis, linear trends in these functions are indicative of power-law dependence. Linear regression is then performed, which suppresses any instabilities arising from log processing artefacts (inflexions seen in Figure 5.5d). The gradients of the trend lines are used to derive a mass exponent, $\tau(q)$ (Figure 5.5e), which is then converted to the singularity spectrum, $f(\alpha)$, by a Legendre transform (Halsey *et al.*, 1986; Mandelbrot, 1989)

The singularity spectrum describes the complexity of the borehole data in several important ways. Firstly, it gives the proportion of α singularities that appear at any scale. In truly monofractal data all singularities would have the same α value, whereas a multifractal signal has a distribution of different singularity styles, and hence a convex singularity spectrum. Figure 5.6 relates the mass exponents $\tau(q)$ to the shape of the singularity spectrum of a theoretical multifractal (after Mandelbrot, 1989). The intensity and intermittency of the signal can thus be quantified.

Routines based on the WTMM technique have been incorporated into Stanford's freeware program WAVELAB, which has been used extensively in the analyses of the Faroes datasets.

5.2.2 CHOICE OF THE ANALYSING WAVELET

As opposed to a complex analytic wavelet (such as described in section 3.3.1), real wavelets are used for detecting sharp signal transitions (Mallat, 2001) and have been implemented in the WTMM algorithm. The wavelet's number of vanishing moments is related to its rate of decay and thus its differentiability. In theory, the analysing wavelet must have at least as many vanishing moments and the same differentiability as the signal under study (Herrmann, 1998). In practice, the analysing wavelet must be able to resolve fluctuations down to the smallest scale, a property which can be checked in the Wavelet Transform space. A range of different wavelet types was tested against this criterion and the Morlet and 'Mexican Hat' wavelets subsequently used.

The real Morlet wavelet is a sinusoid modulated by a Gaussian envelope, and was implemented in the form:

$$\hat{\psi}(\omega) = \frac{1}{\sqrt{s}}\left[\exp\left(-\frac{(\omega-\omega_0)^2}{2}\right) - \exp\left(-\frac{\left(\omega^2+\omega_0{}^2\right)}{2}\right)\right] \qquad \textbf{(5.7)}$$

The Mexican Hat is the second derivative of a Gaussian wavelet and was implemented in the form:

$$\hat{\psi}(\omega) = \frac{1}{\sqrt{s}}\left(\omega^2\right)\exp\left(-\frac{\omega^2}{2}\right) \qquad \textbf{(5.8)}$$

where s is the wavelet scale and ω the frequency. The Morlet wavelet has better frequency localisation, while the Mexican Hat wavelet has better localisation properties in time or space (Torrence & Compo, 1998).

Figures 5.5a and b illustrate the differences between the two Wavelet Transforms. Both analysing wavelets capture details at the finest scale. At intermediate scales, the Mexican Hat wavelet senses the structures more efficiently due to its quicker time decay (e.g. the high amplitude event at ~ 200 m). The Morlet wavelet, which has more peaks and troughs, clouds the transform with extraneous maxima which may adversely affect interpretation. When deriving the fractal partition functions, inflexions are seen at scales corresponding to where the scales interfere (Figure 5.5c). However, taking the gradients of the partition functions suppresses the instabilities, and the resulting singularity spectra are not affected.

5.2.3 RESULTS

The singularity spectra for acoustic impedance logs of the six borehole intervals are shown in Figure 5.7. All six have convex spectra. This indicates that there is a range of intermittent behaviour within each dataset, and therefore that each dataset is multifractal. The lower Lopra interval produces the narrowest spectrum of the six. This corresponds with the comparatively simple fluctuation style seen in the log data (Figure 5.3a).

a

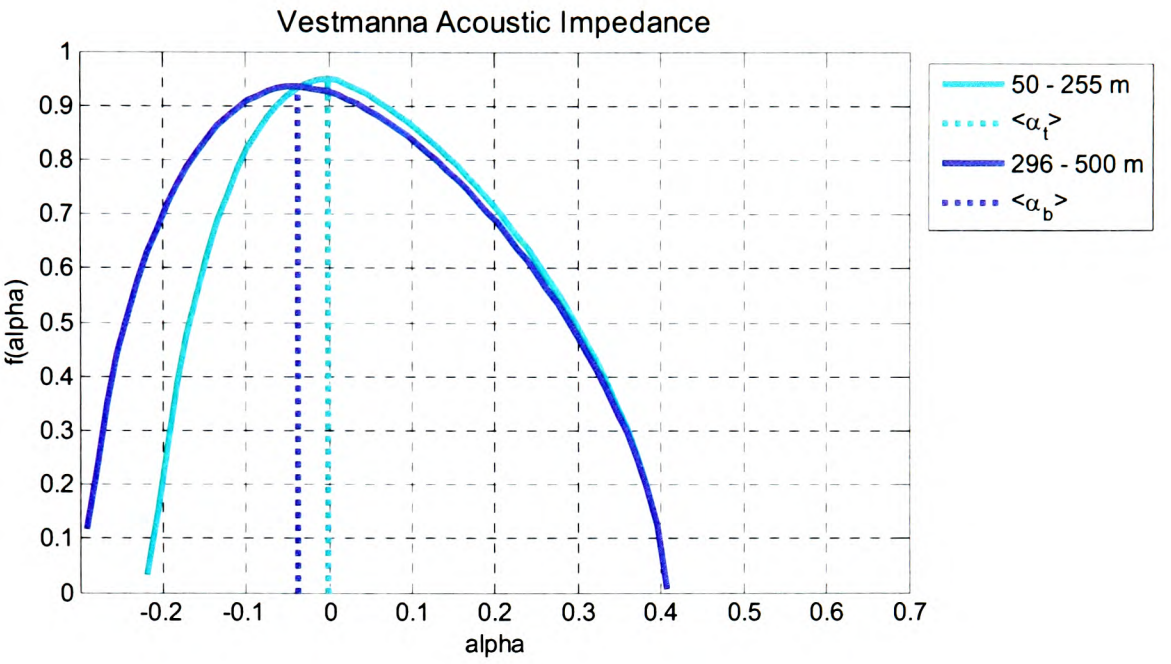

b

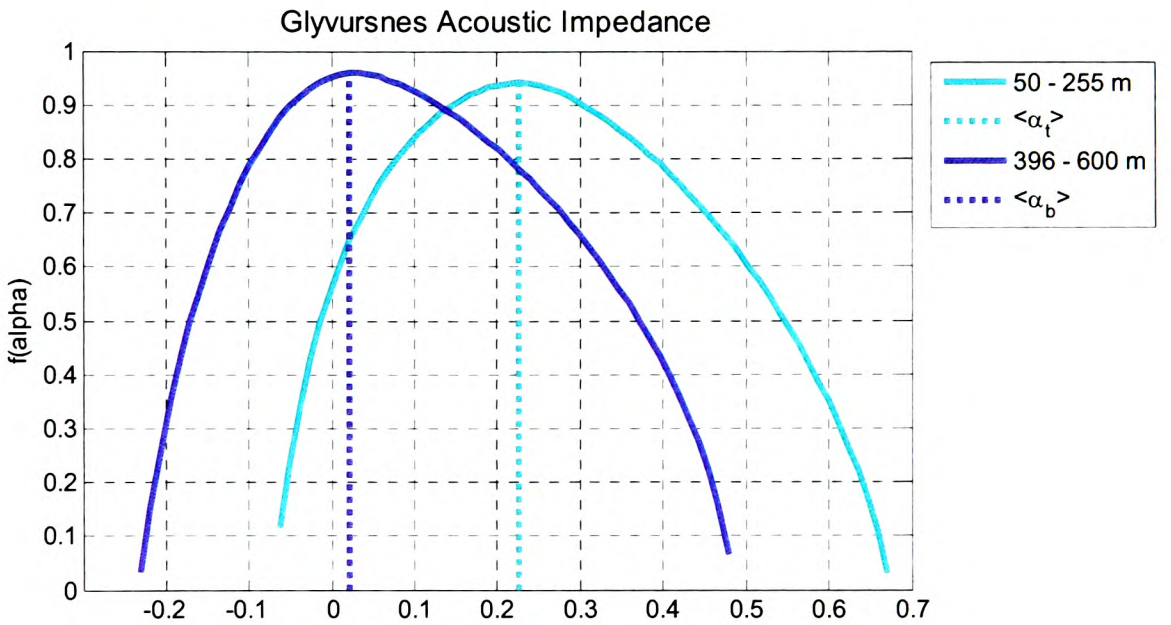

c

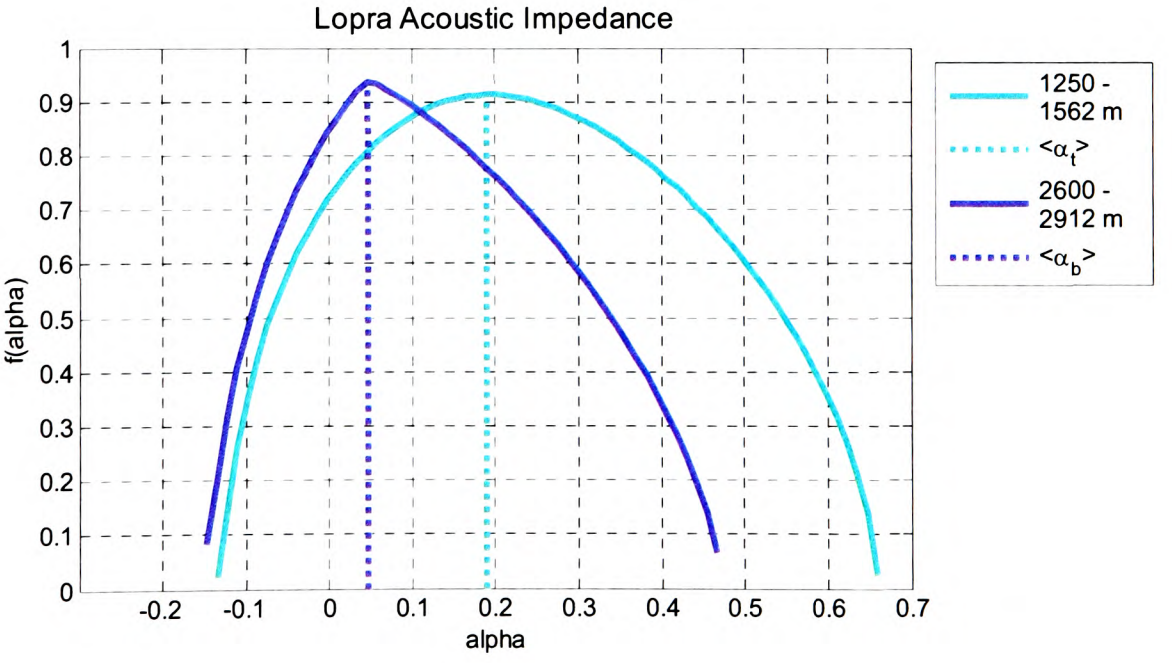

Figure 5.7. Experimental singularity spectra, derived from the WTMM method, of acoustic impedance logs from three Faroes boreholes. a. Vestmanna. b. Glyvursnes. c. Lopra.

Table 5.3 summarises findings from the sixteen datasets analysed. For easy interpretation, minimum α, maximum α and $< \alpha >$ values of the spectra are plotted in three-dimensional space. Results from the Mexican Hat analyses are shown in Figure 5.8a, and results from the Morlet analyses in Figure 5.8b.

Table 5.3

Borehole Interval		Lipschitz / Hölder Exponents		
		α min	$< \alpha >$	α max
Vestmanna 50 – 255 m	AI	-0.23	0	0.41
	V_s	-0.24	0.02	0.47
	Φ_n	-0.18	0.02	0.45
Vestmanna 296 – 500 m	AI	-0.3	-0.04	0.41
	V_s	-0.39	-0.09	0.42
	Φ_n	-0.37	-0.16	0.29
Glyvursnes 50 – 255 m	AI	-0.07	0.23	0.67
	V_s	-0.09	0.21	0.88
	Φ_n	-0.11	0.31	0.89
Glyvursnes 396 – 600 m	AI	-0.24	0.02	0.58
	V_s	-0.18	0.08	0.48
	Φ_n	-0.33	0	0.42
Lopra 1250 – 1562 m	AI	-0.14	0.19	0.66
	V_s	-0.1	0.24	0.68
Lopra 2600 – 2912 m	AI	-0.15	0.05	0.47
	V_s	-0.13	0.08	0.53

Table 5.3. Alpha values for singularity spectra derived from WTMM analysis using the Mexican Hat wavelet.

AI = acoustic impedance
V_s = S-velocity
Φ_n = neutron porosity

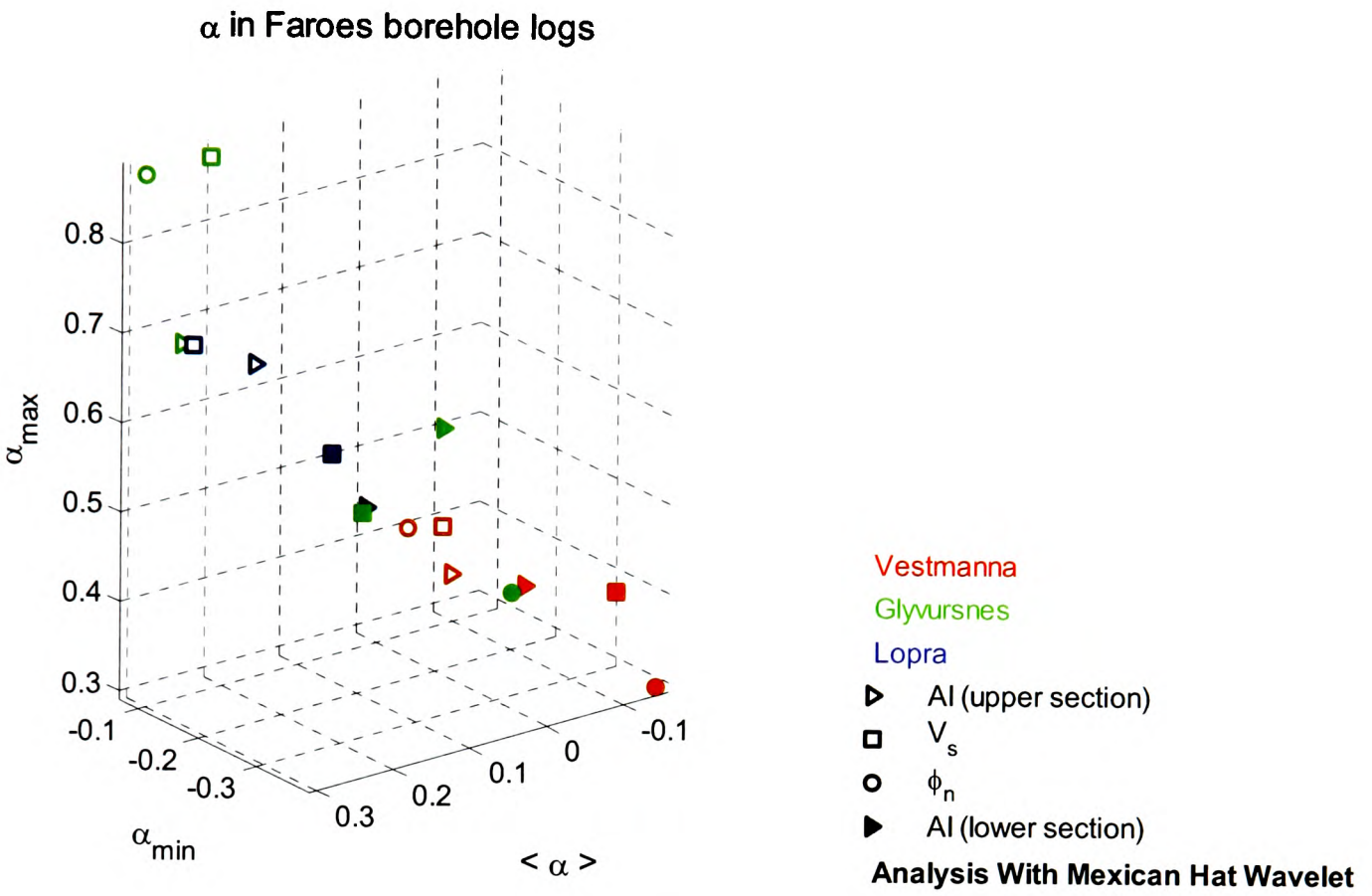

a

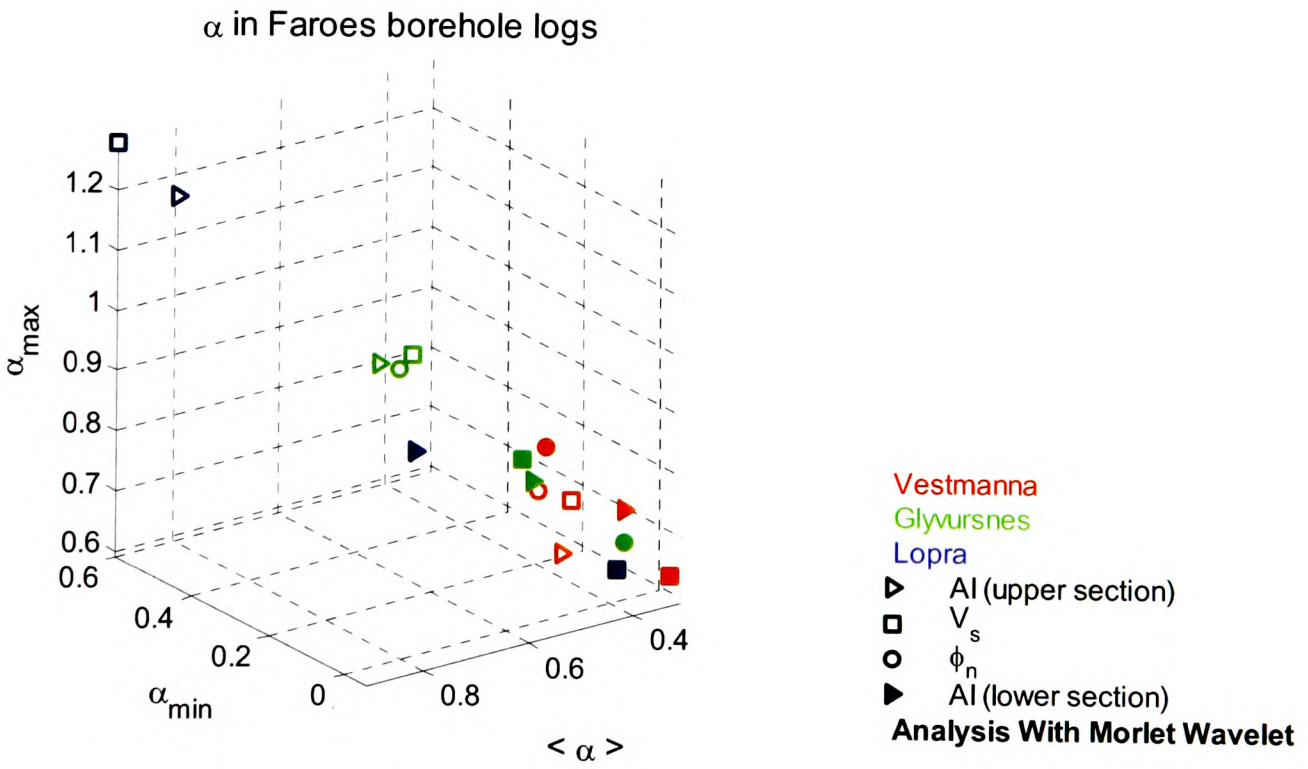

b

Figure 5.8.
a. α exponents of acoustic impedance, S-velocity and neutron porosity logs from the Faroes boreholes. The analyses used a Mexican Hat wavelet.
b. α exponents of the same Faroes borehole logs using a Morlet wavelet in analyses.

As shown in section 5.2.2, the Mexican Hat analyses contained fewer artefacts or extraneous maxima, and were judged to be more reliable than the Morlet wavelet analyses. In Figure 5.8a, α values from the Vestmanna and Lopra boreholes are seen to cluster separately, with further differentiation between their respective upper and lower depth intervals. The Glyvursnes α values, interestingly, show the largest range in their singularity spectra. The 396 – 600 m data plot diffusely in a region spanning the Lopra and Vestmanna clusters, while the 50 – 255 m data have distinctly larger α values than the other five depth sections.

In Figure 5.8b, α values from the upper and lower Vestmanna sections once again display the greatest affinity, and α values from the lower Glyvursnes section overlap with the Vestmanna cluster. α values from the upper Glyvursnes interval are again distinct from other datasets. The main deviation of the Morlet analyses from the Mexican Hat analyses comes from the behaviour of the Lopra logs.

5.3 RELATIONSHIP BETWEEN 1-D SCATTERING ATTENUATION AND MULTIFRACTAL CHARACTER

Using the Wavelet Transform Modulus Maxima method (WTMM), it has been established that the borehole logs of Faroes basalts exhibit a range of multifractal characteristics. A change in multifractal character could be analogous to a real world scenario where the lava emplacement mechanisms are self-similar throughout the

evolution of a volcanic terrane, but deviations in physical attributes such as viscosity and / or lava chemistry alter the extent of self-similarity. A complex pattern of frequency interference arises, which is not adequately modelled as random noise superimposed on low-frequency sinusoids or square-waves. In this section, self-similar methods of model generation are explored, and synthetic seismic responses are analysed.

5.3.1. SYNTHESIS OF MULTIFRACTAL LOGS

Multiplicative cascades are iterative processes that fragment a given set into smaller and smaller sections according to a geometric rule, distributing the total mass of the given set according to another rule (e.g. a random fraction of mass at the previous step). If the redistribution preserves the total mass of the initial set at each stage of the construction, the cascade is 'conservative', and has the same scaling statistics in all directions (Mandelbrot, 1989). Otherwise, the cascade is 'non-conservative'. These terms are related to, but not interchangeable with, 'stationarity' and 'non-stationarity' in geostatistics.

Conservative multifractals can be created by the inverse Fourier transform of a random signal (Mandelbrot, 1987), or by the inverse Wavelet Transform of a random distribution (Arnéodo, 1993). The observations in section 5.2 suggest that the Faroes logs do not have the same scaling statistics in all dimensions, i.e. 'self-affine' rather than strictly self-similar. Other studies of crustal heterogeneity have also concluded that log

data are self-affine rather than self-similar (Marsan & Bean, 2002). Hence conservative multifractals are not an ideal representation.

Non-conservative multifractals can be created by modifying the statistical measures of a conservative multifractal, using schemes such as fractional integration (Schertzer & Lovejoy, 1987), the multifractal operational time method (Mandelbrot, 1997), and hybrid two-step integration (Marsan & Bean, 2002). These three methods have been adapted for Matlab® by Marsan & Bean (2002).

In preliminary tests, the two-step integration method did not produce multifractals with either the visual characteristics or the statistical behaviour of real Faroes borehole logs. Multifractals generated by the multifractal operational time method only superficially resembled the real data, and when analysed by the WTMM, did not approach the statistics of the real data closely enough.

Schertzer & Lovejoy's fractional integration method produced multifractals that resembled the real data both visually and statistically. The method employs two parameters, C1 and χ, to control the apparent roughness of the signal. C1 adjusts the mass of the measure, and is related to the mass exponent, $\tau(q)$, described in section 5.2.1. As C1 increases, the amplitude of the strongest fluctuations increases, creating 'intermittency'. The χ parameter adjusts the slope of the power relations, and as χ increases, the relative intensity of the fluctuations decreases, producing 'smoothness'. Figure 5.9 displays the change in the shape of the signal as C1 and χ are modified.

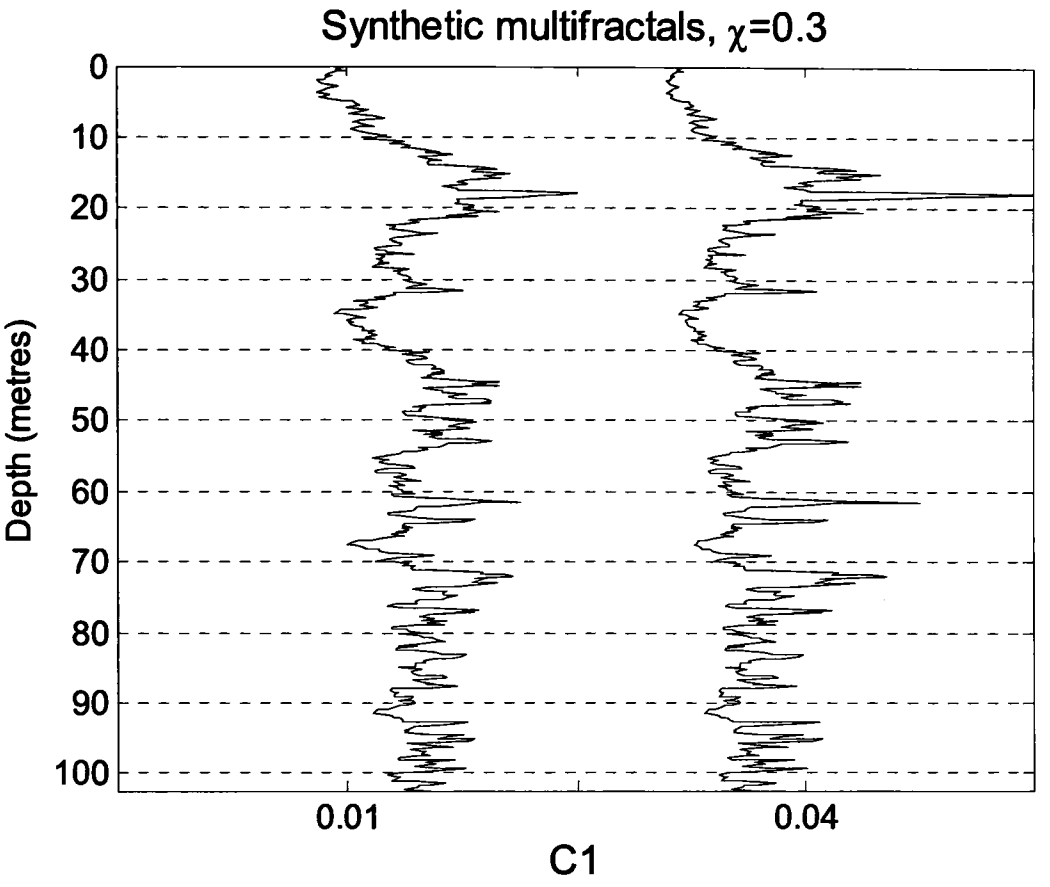

a

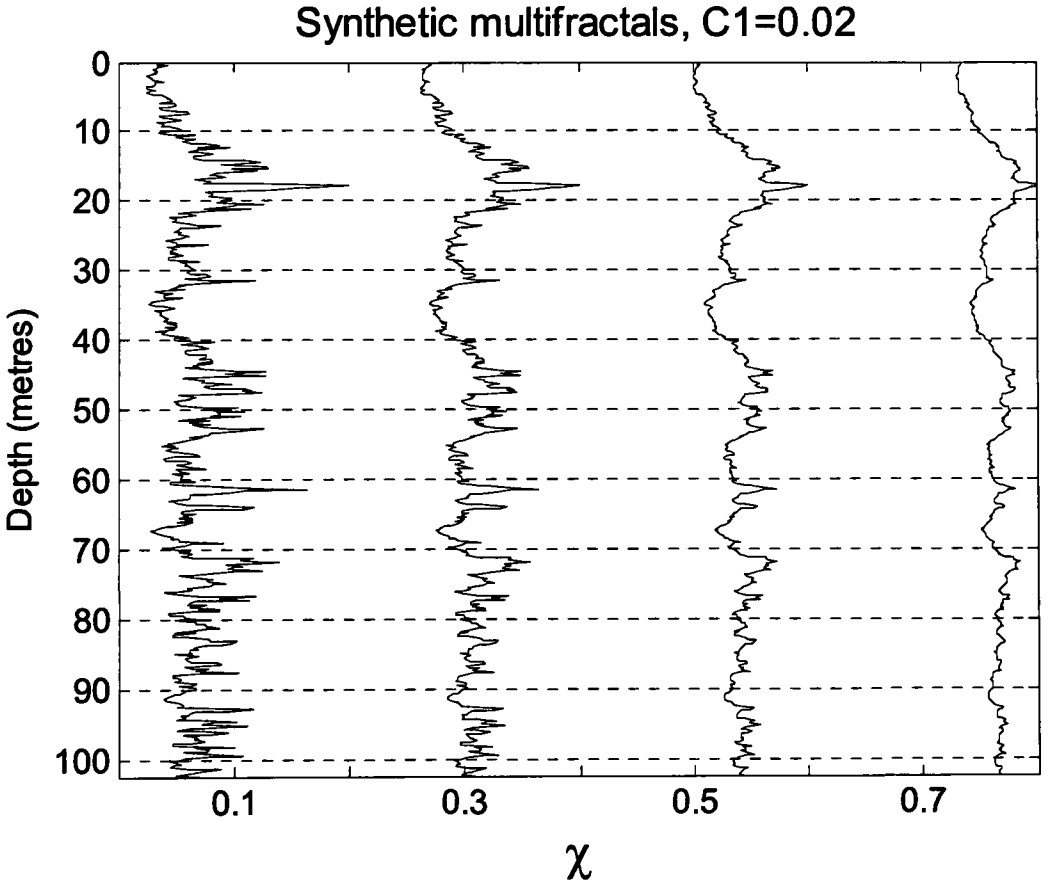

b

Figure 5.9. Normalised synthetic multifractals.
a. Higher C1 values indicate greater intermittency.
b. Lower χ values indicate greater fluctuation.

Fifty-six synthetic logs with C1 values of 0.01 – 0.08 and χ values of 0.1 – 0.7 were generated and analysed via the WTMM method. In Figure 5.10, α exponents of these synthetic logs are presented as a surface, on which the α exponents of the real log data are overlaid. The synthetic log data span the full range of multifractal behaviour exhibited by the Faroes log data.

5.10

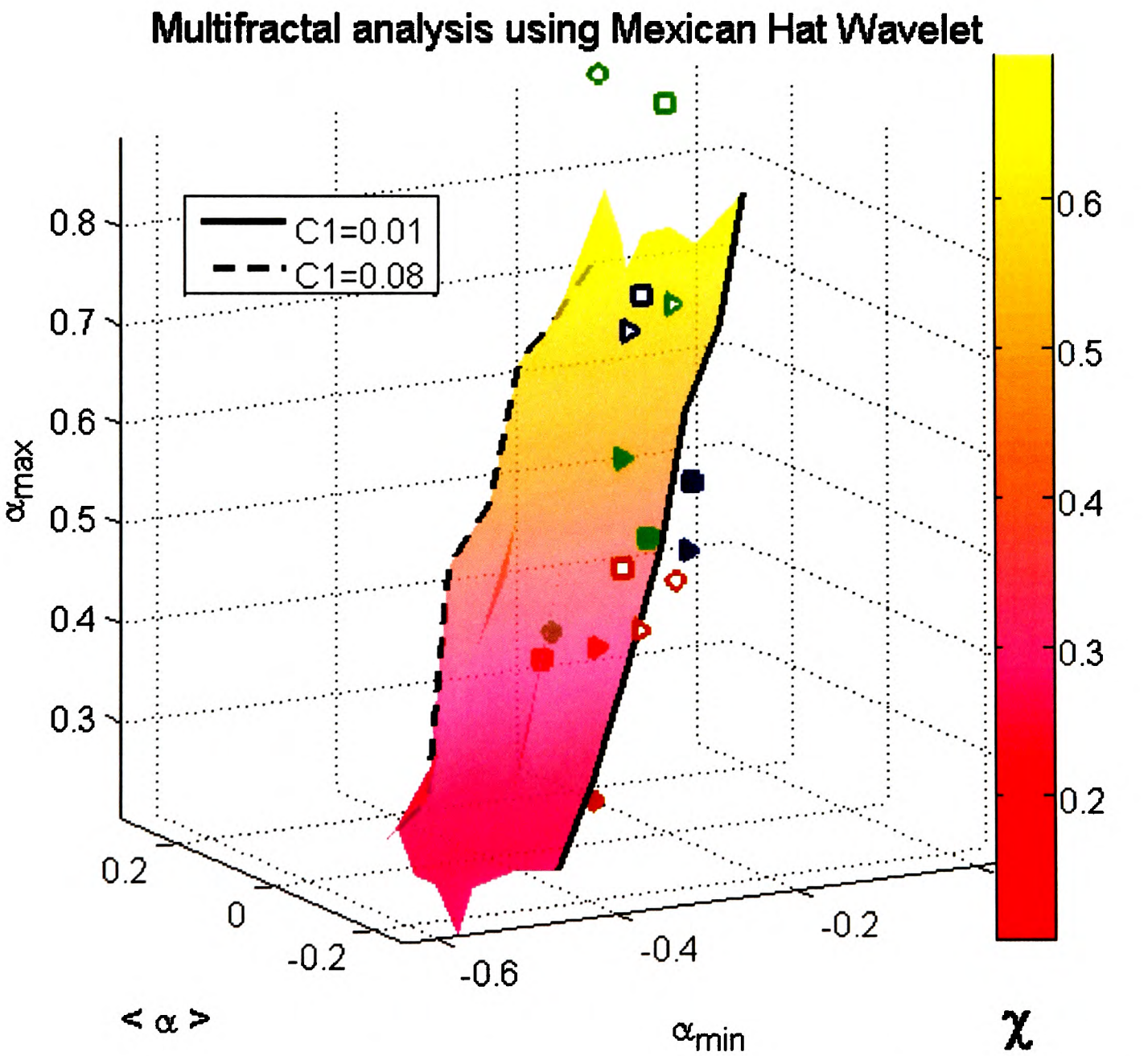

Figure 5.10. Real data points (legend as in Figure 5.8) plotted against the spread of exponents from synthetic multifractals (translucent surface).

5.3.2. SEISMIC RESPONSE OF SYNTHETIC MULTIFRACTAL LOGS

Ten multifractals with the greatest statistical similarity to the real logs were investigated for their seismic response. The multifractals were constructed to the same length as the log intervals analysed (1024 samples). They were then adjusted to the range of P-velocity and density log values in the upper section of Vestmanna (mean velocity 5.1 km/s, mean density 2.7 g/cc). Herrmann (1998) states that such adjustments, effectively the addition of DC components, do not alter the α exponents. This was confirmed by running WTMM analyses on signals normalised to different ranges.

1-D acoustic modelling was then performed using the Kennett algorithm and two synthetic sources: a wavelet with a centre frequency of 150 Hz and a wavelet with broad bandwidth (the modelling scheme is introduced in Chapter 4). 1-D scattering Q estimates, calculated using the spectral ratio method, are listed in Table 5.4.

Table 5.4

Model no.	Statistically closest to:	Parameters		Approx. 1-D Scattering Q	
		C1	χ	800 Hz source	150 Hz source
1	Vestmanna lower porosity	0.01	0.2	296 - 474	170 - 359
2	Vestmanna upper Al, Lopra lower Al	"	0.4	409 - 780	141 - 578
3	Vestmanna lower Al	0.015	0.3	374 - 607	177 - 443
4	Vestmanna upper Vs	"	0.4	442 - 780	161 - 579
5	Vestmanna lower Vs	0.02	0.3	401 - 629	199 - 472
6	Vestmanna upper Vs, Glyvursnes lower Al, Vs	"	0.45	514 - infinity	173 - 727
7	Glyvursnes upper Vs	"	0.6	735 - infinity	164 - infinity
8	Glyvursnes lower porosity	0.04	0.35	510 - 750	260 - 609
9	Lopra upper Al	"	0.6	761 - infinity	211 - 1570
10	Lopra upper Vs, Glyvursnes upper Al	"	0.7	978 - infinity	206 - infinity

Table 5.4. All the datasets above were normalised to the Vestmanna V_p and density logs. The range is given by a 95% confidence interval of the mean response.

For a broadband source with higher frequency content, the roughness of the signal, controlled by χ, has a greater effect on resulting Q values than the intermittency of the signal, controlled by C1. For a 150 Hz source, intermittency appears more significant. However, all the Q estimates are extremely high, notably those designed to resemble the Faroes acoustic impedance logs (Table 5.4, models 2, 3, 6, 9, 10). 1-D scattering Q in the actual upper Glyvursnes interval was estimated to be 28 – 46 with a 150 Hz source (section 4.2 of this thesis), whereas the corresponding multifractal, Model 10, produces Q estimates of between 206 and infinity.

The WT scalogram of Model 10's seismic response is shown in Figure 5.11. The multiples set up weak interference patterns compared to those of the real Glyvursnes data model (Figure 4.10). There are no intense spectral minima and no apparent resonance.

Table 5.5 lists mean values and standard deviation of P-velocity and density for Vestmanna and Glyvursnes data. Model 10 was re-normalised to the upper section Glyvursnes data, which have a larger standard deviation and therefore larger contrasts in velocity and density. The seismic response contained stronger multiple interference, leading to a marginally lower Q value (Figure 5.12).

Earlier, it was stated that the α exponents were unaffected by normalisation to different velocity and density ranges. However, the scattering effect and estimated Q are evidently sensitive to these changes.

Table 5.5

Borehole Interval	Log	Absolute values	
		mean	standard deviation
Vestmanna 50 – 255 m	P-velocity (km/s)	**5.12**	**0.49**
	Density (g/cc)	**2.70**	**0.14**
Vestmanna 296 – 500 m	P-velocity	5.46	0.64
	Density	2.77	0.14
Glyvursnes 50 – 255 m	P-velocity	**4.49**	**0.86**
	Density	**2.74**	**0.18**
Glyvursnes 396 – 600 m	P-velocity	4.26	0.63
	Density	2.63	0.13

Table 5.5. First order statistics seen in Vestmanna and Glyvursnes P-velocity and density logs. Emboldened values are those used in normalising the multifractals for 1-D acoustic modelling.

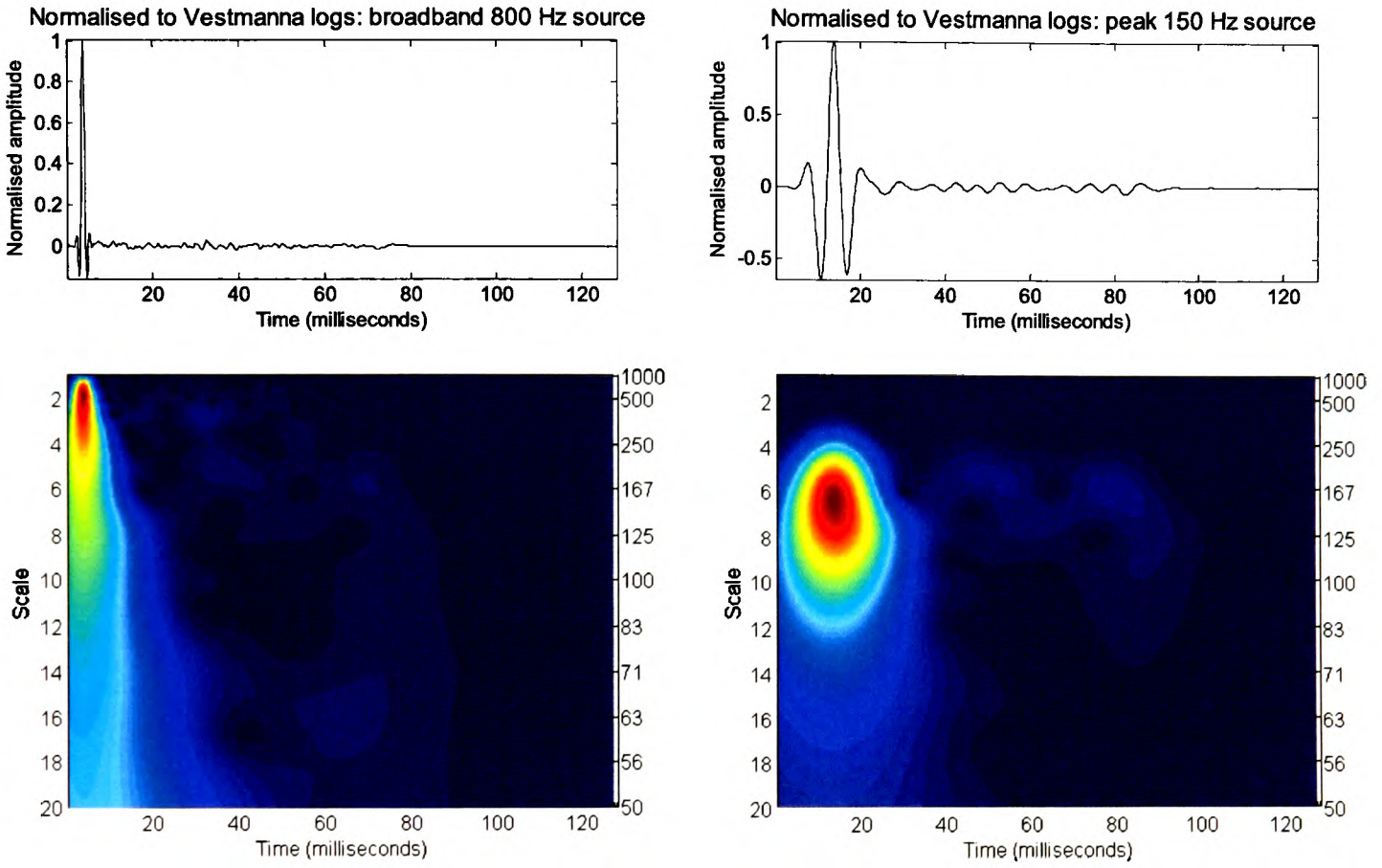

Figure 5.11.
Synthetic seismic responses of multifractal model 10 (see Table 5.4), and corresponding WT scalograms. The full colour scaling covers a linear, normalised amplitude range of 0 - 100%. C1 = 0.04, $\chi = 0.7$. The multifractal was normalised to velocity and density ranges of the upper section of Vestmanna.

Left: The source was a broadband wavelet with frequency content to 800 Hz. Q range ~ 978 - infinity.

Right: The source was a wavelet with peak frequency of 150 Hz. Q range ~ 206 - infinity.

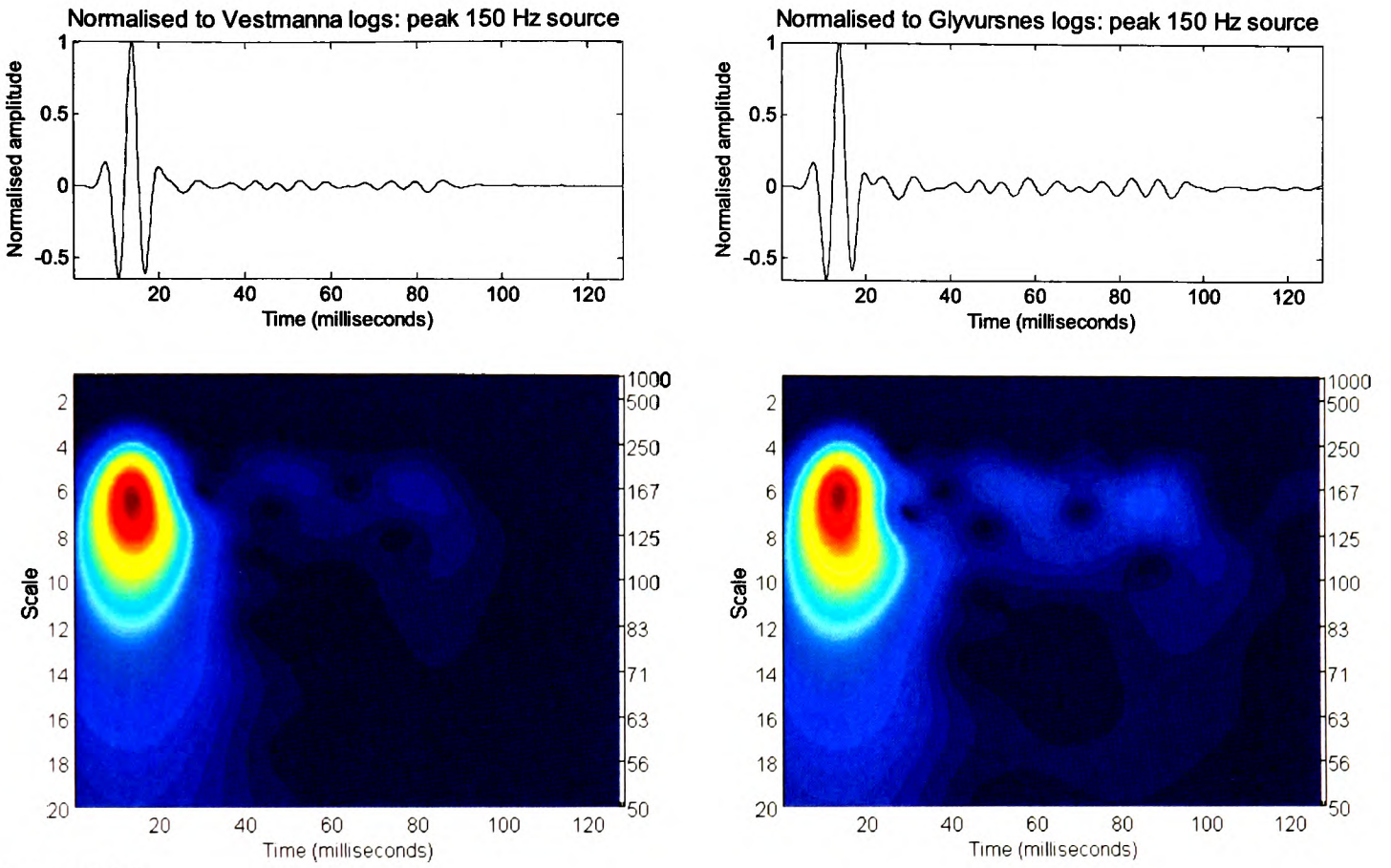

Figure 5.12.
Synthetic seismic responses of multifractal model 10 (see Table 5.4 and Figure 5.11), with corresponding WT scalograms. The full colour scaling covers a linear, normalised amplitude range of 0 - 100%.

Left: The model was normalised to velocity and density ranges of the upper section of Vestmanna. Q range ~ 206 - infinity.

Right: The model was normalised to velocity and density ranges of the upper section of Glyvursnes. While the multifractal statistics are the same, interference from multiples is stronger. Q range ~ 87 - infinity.

The source was a wavelet with peak frequency of 150 Hz.

5.4 DISCUSSION

The Faroes borehole logs are multifractal signals. It is possible to characterise the degree of multifractal behaviour in detail, using the Wavelet Transform Modulus Maxima method of deriving singularity spectra / α exponents. Basalt formations cannot be differentiated from the range of absolute values in log data (i.e. first-order statistics), nor from the autocorrelation of log data (i.e. second-order and monofractal statistics). However, they can be distinguished by their styles of fluctuation, and multifractal statistics could offer powerful support to geological interpretation in basaltic rocks.

One hypothesis is that crustal rocks of widely-differing geological history exhibit similar fractal behaviour due to the distribution of cracks. These cracks would be (mono)fractally distributed and insensitive to petrology (Holliger, 1996). While this study does not contradict this hypothesis, it is likely that here, monofractals are simply a truncated expression of multifractals, which are themselves limited statistical descriptions of basalt characteristics.

In Chapter 4, the strongest 1-D scattering over a bandwidth of 50 – 250 Hz was observed in the upper Glyvursnes log section. This was found to relate to velocity macro-structure controlled by geological factors. Synthetic logs with multifractal statistics similar to the upper Glyvursnes data did not exhibit the same intensity of 1-D scattering. Rather than the multifractal character of the dataset, velocity and density contrasts were again found to have a significant effect on the generation of multiples.

This leads to two conclusions. First, synthetic multifractal logs must be used with caution in modelling studies. Despite superficial similarities, they cannot be assumed to produce the same seismic response as real logs. Second, multifractal character in itself does not generate significant amounts of 1-D scattering.

As demonstrated by Figure 4.14, in section 4.4 it was shown that models with a simple periodic velocity structure produced multiples of a dominant frequency. These set up resonant effects in their seismic responses, which result in frequency-dependent, localised attenuation. The deep spectral minimum in the sensing bandwidth, by extension, was responsible for low Q estimates. In a multifractal model, the distribution of velocity structures over a range of scales is likely to disrupt this resonance. The potential for interference of multiples is reduced, and consequently the scattering attenuation is reduced.

The observations in Chapters 4 and 5 have been made for horizontally planar media. However, there are certain implications for 2-D and 3-D basalt models, which form the basis of the following chapter.

CHAPTER 6

SEISMIC RESPONSE OF 3-D BASALT MODELS

Studies in the Neogene Columbia River Basalts (Reidel & Hooper, 1989), the Entendeka Basalts (Jerram *et al.*, 1999), and the Palaeogene Skye Lava Field (Single *et al.*, 2004) have revealed the complex architecture of flood basalt provinces. Lateral variation is present over a range of spatial scales, and further heterogeneity is created by intrusive bodies (dykes, sills) imprinting or cross-cutting older stratigraphy.

This high degree of heterogeneity has led to 3-D scattering being cited as an important attenuation mechanism (Martini *et al.*, 2002; Ziolkowski *et al.*, 2003). 3-D scattering in basalts has been widely discussed, and the need for dedicated geological models is recognised by various workers (Self *et al.*, 1997; Jerram, 2002; Martini *et al.*, 2005). A key issue is whether the intra-flow region of basalt produces an averaged seismic response, behaving as a transversely isotropic medium (Liu *et al.*, 2000; Christie *et al.*, 2002), and to what extent the precise architecture can be replaced with a general attenuating coefficient.

In preceding chapters of this thesis, the attenuation predicted from 1-D scattering was insufficient to account for low Q values of Middle Basalt Series. However, scattered energy was observed in time-frequency analyses of VSP traces, in the form of spectral interference patterns. These patterns differed from those of 1-D synthetic seismograms, and may have been generated by 3-D structures.

This chapter examines plausible basalt structures on the Faroe Islands, particularly in the Vestmanna field area. Models incorporating flow architecture are constructed, to spatial dimensions compatible with the actual field VSP survey. Observations made in the 1-D scattering experiments (Chapters 4, 5) are reviewed and extended to the 3-D scenario.

6.1 BASALT ARCHITECTURE AND EMPLACEMENT

In this chapter, the terms 'core' and 'crust' generally refer to the components of a basalt flow unit, as defined in Figure 6.1 (Self *et al.*, 1998; Andersen *et al.*, 2005). The core typically consists of massive basalt with few or no vesicles and sometimes displays flow banding. The crusts of lava flows are commonly jointed and highly vesicular. Flow unit cores are not to be confused with 'borehole core(s)' in section 6.2.2, which refer to the cylindrical rock samples extracted from drilling.

6.1.1 MODERN BASALTS – HAWAII

Much current knowledge of lava emplacement has come from observing modern terranes such as Hawaii, where the stages of buildup can be seen in real time (Self *et al.*, 1998).

Hawaiian lavas erupt primarily as pahoehoe, a basaltic lava flow typified by a smooth, wavy, or ropy surface and a glassy outer skin. In contrast, the other major classification of lava, aa, has a rough, rubbly surface composed of broken lava blocks. The critical factors controlling formation of aa and pahoehoe are viscosity and the amount of internal shear. A pahoehoe flow reaches a critical threshold to become aa when the lava is highly viscous, but continues deforming due to changes in flow rate, flow dimension, slope and momentum (Peterson & Tilling, 1980).

Self *et al.* (1998) have studied the emplacement mechanisms of pahoehoe, and have shown that more continuous effusion, lower slopes, and smoother topography have the same effect as increasing effusion rate. If effusion rates are very low, the lava freezes quickly to form a stack of small lobes. At medium effusivity, inflation and crust growth proceed at similar rates. Inflation is confined to discrete tumuli, and the flow advances via smaller breakouts. At high effusion rates, the flow inflates evenly, forming a flat sheet. The sheet may become hummocky if the effusion rate decreases thereafter, but breakouts of lava can occur from any weak region of the crust. With time, the flows build up a field of tumuli and breakouts of various ages, and the path the lava must

travel to the flow front is tortuous. At outcrop, this may manifest as horizontal inflation clefts or large monoclinal folds on the margins of thick sheets.

Fresh pahoehoe flows are typically only 20 – 50 cm thick and can be initially diverted around earlier inflated flows. For the largest flows, there is time for some erosion or sediment deposition to occur before new lava is able to completely 'overtop' the older flow. A key characteristic of pahoehoe flows is that during inflation, the surface topography often becomes inverted; former topographic highs become pits while low areas become tumuli (Figure 6.2, after Self *et al.*, 1998). Pahoehoe crusts are also associated with vesicles (Figure 6.1). These impart lower velocity and density values, amongst other petrophysical characteristics (Cerney & Carlson, 1999).

Chemical changes occur during long-lived eruptions, which increase the difficulty of mapping individual lobes, flows, and / or flow fields.

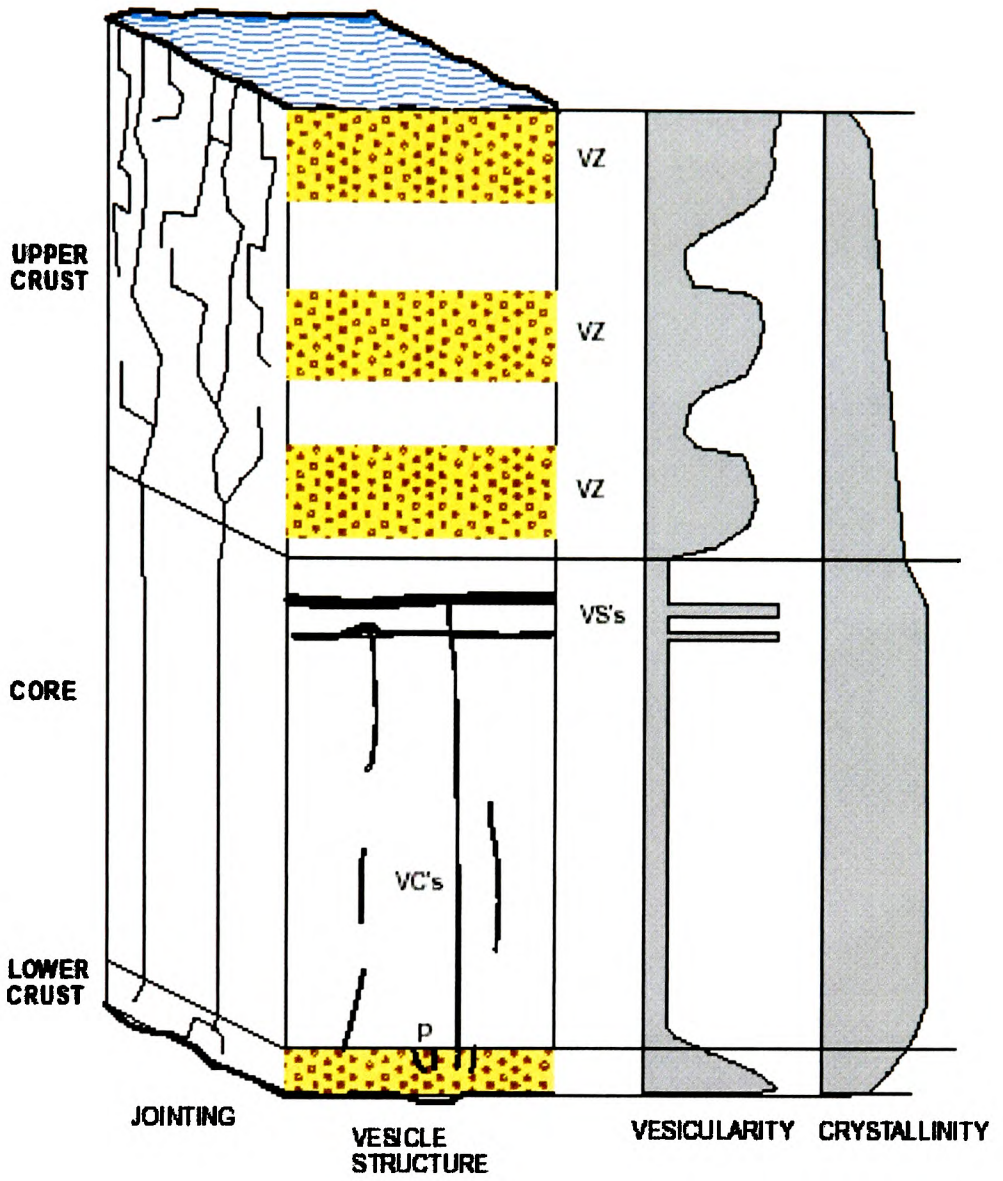

Figure 6.1.

Idealised cartoon of the cross-section through an inflated pahoehoe lobe, from Self *et al.* (1998). The lobe is divided into three sections on the basis of vesicle structures, jointing, and crystal texture.

Upper crust: Vesicular, often with discrete horizontal vesicular zones (VZs) that form during active inflation. Bubble size increases with depth. Prismatic or irregular jointing occurs, sometimes equivalent to the entablature in thick lava flows. Petrographic texture ranges from hypohyaline to hypocrystalline (90–10% glass).

Core: Very few vesicles. Porosity is dominated by diktytaxitic voids. Vesicles are mostly in the silicic residuum, which forms vesicle cylinders (VCs) and vesicle sheets (VSs). Holocrystalline (<10% glass).

Lower crust: Nearly as vesicular as the upper crust, few joints, and 50–90% glass.

This architecture has been observed at smaller scales in Hawaii and Iceland, and on a much larger scale in the Columbia River Basalts (Self *et al.*, 1998).

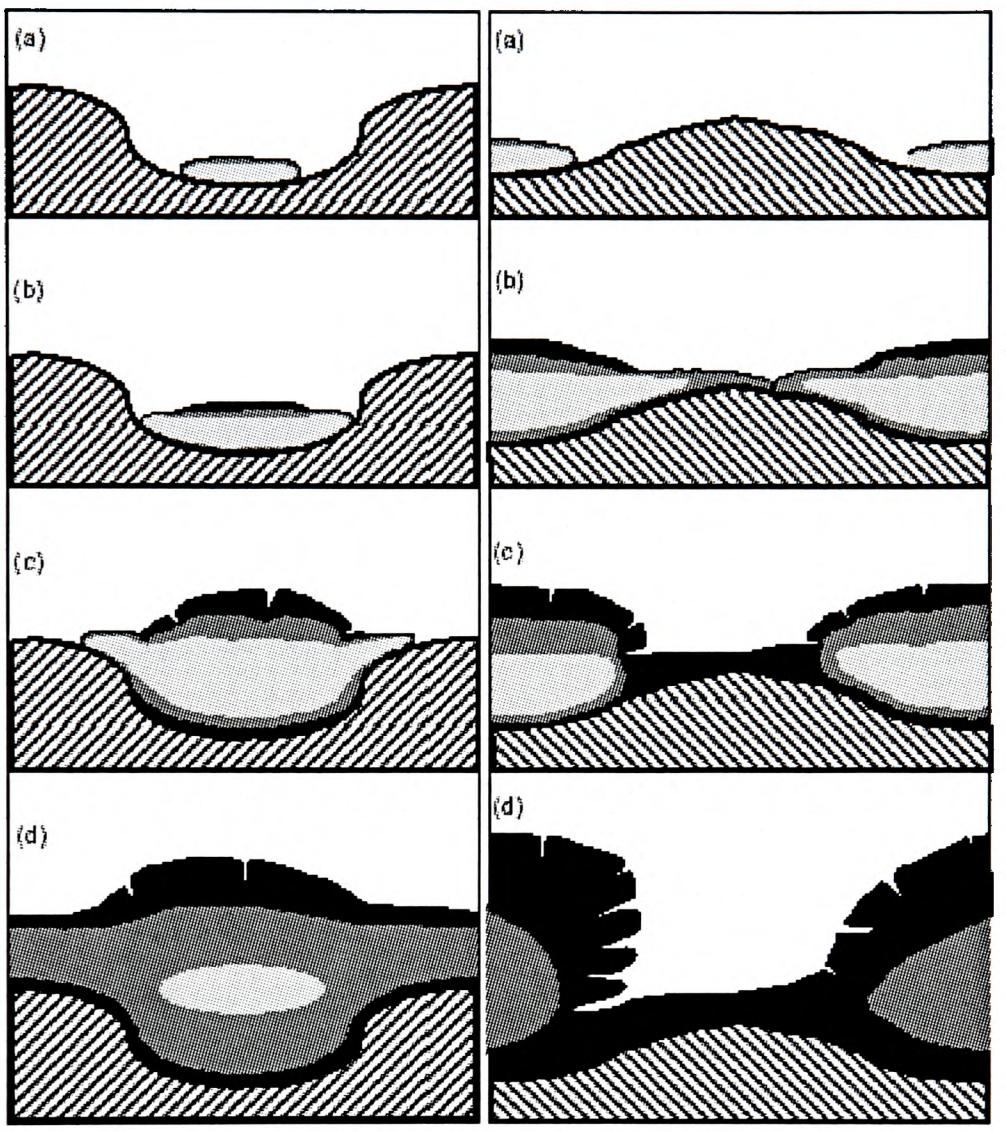

Figure 6.2.

Cartoon cross-sections of the formation of tumuli and inflation pits and the inversion of topography during inflation, from Self *et al.* (1998).

a. Initially, small pahoehoe lobes are confined to the lowest areas.
b, c. As the flows continue to advance, they also inflate and spread laterally, filling the depressions. Because the thickest crust is on the oldest part of the sheet, the highest inflation is over what was originally the lowest ground. Breakouts from the thick inflation features can eventually cover the earlier high ground.
d. Depending on the rate of inflation relative to the rate of crust growth, either a continuous sheet (left) or an inflation pit (right) forms over the previous high points. Most inflation pits widen with depth as the lobe cools inward with time. Inflation pits at the margins of sheet lobes may have steep monoclinal folds.

6.1.2 ANCIENT FLOOD BASALTS

The major difference between ancient flood basalts and modern basalts is the scale and duration of activity (Jerram, 2002). Features seen in the Hawaiian basalts appear to be scaled up in the Columbia River Basalt Group (Self *et al.*, 1997). Other Continental Flood Basalts (CFBs) such as the Deccan Traps, Karoo Basalts and the North Atlantic Igneous Province (NAIP, of which the Faroes are part) appear to be a mixture of different scales of volcanic event. CFBs are interpreted to occur over < 1 million years, originating from both fissure and centre-fed eruptions (Jerram, 2002).

Continental flood basalts and associated rifted volcanic margins are characterised by varying flow thicknesses of 2 – 3 m to several tens of metres, with occasional events generating layers of ~100 m. Planke (2000) uses volcanic sequence stratigraphy (analogous to sedimentary sequence stratigraphy) as a means of describing basalt architecture in seismic sections. Distinctive morphologies created in the buildup of a sequence are interpreted as cyclic flow units. In a typical unit, such as from the Vøring Plateau, Planke observes that P-velocity increases gradually from the top of a basalt flow unit to its interior, corresponding to a decrease in the number of cracks and voids. The interior is treated as homogeneous and high velocity (5 – 6 km/s), decreasing rapidly at the base. Units are assumed to have thin-layer transverse isotropic properties, and to be laterally continuous over hundreds of metres. The smallest sequence components are on the order of kilometres, and the width of the entire volcanic margin is approximately 60 km.

However, detailed geological mapping shows that lateral continuity does not persist at intra-facies scale. Lava conduits, volcanic break-outs, injection / loading structures, small lobes, sills and dykes impart high lateral complexity. For each of these features, P-velocity has been found to vary as much as ± 2 km/s. Within each flow, there may be pahoehoe textures with alternating bands of high and low vesiculation, fanned or columnar jointing, rubbly flow tops and high velocity cores (Single *et al.*, 2004).

Jerram (2002) classifies basalt architecture by tiers. Features are first studied at small scales, identified as intra-facies components, and assigned to one of six facies types. Facies are related to each other by one of five facies associations. Using these guidelines, Single *et al.* (2004) found that basalts in the Skye Lava Field were heterogeneous over a range of scales. Components less than a metre in length were embedded in, and continuous with, kilometre-scale features.

6.2 BASALT ARCHITECTURE OBSERVED IN THE FAROE ISLANDS

6.2.1 FIELD OBSERVATIONS

Exposure in the vicinity of the VSP experiments is varied. The Glyvursnes field area contains several clean quarry faces and sea cliffs, whereas the Vestmanna field area is

largely covered by Quaternary soils and by human habitation. However, observations have been made from the closest rock outcrops and across the Faroe Islands.

Two distinct basalt morphological types occur in the Faroe Plateau Lava Group. The first morphological type is a quasi-planar lithology, with flows greater than 5 m in thickness. This is seen both at exposure and suggested by petrophysical log characteristics (Andersen *et al.*, 2005). In the field, such flows between 10 and 30 m thick can be observed around the Glyvursnes locality. These may be akin to '*massive tabular*' flows (Figure 6.3) described from the Entendeka Basalts by Jerram (2002) and to the '*rubbly pahoehoe*' of the Deccan Basalts, described by Bondre *et al.* (2004). Passey (2005) reported that structures seen in the quarry north of the VSP area (Figure 6.4) appear to be inflation features as described by Self *et al.* (1998).

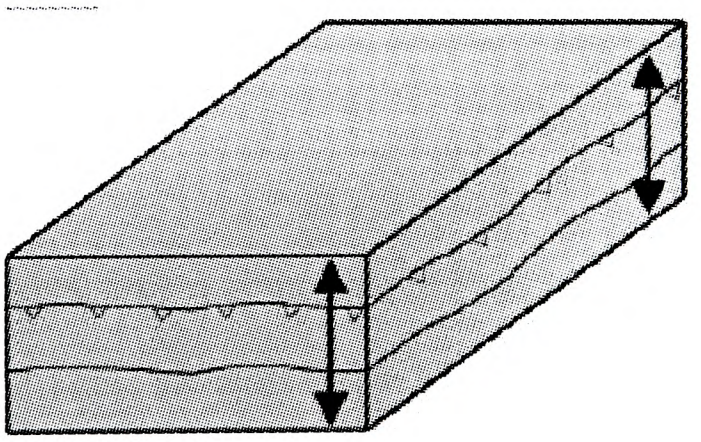

Figure 6.3. Massive tabular flow (from Single *et al.*, 2004).



Figure 6.4. Possible pahoehoe inflation structure, old quarry above Glyvursnes. Fence posts are 1.5 metres high.

The second morphological type is composed of hummocky flows of between 1 and 5 m in thickness. These are akin to *'compound braided'* basalts (Figure 6.5) described by Jerram (2002), and may be tube-fed (Passey in Bondre *et al.*, 2004). In cross-section, they appear as lobes, tens of metres in length, and are thought to be predominant in the Vestmanna locality. The smoother weathering profile of the landscape around Vestmanna has been attributed to the relatively small flow lobes of the Middle Basalt Series. Rasmussen & Noe-Nygaard (1970) have observed that the

Middle Basalt Series contains lava flows or breakouts which are usually under 2 m thick, building up to form small sequences of about 20 m in thickness. Sub-horizontal vesicle sheets, alternating amygdale-rich/poor sheets, lava tongues, lava tubes and ropy lava surfaces are commonly observed in this geological formation, and are all characteristic of pahoehoe (Ellis *et al.*, 2002).

6.5

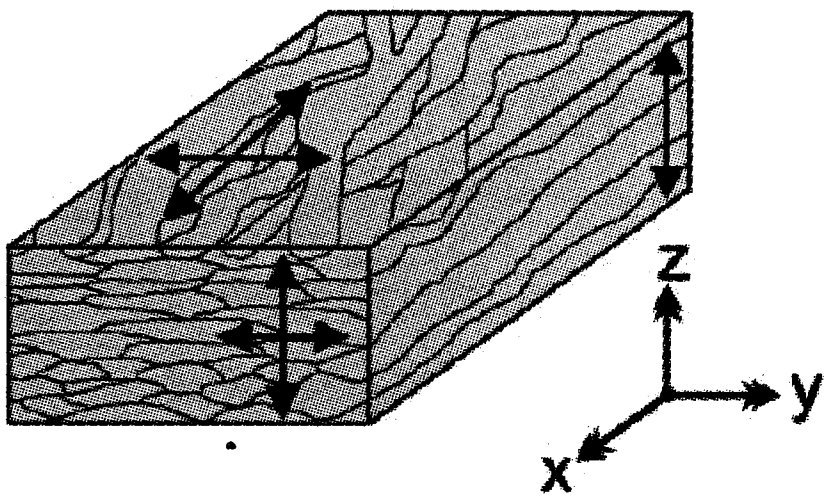

Figure 6.5. Compound braided flow (from Single et al, 2004).

The Middle and Upper Basalt Series are distinguished by the relative proportions of these two lithological types (Passey, 2005). At the resolution of seismic wavelengths, the massive tabular type can be approximated to a planar model such as those studied in Chapter 4. The compound braided type has greater variation in three dimensions, possibly giving rise to more 3-D scattering than the tabular form.

Upper Series basalts in the Glyvursnes well-tie exhibit clear upgoing events which correlate well with impedance contrasts seen in the borehole logs. In comparison, Middle Series basalts in the Vestmanna well-tie show a relatively sparse distribution of

reflections (section 2.3 of this thesis). This may indicate that Middle Series basalts are laterally discontinuous, a scenario which is compatible with the compound flow model.

6.2.2 OBSERVATIONS FROM OPTICAL TELEVIEWER IMAGES AND BOREHOLE CORES

Optical televiewer (OPTV) images were used to trace the distribution of vesicles and in-situ discontinuities in the boreholes. The OPTV images of both Glyvursnes and Vestmanna show ovoid vesicles (in various degrees of calcification / zeolite alteration), often confined to vesiculated bands of up to a few metres in thickness. These regions have largely been interpreted by Waagstein *et al.* (2003) to be flow crusts. The roundness of the vesicles and the limited vertical extent of the vesicular region can clearly be seen in the borehole core, and strongly favours a pahoehoe flow mechanism rather than an aa flow mechanism.

Dark bands and subhorizontal features in the cores / OPTV images may represent flow tops, or individual viscoelastic skins of the flows which have subsequently cooled and compacted. Pipe vesicles (Glyvursnes, 10.35, 447.2 m) and half-moon / bell jar vesicles (Glyvursnes, 380.0, 438.3 – 438.8 m) are also visible. Examples of vesicle sheets can be observed at 24.0 and 451.3 m in Glyvursnes (Figure 6.6). Flow crust cracks are harder to identify, as resolution of the images is not sufficiently high. The original glassy material in the flow crusts may also have recrystallised with age.

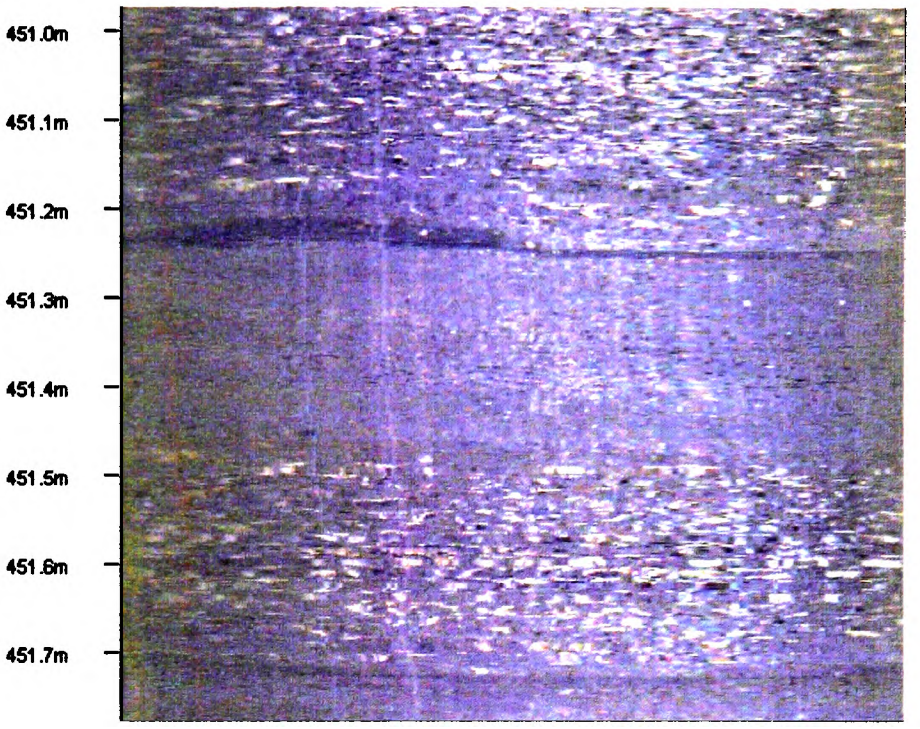

Figure 6.6. Optical televiewer image from Glyvursnes borehole, 451.0 m (Middle Basalt Series), showing bands of vesicles.

The Glyvursnes borehole core has been interpreted as comprising 73 units and 37 flow groups (Waagstein *et al.*, 2003). In the lower section of the borehole, classified as the Middle Basalt Series, the flow units have a mean thickness of 2.1 m and do not exceed 10 m in thickness. Alternating vesicular regions and massive regions, similar to those represented schematically in Figure 6.1, can be seen in the borehole cores, an example of which is given in Figure 6.7.

6.7

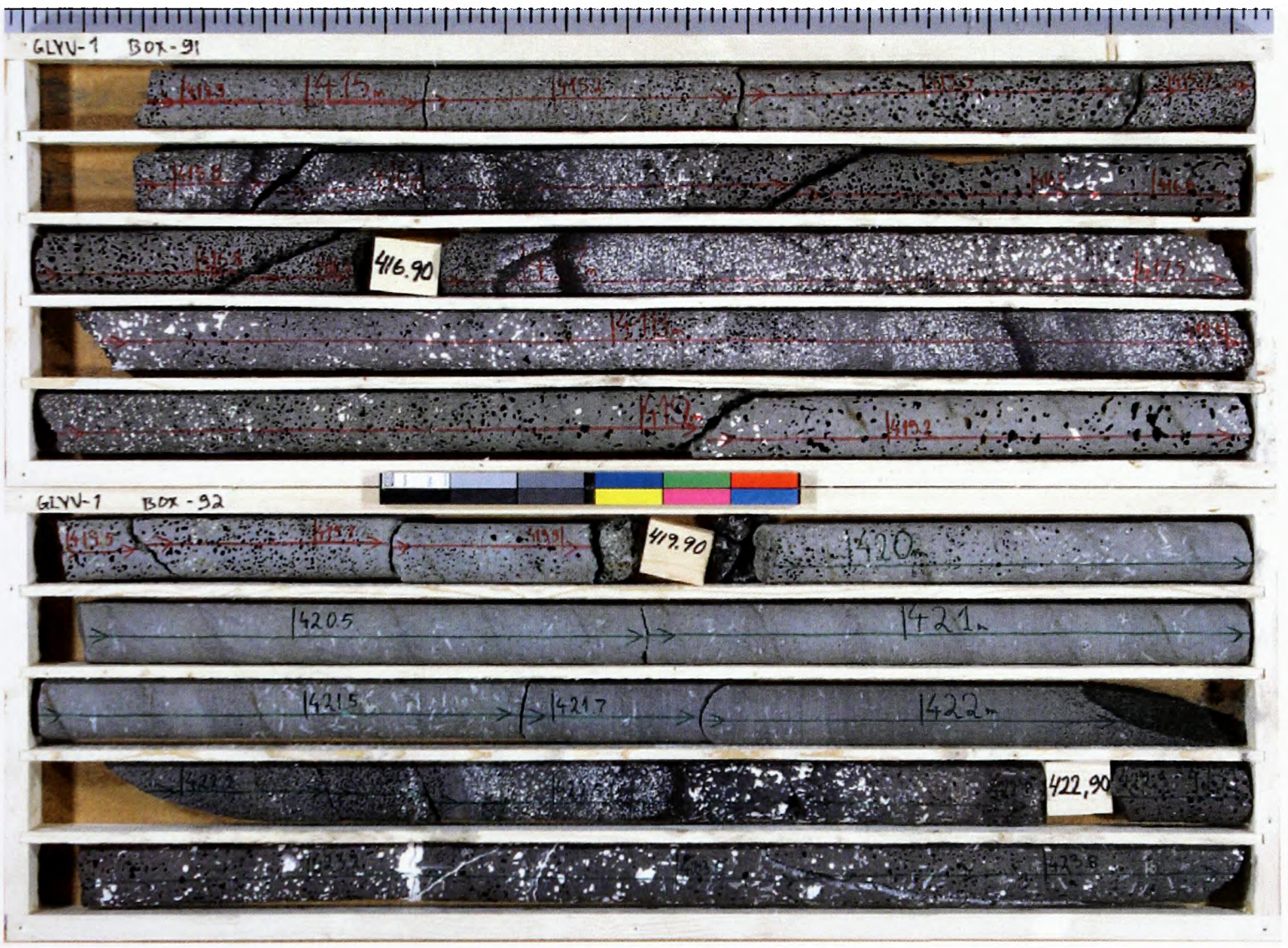

Figure 6.7.
Top down view of core boxes 091 / 092 from Glyvursnes borehole, 415 – 423 m (Middle Basalt Series). Vesicular zones and sheets are visible from 419 to 420 m, and a high velocity flow core is visible between ~ 420 and 422 m.

6.3 PAHOEHOE-BASED BASALT MODELS

Field studies in the Faroes, OPTV images, and knowledge gleaned from other basalt provinces suggest that pahoehoe flows are the building blocks for a geologically plausible 3-D basalt volume.

Essential features of a pahoehoe-based model are:

- hummocky surfaces,
- inversion of topography by successive flows (as described in section 6.1.1 and Figure 6.2),
- dense, high velocity flow cores with lower velocity regions relating to flow crusts and / or brecciated regions, and
- dependence of morphology on propagation direction.

An algorithm was designed to propagate basalt flows of a specified thickness and width over the surface of existing terrain. In the routine, a multifractal topography with low relief (<5 m) is used as the first surface.

(A) A template is first created, using a half-cosine function to define the upper surface of a single flow. The width and height can be scaled according to the desired dimensions of the cross-section. This template is used for all subsequent flows in the model.

(B) The flow path is then mapped out. Due to important morphological and thermodynamic distinctions between ponded flows and pahoehoe (Self *et al.*, 1998), each flow is allowed to meander towards lower topography but is not allowed to pool laterally or terminate before reaching the other side. This is achieved via a simple decision–making process. The flow starts at the lowest point on a fixed side of the model (the 'southern' edge) and propagates northward. At each step, the flow has the option of moving to the northwest (left), northeast (right), or north (centre), but is forced to take the option with the lowest surface height. If all three options are at the same level, the move is made randomly. The new centre of the flow front is defined, and the process is repeated until the flow reaches the opposite edge of the model. If the flow encounters the western or eastern edges of the model, it is reflected back into the model volume.

(C) The flow path is then 'covered' with the cross-sectional template defined in (A). The template is centred on the flow path. As the existing topography is uneven, the edges of the template are adjusted at each step to conform with the underlying surface. This distorts the template and adds slight variation to the internal structure. The updated surface topography, including the new flow, is stored.

The routine cycles through (B) and (C) until the accumulated flows reach a specified thickness. The model is truncated by 20 elements on each side so as to remove edge artefacts. A flow field with pahoehoe 'tubes' of fairly regular size, but with varying sinuosity and at varying positions is thus simulated. Overall, the structure is

heterogeneous and anisotropic, with greater lateral continuity in the plane parallel to flow direction.

(D) The skins (or crusts) of the flows are then defined from the surfaces of the flows, according to a specified thickness (1 m in all models specified here). Velocities can then be assigned to the framework of pahoehoe tubes. The distribution of velocity values affects the degree of heterogeneity and anisotropy of the overall model, and an array of geological scenarios can be modelled.

The main aims were to build a plausible Middle Basalt Series volume, and to contrast the seismic responses of 2-D and 3-D architecture with the 1-D velocity models investigated in Chapters 4 and 5 of this thesis. To this end, out of innumerable emplacement scenarios, only several key morphologies are presented here. The experiments focus on the effect of flow variation and no intrusions are explicitly modelled.

Basalt 1, a narrow-flow, two-velocity basalt, was built from flows which were 12 m wide, and which had minimum a thickness of 4 m. The flow cores were set to a velocity of 5750 m/s, while the outer crusts of the flows set to a velocity of 3750 m/s. The effects of a 3750 - 5750 m/s velocity contrast on the spectrum of a synthetic wave have been studied in 1-D models (section 4.3 of this thesis). Any additional attenuation in Basalt 1 thus results from the 3-D architecture of the model.

Basalt 2, a wide-flow, two-velocity basalt, was built from flows with a width of 50 m, with a minimum flow thickness of 3 m. As in Basalt 1, the velocity of the cores was set to 5750 m/s, while the outer crusts of the flows were set to 3750 m/s. The flows in Basalt 2 have a larger lateral-to-vertical aspect ratio, and have a greater degree of planarity than Basalt 1.

Basalt 3, a lobular, four-velocity basalt, was based on the same pahoehoe structure as Basalt 1. Flow width and thickness were 12 m and 4 m respectively. However, in addition to the 3750 - 5750 m/s velocity contrast, a second velocity contrast, 3000 - 4600 m/s, was introduced to groups of flows. This crudely simulated changes in lava chemistry and produced velocity macro-structures. The lobes had a maximum thickness of 100 m, with varying thickness intersected by the vertical receiver array. In this sense, Basalt 3 expresses periodicity / fractality, as the shape of the larger lobes resembles that of the individual flows (Figures 6.10a,c).

Basalt 4, a varied-velocity basalt, was also based on the framework of Basalt 1. Vestmanna P-velocity log values (between 50 and 600 m depth) were separated into two categories: crust-range (low velocity) and core-range (high velocity). Each flow was assigned a core velocity and a crust velocity from these respective lists. Although this model has only weak depth correlation with the actual Vestmanna rock volume, its velocity distribution is realistic. This basalt model is the closest analogue to Middle Series rocks.

6.4 DISCRETE PARTICLE SCHEME (DPS) IMPLEMENTATION

The discrete particle scheme (DPS) is a numerical lattice method used to simulate elastic wave propagation through a given volume. The algorithm is described in detail by O'Brien & Bean (2004), with supporting theoretical and practical detail to be found in Monette & Anderson (1994) and Toomey & Bean (2000). The 2-D and 3-D implementations in this work were adapted for Fortran by M.H. Worthington.

In summary, blocks of intact rock are represented as particles arranged on a cubic lattice, which interact at each of their 18 contact points. The source is a point force acting downward in the z-direction, and the particles subsequently undergo forces proportional to their displacement from equilibrium: a central force term obeying Hooke's Law, and a bond-bending force, proportional to the angles between adjacent particles. Particle disturbances are followed through space by numerically solving their equations of motion. The boundary condition is implicitly a free-surface vacuum.

The input models for DPS comprise compressional velocity and density models. Based on an approximate linear relationship established from log data, density ρ was set according to:

$$\rho = 0.15 \text{ kg s m}^{-4} V_p + 2000 \text{ kg m}^{-3} \qquad \textbf{(6.1)}$$

Within the scheme, shear velocities are related to compressional velocities by specifying the Poisson's ratio. In this work, Poisson's ratio was fixed at 0.25 by setting the bond-bending constant to zero as described in O'Brien & Bean (2004).

Basalts 1- 4 were built up as 3-D volumes using the pahoehoe algorithm outlined in section 6.3. Edge artefacts arising from the algorithm were removed by truncating the models to dimensions of 280 x 280 x 400 m, the optimum grid size under available computing resources. The source was positioned at the top-centre of the basalt volume, and 25 receivers placed at 10 m intervals from the source down to the base of the model. A further 50 receivers were positioned in a cruciform pattern with a total horizontal coverage of 250 m, centred on the deepest receiver in the vertical array. Figures 6.8a,b,c – 6.11a,b,c show cross-sections of the 3-D models, and locations of both the source and receivers.

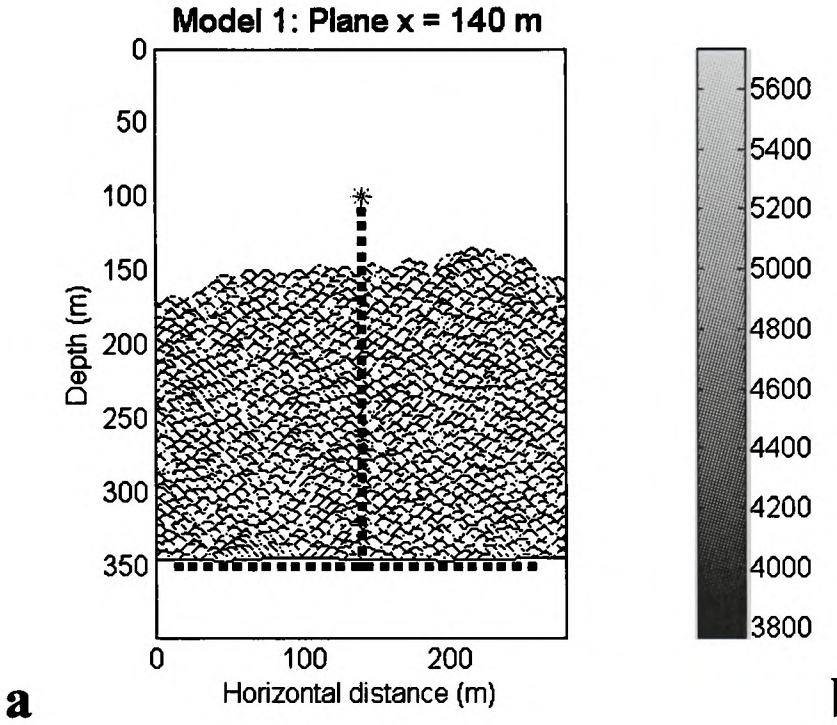

a

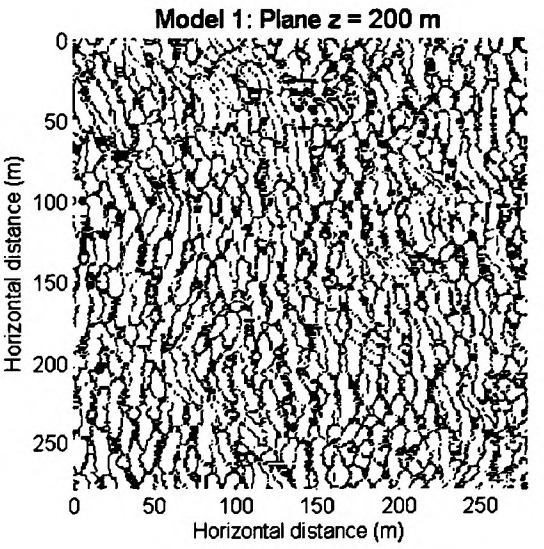

b

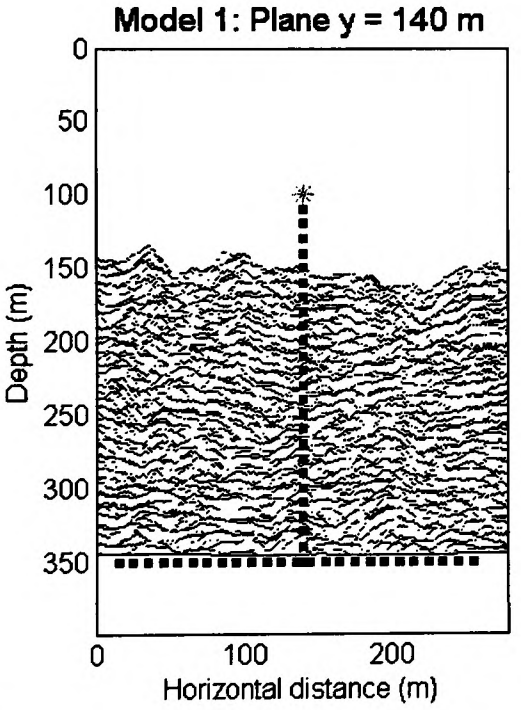

c

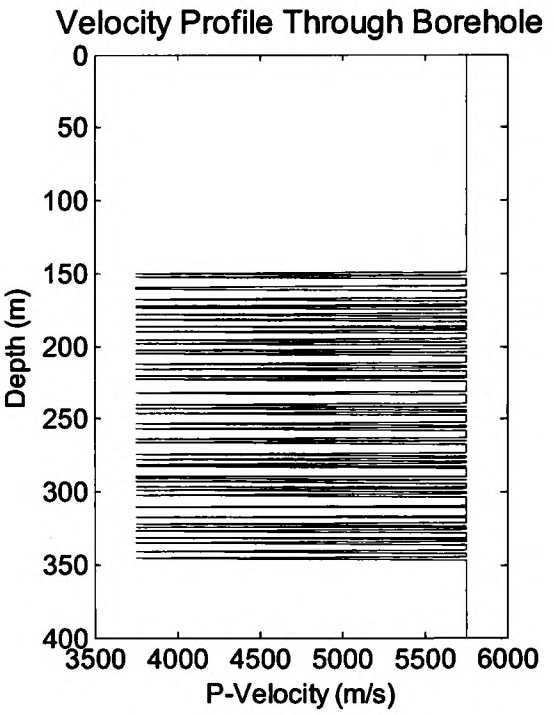

d

Figure 6.8. Model 1, narrow flows, two velocities.
a. Cross-section through midpoint of model, plane perpendicular to lava propagation direction. An asterisk represents he source position. Velocity colour scale is in m/s.
b. Horizontal cross-section through the 200 m depth level.
c. Cross-section through midpoint of model, plane parallel to lava propagation direction.
d. P-velocity profile through the borehole.

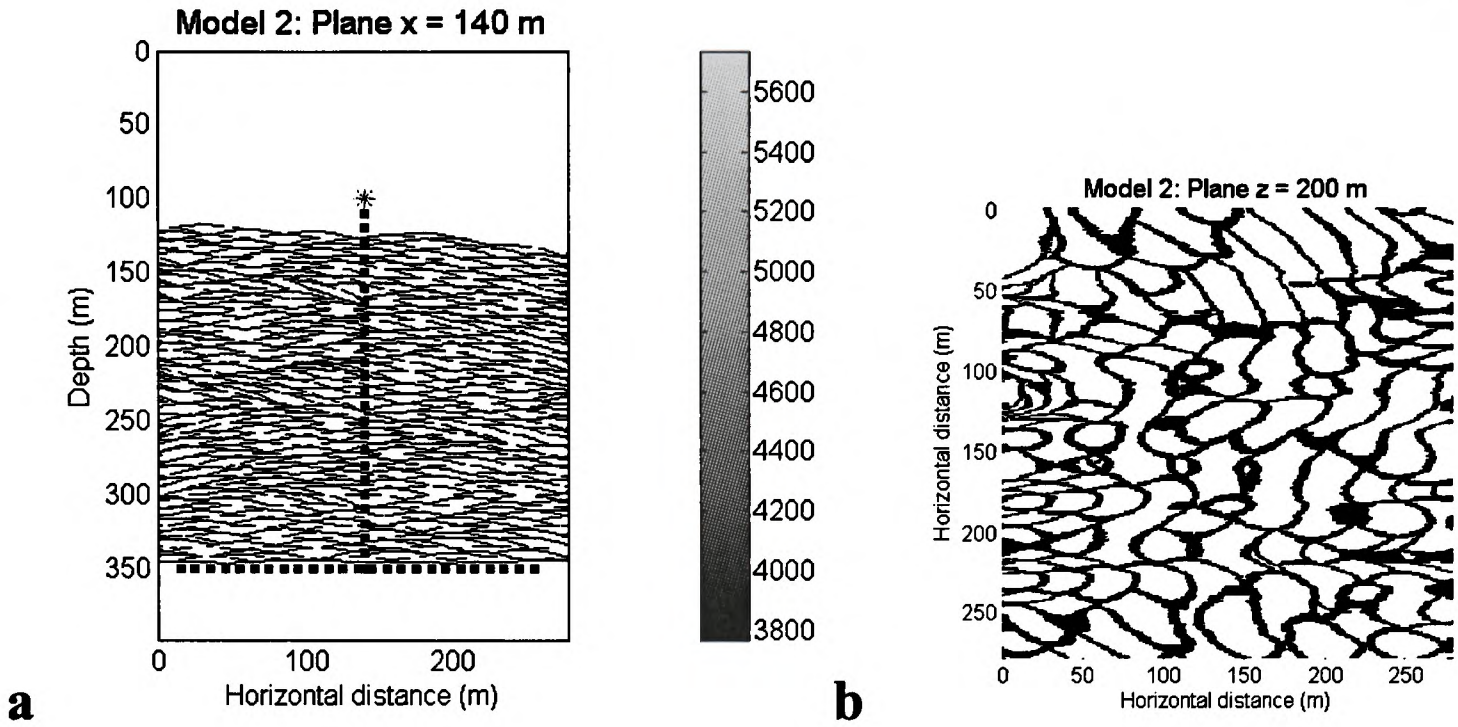

Figure 6.9. Model 2, wider flows, two velocities.
a. Cross-section through midpoint of model, plane perpendicular to lava propagation direction. An asterisk represents he source position. Velocity colour scale is in m/s.
b. Horizontal cross-section through the 200 m depth level.
c. Cross-section through midpoint of model, plane parallel to lava propagation direction.
d. P-velocity profile through the borehole.

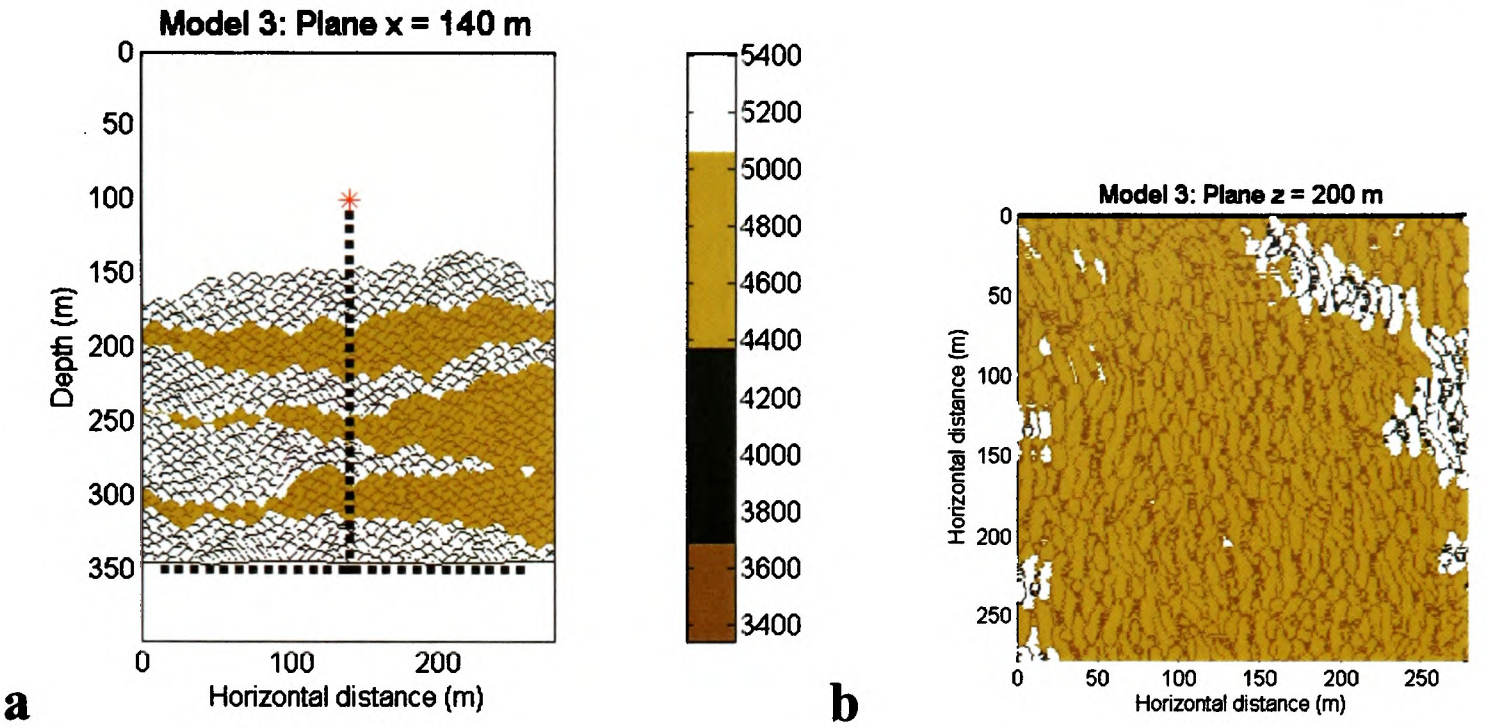

Figure 6.10. Model 3, narrow flows, four velocities.
a. Cross-section through midpoint of model, plane perpendicular to lava propagation direction. An asterisk represents he source position. Velocity colour scale is in m/s.
b. Horizontal cross-section through the 200 m depth level.
c. Cross-section through midpoint of model, plane parallel to lava propagation direction.
d. P-velocity profile through the borehole. Larger lobes appear to have a thickness of between 20 and 50 m.

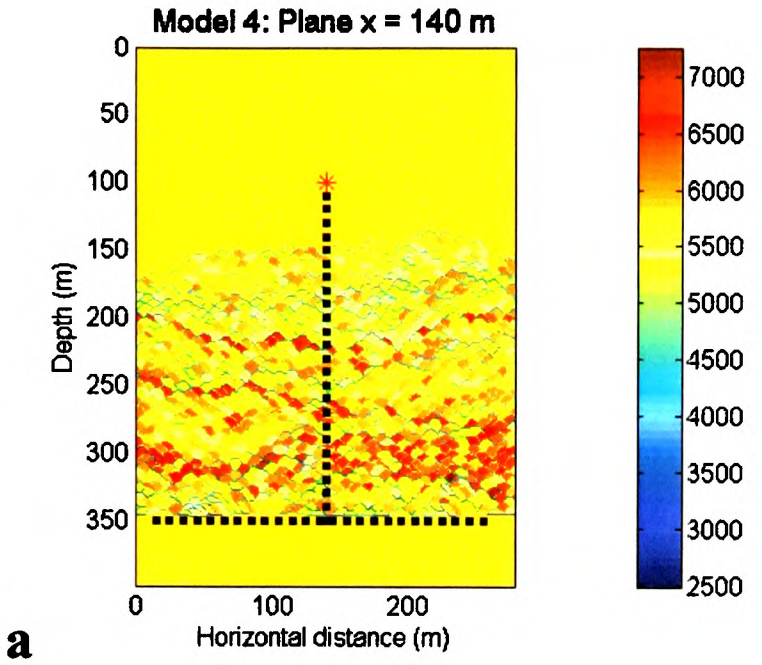

a

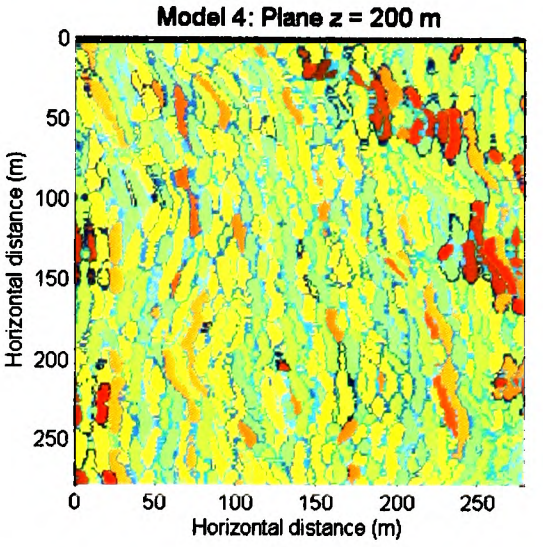

b

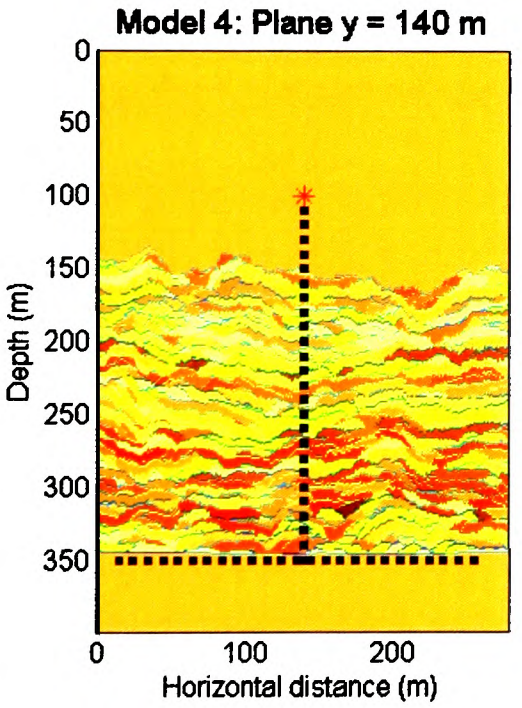

c

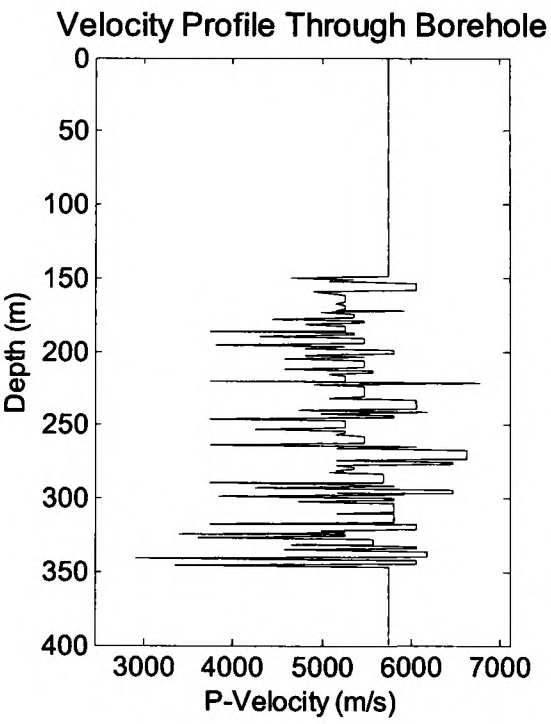

d

Figure 6.11. Model 4, narrow flows, varied velocities.
a. Cross-section through midpoint of model, plane perpendicular to lava propagation direction. An asterisk represents he source position. Velocity colour scale is in m/s.
b. Horizontal cross-section through the 200 m depth level.
c. Cross-section through midpoint of model, plane parallel to lava propagation direction.
d. P-velocity profile through the borehole.

While the 3-D implementation was ideal for studying whole volumes, 2-D DPS enabled each plane of anisotropy to be studied in isolation. Broader and deeper cross-sections could also be modelled, with wider buffers between the synthetic basalt and the lattice boundaries. This allowed longer time signals to be recorded without contamination by side-wall reflections.

A suite of 2-D models was built using the same pahoehoe algorithm. After removal of edge artefacts, the models measured 1000 m horizontally and 600 m vertically, and were further buffered to dimensions of 2000 x 2000 m. Each basalt type was studied in two cross-sections: the planes perpendicular to flow direction were given the suffix 'X', and those parallel to flow were given the suffix 'Y'. The source was once again positioned at the top-centre of the basalt model, and 55 receivers placed at 10 m intervals from the source down to 550 m. 40 receivers were distributed on either side of the lowermost receiver in the vertical array, at 20 m intervals. Their total horizontal coverage was 800 m. Figures 6.13a – 6.20a show the 2-D models and positions of the receivers.

Spatial resolution was set to 1.0 m. In order to capture the effects seen in the real VSPs, centre frequency of the source wavelet was set to 150 Hz, with a main data-carrying bandwidth of 50 – 250 Hz (identical to the synthetic source used in 1-D experiments, Chapter 4). The optimum time sampling interval was fixed at 0.0001 s, calculated to avoid numerical instability and dispersion. Poisson's ratio was fixed at 0.25 by setting the bond-bending constant to zero as described in O'Brien & Bean (2004).

Damping zones of 40 m thickness were imposed on the lattice boundaries of all models, but side-wall reflections could not be completely suppressed. In all 2-D and 3-D models, the primary waves were free of interference. There is some evidence of contamination in the coda, occurring much later in records for the 2-D cases than for the 3-D cases.

As a control experiment, DPS was run on a lattice with homogeneous velocity of 5250 m/s (the average velocity of the basalt models). The source in this, and all succeeding experiments, was input as a force in the z (depth) direction. The resulting wavefield is shown in Figure 6.12.

6.12

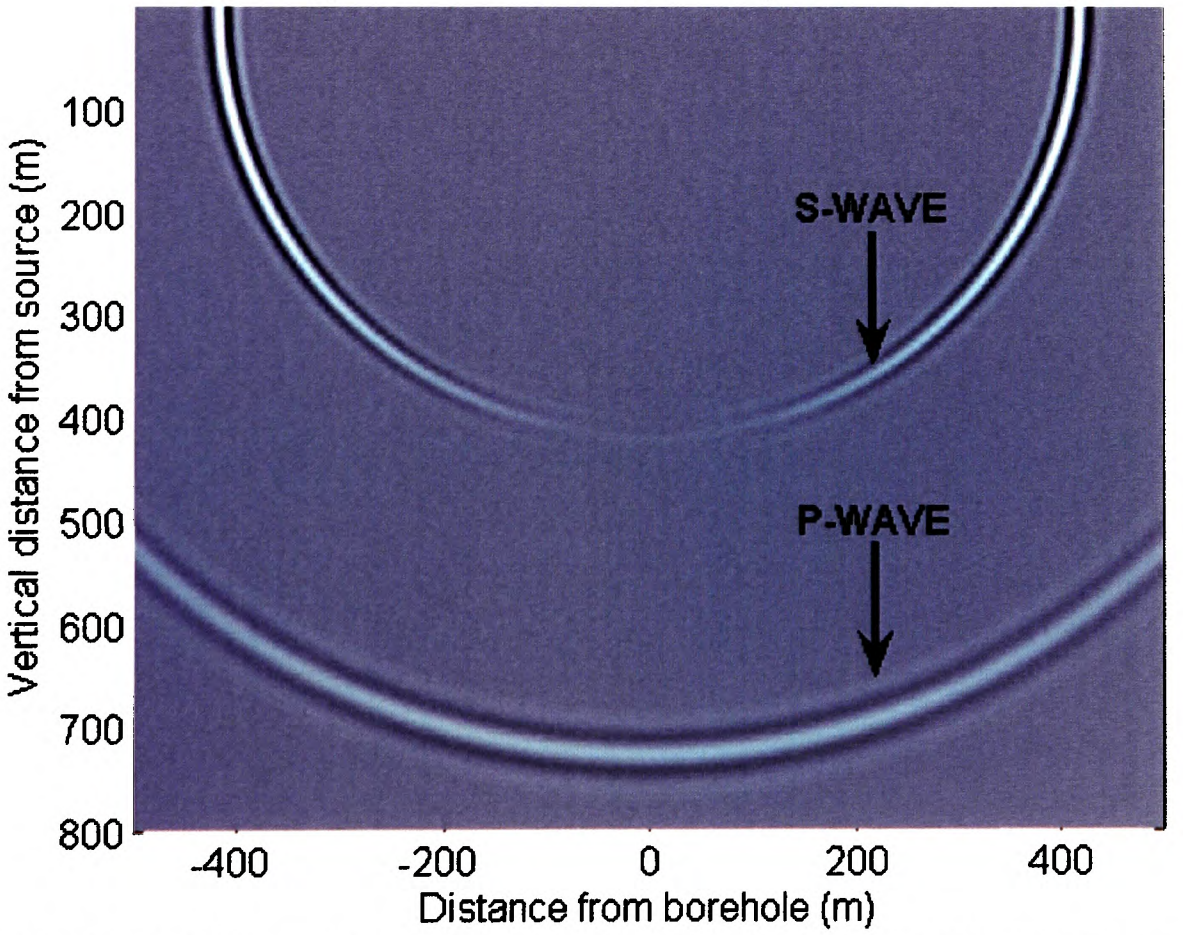

Figure 6.12. Wavefield from a homogeneous model, with uniform velocity 5250 m/s, run through 2-D DPS. The source is a force acting in the z-direction, hence the S-wave amplitude approaches zero in the line of the borehole.

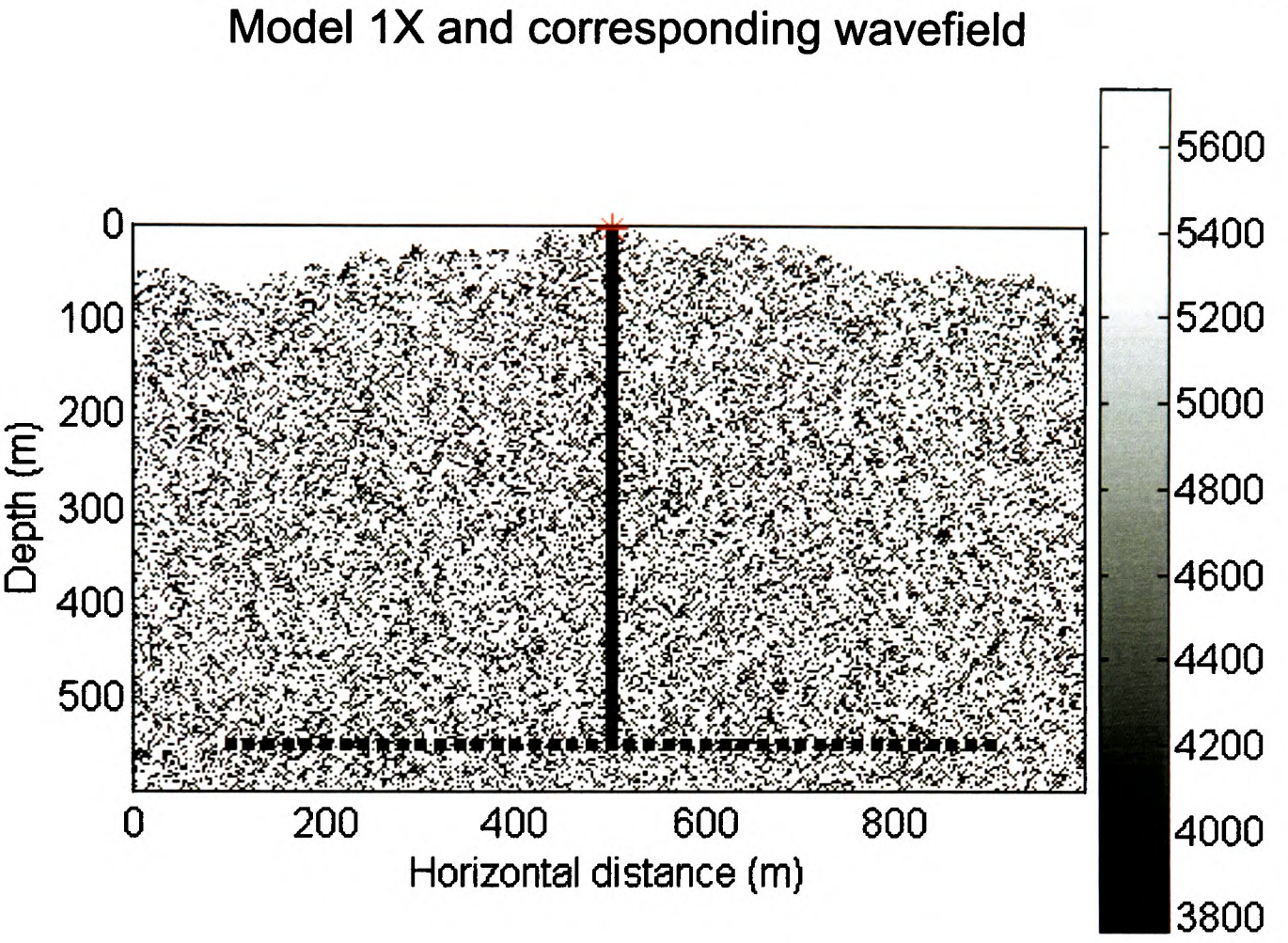

a

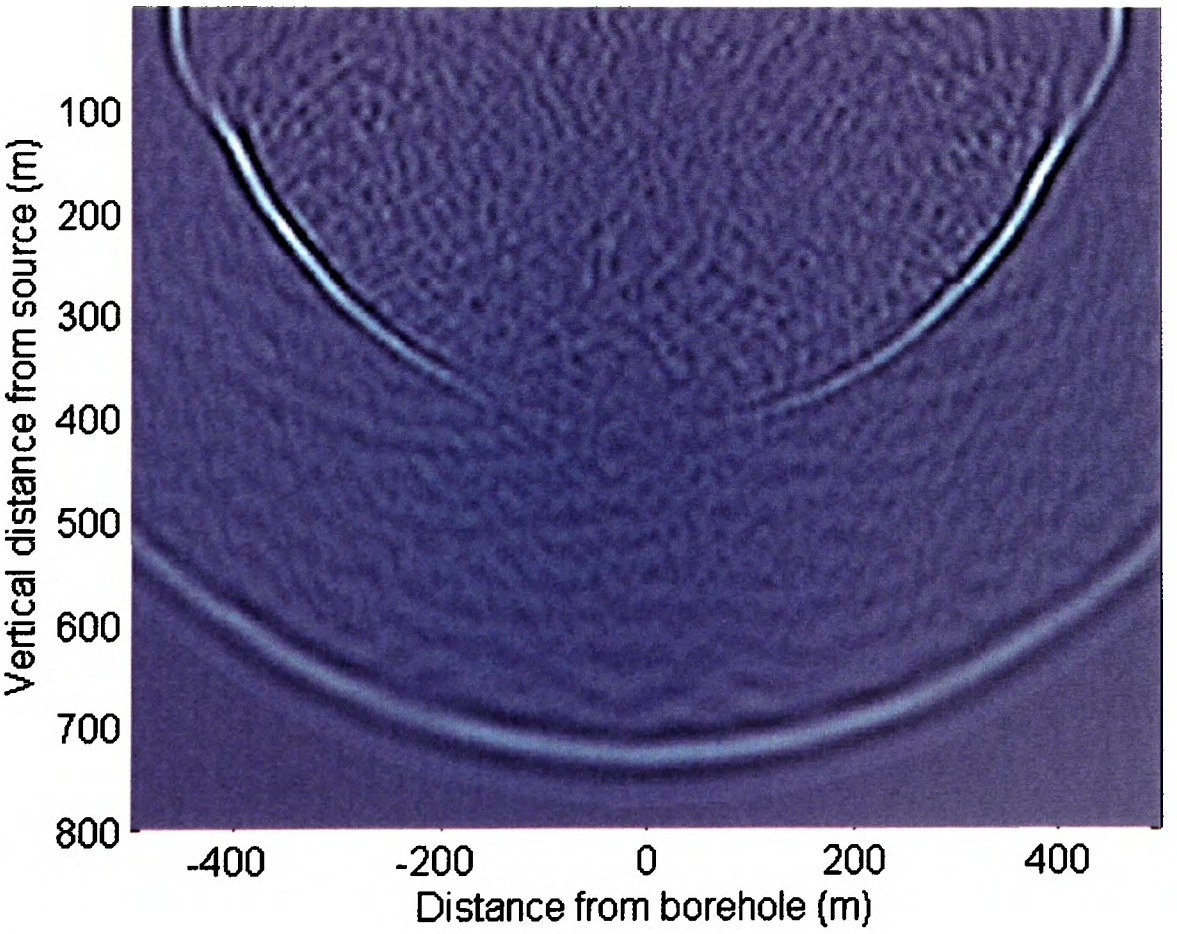

b

Figure 6.13.
a. Model 1X. Receivers are represented by black squares.
b. The corresponding wavefield.

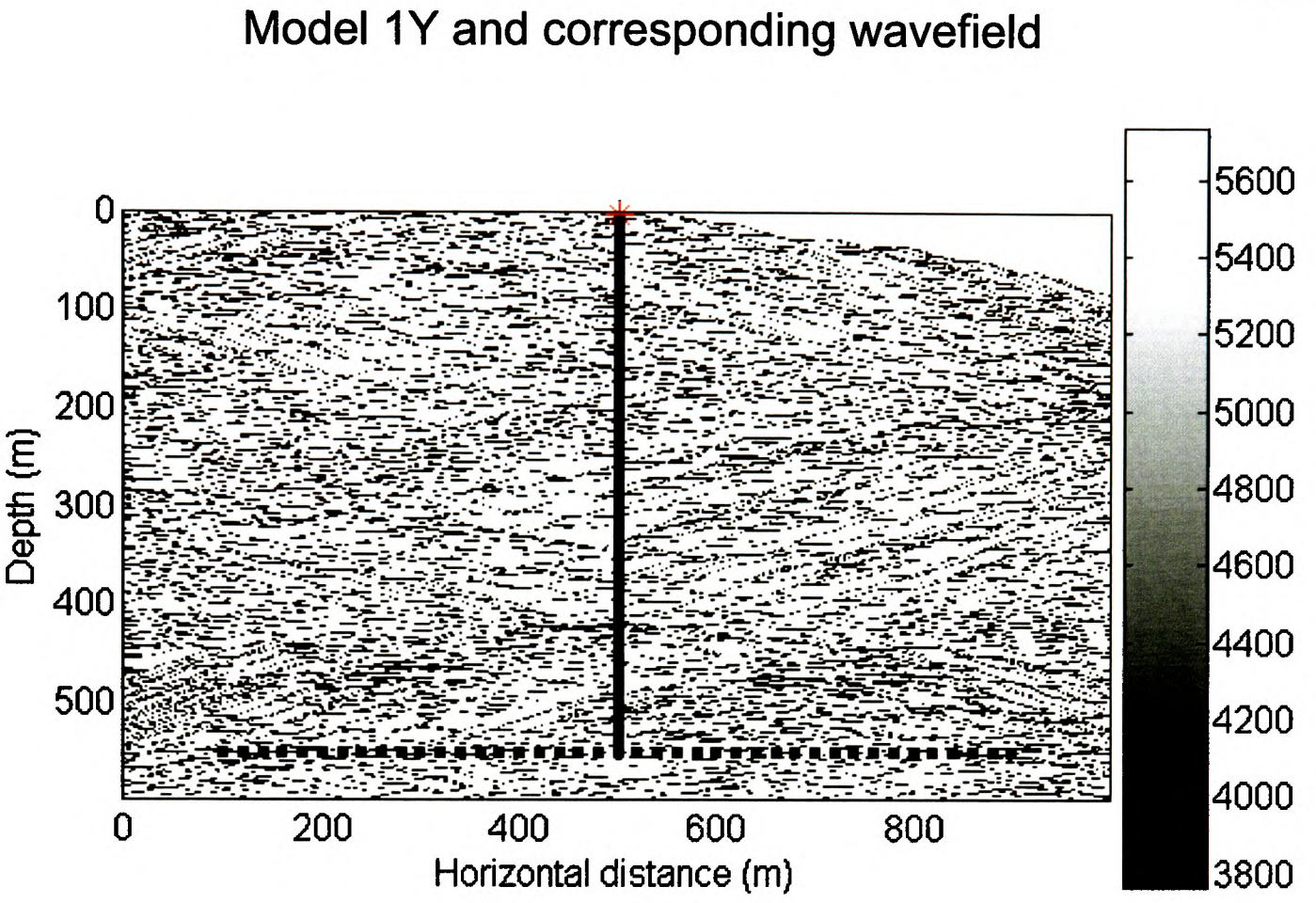

Figure 6.14.
a. Model 1Y. Receivers are represented by black squares.
b. The corresponding wavefield.

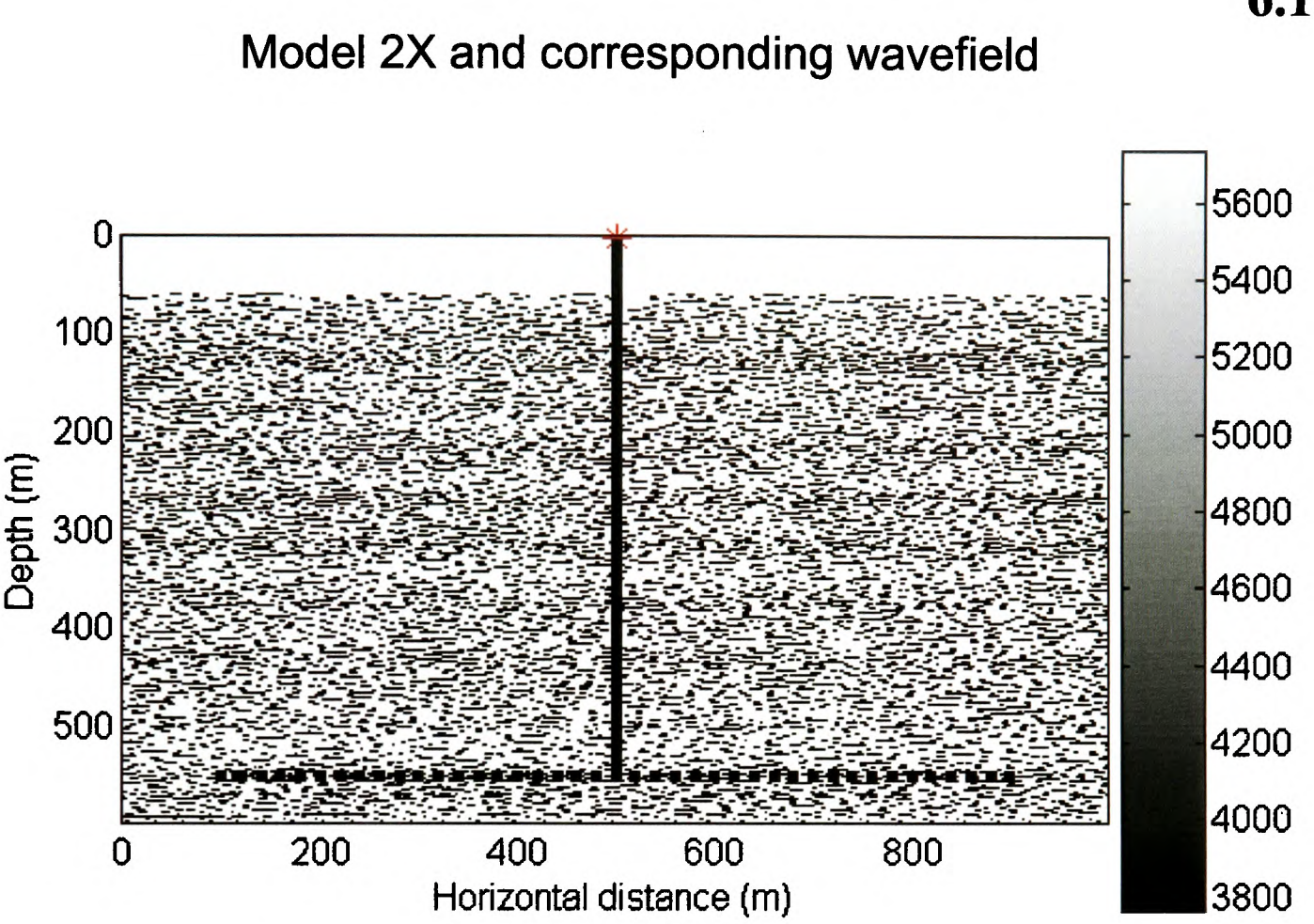

a

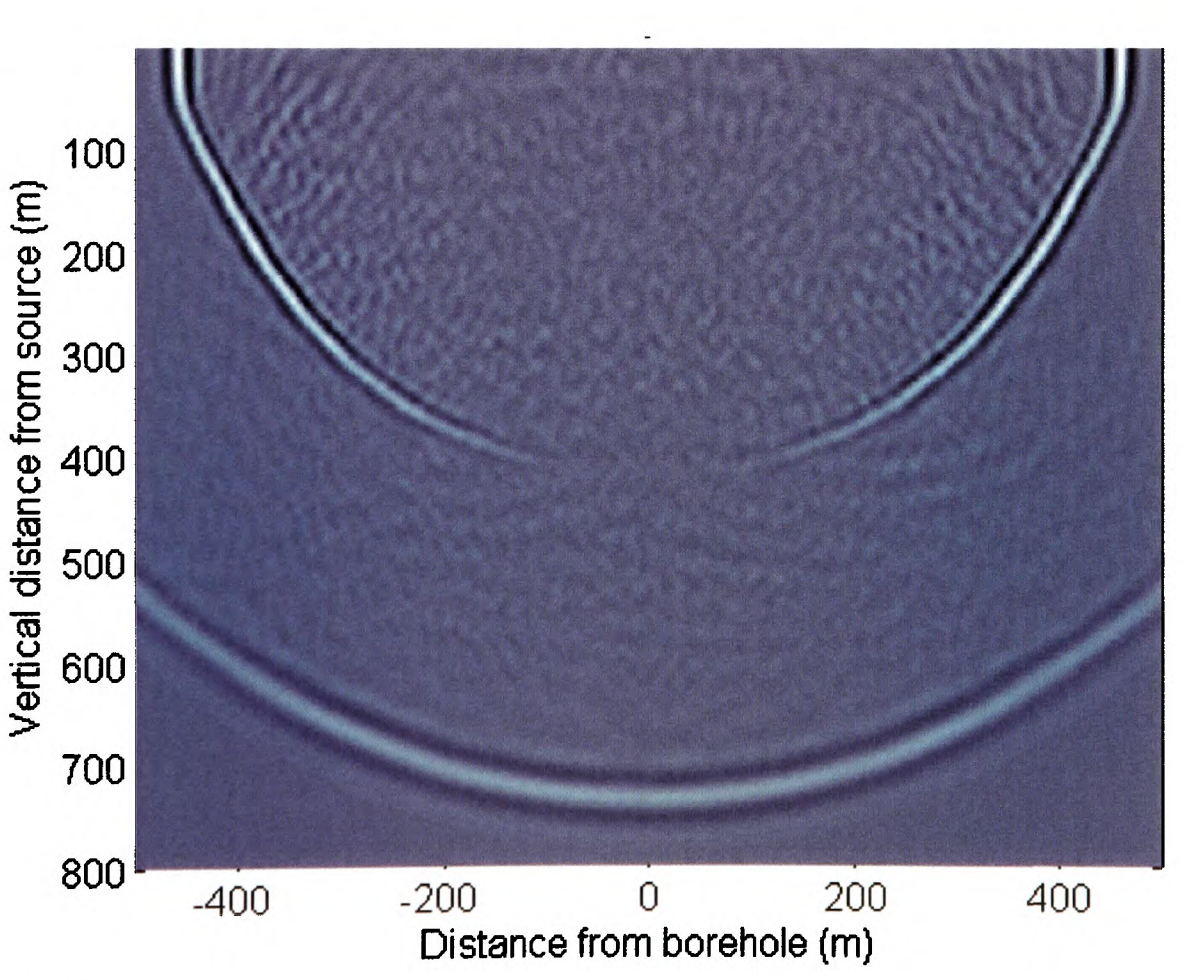

b

Figure 6.15.
a. Model 2X. Receivers are represented by black squares.
b. The corresponding wavefield.

Model 2Y and corresponding wavefield

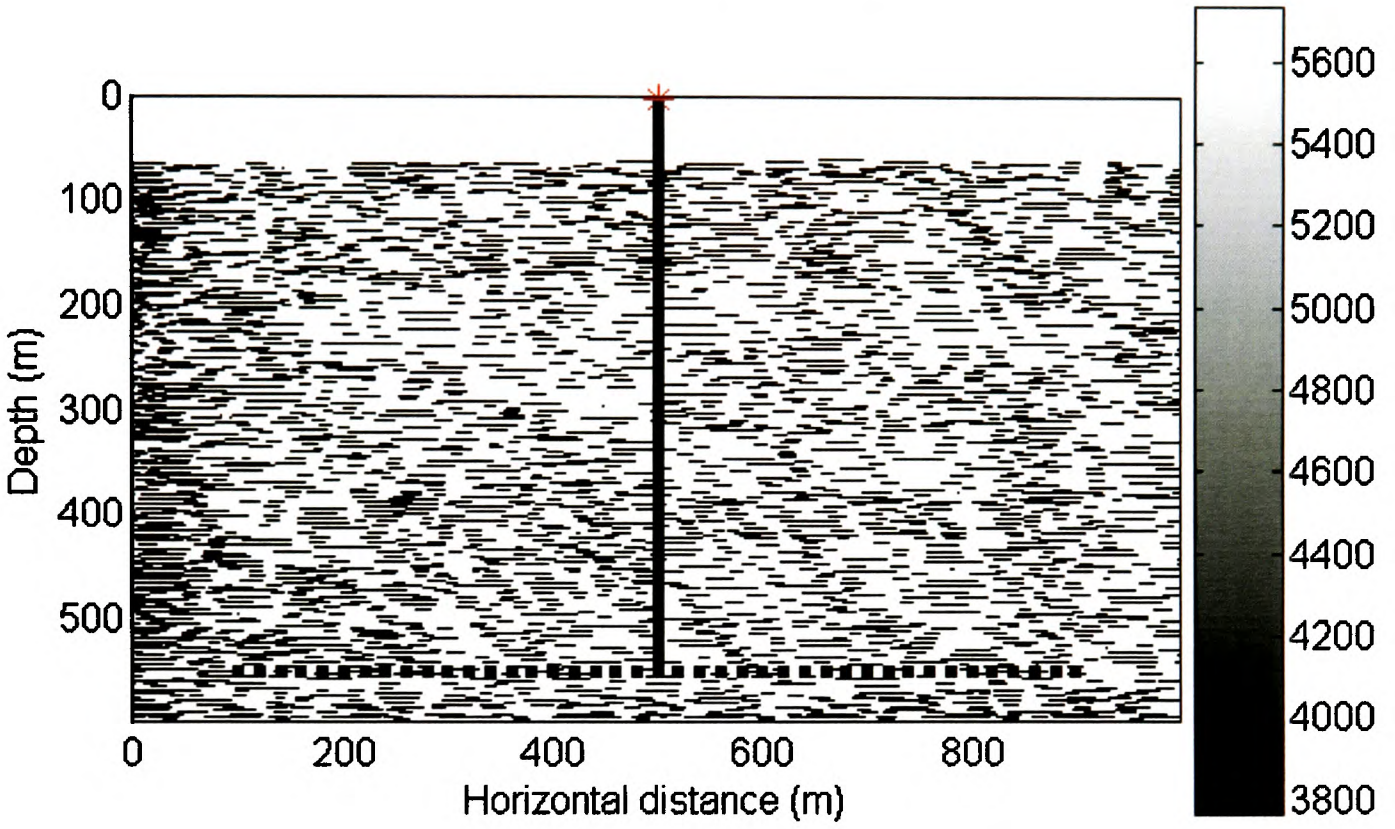

a

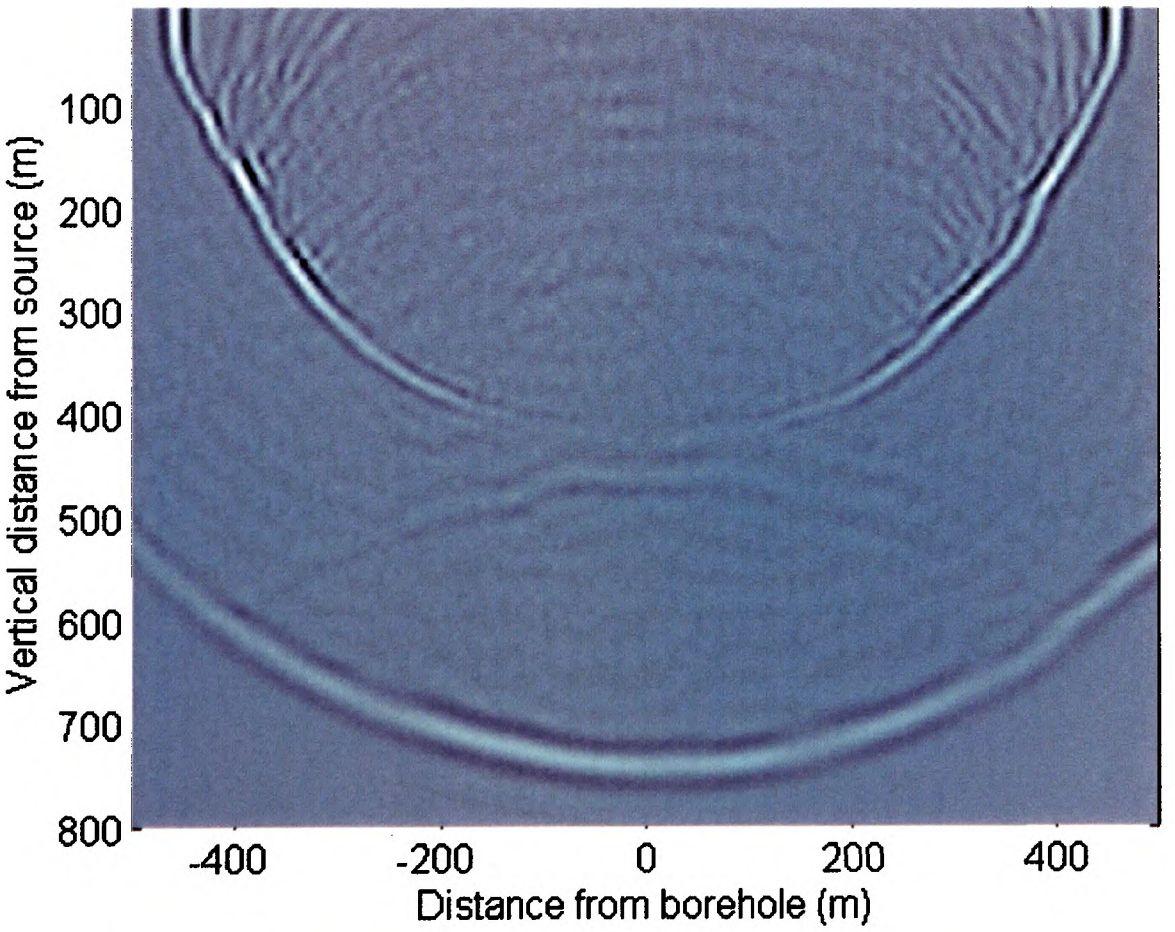

b

Figure 6.16.
a. Model 2Y. Receivers are represented by black squares.
b. The corresponding wavefield.

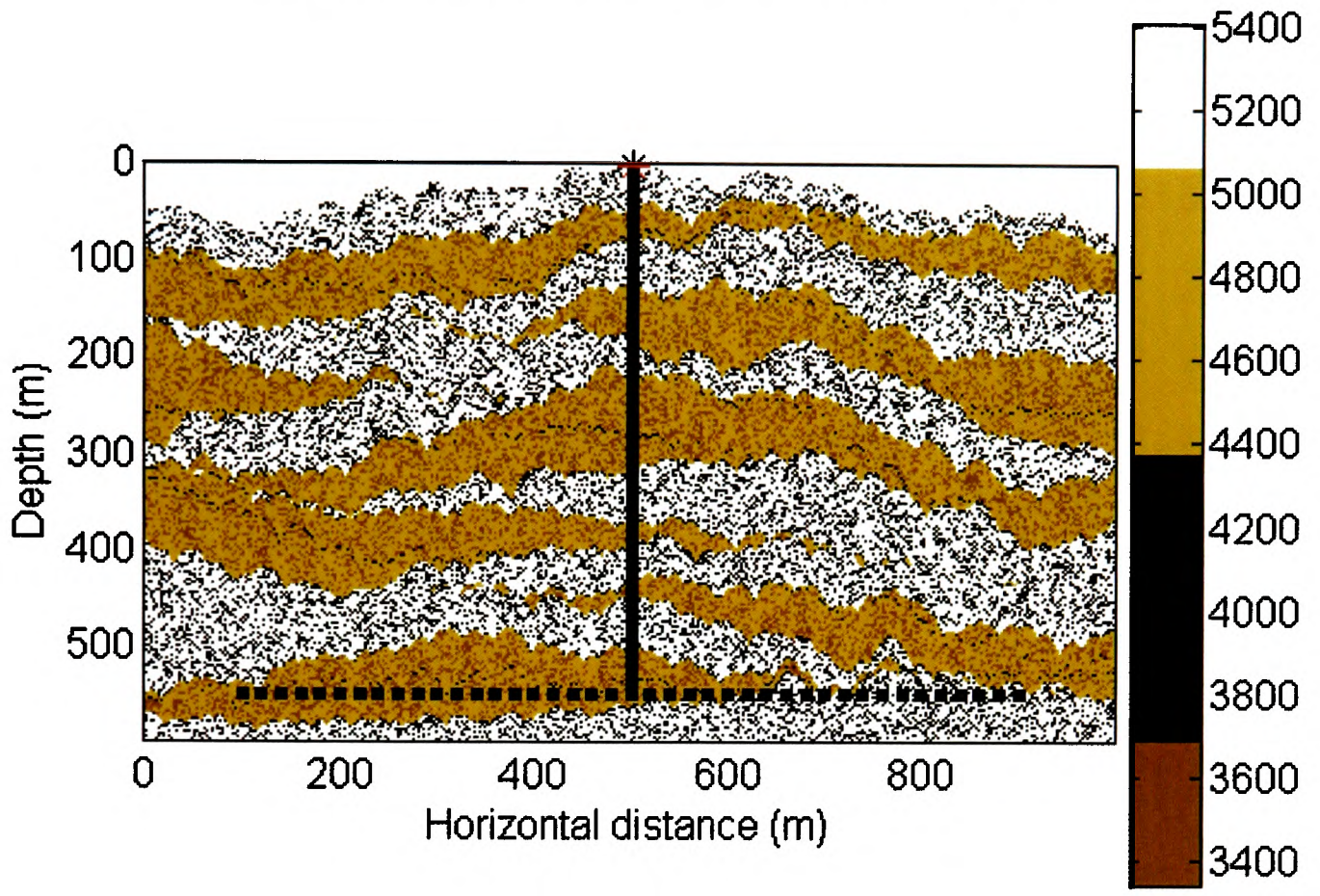

a

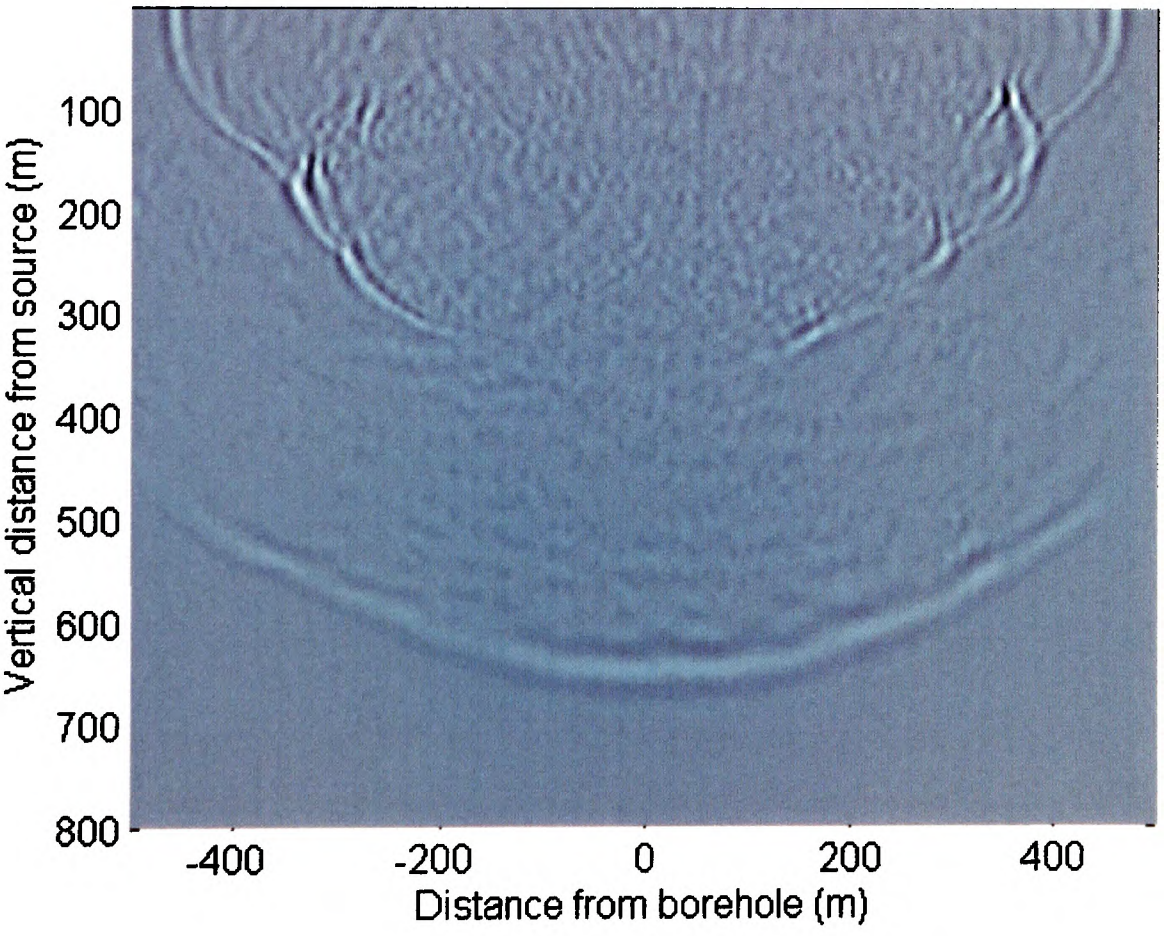

b

Figure 6.17.
a. Model 3X. Receivers are represented by black squares.
b. The corresponding wavefield.

Model 3Y and corresponding wavefield

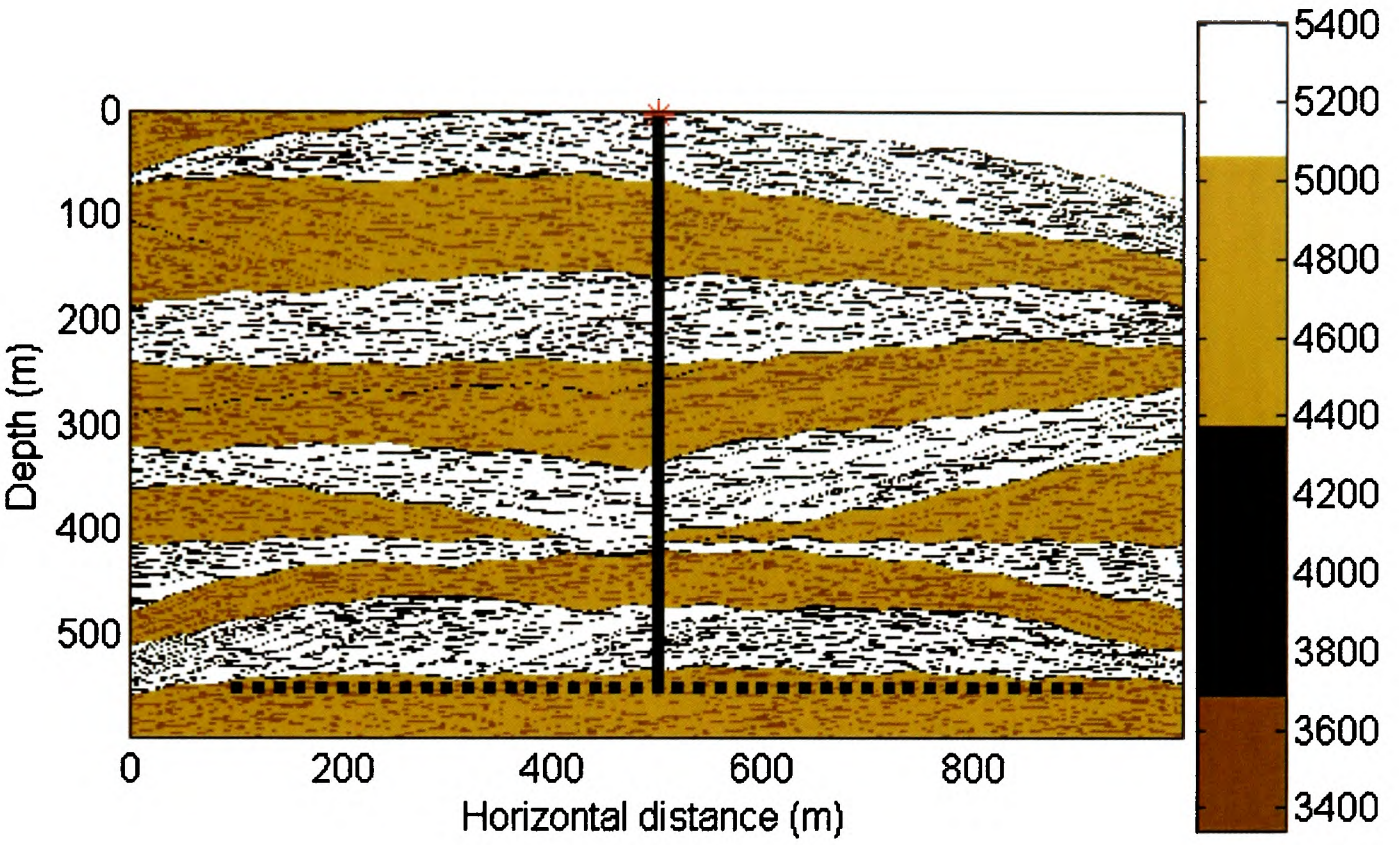

a

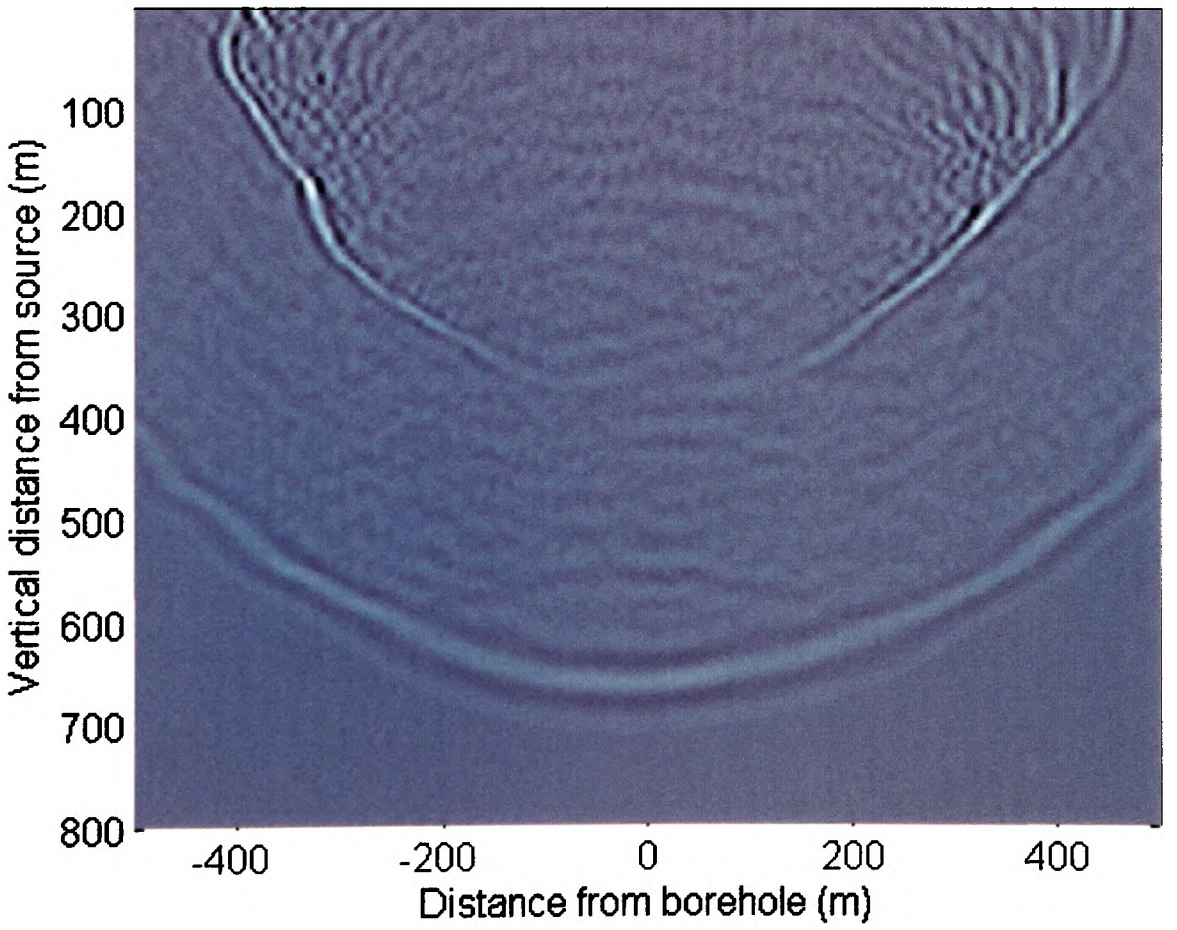

b

Figure 6.18.
a. Model 3Y. Receivers are represented by black squares.
b. The corresponding wavefield.

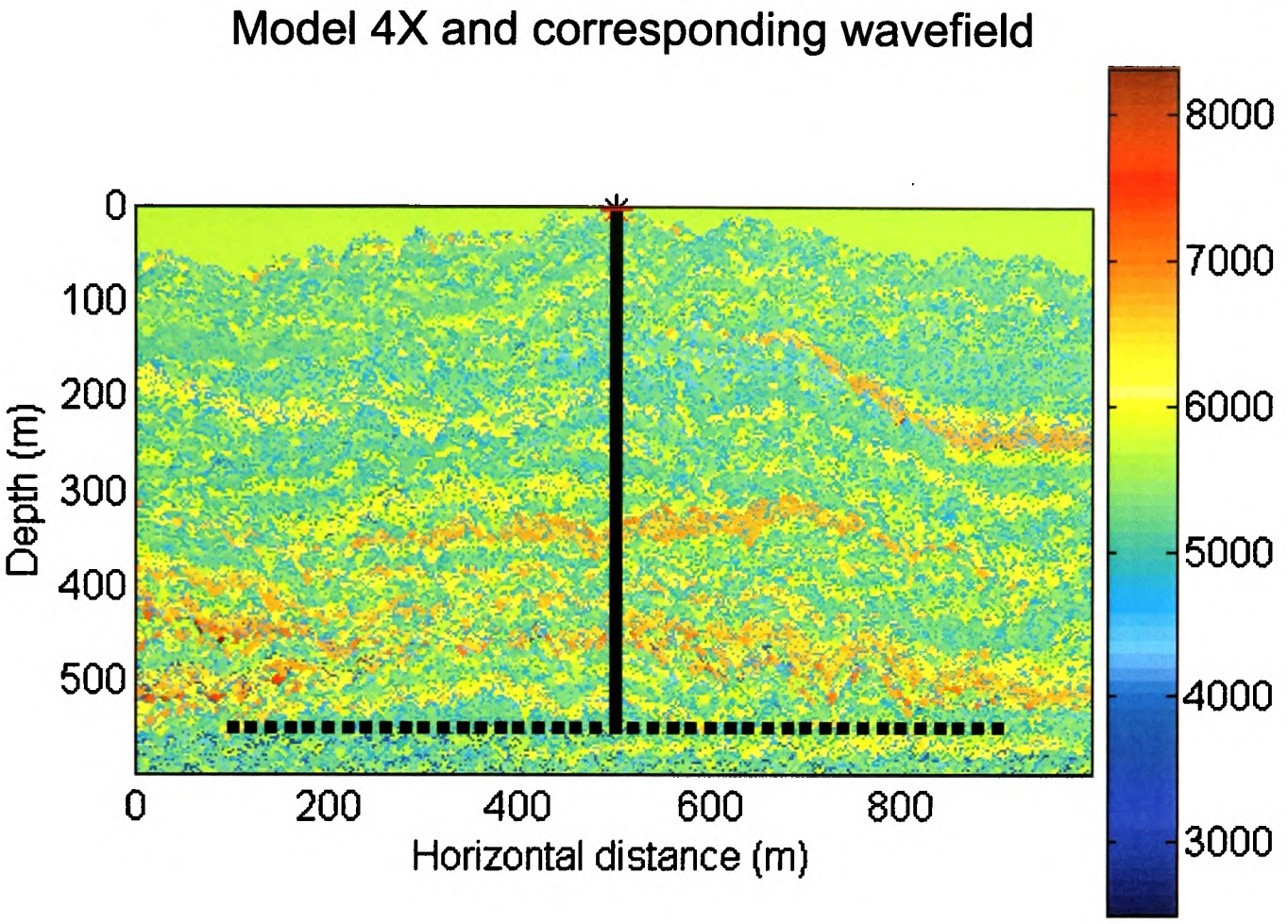

a

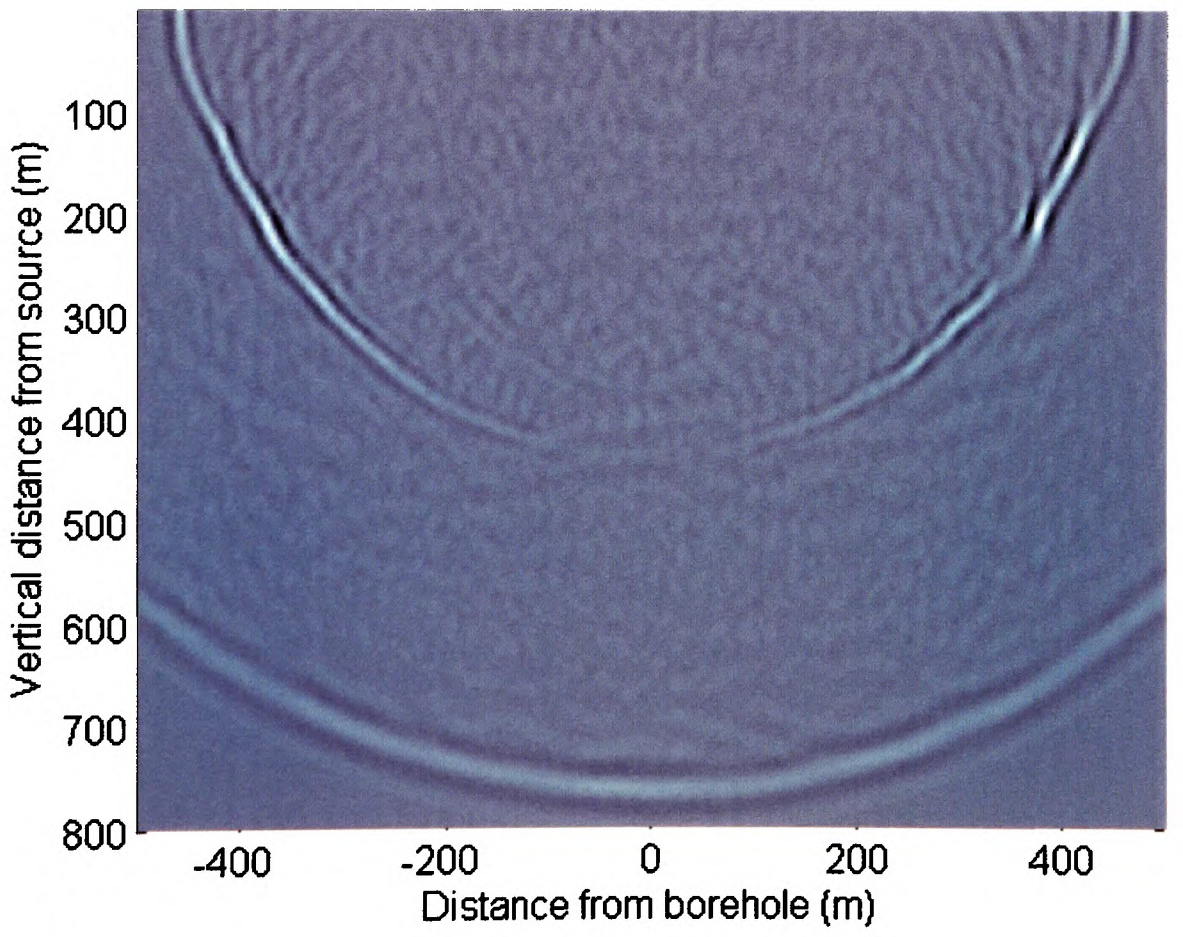

b

Figure 6.19.
a. Model 4X. Receivers are represented by black squares.
b. The corresponding wavefield.

Model 4Y and corresponding wavefield

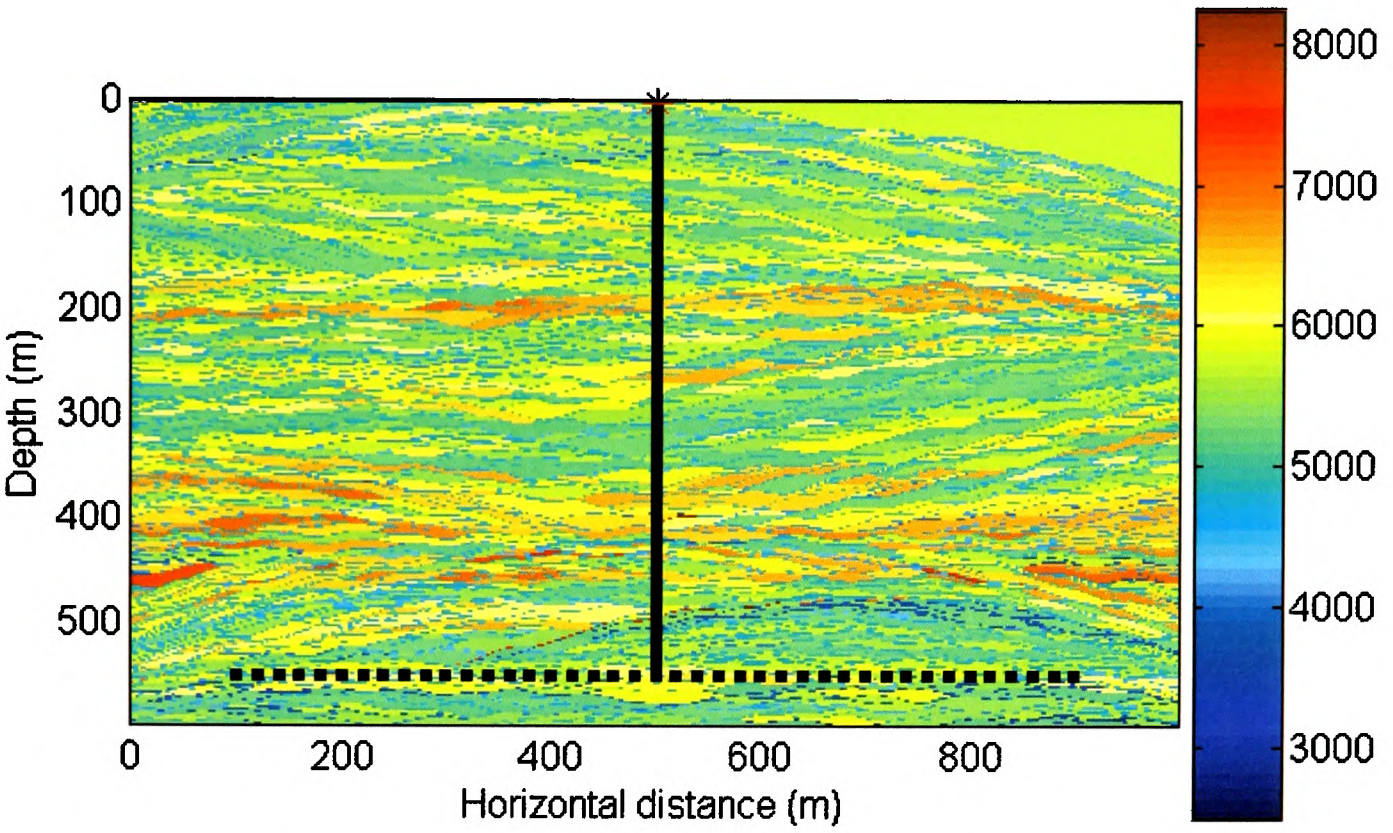

a

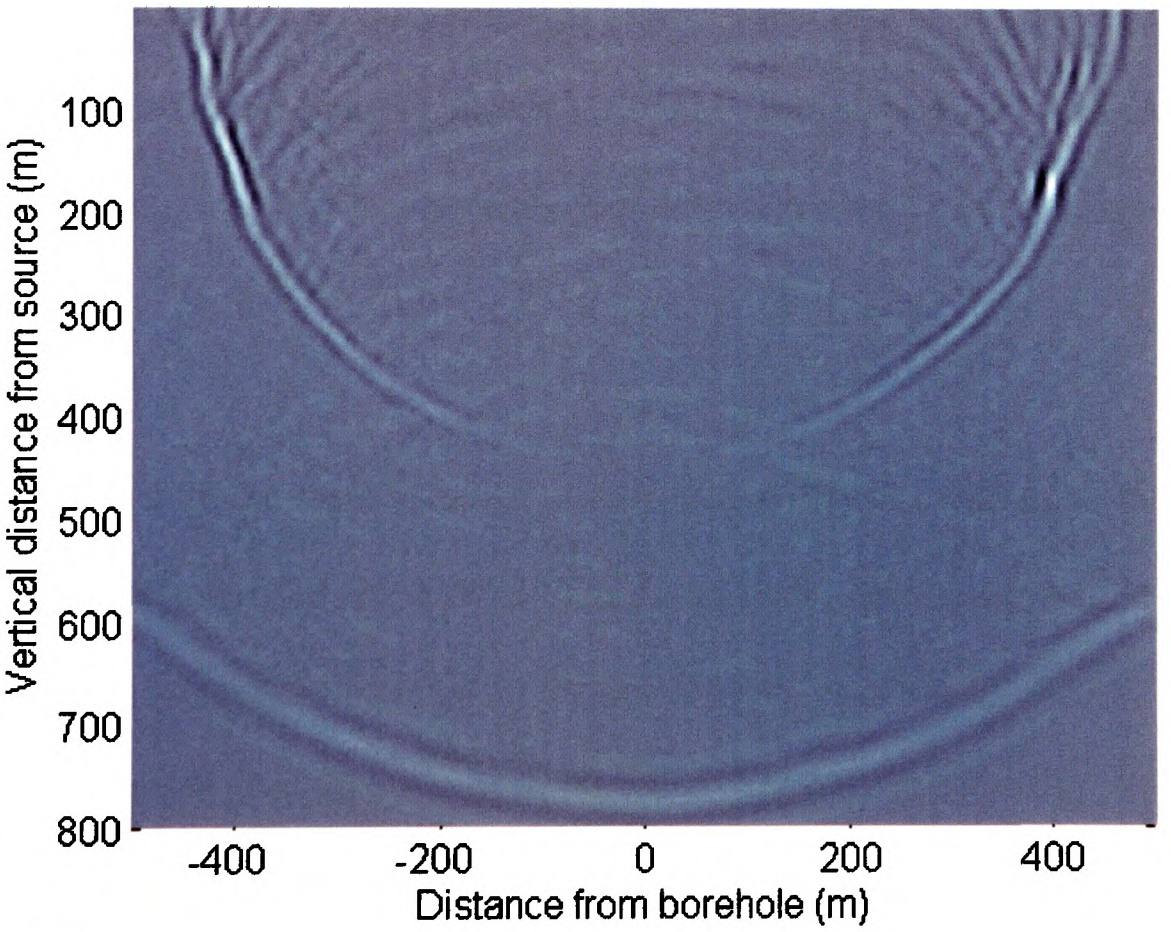

b

Figure 6.20.
a. Model 4Y. Receivers are represented by black squares.
b. The corresponding wavefield.

6.5 RESULTS FROM BASALT MODELLING

6.5.1 COHERENCE OF THE WAVEFRONT

Z-component wavefields from the 2-D experiments had a longer propagation distance than their 3-D counterparts, and therefore provided better visualisation of scattered energy. These are presented in Figures 6.13b – 6.20b, captured after 0.15 seconds of propagation.

The extent to which the wavefronts were perturbed varied between experiments. First, wavefields from all cross-sections perpendicular to flow direction, X, were compared (Figures 6.13, 6.17, 6.19). The intensity of scattering appeared to follow this hierarchy: lobular Basalt 3 >> two-velocity Basalt 1 ≥ varied-velocity Basalt 4. The same hierarchy was apparent in cross-sections parallel to flow direction, Y (Figures 6.14, 6.18, 6.20).

X and Y sections of the same basalt type were then compared with each other. In general, models in the X plane exhibit stronger scattering than models in the Y plane. There is thus a correlation between an increased proportion of low-velocity interfaces and increased scattering. The use of a realistic velocity range, however, diminishes this anisotropy (Basalt 4, Figures 6.19, 6.20).

The wavefields of Basalt 2 (Figures 6.15, 6.16) require separate treatment as the Y section appears to create stronger scattering than the X section, a reverse relationship to other models. In 2Y, sub-vertical low-velocity zones are formed by the alignment of tapered ends of flows. This is a secondary effect due to larger horizontal-to-vertical aspect ratio in the flows (see section 6.3 of this chapter, and Figure 6.21). The packing geometry of 2Y therefore has a greater potential to disrupt the wavefront than that of model 2X.

Surficial rugosity, thought to be a prime cause of 3-D scattering (Martin & Bean, 2002; Makinde *et al.*, 2005), could also have induced greater scattering in 2Y. A surface appears 'rough' or rugose to the sensing wave if:

$$h > \frac{\lambda}{8 \cos \theta}$$ **(from Equation 1.17, Chapter 1)**

h is the threshold root-mean-square height of the irregularities, λ is the wavelength of energy travelling through the rock (between 25 and 40 m in Basalt 2), and θ is incidence angle (zero in these experiments). The geometry of the flows produces a modal height of ~ 2 m for surfaces in 2X and ~ 3 m for 2Y. The lower limit of h is 3.125 m, larger than the flow height of 2X but approaching the flow height of 2Y.

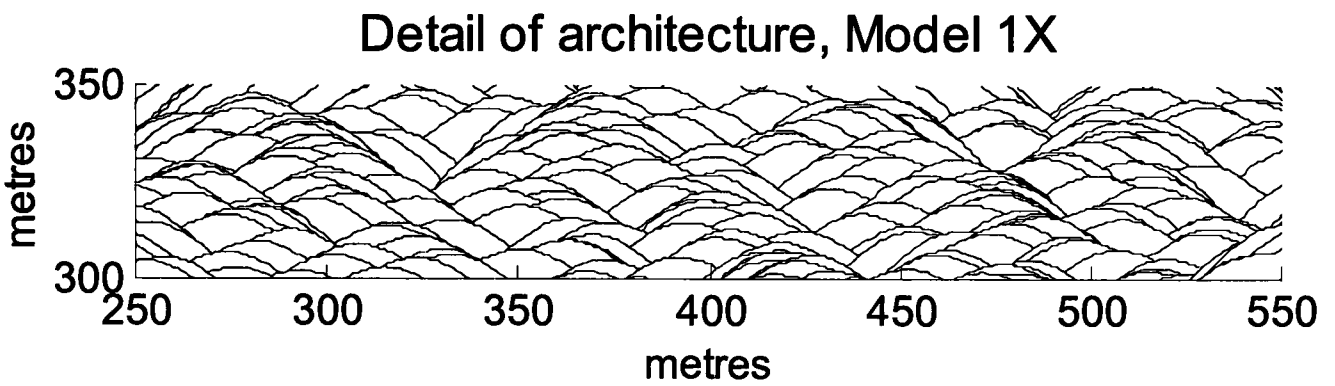

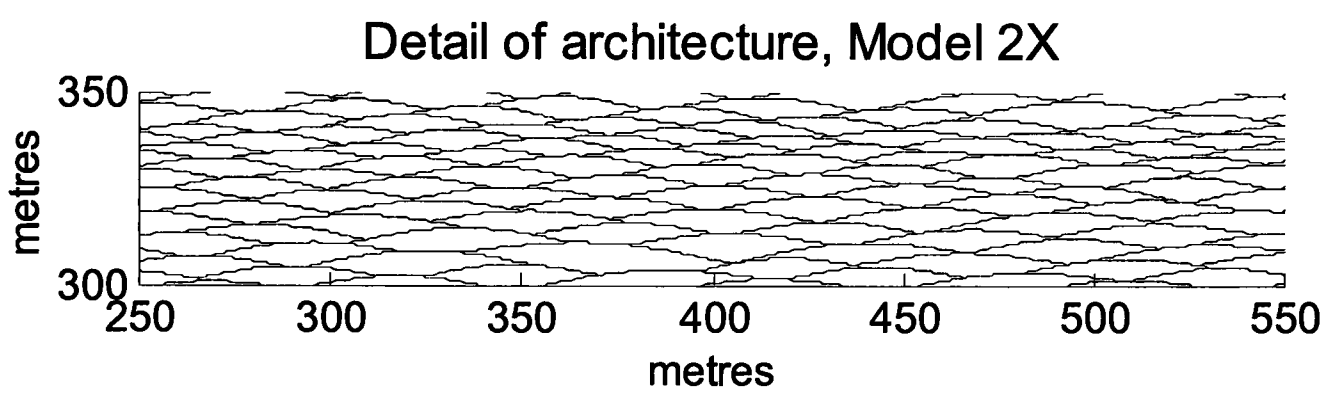

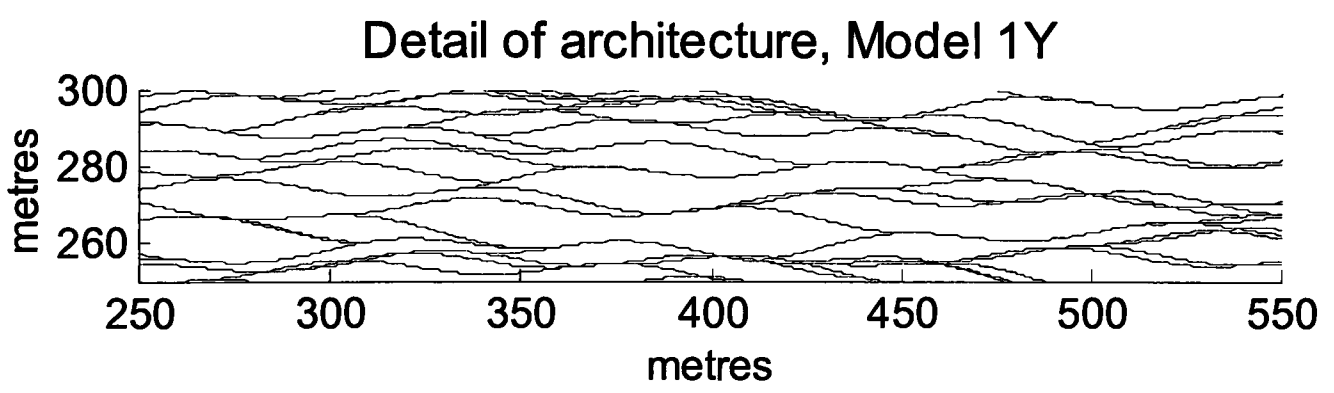

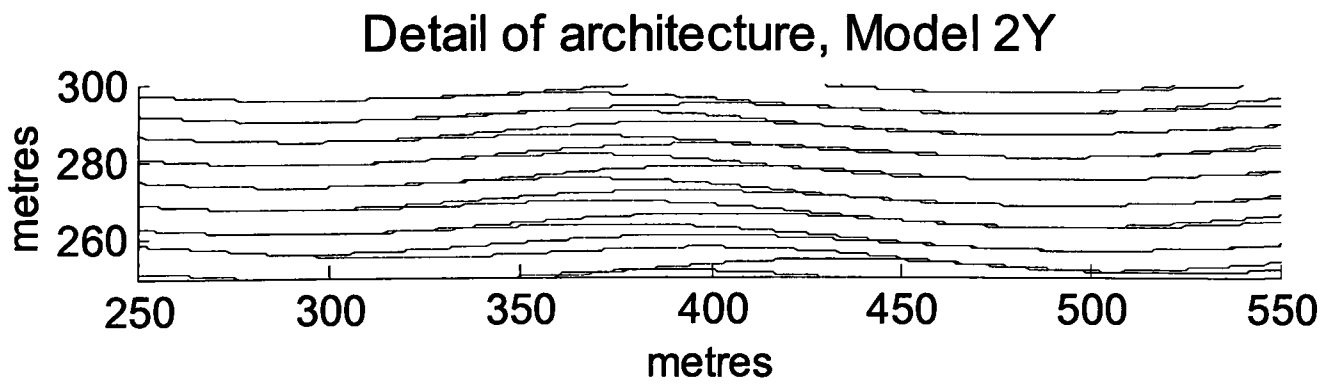

Figure 6.21. Details of Models 1 and 2, showing relative rugosity of surfaces.

6.5.2 AMPLITUDE OF THE PRIMARY WAVE

For each basalt model, maximum absolute amplitudes from the receiver traces were normalised to amplitudes derived from the homogeneous control experiment. This approximately corrected for geometric spreading and more clearly revealed any changes with depth.

Vertical array receivers in plane X of lobular Basalt 3 registered the greatest relative fluctuation in amplitude with depth, while vertical array receivers in plane X of varied-velocity Basalt 4 registered the least (Figure 6.22a). In plane Y, parallel to the direction of flow propagation, Basalt 4 again registered the least overall amplitude reduction and fluctuation (Figure 6.22b). Normalised maximum amplitudes from horizontal array receivers are compared in Figures 6.22c and d. In both planes, Basalt 3 showed the greatest deviation from a homogeneous case.

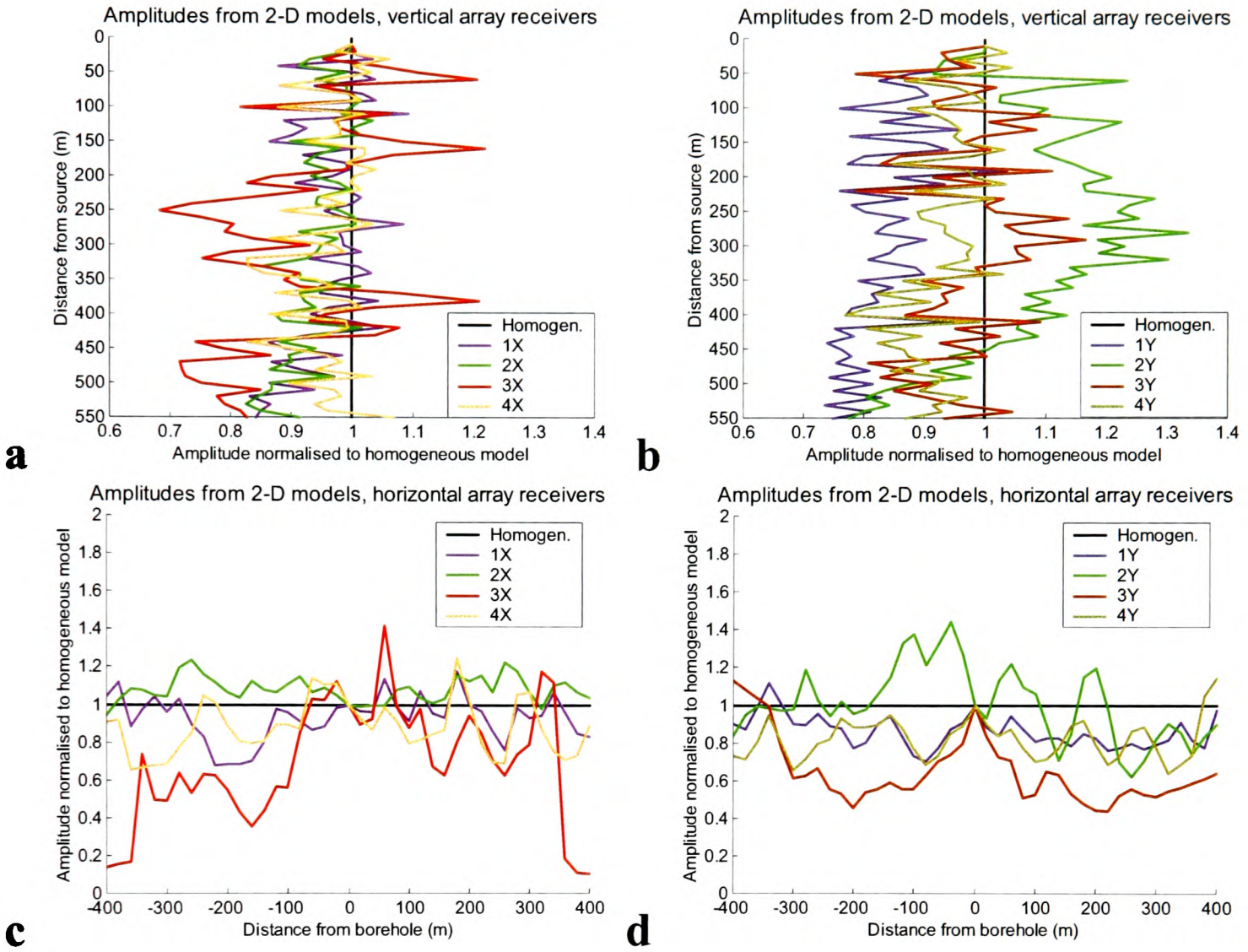

Figure 6.22.

Gain / loss in amplitude with depth, relative to propagation through a homogeneous model with velocity 5250 m/s.

a. Vertical receiver amplitudes in plane X, perpendicular to basalt flow direction.
b. Vertical receiver amplitudes in plane Y, parallel to basalt flow direction.
c. Horizontal receiver amplitudes in plane X, perpendicular to basalt flow direction.
d. Horizontal receiver amplitudes in plane Y, parallel to basalt flow direction.

1 **= narrow-flow, two-velocity basalt**
2 **= wide-flow, two-velocity basalt**
3 **= lobular basalt**
4 **= varied-velocity basalt**

Data from the separate 2-D cross-sections were then compared with responses from the full 3-D models, in order to study their amplitude relationships. In Figure 6.23, maximum amplitudes from lobular Basalt 3 and varied-velocity Basalt 4 are displayed, once again normalised to amplitudes from a homogeneous control experiment. For the vertical receivers, it was found that regardless of basalt type, normalised amplitudes in the 3-D case were roughly the average of those from the 2-D cross-sections. For the horizontal arrays, a weak correlation was observed between receivers in plane X of the 2-D and 3-D models. In plane Y there was almost no similarity (Figure 6.24).

6.23

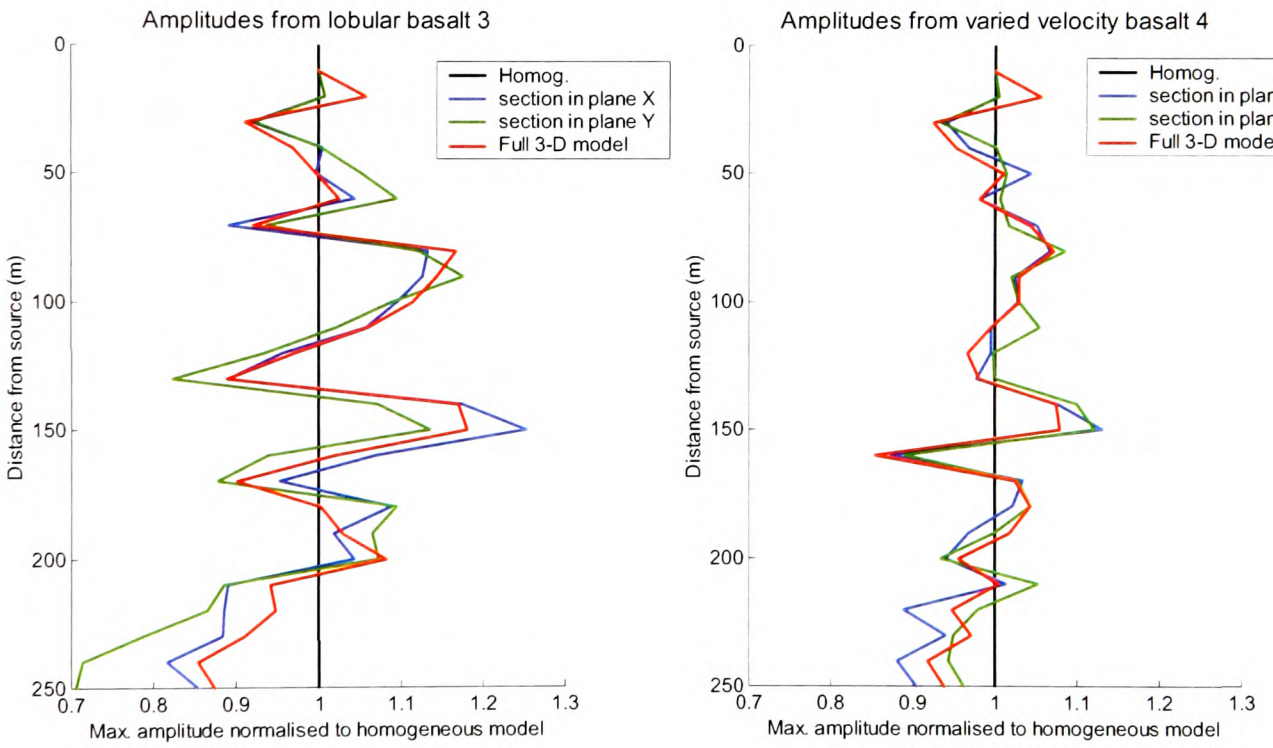

Figure 6.23.

Normalised vertical receiver array amplitudes from basalt types 3 and 4. Plane X is perpendicular to pahoehoe flow direction, plane Y is parallel to flow. Full 3-D model amplitudes are compared with separately modelled 2-D cross-sections.

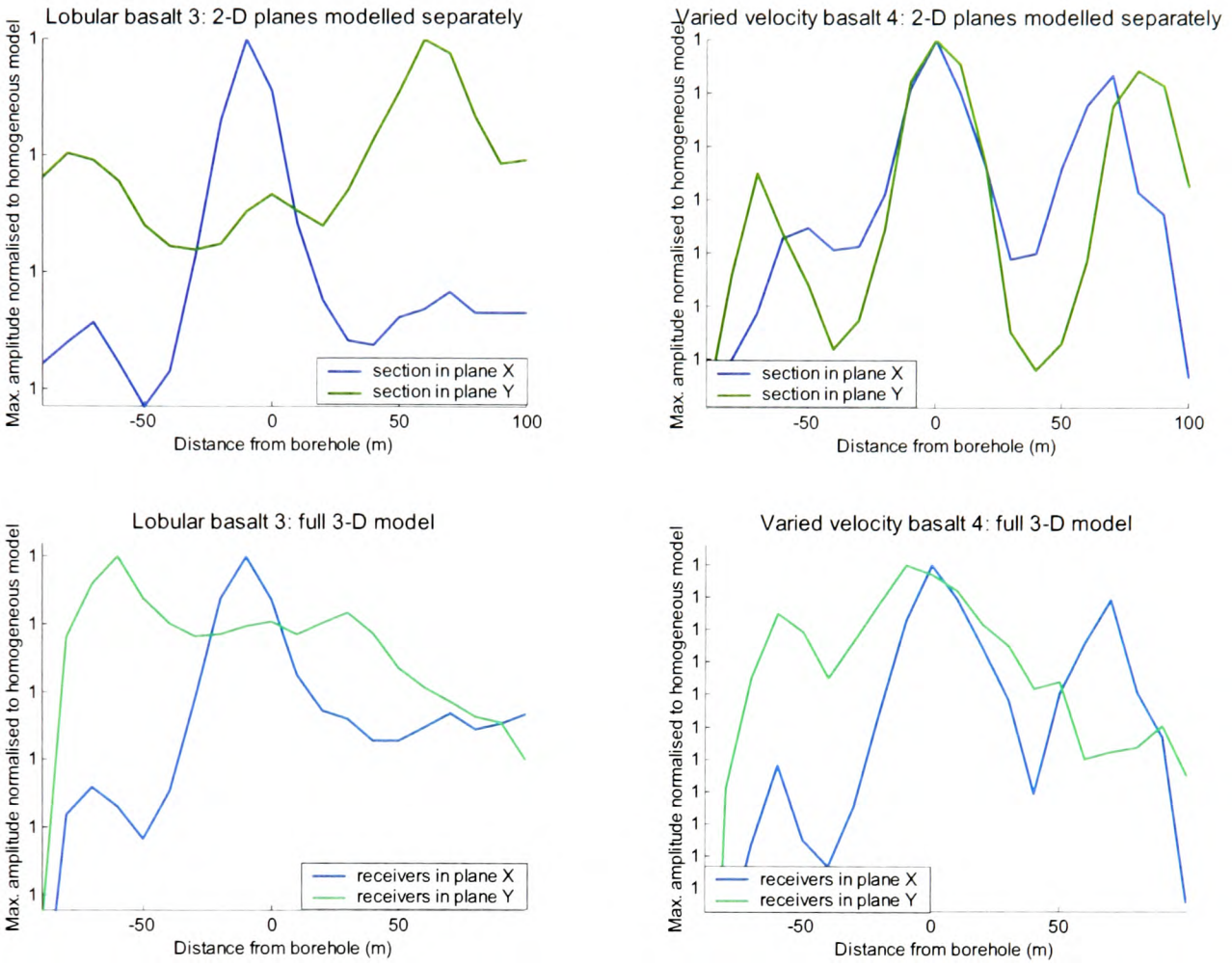

Figure 6.24.

Normalised horizontal receiver array amplitudes from basalt types 3 and 4. Plane X is perpendicular to pahoehoe flow direction, plane Y is parallel to flow. Full 3-D model amplitudes are compared with separately modelled 2-D cross-sections.

Maximum amplitudes for vertical array receivers in hypothetical 1000 x 1000 x 600 m 3-D volumes were predicted by averaging amplitudes from the 1000 x 600 m 2-D cross-sectional models (Figure 6.25). In comparison with Figure 6.22, the intensity of fluctuation is diminished. Once again, the 'large' model of lobular Basalt 3 deviated most from the homogeneous control, while varied-velocity Basalt 4 deviated least. No prediction was made for the horizontal array receivers; however it was noted that laterally propagating waves experienced the greatest amplitude reduction in Basalt 3.

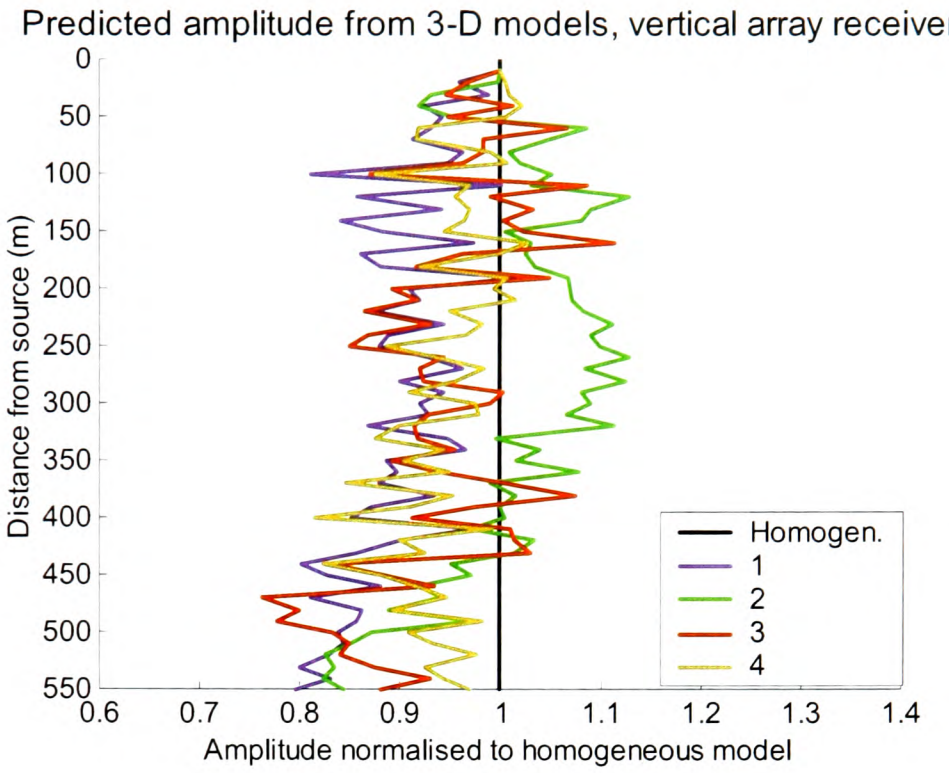

Figure 6.25.

Predicted relative amplitudes for a 3-D basalt volume of 600 m depth and 1000 m width, based on 2-D vertical receiver arrays in Figure 6.22. No averaged prediction for the horizontal receivers was made.

1 **= narrow-flow, two-velocity basalt**
2 **= wide-flow, two-velocity basalt**
3 **= lobular basalt**
4 **= varied-velocity basalt**

Q can be estimated from the decay of amplitude with depth, assuming the velocity and frequency are constant over the interval studied (see section 3.2.1 of this thesis). In all cases frequency, f, was fixed at 150 Hz. Velocity, c, was taken to be the mean value of the central vertical profile, which ranged between 4650 m/s and 5600 m/s in the 4 basalt types. As in the VSP studies, while the assumptions are not strictly correct, this method of Q derivation is useful in comparing model characteristics.

For a constant seismic quality factor over a certain bandwidth, the log amplitude ratio in relation to propagation distance is given by:

$$\ln\left(\frac{A}{A_0}\right)=\left(\frac{-\pi f}{Qc}\right)r \qquad \textbf{(from Equation 3.7, Chapter 3)}$$

The reference amplitude A_o was taken to be the maximum amplitude of the first trace. r represents the distance from the first receiver. After normalisation to amplitudes from the homogeneous model, log amplitude ratio was plotted against depth. Least-squares linear regression was applied, and Q was calculated from the gradient of the trend-line (Figure 6.26).

The two-velocity, narrow-flow basalt produced the most diffuse spread of data points and the highest mean Q value of ~ 520, while the two-velocity wide-flow basalt produced the lowest mean Q value of 26. Mean Q estimates in the region of 100 were obtained from the lobular basalt and varied velocity basalt. However, in all cases excepting Basalt 2, the range of Q values from 95% confidence limits is large.

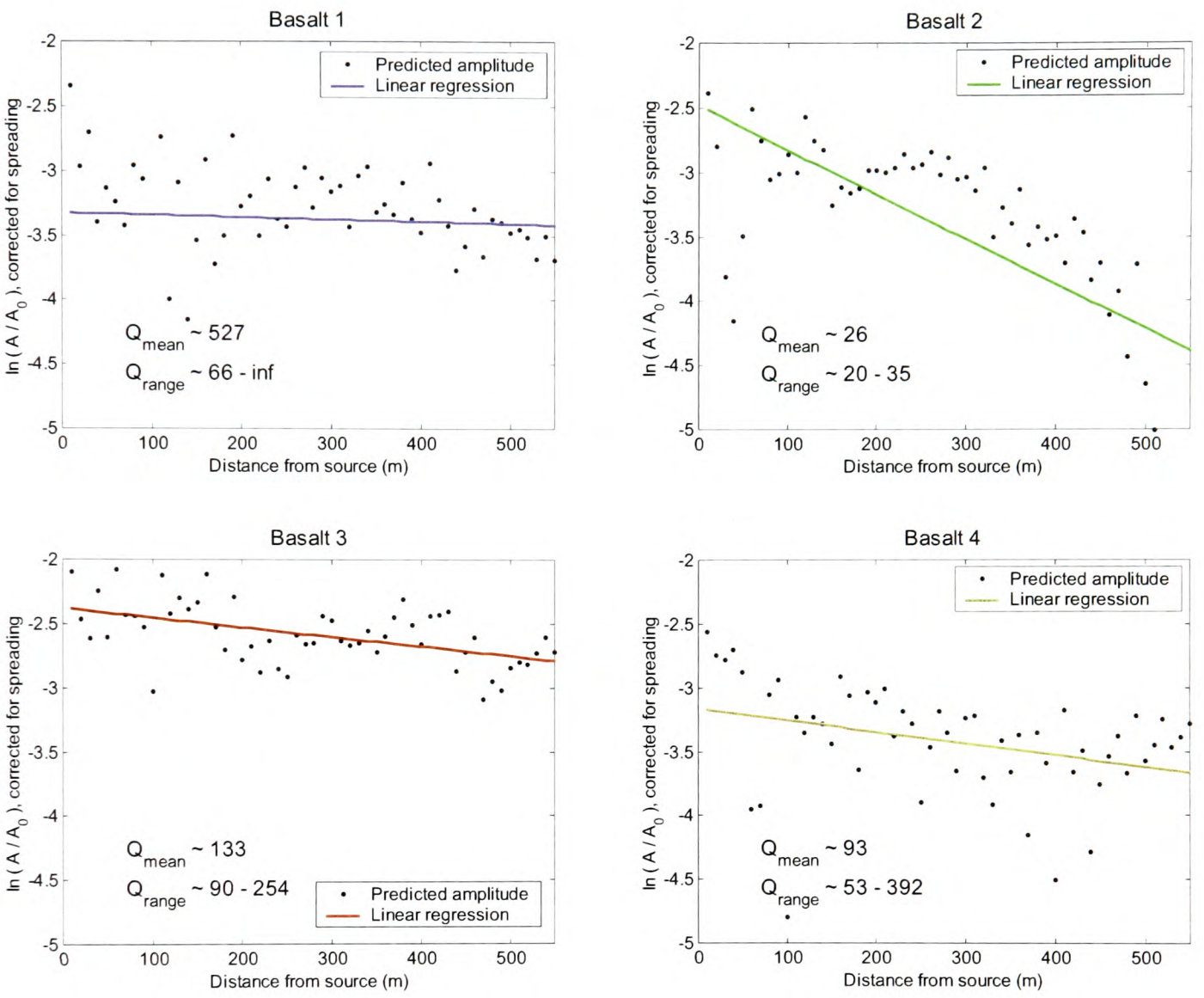

Figure 6.26.

Log of amplitude ratios versus depth for hypothetical 3-D models. (Also see Figure 6.25.) Mean Q estimates corresponding to regression lines are ~ 530, 30, 130 and 90 for Basalts 1- 4 respectively. The range in Q is given by a 95% confidence interval for the mean response.

Basalt 1 = narrow-flow, two-velocity basalt
Basalt 2 = wide-flow, two-velocity basalt
Basalt 3 = lobular basalt
Basalt 4 = varied-velocity basalt

6.5.3 SPECTRAL CONTENT OF THE PRIMARY WAVE

The primary wavelet from the deepest vertical receiver in each model was isolated using time-gates of a fixed length and taper for all waves, and log spectral ratios were taken with respect to the source spectrum. Spectral minima are clustered in the region between 200 and 300 Hz in all the 2-D models, but appear most strongly in 2X, 3X, 1Y, 2Y and 3Y. Figures 6.27a and b show the spectral content of this wavelet after 550 m of propagation through the 8 models.

These spectral minima are due to the velocity contrasts between crusts and cores, which are spaced approximately 5 m apart. Their positions in the spectrum correspond well with experimental results in Chapter 4: alternating velocity models with 5 m-thick layers produced interference minima centred on 225 Hz (Figure 4.14b).

The issue of persistent versus ephemeral multiples interfering with the primary wave was also introduced in Chapter 4, where WT scalograms were used to visualise coda content relative to the primary waves. Time-frequency analyses show that multiples in the pahoehoe models are persistent but low in intensity.

To contrast the spectral effects of 1-D and 2-D structure, horizontally planar models were constructed from vertical velocity profiles taken through the centre of the 2-D models. The resulting log spectral plots are shown in Figures 6.27c and d. Wide-flow Basalt 2X and the Y cross-sections already possess a significant degree of planarity,

hence the position of the notches remains virtually unchanged from the 1-D cases (Figures 6.27b,d). In 1X, 3X and 4X, which are more laterally variable, the minima are shifted in position. In the narrow-flow and varied velocity models, lateral variation also substantially reduces the intensity of the minima (Figures 6.27a,c).

6.27

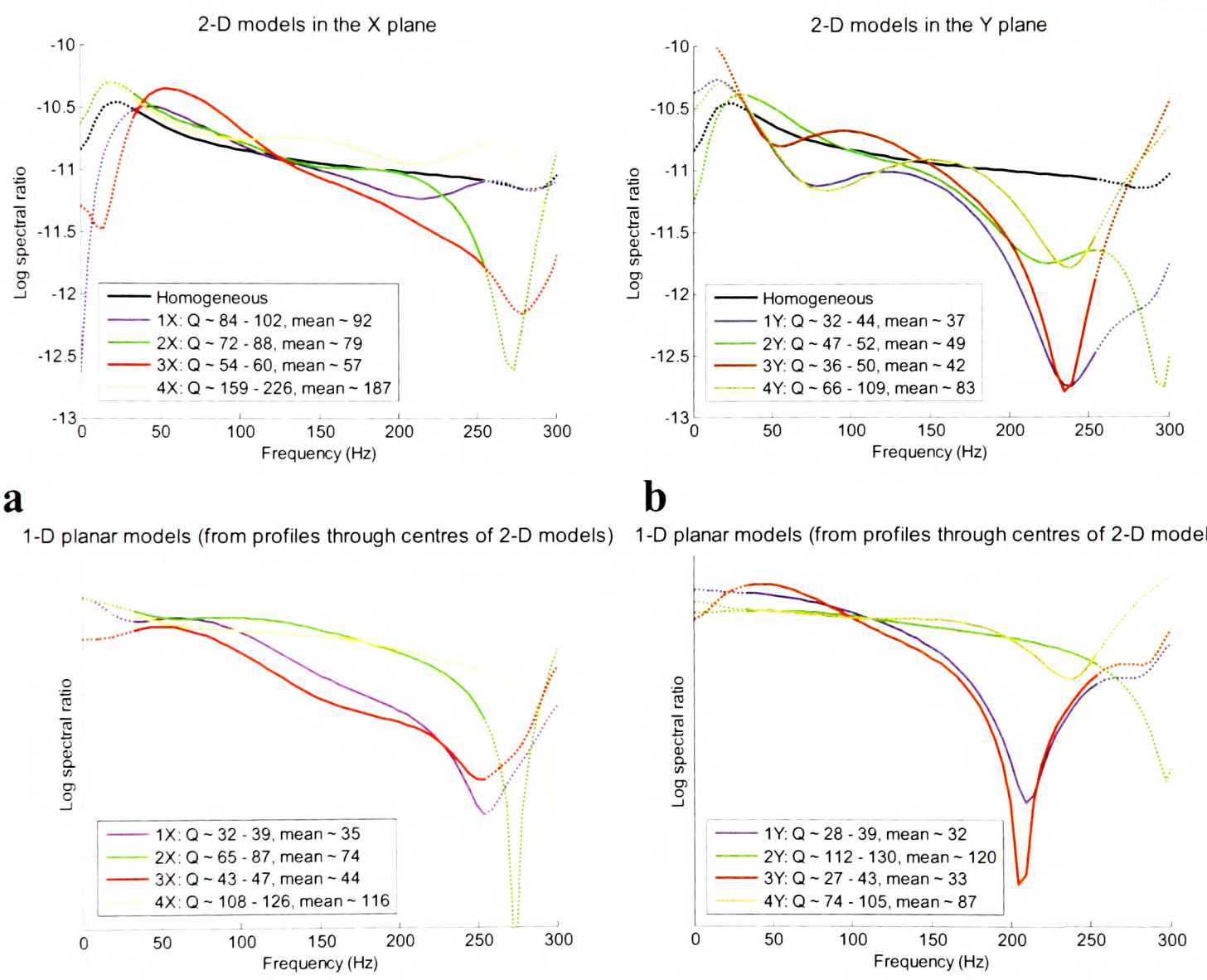

Figure 6.27. Log spectral ratios of a receiver at 550 m compared to the source in:
a, b. 2-D models.
c, d. 1-D planar models constructed from vertical velocity profiles through centres of the 2-D models.

***1* = narrow-flow, two-velocity basalt**
***2* = wide-flow, two-velocity basalt**
***3* = lobular basalt**
***4* = varied-velocity basalt**
X and Y are planes perpendicular and parallel to flow propagation, respectively.

Emboldened lines represent the bandwidth over which linear regression analysis was performed. Corresponding Q estimates are presented in the legend, ranging over a 95% confidence interval.

Linear regression analysis was performed over the main data-carrying bandwidth of 50 – 250 Hz and Q values were estimated from the 2-D models. Q was highly dependent on the sharpness of the spectral minimum as well as its position. Considering both planes X and Y, wide-flow Basalt 2 produced a Q range of 32 – 88 within 95% confidence limits. Lobular Basalt 3 produced Q values of 36 – 60. Narrow-flow Basalt 1 exhibited strong anisotropic behaviour in this experiment: Q of 1X lay between 84 and 102 while Q of 1Y ranged from 32 to 44. Varied-velocity Basalt 4 also exhibited dichotomous behaviour: a wave travelling through the plane parallel to flow direction produced Q values of 66 – 109; whereas propagation in the plane perpendicular to flow direction returned the highest Q estimates in this category of models, in excess of 150.

A major issue is whether higher-dimensional spectral effects arise in waves travelling through true 3-D basalt volumes. Log spectral ratios from the 200 m traces of the separate 2-D cross-sections were compared with those of the full 3-D models. Normalised log spectral ratios from lobular Basalt 3 and varied-velocity Basalt 4 are displayed in Figure 6.28. Here, as in all the 3-D basalt models, the influence of the velocity contrasts persisted and log spectral ratios were once again dominated by localised minima. In the central region of bandwidth (bold lines in Figure 6.28) the spectra appeared largely featureless. The 3-D responses appear to be averages of their corresponding 2-D responses, however this relationship is tenuous and the normalised graphs are inconclusive.

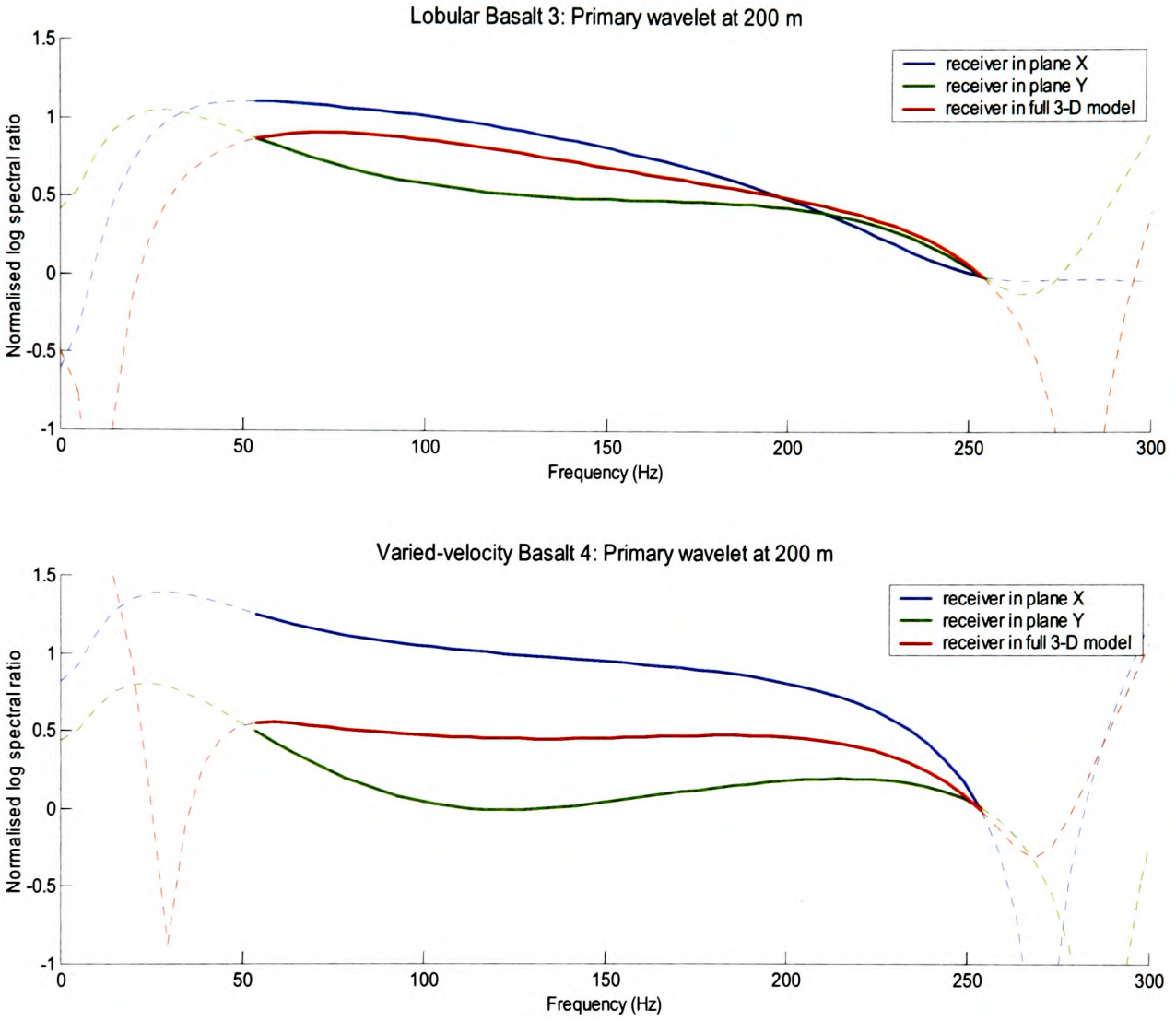

Figure 6.28.

Normalised log spectral ratio of primary wavelet at 200 m relative to the source, in basalt types 3 and 4. Plane X is perpendicular to pahoehoe flow direction, plane Y is parallel to flow. Log spectral ratios from the full 3-D model are compared with separately modelled 2-D cross-sections.

To track the response of primary waves as they travelled into the volume, log spectral ratios at each depth level were composited into a depth-frequency image. Figure 6.29 displays spectral responses of vertical receiver responses in Basalts 3 and 4, taken relative to the source. Light areas represent high values, and dark areas represent spectral minima.

The notches related to the crust-core velocity contrast can be seen undergoing subtle shifts at each depth level. For the lobular basalt, the minima appeared to shift towards lower frequencies when the wave propagates through the 3000 - 4600 m/s lobes (Figures 6.17 and 6.18). This correlation between velocity structure and the position of minima is echoed in the varied-velocity basalt, but not as clearly. Interestingly, at key velocity transitions, the shifts in minima take on a convex shape which arcs upwards. This phenomenon is most marked in the basalt models with greater planarity (3Y and 4Y, see Figure 6.29), and may be caused by interaction of the spherical (as opposed to planar) wavefront with the geometry of the scatterers.

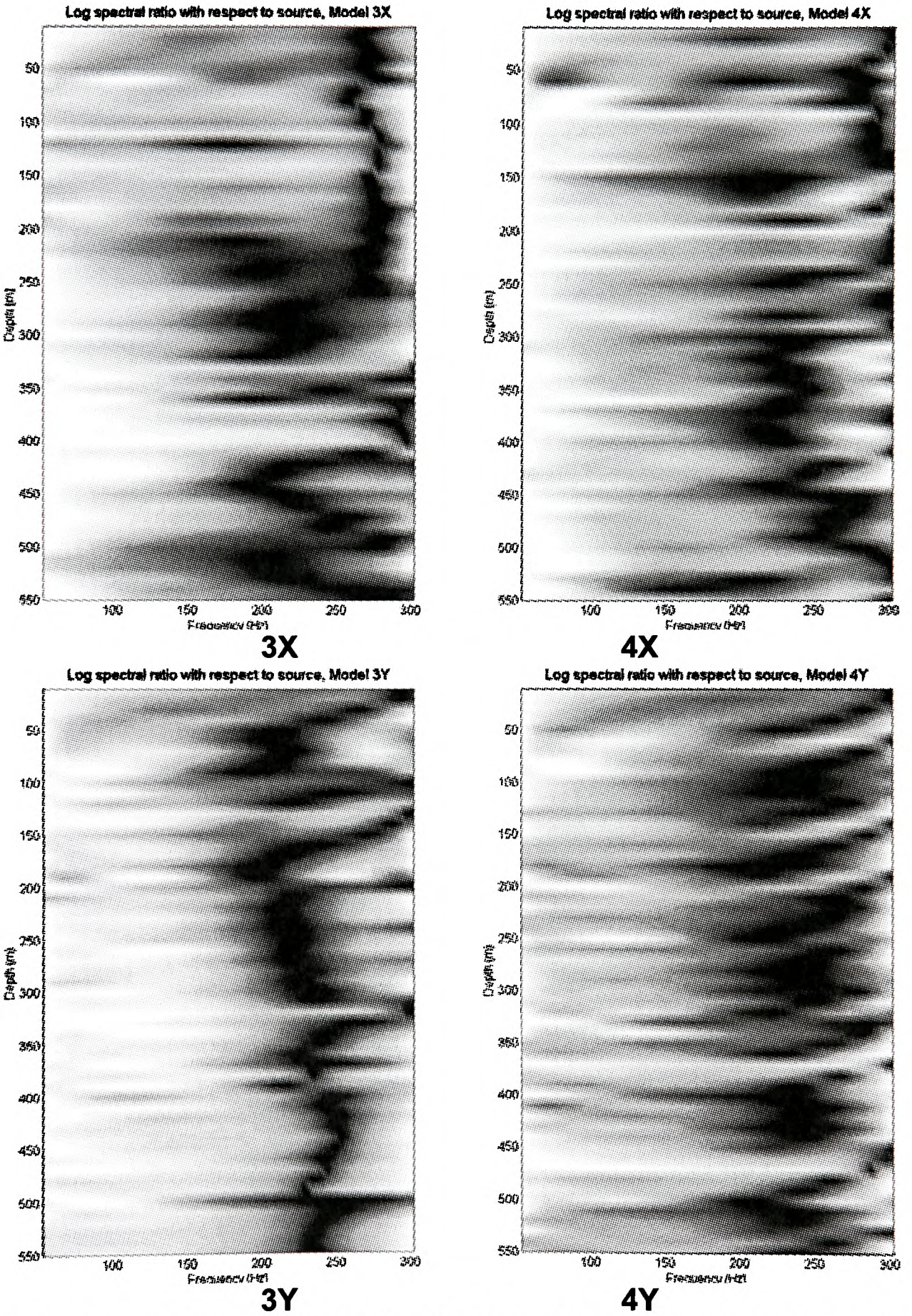

Figure 6.29. Composite view of log spectral ratios taken with respect to the same source signature. Frequency (Hz) is plotted on the x-axis, depth (m) on the y-axis. Dark areas are spectral minima.

6.6 DISCUSSION

2-D and 3-D models have been constructed in order to investigate volume scattering in basalts, particularly in the Middle Basalt Series, where high effective attenuation is not explicable by 1-D attenuation mechanisms. Multifractal behaviour has been observed in 1-D profiles of the basalt (Chapter 5, this thesis), and fractal noise models have been extended into two and three dimensions by other workers to investigate scattering (Martini & Bean, 2002). This work, however, favours the modelling of pahoehoe structures informed by geological fieldwork, optical televiewer images and borehole studies. A basic hummocky flow geometry is repeated over different scales, imparting loose multifractal and periodic characteristics to the structure of the models. The volumes increased in complexity from simple two-velocity models, through to a four-velocity lobular model and finally to a model with P-velocities drawn directly from the Vestmanna log data.

Q values derived from the various models and methods are summarised in Table 6.1. For all basalt types except the narrow-flow two-velocity case, greater complexity in spatial structure and velocity distribution lead to increased Q. This arises because resonance effects created by quasi-planar, periodic structures are diminished by lateral variation.

Table 6.1

Basalt Model Type		Q (spectral ratio)		Q (amplitudes)
		1-D ←	→ 2-D	3-D
Narrow-flow, 1	X	32 – **35** – 39	84 – **92** – 102	66 – **527** - inf
	Y	29 – **32** – 39	32 – **37** – 44	
Wide-flow, 2	X	65 – **74** – 87	72 – **79** – 88	20 – **26** – 35
	Y	112 – **120** – 130	47 – **49** – 52	
Lobular, 3	X	43 – **44** – 47	54 – **57** – 60	90 – **133** – 254
	Y	27 – **33** – 43	36 – **42** – 50	
Varied-velocity, 4	X	108 – **116** – 126	159 – **187** – 226	53 – **93** – 392
	Y	74 – **87** – 105	66 – **83** – 109	

Sections X and Y are perpendicular and parallel to flow direction, respectively.

Table 6.1. Q values derived from various models and methods in Chapter 6. The range is given by a 95% confidence interval of the mean response. Mean Q values are emboldened.

Lobular Basalt 3 produces strong fluctuations in amplitude with depth, a spatial manifestation of resonance discussed in section 4.4 of this thesis. In zones of transition between geological formations, proportions of massive tabular and compound braided flows are likely to vary, juxtaposing meso- and macro-scale flow structures. Potentially, low amplitude 'blind spots' could occur over tens to hundreds of metres. This may account for the changing amplitude trends seen in Glyvursnes (section 3.2). However, no strong amplitude fluctuations are apparent in Vestmanna.

Varied-velocity Basalt 4 is of greatest interest as it is the closest analogue of the Vestmanna rock volume. Q estimates from this model's 1-D profiles are similar to those

of the 1-D wireline log models ($Q_{Vestm.\ 1\text{-}D} \sim 47 - 96$, see Chapter 4). However, the 3-D model does not produce sufficient attenuation to match lower-bound estimates from the VSP data ($Q_{Vestmanna\ VSP} \sim 20 - 90$, mean Q in the region of 24 to 30). The main conclusion is that 3-D scattering cannot be the dominant mechanism of attenuation in the Middle Basalt Series.

CHAPTER 7

OVERVIEW AND CONCLUSIONS

7.1 OVERVIEW

This work has focused on the attenuating properties of Faroes basalts, combining observations from vertical seismic profiles and wireline log data with numerical modelling. In field data, measurement accuracy is limited by the circumstances of acquisition, whilst numerical experiments are limited by simplified physical principles and computing constraints. Energy loss has been quantified using seismic quality factor, Q, keeping in mind the gulf between attenuation theory and physical reality.

The synthetic models in this thesis follow a progression of increasing vertical and lateral complexity, related to various components of real basalt structure. Their associated Q values signify the proportion of energy loss, out of the total, that can result. Key estimates from all field data and numerical experiments are compiled in

Figure 7.1, noting in each case the method of analysis and the bandwidth over which it is applied. This provides a framework for comparison, but an important first principle is that 'correlation is not (necessarily) causation'. Where possible, efforts have been made to find more direct indication that certain attenuation mechanisms operate.

The consistent strategy of comparing synthetic data with field results means that the scale of investigation does not exceed 1 km^3 in volume. However, by filling the continuum between centimetre-scale wireline log data and the expansive coverage of conventional seismic surveys, VSP plays an important role in the wider area of basalt research.

7.2 EFFECTIVE ATTENUATION IN FAROES BASALTS

In **Chapters 2** and **3**, data from the two main field sites were pre-processed, and effective Q derived from an amplitude decay method and the spectral ratio method.

Seismic quality factor was found to be extremely low in both Glyvursnes and Vestmanna boreholes. These low estimates are compatible not only with findings from other localities in the North Atlantic Igneous Province (Christie *et al.*, 2002; Maresh *et al.*, 2003; Droujinine, 2005), but also with the Columbia River Basalts (Pujol & Smithson, 1991). Effective Q ranges between 10 and 45 in these previous basalt studies. It can therefore be assumed that even given a wide range of eruption scenarios, basalts share certain characteristics that impart low Q.

A *caveat* to comparing effective Q values is the difference in source bandwidth of surveys and the margin of error encountered in considering a constant Q model (Figure 7.1). Of the two VSPs studied here, the Glyvursnes data were of a much narrower bandwidth, and this had follow-on effects for all subsequent modelling and analyses. Despite this, there is robust evidence that effective Q increases with depth in Glyvursnes, but remains steady at all depths in Vestmanna.

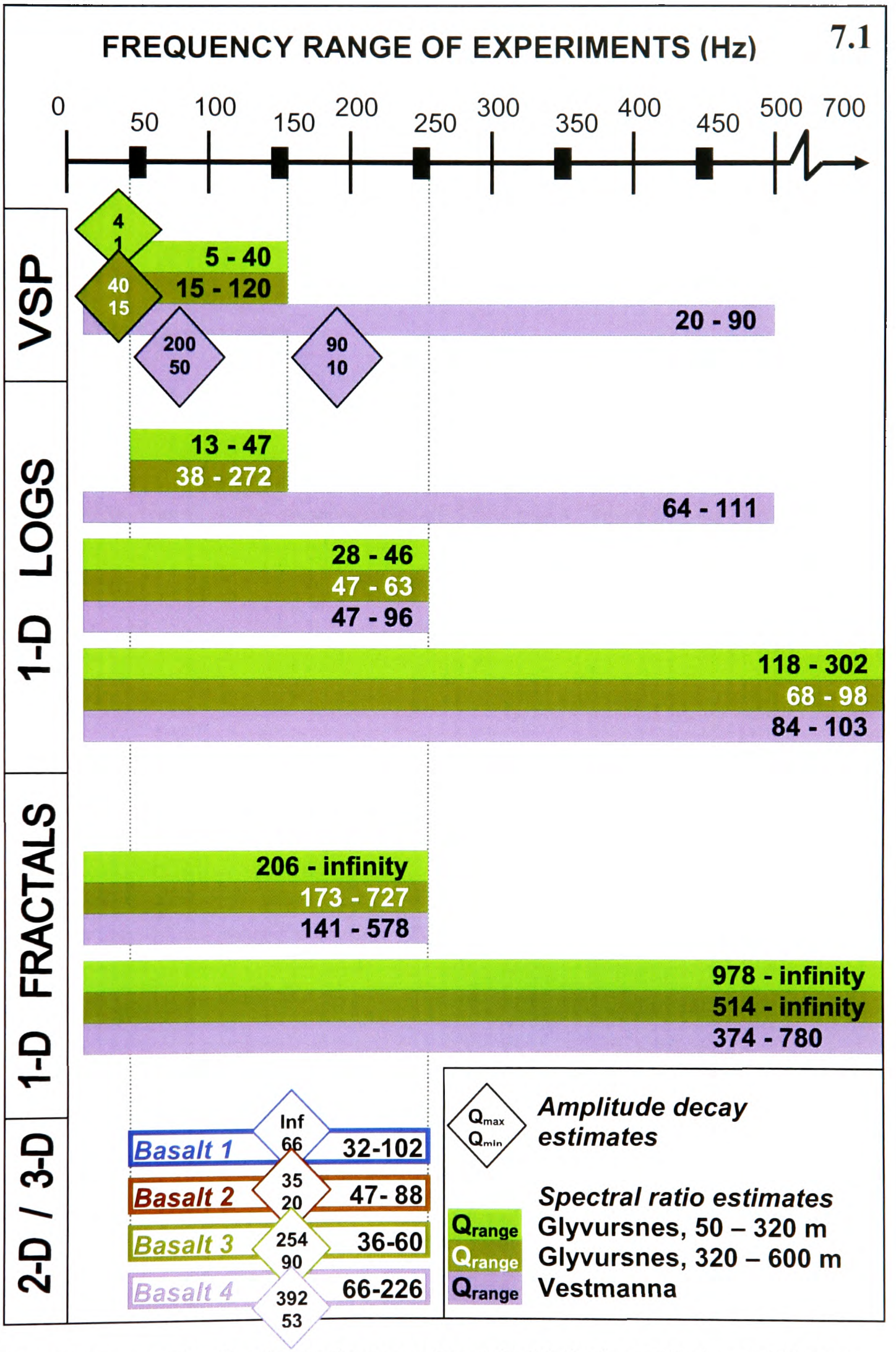

Figure 7.1. The range of key Q estimates from experiments in this thesis, and the bandwidths over which they were calculated.

7.3 MODELLING OF POSSIBLE ATTENUATION MECHANISMS

7.3.1 MULTIPLE SCATTERING FROM NEAR-PLANAR LAYERS

In **Chapter 4**, acoustic modelling was performed on horizontally layered models constructed from wireline log data.

For synthetic sources derived from VSP traces, 1-D scattering Q estimates were comparable to effective Q in the upper section of Glyvursnes. Despite some spread from error estimation, 1-D scattering Q was substantially higher in the lower section of Glyvursnes and both sections of Vestmanna. The interim conclusion was that 1-D scattering was dominant in the upper section of Glyvursnes and less significant in the other basalt intervals.

However, important features of multiple scattering were revealed through acoustic modelling with zero-phase source wavelets. Short-lag multiples have a large effect on the estimation of Q. These multiples may be ephemeral and thus do not accurately represent the true scattering potential of the sequence. In cases where multiples are persistent, intense destructive / constructive interference occurs in both time and frequency domains. This resonance phenomenon is controlled by periodicity in the velocity structure, which creates spectral minima at preferred frequencies. The disruptive effect of multiples on the propagating wavelet is therefore frequency-dependent.

This has several implications. The assumption of approximately exponential loss from 1-D scattering (Equation 1.15) is based on statistical averaging (Burridge *et al.*, 1988). However, if the rock structure has a dominant periodicity, the averaging effect is non-uniform, and exponential loss cannot be automatically assumed. The applicability of the additive relationship in Equation 1.16 must therefore be considered in context.

Amongst the 1-D models considered, the 50 – 320 m interval of Glyvursnes was alone in generating persistent, intense multiples. It was also the only model to reproduce specific interference features seen in corresponding VSP data. This is directly linked to its coarse-layered macro-structure, and to the emplacement style of flows in the Upper Basalt Series.

7.3.2 FRACTALS IN NEAR-PLANAR LAYERS

The heterogeneity of wireline log data, and its impact on seismic response, was assessed in **Chapter 5**.

Analyses based on second-order statistics determined that log data from the Glyvursnes, Vestmanna and Lopra boreholes were fractal in nature. More sophisticated analysis, using Continuous Wavelet Transforms, enabled the intermittency of the log data to be quantified. These signals were found to be multifractal, and furthermore, data from different geological formations could be distinguished by their multifractal exponents.

Multiplicative cascade algorithms were used to generate synthetic signals with the same multifractal character, and the same range of velocity and density values as the Faroes wireline logs. Acoustic modelling was performed. Subsequent spectral ratio analysis returned very low levels of 1-D scattering attenuation. This demonstrated that multifractal character does not in itself produce intense multiples. Instead, the redistribution of energy over a range of scales prevents resonant interference at seismic frequencies. This reinforces observations from **Chapter 4** that attenuation is an interaction between the spatial structure of the rock and the bandwidth of the sensing wavelet.

The fractal nature of basalts must be considered carefully, as fractal statistics are increasingly a part of research into crustal heterogeneity. This work has shown that 1-D multifractals can produce a vastly different seismic response to real log data. This problem is compounded when extrapolating fractals into two and three dimensions. A 1-D signal taken from a volume is a form of statistical sampling or 'cut'. The constraints placed on the true 3-D nature can be weak or strong and cannot be assumed beforehand (Mandelbrot, 1989).

7.3.3 SCATTERING IN PAHOEHOE-TYPE BASALTS

In **Chapter 6,** the architecture of modern and ancient basalt terranes was reviewed, including observations from the Faroes field sites. Pahoehoe lava flows were identified as the primary building block of basalts. Their low-velocity vesiculated crusts, high-velocity cores and variable flow patterns can be a major source of heterogeneity on the scale of a VSP survey.

3-D basalt models were generated from a pahoehoe flow algorithm. *Basalt 1* was a 3-D extrapolation of the periodic two-velocity model studied in **Chapter 4**. *Basalt 2* tested the effect of larger lateral-to-vertical aspect ratio on seismic response, and was intermediate in structure between a 1-D planar model and *Basalt 1*. *Basalt 3* had a lobular structure superposed on the framework of smaller flows. The lobes had a maximum thickness of 100 m, with varying thickness intersected by the vertical receiver array. This introduced macro-scale velocity structure with a degree of spatial periodicity. *Basalt 4* had a varied velocity structure based on the log values of the Vestmanna VSP interval, and expressed the highest degree of heterogeneity. This model was considered to be a plausible analogue for Middle Series rocks.

All the models were designed to have a degree of anisotropy, inherent from the flow algorithm. One major assumption was that the aspect ratio of lava flows is smaller in the plane perpendicular to flow direction.

The basalt models were run through a numerical algorithm simulating elastic wave propagation (the Discrete Particle Scheme), in 3-D and in 2-D (allowing the anisotropic effects to be distinguished). The resulting seismograms were studied using both an amplitude decay method and the spectral ratio method of Q analysis. Wavefront coherence and the intensity of scattered energy were also assessed.

The nature of basalt emplacement creates a complex inter-relationship between velocity variation, morphology of scatterers, surface rugosity and anisotropy. However, some distinction between the effects is made here:

- **Incoherence of the wavefront**

Morphology of scatterers / velocity variation: The greatest disruption to the wavefront is caused by macro-scale velocity structures. Between models with only flow-scale structures, lava flows with a higher aspect ratio generate less wavefront disruption. Increased velocity variation in pahoehoe flows further reduces any scattering effects.

Anisotropy: The wavefield is generally more scattered in the plane perpendicular to flow than in the plane parallel to flow.

Surface rugosity: The exception to the above anisotropic effect occurs when packing geometry, rather than flow shape, controls the rugosity of surfaces. This may lead to increased surficial scattering, as described by Makinde *et al.* (2005).

- **Amplitude decay in the downgoing P-wave**

Amplitudes fluctuate significantly over a 550 m interval, and at certain depths are higher than amplitudes in a homogeneous control volume. The magnitude of attenuation thus varies across different intervals and velocity structures. Averaged Q estimates were taken over the full depth interval of the models, but these may give a poor indication of the style and intensity of the scattering effect.

Morphology of scatterers / velocity variation: A realistic velocity distribution produces little apparent energy loss after 550 m of propagation.

Anisotropy: At vertical incidence, normalised amplitudes from a combined 3-D volume are approximately the average of amplitudes from the orthogonal cross-sections. With increasing lateral variation, this relationship no longer holds true.

- **Spectral effects in the downgoing P-wave**

The velocity contrast between pahoehoe crusts and cores creates spectral minima akin to those seen in 1-D wireline log models. These spectral minima are reinforced by periodicity in the 3-D volume.

Morphology of scatterers / surface rugosity: The spectral minima significantly shift in position due to interaction between the geometry of the scatterers and the spherical

shape of the wave envelope. While this is expected in lateral wave propagation, this is also observed in the vertically propagating P- wave, and has an impact on the calculation of Q.

Overall, increased velocity variation at the scale of individual pahoehoe flows diminishes the resonant interference effect discussed in **Chapter 4**. This decreases the intensity of total scattering attenuation. Macro-scale lobular structures (from hypothetical changes in lava chemistry) introduce fluctuations in amplitude decay and spectral effects. Within seismic bandwidths, these are relatively more significant than pahoehoe-scale heterogeneity. However, neither of these elements appears to be a dominant source of attenuation within the Middle Basalt Series.

7.4 INTRINSIC ATTENUATION IN BASALTS

Crystalline rocks have been associated with high Q in various studies. Q was found to be 2000 at 20 Hz in the 4 – 9 km interval of the KTB continental deep borehole (Jia & Harjes, 1997), and lunar basalts were found to have a P-wave Q of ~ 3000 at seismic wavelengths (Nakamura & Koyama, 1982). At the kHz and MHz scale, compressional wave Q values of 120 to 250 have been reported from dry basalt samples by Gordon & Davis (1968) and from an Oman ophiolite by Wepfer & Christensen (1990).

Recently, far lower values have been derived from saturated vesicular and pillow basalts at elevated pressures (Wepfer & Christensen, 1991). The attenuation was directly related to strong alteration of the oceanic basalts, accompanied by low density and high porosity measurements. Tompkins & Christensen (2001) conducted experiments on a further 30 basalt samples from the Bermuda Rise, the Gulf of California and the Costa Rica Rift. These rocks varied in their ages and proximity to spreading ridges, and produced P-wave intrinsic Q values of 10 and 110 under saturated conditions. Two experiments on dry samples yielded intrinsic Q of ~ 15 and ~ 56 for pressures of 50 MPa. At pressures of 300 MPa, Q values still reached a minimum of 16 in 110 Ma-old samples. These samples were again associated with high porosity (8.8 %) and low density (2565 kg/m^3).

Having concluded that scattering is of diminished importance in Vestmanna and the lower 300 m of Glyvursnes, the remaining feasible mechanism of energy loss is that of anelastic attenuation from the presence of volatiles.

The structure of the Southeast Greenland Margin is extremely similar to that of the Faroes. Detailed studies of flow zonation and alteration in Greenland basalts, undertaken by Planke *et al.* (1999), suggest that during emplacement there is rapid alteration of the exposed flows, with pathways provided by high vesicularity and jointing in the young lava crusts. This creates an impermeable surficial layer, under which continued hydrothermal flow could occur in the rest of the vesicular / fractured crust. The alteration products of basalt are clay minerals known by the general term of

zeolites. McGreevy (1982) suggests that small amounts of clay mineral may cause microfissures to form when basalts are periodically exposed to moisture. Rather than closing the fractures completely, the cyclic expansion and dehydration of clays might cause the rock fabric to deteriorate.

As in the Greenland basalts, alteration and high vesicularity (strongly associated with the lava crusts) are observed at all depth intervals in both Vestmanna and Glyvursnes (Waagstein & Andersen, 2003; Jørgensen, 2005). Glyvursnes and Vestmanna rock samples have been analysed for gas permeability, He-porosity and grain density determination by Olsen (2005). P and S-wave velocities were also measured at different hydrostatic pressure conditions relevant to reservoir conditions. Porosity was highest in lava crusts and breccias, up to 10 % in Vestmanna, and up to 28 % in Glyvursnes. Maximum permeability was 0.58 mD in Glyvursnes lava crust samples, and 1.79 mD in Vestmanna lava crust samples. In comparison, samples from the interior lava cores had low porosity of typically 0 – 5 %, and low permeability of less than 0.03 mD (Olsen, 2005; Japsen & Waagstein, 2005).

Direct modelling of intrinsic attenuation is problematic, for a number of reasons. There is the general dilemma of upscaling from the domain of poroelastic theory to the domain of seismic wavelengths. Various workers (e.g. Berryman & Wang, 1995; Pointer *et al.*, 2000; Chapman, 2003) address the issue of upscaling by incorporating meso-scale features (usually fractures or joints) with micro- or grain scale features (porosity) into theoretical rock models. Their modelling results suggest that cracks and

pores in the rock enable fluid movement to significantly affect wave propagation in the exploration frequency band.

A related problem is that conceptual rock models are almost exclusively based on reservoir sandstones with mixtures of clay or shale. While theoretical models employ simple geometries which are applicable over a range of pore shapes and crack aspect ratios (e.g. Chapman *et al.*, 2002), certain parameters used in effective media simulations (such as those described by Pointer *et al.*, 2000; Chapman, 2003) translate awkwardly between sedimentary and crystalline rocks. For instance, primary porosity in sedimentary rocks is governed by interstitial grain space, whereas basalt 'porosity' derives from vesicles, amygdales and large vugs in brecciated horizons. In both cases, the void spaces can be treated as approximately spherical, and analogies can be drawn between grain size and the average distance between void spaces in basalt. However, there are fundamental differences in the distribution and interconnectivity of these spaces, as well as differences in the provenance of the fluids in them. Such factors bring into question the applicability of these models for quantifying intrinsic Q in basalts.

One variant rock model incorporates equant porosity with randomly orientated cracks (Pointer *et al.*, 2000). To estimate the extent of intrinsic attenuation possible in Faroes basalts, velocity, density, permeability and porosity values were taken from laboratory petrophysical measurements (Olsen, 2005). The radii, aspect ratios and density of cracks in Faroes rocks were unknown and the values used are largely arbitrary.

The crack density, ε, is a dimensionless parameter. It is given by:

$$\varepsilon = \frac{Na^3}{V} \qquad \textbf{(7.1)}$$

where N is the number of cracks of radius a, in a volume V. Crack densities of 0.05 – 0.07 are thought to be characteristic of crustal rocks which have exceeded fracture criticality (Crampin, 1994). By trial substitution of parameter values, it was found that lava core samples with a crack density of 0.05, a crack aspect ratio of 0.001 and a crack radius of 3×10^{-3} m produce Q estimates of 35 – 55. Lava crusts with an arbitrary crack density of 0.07, a crack aspect ratio of 0.001 and a crack radius of 3×10^{-3} m were found to produce Q of 33 – 40. These Q values only serve as guidelines, but show that over the 100 – 1000 Hz frequency range, intrinsic mechanisms are possible sources of attenuation in basalts. The corresponding hypothetical 1/Q curves are plotted in Figure 7.2.

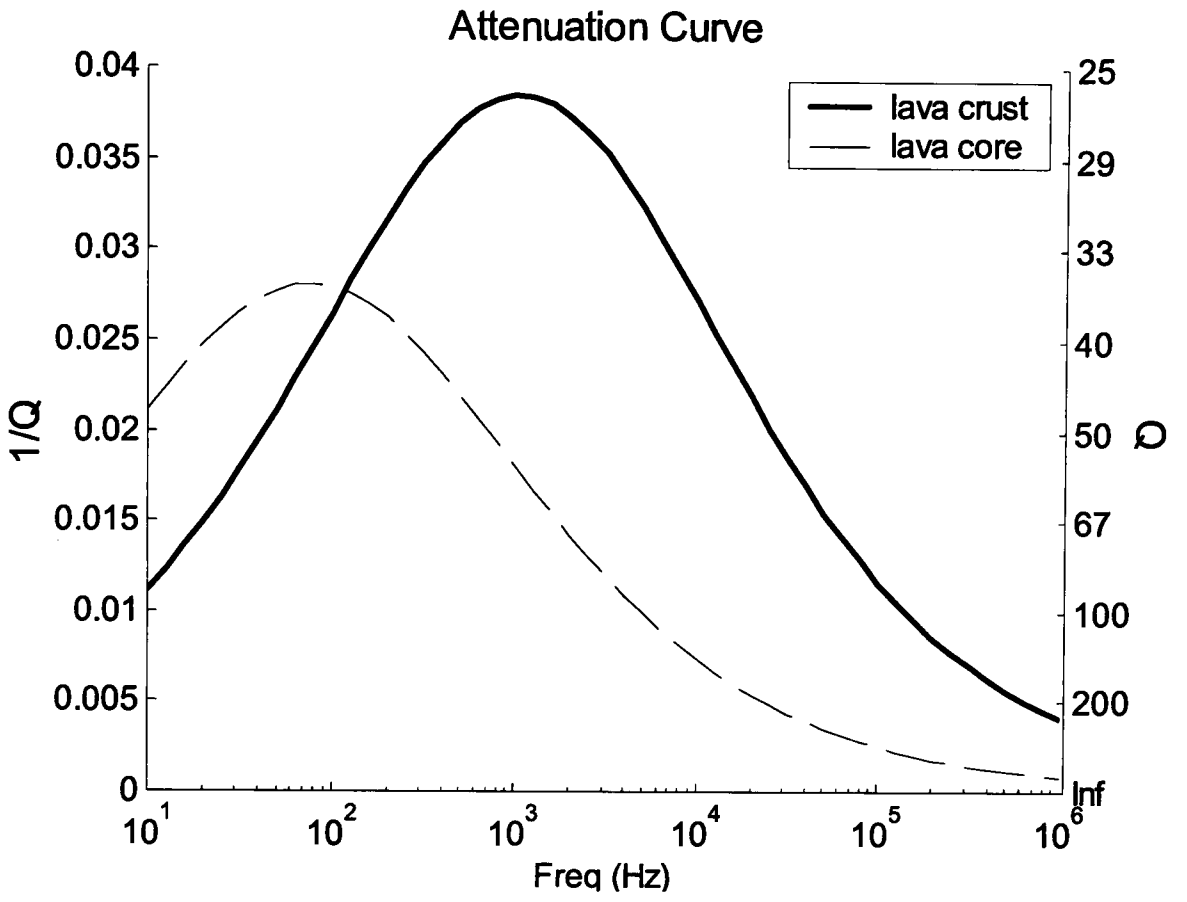

Figure 7.2. Attenuation curves for theoretical rock models with petrophysical characteristics of Faroes rock samples.

Lava crust: crack density = 0.07, crack aspect ratio = 0.001, crack radius = 3 x 10^{-3} m, permeability = 5.72 x 10^{-16} m^2, porosity = 0.206. Q ~ 33 – 40.

Lava core: crack density = 0.05, crack aspect ratio = 0.001, crack radius = 3 x 10^{-3} m, permeability = 1.97 x 10^{-17} m^2, porosity = 0.072. Q ~ 35 – 55.

Tompkins & Christensen (2001) tackle the issue of upscaling by successfully matching velocity–density relationships measured at ultrasonic frequencies to borehole-scale velocity–density relationships. Their intrinsic Q estimates lie within the range of seismic Q measurements from oceanic basalts, and increasing attenuation is shown to be on a linear trend with increasing porosity. Fluid flow is again suggested as the attenuation mechanism common to both seismic and ultrasonic scales in oceanic basalts (Lewis & Jung, 1989).

7.5 CONCLUSIONS

The observations compiled in this thesis do not fully quantify the different forms of attenuation, but show a range of seismic responses from basalt complexity at the sub-kilometre scale.

There is strong evidence that on the scale of the field experiments, 3-D scattering is negligible. 1-D scattering dominates in the Upper Basalt Series at Glyvursnes, but its effect is diminished in the Middle Basalt Series, which lacks a latent periodic velocity structure. While evidence for the necessary fluid flow is inconclusive, the low effective Q observed in field data indicates intrinsic attenuation to be a significant component of energy dissipation in Faroe Island basalts.

Distinguishing scattering losses from intrinsic losses remains difficult, which has implications for practical problems such as sub-basalt imaging. For a survey within a 'black-box', uncharacterised basalt volume, the low-pass filtering effect of the volume may make low-frequency exploration seismic sources attractive (e.g. Ziolkowski *et al.*, 2003). However, deleterious multiple energy (from layers with unknown spatial periodicity) could combine with intrinsic attenuation (operating at frequencies controlled by open fracture sets). Coupled with narrow bandwidth, this becomes disadvantageous to detecting and interpreting structures under the basalt layer. The presence of dominantly compound braided flows may decrease overall scattering loss. However, the increased ratio of weathered surfaces to unaltered lava cores may be a factor in fluid flow and intrinsic attenuation.

It is stressed that understanding the regional heterogeneity and loss mechanisms outweighs the importance of the Q estimates themselves. The techniques of analysis and modelling explored in this thesis could realistically be applied to other terranes, with the aim of further linking seismic properties to geological characteristics.

REFERENCES

Anderson, D. L. 1994. Sublithospheric mantle as the source of continental flood basalts – the case against the continental lithosphere and plume head reservoirs. *Earth. Planet. Sci. Lett.* **123**, 269 – 280.

Andersen, M. S., Boldreel, L. O. Hansen, H. K. 2005. Analysis of wireline logs through basaltic successions in nine wells from the Faroe-Shetland area. *SeiFaBa Report, Geological Survey of Denmark and Greenland (GEUS).*

Backus, G. E. 1962. Long-wave anisotropy produced by horizontal layering. *Journal of Geophysical Research*, **66**, 4427 – 4440.

Bacry E., Muzy, J-F. & Arneodo, A. 1993. Singularity spectrum of fractal signals from wavelet analysis: Exact results. *Journal of Statistical Physics*, **70**, 635 – 674.

Balch, A. H., Lee, M. W., Miller, J. J. & Ryder, R. T. 1982. The use of vertical seismic profiles in seismic investigations of the earth. *Geophysics,* **47**, 906 – 918.

Båth, M. 1974. Spectral Analysis in Geophysics, *In: Developments in Solid Earth Geophysics, Elsevier, Amsterdam.*

Beaty, K. S., Bellefleur, G., Kay, I., Mah, M., Perron, G. & contributors. 1998-2003. DSISoft customized VSP processing software (freeware). *Seismology and Electromagnetic Section/ Continental Geosciences Division/Geological Survey of Canada.*

Berryman, J. G. & Wang, H. F. 1995. The elastic coefficients of double-porosity models for fluid transport in jointed rocks. *J. Geophys. Res.*, **100**, 24611 – 24627.

Biot, M. A. 1956. Theory of propagation of elastic waves in a fluid saturated porous solid. I. Low frequency range and II. High frequency range. *J. Acoust. Soc. Am.*, **28**, 168 – 191.

Boldreel, L. O. & Andersen, M. S. 1993. Late Paleocene to Miocene compression in the Faroe–Rockall area. *In: Parker, J.R. (ed.): Petroleum geology of Northwest Europe: Proceedings of the 4th Conference, 1025–1034. London: Geological Society.*

Bondre, N. R., Duraiswami, R. A. & Dole, G. 2004. A brief comparison of lava flows from the Deccan Volcanic Province and the Columbia-Oregon Plateau Flood Basalts: Implications for models of flood basalt emplacement. *Proc. Indian Acad. Sci. (Earth Planet. Sci.)*, **113**(4), 809 – 817.

Bourbié, T., Coussy, O. & Zinszner, B. 1987. Acoustics of porous media. *Institut Français du Pétrole Publications, 334 pages.*

Bruno, B. C., Taylor, G. J., Rowland, S. K., Lucey, P. G. & Self, S. 1992. Lava flows are fractals. *Geophysical Research Letters*, **19**, 305 – 308.

Burridge, R., Papanicolaou, G. & White, B. 1988. One-dimensional wave propagation in a highly discontinuous medium. *Wave Motion*, **10**, 19 – 44.

Carcione, J. M. 2001. Wave fields in real media: wave propagation in anisotropic, anelastic and porous media. *Pergamon. 390 pages.*

Cerney, B. & Carlson, R. L. 1999. The effect of cracks on the seismic velocities of basalt from Site 990, Southeast Greenland Margin. *Proceedings of the Ocean Drilling Program, Scientific Results*, **163**, 29 – 35.

Chapman, M. 2003. Frequency-dependent anisotropy due to meso-scale fractures in the presence of equant porosity. *Geophysical Prospecting*, **53**, 369 – 379.

Chapman, M., Zatespin, S.V. & Crampin, S. 2002. Derivation of a microstructural poroelastic model. *Geophys. J. Int.*, **151,** 427 – 451.

Christie, P.A.F., Gollifer, I. & Cowper, D. 2006. Borehole seismic studies of a volcanic succession from the Lopra-1/1A borehole in the Faroe Islands, northern North Atlantic: *Geological Survey of Denmark and Greenland Bulletin* **9**, 23 – 40.

Crampin, S. 1994. The fracture criticality of crustal rocks. *Geophys. J. Int.,* **118**, 428 – 438.

Der, Z. 1998. High-frequency P- and S- wave attenuation in the Earth. *Pure Appl. Geophys*, **153**, 273 – 310.

Dolan, S., Bean, Christopher J. & Riollet, B. 1998. The broad-band fractal nature of heterogeneity in the upper crust from petrophysical logs. *Geophys. J. Int.,* **132**, 489 – 507.

Droujinine, A. 2005. Sub-basalt decoupled walkaway VSP imaging. *Geophysical Prospecting*, **53**, 37 – 63.

Dvorkin, J. & Nur, A. 1996. Elasticity of high-porosity sandstones: Theory for two North Sea datasets. *Geophysics*, **61**, 1363 – 1370.

Eldholm, O. & Grue, K. 1994. North Atlantic volcanic margins: dimensions and production rates. *J. Geophys. Res.*, **99**, 2955 – 2968.

Ellis, D., Bell, B. R., Jolley, D. W. & O'Callaghan, M. 2002. The stratigraphy, environment of eruption and age of the Faroes Lava Group, NE Atlantic ocean. *In: Jolley, D. W. & Bell, B. R. (eds). The North Atlantic Igneous Province: Stratigraphy, Tectonic, Volcanic and Magmatic Processes. Geological Society Special Publications,* **197**, 253 – 269.

Esmersoy, C. 1984. Polarization analysis, rotation and velocity estimation in three-component VSP. *In: Toksöz, M. N. & Stewart, R. S. (eds.) Vertical Seismic Profiling, part B, Advanced Concepts. Handbook of Geophysical Exploration,* **14B**, 236 – 255.

Frankel, A. & Wennerberg, L. 1987. Energy-flux model of seismic coda: Separation of scattering and intrinsic attenuation, *Bulletin of the Seismological Society of America*, **77**(4), 1223 – 1251.

Futterman, W. 1962. Dispersive body waves. *J. Geophys. Res.*, **67**, 5279 – 5291.

Hald, N. & Waagstein, R. 1984. Lithology and chemistry of 2-km sequence of Lower Tertiary tholeiitic lavas drilled on Suðuroy, Faeroe Islands (Lopra-1). *In: Berthelsen, O., Noe-Nygaard, A. & Rasmussen, J. (eds) The deep drilling project 1980-1981 in the Faeroe Islands. Føroya Fróðskaparfelag, Tórshavn*, 15 – 38.

Halsey, T.C., Jensen, M. H., Kadanoff, L. P., Procaccia, I. & Shraiman, B. I. 1986. Fractal measures and their singularities: The characterization of strange sets. *Physical Review A,* **33**, 1141 – 1151.

Hardage, B.A. 2000. Vertical Seismic Profiling: Principles. *Handbook of Geophysical Exploration, 14. 3rd edn. Pergamon.*

Harris, P. E., Kerner, C. & White, R. E. 1997. Multichannel estimation of frequency-dependent Q from VSP data. *Geophysical Prospecting*, **45**, 87 – 109.

Herrmann, F. 1998. Multiscale analysis of well and seismic data. *Mathematical Methods in Geophysical Imaging V, Proceedings of SPIE*, **3453**, 180 – 208.

Holliger, K. 1996. Upper-crustal seismic velocity hetereogeneity as derived from a variety of P-wave sonic logs. *Geophysical Journal International*, **115**, 813 – 829.

Hudson, J. A. 1981. Wave speeds and attenuation of elastic waves in material containing cracks. *Geophys. J. Royal Astronom. Soc.*, **64**, 133 – 150.

Hurst, H. E., Black, R. P. & Simaika, Y. M. 1965. Long Term Storage; An Experimental Study. *(Constable, London).*

Ishimaru, A. 1997. Wave Propagation and Scattering in Random Media. *Oxford Academic Press, New York.*

Japsen, P. & Waagstein, R. 2005. Preliminary analysis of ultrasonic and geochemical

properties of core samples from Glyvursnes-1 and Vestmanna-1, Faroe Islands. *SeiFaBa Report. Geological Survey of Denmark and Greenland (GEUS).*

Jensen, A. & la Cour-Harbo, A. 2000. Ripples in Mathematics: The Discrete Wavelet Transform. *Springer.*

Jerram, D. A. 2002. Volcanology and facies architecture of flood basalts. *In: Menzies, M. A., Klemperer, S. L., Ebinger, C. J. & Baker, J. (eds) Volcanic rifted margins. Geological Society of America, Special Papers*, **362**, 121 – 135.

Jerram, D. A., Mountney, N., Holzförster. F. & Stollhofen, H. 1999. Stratigraphic relation in the Etendeka Group in the Huab Basin, NW Namibia: Understanding the onset of flood volcanism. *Journal of Geodynamics*, **28**, 393 – 418.

Jia, Y. & Harjes, H-P. 1997. Seismische Q-Werte als Ausdruck von intrinsischer Dämpfung und Streudämpfung der kristallinen Kruste um die KTB-Lokation. *ICDP-Kolloquium, Bochum.*

Jørgensen, O. 2005. Zeolites and other secondary minerals in the drill core Glyvursnes-1, Faroe Islands. *SeiFaBa Report. Geological Survey of Denmark and Greenland (GEUS).*

Kang, I. B. & McMechan, G. A. 1994. Separation of intrinsic and scattering Q based on frequency-dependent amplitude ratios of transmitted waves. *Journal of Geophysical Research,* **99**, B12, 23875 – 23885.

Kennett, B. L. N. 1979. Theoretical reflection seismograms for elastic media. *Geophysical Prospecting*, **27**, 301 – 321.

King, M. S. 2005. Rock-physics developments in seismic exploration: A personal 50-year perspective. *Geophysics*, **70**(6), 3ND-8ND.

Kiørboe L & Petersen S, A. 1995. Seismic investigation of the Faeroe basalts and their substratum. *In: Scrutton, R.A., Stoker, M.S, Shimmield, G. B. & Tudhope, A. W. (eds), The Tectonics, Sedimentation and Palaeoceanography of the North Atlantic Region. Geological Society Special Publication*, **90**, 111 – 122.

Kjartansson, E. 1979. Constant Q-wave propagation and attenuation. *J. Geophys. Res.*, **84**, 4737 – 4748.

Knopoff, L. 1964. *Q. Rev. Geophys*, **2**, 625 – 660.

Lerche, I. & Menke, W. 1986. An inversion method for separating apparent and intrinsic attenuation in layered media. *Geophys. J. Royal Astronom. Soc.*, **87**, 333 – 347.

Levander, A. R. 1990. Seismic scattering near the Earth's surface. *Pure and Applied Geophysics*, **132**, 21 – 47.

Lewis, B. T. R. & Jung, H., 1989. Attenuation of refracted seismic waves in young oceanic crust. *Bull. Seism. Soc. Am.*, **79**, 1070 – 1088.

Liu, H. P., Anderson, D. L. & Kanamori, H. 1976. Velocity dispersion due to anelasticity; implications for seismology and mantle composition. *Geophys. J. Royal. Astr. Soc.*, **47**, 41 – 58.

Liu, E., Hudson, J. A. & Pointer, T. 2000. Equivalent medium representation of fractured rock. *Journal of Geophysical Research, B, Solid Earth and Planets*, **105**(2), 2981 – 3000.

Macbeth, C. 2002. Multi-Component VSP Analysis for Applied Seismic Anisotropy. *Handbook of Geophysical Exploration, 26. Pergamon.*

Mahoney, J. J. & Coffin, M. F. (eds) 1997. Large Igneous Provinces: Continental, Oceanic and Planetary Volcanism. *American Geophysical Union, Geophysical Monograph, **100**.*

Makinde, W., Favretto-Cristini, N. & de Bazelaire, E. 2005. Numerical modelling of interface scattering of seismic wavefield from a random rough interface in an acoustic medium: comparison between 2D and 3D cases. *Geophysical Prospecting*, **53**, 373 – 397.

Mallat, S. 2001. A wavelet tour of signal processing, 2nd edn. *Academic Press.*

Mandelbrot, B. 1989. Multifractal measures, especially for the geophysicist. *PAGEOPH.* **131**, 5 – 42.

Mandelbrot, B. 1990. Negative fractal dimensions and multifractals. *Physica A*, **163**, 306 – 315.

Mandelbrot, B. 1997. Fractales, Hasard et Finance. *Flammarion.*

Maresh, J., Hobbs, R. W., White, R. S. & Smallwood, J. R. 2003. Attenuation of Atlantic margin basalts using downhole VSP. *73rd Meeting, Society of Exploration Geophysicists, Expanded Abstracts*, 1310 – 1313.

Maresh, J. & White, R. S. 2005. Seeing through a glass, darkly: strategies for imaging through basalt. *First Break,* **23**(5), 27 – 33.

Marsan, D. & Bean, C. J., 2002. Multifractal modeling and analyses of crustal heterogeneity. In: Holliger, K. & Goff, J. A. (eds) *Heterogeneity in the Crust and Upper Mantle: Nature, Scaling and Seismic Properties, Kluwer Academics.*

Martini, F. & Bean, C. J. 2002. Interface scattering versus body scattering in sub-basalt imaging and application of prestack wave equation datuming. *Geophysics*, **67**(5), 1593 – 1601.

Martini, F., Hobbs, R. W., Bean, C. J. & Single, R. 2005. A complex 3D volume for sub-basalt imaging. *First Break*, **23**, 41 – 51.

Mavko, G. M. & Nur, A. 1979. Wave attenuation in partially saturated rocks. *Geophysics*, **44**, 161 – 178.

Mavko, G., Mukerji, T. & Dvorkin, J. 1998. The Rock Physics Handbook. Tools for seismic analysis in porous media. *Cambridge University Press.*

McDonal, F. J., Angona, F. A., Milss, R. L., Sengbush, R. L. van Nostrand, R. G. & White, J. E. 1958. Attenuation of shear and compressional waves in Pierre shale. *Geophysics*, **23**, 421 – 439.

McGreevy, J. P. 1982. Hydrothermal alteration and earth surface rock weathering: a basalt example. *Earth Surf. Processes Landforms*, **7**, 189 – 195.

Monette, L. & Anderson, M. P. 1994. Elastic and fracture properties of the two-dimensional triangular and square lattices. *Modelling and Simulation in Materials Science and Engineering*, **2**, 53 – 66.

Morlet, J., Arens, G., Fourgeau, E. & Giard, D. 1982. Wave propagation and sampling theory:
- Part I: complex signal & scattering in multilayered media.
- Part II: sampling theory and complex waves.

Geophysics, **47**, 203 – 236.

Nakamura, Y. & Koyama, J. 1982. Seismic Q of the lunar upper mantle. *J. Geophys. Res.*, **87**, 4855 – 4861.

Newman, P. 1973. Divergence effects in a layered earth. *Geophysics*, **38**, 481 – 488.

O'Brien, G. S. & Bean, C. J. 2004. A 3D discrete numerical elastic lattice method for seismic wave propagation in heterogeneous media with topography. *Geophysical Research Letters*, **31**, L14608, doi:10.1029/2004GL020069.

O'Brien, P. & Lucas, A. L. 1971. Velocity dispersion of seismic waves. *Geophysical Prospecting*, **19**, 1 – 26.

O'Doherty, R. F. & Anstey, N. A. 1971. Reflections on amplitudes. *Geophysical Prospecting*, **19**, 430 – 458.

Ogilvie, J. S., Crompton, R. & Hardy, N. M. 2001. Characterization of volcanic units using detailed velocity analysis in the Atlantic Margin, West of Shetlands, United Kingdom. *The Leading Edge, January 2001*, 34 – 50.

Olsen, D. 2005. Special Core Analysis for the SeiFaBa Project: Ultrasonic velocity measurements on plug samples from the Vestmanna-1 and Glyvursnes-1 wells, Faroe Islands. *SeiFaBa Report. Geological Survey of Denmark and Greenland (GEUS).*

Papworth, T. J. 1985. Seismic exploration over basalt covered areas in the U.K. *First Break*, **3**(4), 20 – 32.

Passey, S. R. 2005. Geology of Glyvursnes, Streymoy, Faroe Islands. A contribution to the SeiFaBa project. *Faroese Geological Survey.*

Peterson, D. W. & Tilling, R. I., 1980. Transition of basaltic lava from pahoehoe to aa, Kilauea Volcano, Hawaii: field observations and key factors. *Journal of Volcanology and Geothermal Research*, **7**, 271 – 293.

Planke, S. & Cambray, H. 1998 Seismic properties of flood basalts from hole 917A downhole data, Southeast Greenland volcanic margin. *Proceedings of the Ocean Drilling Program, Scientific Results*, **152**(5), 453 – 462.

Planke, S., Cerney, B. Bücker, C. J. & Nilsen, O. 1999 Alteration effects on petrophysical properies of subaerial flood basalts: site 990, Southeast Greenland margin. *Proceedings of the Ocean Drilling Program, Scientific Results*, **163**, 17 – 28.

Planke, S., Symonds, P. A., Alvestad, E. & Skogseid, J. 2000. Seismic volcanostratigraphy of large-volume basaltic extrusive complexes on rifted margins. *Journal of Geophysical Research*, **105**, 19335 – 19351.

Pointer, T., Liu, E. & Hudson, J. A. 2000. Seismic wave propagation in cracked porous media. *Geophys. J. Int.*, **142**, 199 – 231.

Pride, S. R., Tromeur, E. & Berryman, J. G. 2002. Biot slow-wave effects in stratified rock. *Geophysics*, **67**, 271 – 281.

Pujol, J., Fuller, B. N. & Smithson, S. B. 1989. Interpretation of a vertical seismic profile conducted in the Columbia Plateau basalts. *Geophysics*, **54**(10), 1258 – 1266.

Pujol, J. M., Lüschen, E. & Hu, Y. 1998. Seismic wave attenuation in metamorphic rocks from VSP data recorded in Germany's continental super-deep borehole. *Geophysics*, **63**, 354 – 365.

Pujol, J. & Smithson, S. 1991. Seismic wave attenuation in volcanic rocks from VSP experiments. *Geophysics*, **56**(9), 1441 – 1455.

Pujol, J. 2003. Elastic wave propagation and generation in seismology. *Cambridge University Press, 444 pages.*

Rasmussen, J. & Noe-Nygaard, A. 1970. *Geology of the Faeroe Islands (pre-Quaternary). Geological Survey of Denmark & Iceland Series, no. 25.*

Reidel, S.P. & Hooper, P.R., (eds). 1989. Volcanism and Tectonism in the Columbia River Flood Basalt Province. *Geol. Soc. Am. Spec. Pap.* **239**. 386 pp.

Renne, P. R., Zichao, Z., Richards, M. A., Black, M. T. & Basu, A. R. 1995. Synchrony of causal relations between Permian-Triassic boundary crises and Siberian Flood Volcanism. *Science*, **269**, 1413 – 1416.

Richards P. G. and Menke W., 1983. The apparent attenuation of a scattering medium, *Bulletin of the Seismological Society of America*, **73**(4), 1005 – 1021.

Richardson, K. R., Smallwood, J. R., White, R. S., Snyder, D. B. & Maguire, P. K. H. 1998. Crustal structure beneath the Faroe Islands and the Faroe-Iceland Ridge. Tectonophysics, **300**, 159 – 180.

Saunders, A. D., Fitton, J. G., Kerr, A. C., Norry, M. J. & Kent, R. W. 1997. The North Atlantic Igneous Province. *In: Mahoney, J.J. & Coffin, M.F. (eds) Large Igneous Provinces: Continental, oceanic, and planetary flood volcanism. American Geophysical Union, Geophysical Monograph*, **100**, 45 – 94.

Schertzer, D. & Lovejoy, S. 1987. Physically based rain and cloud modeling by anisotropic, multiplicative turbulent cascades. *J. Geophys. Res.*, **92**, 9692 – 9714.

Schoenberg, M. 1993. Isotropic constituent layers equivalent to a transversely isotropic medium. *European Association of Exploration Geophysists 55th meeting and technical exhibition; Stavanger; extended abstracts of papers.*

Schoenberger, M. & Levin, F. 1978. Apparent attenuation due to intrabed multiples, II. *Geophysics*, **43**, 730 – 737.

Schwab, F. & Knopoff, L. 1971. Surface waves on multilayered anelastic media. *Bull. Seism. Soc. Am.,* **61**, 893 – 912.

Self, S., Keszthelyi, L. & Thordarson, Th. 1998. The importance of pahoehoe. Annual Review of Earth and Planetary Sciences, **26**, 81 – 110.

Self, S., Thordarson, Th. & Keszthelyi, L. 1997. Emplacement of continental flood basalt lava flows. *In: Mahoney, J.J. & Coffin, M.F. (eds) Large Igneous Provinces: Continental, Oceanic and Planetary Volcanism. American Geophysical Union, Geophysical Monograph*, **100**, 381 – 410.

Single, R. T. & Jerram, D. A. 2004. The 3D facies architecture of flood basalt provinces and their internal heterogeneity: examples from the Palaeogene Skye Lava Field. *Journal of the Geological Society, London*, **161**, 911 – 926.

Smith, R. B., 2000. Classification of Synthetic Seismogram Methods. http://www.mines.utah.edu/~rbsmith/TEACHING/GG6220/IntriWaveTheory.htm

Stacey, F. 1992. Physics of the Earth. *Brookfield, Brisbane.*

Stainsby, S. D. & Worthington, M. H. 1985. Q estimation from vertical seismic profile data and anomalous variations in the central North Sea. *Geophysics*, **50**(4), 615 – 626.

Staples, R. K., White, R. S., Bransdóttir, B., Menke, W. H., Maguire, P. K. H. & McBride, J. H. 1997. The Faeroe-Iceland Ridge Experiment 1: Crustal structure of northeastern Iceland. *J. Geophys. Res.*, **102**, 7849 – 7866.

Strang, G. 1993. Wavelet transforms versus Fourier transforms. *Bulletin of the AMS*, **28**(2), 288 – 305.

Tompkins, M. J. & Christensen, N. I. 2001. Ultrasonic P- and S-wave attenuation in oceanic basalt. *Geophys. J. Int.*, **145**, 172 – 186.

Tonn, R. 1990. The determination of seismic quality factor from VSP data: A comparison of different computational methods. *Geophysical Prospecting*, **39**, 1 – 27.

Toomey, A. & Bean, C. J. 2000. Numerical simulation of seismic waves using a discrete particle scheme. *Geophysical Journal International*, **141**, 595 – 604.

Torrence, C. & Compo, G. 1998. Practical Guide to Wavelet Analysis. *Bulletin of the American Meteorological Society*, **79**(1), 61 – 78.

Turcotte, D. L. 1997. Fractals and Chaos in Geology and Geophysics, 2nd edn. *Cambridge University Press.*

Uvi_Wave Wavelet Toolbox for Matlab
© University of Vigo
http://www.gts.tsc.uvigo.es/~wavelets/matlab_uvi_wave.html

Waagstein, R. 1988. Structure, composition and age of the Faeroe basalt plateau. *In: Morton, A.C. & Parson, L.M. (eds) Early Tertiary Volcanism and the opening of the NE Atlantic. Geological Society, London, Special Publications*, **39**, 225 – 238.

Waagstein, R. and Andersen, C. 2003. Well completion report: Glyvursnes-1 and Vestmanna-1, Faroe Islands. *SeiFaBa Report. Geological Survey of Denmark and Greenland (GEUS).*

Waddams, P. & Cordingley, T. 1999. The regional geology and exploration potential of the NE Rockall Basin. *In: Fleet, A. J. & Boldy, S. A. R. (eds) Petroleum Geology of Northwest Europe: Proceedings of the 5th Conference. Geological Society, London,* 379 – 390.

Warner, M., Morgan, J., Chironi, C., Tong, C. H. & Stekl. I. 2002. Sub-basalt: what's the problem? *Journal of Conference Abstracts*, 7(2), 197.

WaveLab Library of Routines for Matlab version 8.02
© Stanford Statistics Department
http://www-stat.stanford.edu/~wavelab/

Wepfer, W. W. & Christensen, N. I., 1990. Compressional wave attenuation in oceanic basalts. *J. Geophys. Res.*, **95**, 17431 – 17439.

Wepfer, W. W. & Christensen, N. I., 1991. Q structure of the oceanic crust. *Mar. Geophys. Res.*, **13**, 227 – 237.

White, J. E. 1965. Seismic waves: radiation, transmission and attenuation. *McGraw-Hill, New York.*

White, R. E. 1992. The accuracy of estimating Q from seismic data. *Geophysics*, **57**(11), 1508 – 1511.

White, N. & Lovell, B. 1997. Measuring the pulse of a plume with the sedimentary record. *Nature*, **387**, 888 – 891.

White, R. S. & McKenzie, D. 1989. Magmatism at rift zones: the generation of volcanic continental margins and flood basalts. *J. Geophys. Res.*, **94**, 7685 – 7729.

White, R. S., Smallwood, J. R., Fliedner, M. M., Boslaugh, B., Maresh, J., Fruehn, J. 2003. Imaging and regional distribution of basalt flows in the Faeroe-Shetland Basin. *Geophysical Prospecting*, **51**, 215 – 231.

Wiener, N. 1949. Extrapolation, Interpolation, and Smoothing of Stationary Time Series. *Wiley, New York.*

Wood, D. A. 1979. Dynamic partial melting: its applications to the petrogeneses of basalts erupted in Iceland, the Faeroe Islands, the Isle of Skye (Scotland) and the Troodos massif (Cyprus). *Geochim. Cosmochim. Acta.*, **43**, 1031 – 1046.

Wright, T. L., Grolier, M. J. & Swanson, D. A. 1973. Chemical variation related to the stratigraphy of the Columbia River Basalt. *Geol. Soc. Am. Bull.*, **84**, 371 – 386.

Wu, R. S. & Aki, K. 1988. Scattering and Attenuation of Seismic Waves. *Birkhauser.*

Zener, C. 1948. Elasticity and Anelasticity of Metals. *University of Chicago Press.*

Ziegler, P. A. 1988. Evolution of the Arctic-North Atlantic and the western Tethys. *American Association of Petroleum Geologists Memoir*, **43**.

Ziolkowski, A., Hanssen, P., Gatliff, R., Jakubowicz, H., Dobson, A., Hampson, G., Li, X-Y., & Liu, E., 2003. Use of low frequencies for sub-basalt imaging. *Geophysical Prospecting*, **51**, 169 – 182.